UiT The Arctic University of Norway

Faculty of Engineering Science and Technology

Institute of Industrial Technology

Study of the in-cloud droplet impingement on cylinders for low values of the Stokes number

Pavlo Sokolov

A dissertation for the degree of Philosophiae Doctor in Engineering Science, March 2021

Table of Contents

List of Tables

List of Figures

List of Abbreviations and Definitions

1D	One-Dimensional
2D	Two-Dimensional
3D	Three-Dimensional
AOA	Angle of Attack
BBO	Basset-Boussinesq-Oseen
CAPS	Cloud, Aerosol and Precipitation Spectrometer probe
CFD	Computational Fluid Dynamics
CRREL	Cold Regions Research and Engineering Laboratory
CU	Cranfield University
FRonTLINES	Frost and rime icing impact on overhead transmission lines
FSSP	Forward Scatering Spectrometer Probe
Icebox	Ice monitoring, forecasting, mapping, prevention and removal toolbox
ISO	International Standard Organization
IWAIS	International Workshop on Atmospheric Icing of Structures
LB	Langmuir and Blodgett
LWC	Liquid Water Content
M&S	Makkonen and Stallabrass
MR	Maxey and Riley
MVD	Median Volume Diameter
NASA	National Aeronautics and Space Administration
NFR	Research Council of Norway (Norges Forskningsråd)
ODE	Ordinary Differential Equation
RANS	Reynolds Averaged Naiver-Stokes
RMC	Rotating Multi-Cylinder
SA	Spalart-Allmaras
SLD	Supercooled Large Droplets
SST	Shear Stress Transport
UDF	User Defined Function
UiT	UiT – The Arctic University of Norway
URANS	Unsteady Reynolds Averaged Naiver-Stokes

VTT	VTT Technical Research Centre of Finland
VWD	Volume Weighted Diameter

Foreword

The work described within this thesis is primarily conducted under the FRonTLINES ("Frost and rime icing impact on overhead transmission lines") and Icebox ("Ice monitoring, forecasting, mapping, prevention and removal toolbox") projects. Both projects are funded by the Research Council of Norway (Norges Forskningsråd; NFR) and Statnett SF, and are conducted by consortium of partners, with UiT being one of them. The primary contribution of the UiT (and by extension – this thesis) to the both projects is the analytical and numerical modeling of the supercooled water droplets impingement on the circular cylinders for the practical application in the modeling of the atmospheric ice accretion on the power lines.

Acknowledgements

Throughout the writing of this dissertation, I have received a great deal of support and assistance.

I would first like to thank my supervisor, Professor Muhammad Shakeel Virk, whose expertise was invaluable in formulating the research questions and methodology. Your insightful feedback pushed me to sharpen my thinking and brought my work to a higher level.

I would also like to thank my tutors, Dr. Klas Pettersson and Dr. Bjørn Egil Nygaard, for their valuable guidance throughout my work. You provided me with all the tools that I needed to choose the right direction and successfully complete my dissertation. I would also want to thank Dr. Bjørn Egil Nygaard for all of the opportunities, I was given in terms of project work to further my research.

In addition, I would like to thank my parents for their counsel and sympathetic ear. You are always there for me. Finally, I could not have completed this dissertation without the support of my dear friend and colleague, Jia Yi Jin, who provided wonderful discussions as well as happy distractions to rest my mind outside of my research.

Abstract

The study of the atmospheric ice accretion has received some attention in the previous decades, with the available knowledge spanning from the works of the Langmuir and Blodgett (1946) on the Mt. Washington Observatory till the analytical parameterization of the Finstad et al. (1988), with the latter being the current analytical benchmark and the integral part of the ISO 12494 "*Atmospheric Icing on Structures*", which is a current guideline for the analytical estimation of the ice loads on structures. A detailed literature review of the present and past analytical parameterizations of the in-cloud/droplet impingement on circular cylinders is carried out as a part of this thesis.

One of the major limitations of the Finstad et al. parameterization is its applicability for the range of the overall collision efficiencies of $0.07 < E < 0.63$, resulting from the experimental verification by (Makkonen and Stallabrass, 1987). Furthermore, the ISO 12494 standard states that the current analytical model underestimates the accreted ice masses for the collision efficiencies values below $E < 0.10$ and the Finstad et al. themselves postulate that they consider the lower limit of droplet inertia parameter being $K = 0.25$ in their model. Below this limit Finstad et al. advise to "*recalculate the droplet trajectories using the appropriate drag coefficients for each droplet size in the spectra*". As evidenced by the available data from the test span measurements at the Ålvikfjellet test span in Norway, the majority of the extreme ice loads occur for the value of K below the critical value of 0.25.

Thus, there is a need for a method which allows for better prediction and estimation of ice loads for such conditions. However, the calculation of the "history" term, which is a non-steady state drag coefficient, which needs, ideally, to be taken into account in the modeling of the atmospheric ice accretion for the cases when $K < 0.25$ is rather challenging. Instead, the usage of the "idealized" Langmuir distributions is suggested, those originally proposed by (Langmuir and Blodgett, 1946) and (Howe, 1990). Those distributions have the same values of the Median Volume Diameter (MVD) as the typically postulated assumption of the monodispersed distribution from the ISO 12494, which makes them suitable under the current framework.

One major advantage of using the Langmuir distributions is that they effectively have a higher value of the droplet inertia parameter K, due to the nature of the "spectrum-averaging" procedure, when compared to the simple monodispersed distribution, while maintaining all other parameters, primarily the MVD and the Liquid Water Content (LWC) constant. Within the scope of this work this analytical calculation procedure using the Langmuir distribution spectra for both the analytical formulae of (Finstad et al., 1988) and the (Finstad, 1986) droplet trajectory equations is presented. Moreover, the "generalized" setup of the numerical Computational Fluid Dynamics (CFD) simulations is also presented for the purpose of modeling the ice accretions in the low limit of K. The potential usage, possible advantages and comparison of the results of the CFD modeling are discussed, as the current available CFD tools are well suitable for general modeling of ice accretion on structures (Makkonen and Lozowski, 2005).

The performed validation of the new calculation procedure was done using both the original (Makkonen and Stallabrass, 1984) and the FRonTLINES ("Frost and rime icing impact on overhead transmission lines") project data, with the experimental data of later dealing almost exclusively for the dry ice growth accretions in the range of $K \leq 0.25$. The conducted analyses, using both the analytical and the numerical

tools, indicate that the usage of the Langmuir droplet distribution spectra can result in large variance of the overall collision efficiencies and, as a result, the accreted ice masses, even under the same operating conditions, due to the way distributions change the value of the droplet inertia parameter *K*.

The conducted analytical and numerical calculations along with analysis of the available experimental data suggests that the Langmuir distributions C and D are consistently good in estimation for both the Makkonen and Stallabrass and the FRonTLINES experimental data. In addition, the available experimental distribution for the FRoNTLINES test cases has a tendency of slight overestimation of the results for the overall collision efficiencies and the accreted ice masses using the analytical calculations. The reason for this is believed to primarily be the constraining the cloud impingement parameters to 0.01 for the values of $K < 0.17$. While this constraint allows analytical model to predict non-zero ice masses under any arbitrary conditions, it may result in the overestimation of the accreted ice masses. However, it may not be sufficiently detrimental for the purposes of the extreme value analysis.

For the CFD calculations of the same data, the absolute error is approximately 0.01, and using the experimental distribution, Langmuir C and D distributions yield close agreement with the obtained results. Overall, the numerical simulations are well suited for detailed studies of the droplet distribution spectrum effects and the ice accretion modeling in general, as multiple different cloud impingement parameters can be investigated and compared in detailed manner, which is not possible just by using analytical approach.

In addition, while performing analytical calculations for the FRonTLINES experiments it was noted that the empirical icing density parameterization used (Makkonen and Sallabrass fit to the Macklin equation) resulted in the end cylinder diameters to be a fraction of a millimeter larger than the initial ones, while the accreted ice densities were in the "expected range" based on the ISO 12494 classification. The analytical calculations using the same empirical icing density parameterization against the original data (that being the Makkonen and Stallabrass experiments) showed that the end cylinder diameter values calculated using the analytical model match the experimental results well, while the accreted ice densities are underestimated slightly. These results necessitated the investigation into the available empirical icing density parameterizations. The obtained results suggest that there are fundamental limitations with the empirical icing density parameterizations based on the so-called Macklin parameter, in the analytical calculations as the obtained results with it for the low values of K ($K \leq 0.25$) show that the end cylinder diameters barely change from the initial ones, while the density values quickly reach the lower constraint of the 100 kg/m^3 employed in the analytical calculations.

Based on the conducted analysis with the Langmuir droplet distribution spectra, some possible applications and comparisons of the methodology presented within this work is discussed. In addition, this work presents the conclusions and the existing knowledge gaps. The latter, in particular being the challenges with the "history" term and the need to incorporate it in the analytical and the numerical calculations. Furthermore, there is need to take the ice ablation into the account, as no known empirical icing model takes it into the account and based on the observations on the Ålvikfjellet test span, periods of ice accretion are followed by the periods of ice shedding/ablation which reduces the accumulated ice loads.

1 Introduction

This thesis in the field of the Engineering Science concerns itself with the study of impingement of supercooled water droplets on the circular cylinders for the "dry growth" icing conditions. The work described within this thesis is primarily conducted under the FRonTLINES ("Frost and rime icing impact on overhead transmission lines") and Icebox ("Ice monitoring, forecasting, mapping, prevention and removal toolbox") projects. Both projects are funded by the Research Council of Norway (Norges Forskningsråd) and Statnett SF, and are conducted by consortium of partners, with UiT being one of them. The primary contribution of the UiT (and by extension – this thesis) to the both projects is the analytical and numerical modeling of the supercooled water droplets impingement on the circular cylinders for the practical application in the modeling of the atmospheric ice accretion on the power lines.

Icing on power lines can cause major disruptions in electricity supply networks. These disruptions can lead to excessive costs for repairs as well as other consequential losses. There is also a risk to human safety for employees tasked with the repair of power lines in harsh environmental conditions. Icing on power lines is a problem experienced in most high-latitude countries of which Norway has some of the highest recorded ice loads (Nygaard & Fikke, 2012). The most adverse weather factors concerning electric power lines, masts and towers for telecommunication are generally related to extreme winds and icing from wet snow and rime (in-cloud) icing conditions (Fikke et al. 2008). As an example of adverse effects, the atmospheric ice accretion can cause on the power lines, during the winter seasons 2013/2014 and 2014/2015 Statnett SF, the transmission system operator in Norway, experienced cases of severe atmospheric icing causing the collapse of transmission towers and the failure of other components (Nygaard et al. 2017). One of the affected lines was an entirely new 420 kV transmission line crossing an exposed mountain area just north of the Hardanger Fjord in Norway (Figure 1). The measured ice load was more than double the design load, indicating that the ice loads had been significantly underestimated in the pre-construction phase. At that time, the design load had been estimated by applying the best available meteorological expertise (Nygaard et al. 2017).

Figure 1 – Accumulated rime ice on a broken ground wire, January 2014. An ice load of 68 kg/m was estimated based on its diameter and an ice density sample (Nygaard et al., 2017). (Photo: Ole Gustav Berg, Statnett).

However, before discussing the main results achieved within this thesis, it is important to give a background overview about the atmospheric icing itself and the previous works in the field of the atmospheric icing on structures.

1.1 Atmospheric icing on structures: an overview

Ice mass accumulation on the human-made objects primarily comes from atmospheric icing, i.e., in-cloud or precipitation icing. For both the in-cloud icing and freezing rain/drizzle, the ice mass, accreted on the object, originates from the impingement of the supercooled water droplets onto the object in question.

The supercooled water droplets originate from water-saturated air, originating, for example, from the evaporation of water from the surface of large bodies of water, such as oceans, seas, large lakes etc. or wet land, which cools down, as the vapor rises in altitude, and, the presence of the Cloud Condensation Nuclei (CCN), a small, (sub) micron-sized liquid or solid particles, onto which the water vapor condenses. In the absence of the ice nucleation, the supercooled water droplets in atmosphere can be encountered in the temperature range of about $-37°\text{C} < T < 0°\text{C}$, below which the homogeneous freezing of the supercooled water droplets will occur (Murray et al., 2012).

The supercooled droplets can be transported by the air, normally in the form of clouds, over significant distances. Thus, the occurrence of icing events directly correlates with the weather, i.e., low temperatures, low cloud base, dense fog, high humidity, etc. At this point, the similarities between the precipitation and the in-cloud icing end, as the "mechanism" by which they cause the accumulation of the ice mass is different. For the precipitation icing, it is a freezing rain or drizzle, falling down from the sky onto the object. In case of precipitation icing the dominant "force" behind it is gravity, not the flow, and it is commonly assumed that the collision efficiency, α_1 (also referred as E) of the "droplets" in the case of precipitation icing is equal to 1, i.e., $\alpha_1 = 1$. The primary reason behind this is two-fold. First, is the "trajectory" of such a droplet falling under the influence of gravity – it is a straight line with no assumed deviation due to the influence of wind. Second, is the size of the "droplets" in the precipitation icing. The size of a typical drop(let) in a rainfall is of an order $10^{-1} – 10^{0}$ mm ($10^{2} – 10^{3}$ μm), while for in-cloud icing the typical size of droplets is of an order $10^{0} – 10^{1}$ μm ($10^{-3} – 10^{-2}$ mm).

The main equation in the analytical modelling of icing, which describes the rate of icing per unit time is given as (ISO 12494, 2001):

$$\frac{\mathrm{d}M}{\mathrm{d}t} = \alpha_1\alpha_2\alpha_3 wAv \tag{1.1}$$

In this equation, otherwise known as "*Makkonen model*" (Makkonen, 2000), A is the cross-sectional area of the object (with respect to the direction of the particle velocity vector, v; $A = LD$, where L is the length of the object in z-direction, and D is the characteristic length of the object, i.e. chord length, leading edge diameter, cylinder diameter, etc.), w is the liquid water content, α_1 is the collision efficiency, α_2 is the sticking efficiency, α_3 is the accretion efficiency. The correction factors α_1, α_2 and α_3 represent different processes that may reduce $\mathrm{d}M/\mathrm{d}t$ from its maximum value wAv (the units of vAw term are in g/s = $\mathrm{d}M/\mathrm{d}t$. The value of $\mathrm{d}M/\mathrm{d}t = vAw$ is the theoretical maximum impingement rate.). These

correction factors vary between 0 and 1. Factor α_1 represents the efficiency of collision of the droplets, i.e. it is the ratio of the flux density (in this particular case it is the mass flux (flow) rate) of the droplets that hit the object, to the maximum flux density, which is a product of the mass concentration of the droplets, *w*, and the velocity, *v*, of the droplets with respect to the object.

Thus, the rain drops have considerably higher "inertia" than the droplets in the in-cloud icing, due to their larger sizes and gravity-dominated (i.e., inertia-dominated) behavior. The primary determining characteristic in the precipitation icing is the freezing efficiency, α_3 and the sticking efficiency, α_2, which can be calculated as a reciprocal of wind speed, i.e., $\alpha_2 \approx 1/v$, although this assumption is mostly valid for the wet snow precipitation accretion, while for the (supercooled) water droplets $\alpha_2 = 1$ is a typical assumption (ISO 12494, 2001). However, for the in-cloud icing the dominating process behind the ice accretion is the (overall) collision efficiency α_1 which is a result of inertia and a drag, acting on the droplet. As with precipitation icing, it is generally assumed that the $\alpha_2 = 1$ for the in-cloud icing of the supercooled water droplets and $\alpha_3 = 1$ for "dry growth" (all droplets freeze on impact; rime ice; no water runback or water film) and $\alpha_3 \neq 1$ ($\alpha_3 < 1$; "wet growth"; glaze ice; water film and water runback are present) conditions. Within the scope of this thesis, the assumption of the "dry growth" is made, i.e., $\alpha_2 = \alpha_3 = 1$ and thus the main focus is on the pure impingement of the supercooled water droplets.

In studying in-cloud icing the main interest lies in the parameterization of characteristics of an in-cloud droplet impingement on cylinders. The study of in-cloud icing is not a new scientific field with some major milestones in terms of mathematical models being works by (Langmuir and Blodgett, 1946), (Cansdale and McNaugthon, 1977), (Lozowski et al., 1979), (Stallabrass, 1980), (Makkonen, 1984) and (Finstad et al., 1988a). The latter being independently verified by (Stallabrass and Makkonen, 1987) serves as a current benchmark model for atmospheric icing and it is a part of the governing standard ISO 12494 "*Atmospheric Icing of Structures*" (ISO 12494, 2001). The core of the Finstad et al. model uses a so-called "Median Volume Diameter approximation" (MVD) in order to parameterize the in-cloud droplet spectrum using a singular value, and an assumption that the cloud droplet distribution can be adequately represented using a uniform droplet distribution, where all the droplets have the same diameter, that is corresponding to cloud MVD. The verification of the concept was carried out by Finstad in her doctoral thesis (Finstad, 1986), later expanded in paper of (Finstad et al., 1988a) and based on the results of (Makkonen and Stallabrass, 1987) it can be stated that the Finstad et al. model is applicable for the range of droplet overall collision efficiencies of $0.07 < \alpha_1 < 0.63$.

Consequently, the collision efficiency α_1 is reduced from 1, because small droplets tend to follow the air streamlines and may be deflected from their path towards the object, as shown in Figure 2.

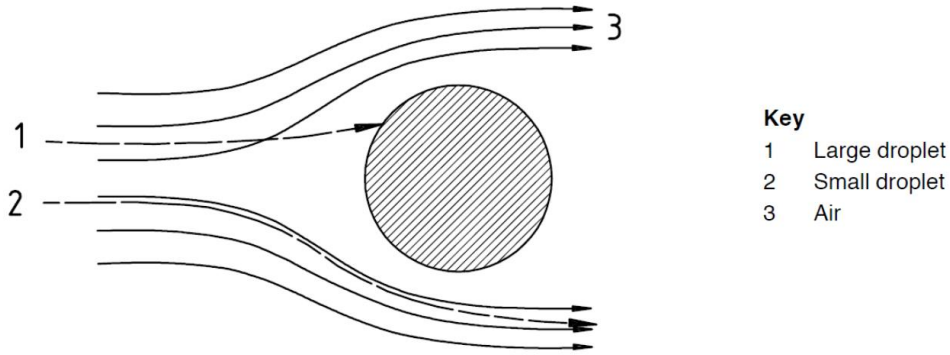

Figure 2 – Air streamlines & droplet trajectories around a cylindrical object (ISO 12494, 2001).

In the broadest case of a given fluid flow, the "behavior" of water droplets can be explained using the definition of the Stokes number (which is also known as the “droplet inertia parameter”, *K*):

$$Stk = \frac{t_0 u}{L} = K \tag{1.2}$$

where L is the characteristic length of the obstacle and t_0 is the relaxation time of the particle, which describes its exponential velocity decay due to influence of drag and it is defined as:

$$t_0 = \frac{\rho_p d_p^2}{18\mu_f} \tag{1.3}$$

in which ρ_p is the particles density, d_p is the particle’s diameter and μ_f is the absolute viscosity of the fluid. A particle with a low Stokes number follows fluid streamlines (perfect advection), while a particle with a large Stokes number is dominated by its inertia and continues along its initial trajectory, thus colliding with the object. In the most extreme cases, if $Stk \rightarrow 0$ the droplet will follow the streamline *perfectly*. On the contrary, if $Stk \rightarrow \infty$, the droplet trajectory will be a *perfectly* straight line. As it can be seen from Equations (1.2) and (1.3), larger particles, or those moving at higher velocities, will have higher Stokes number and thus – higher possibility of collision with the object, hence defining physical meaning of the collision efficiency.

However, in reality, the behavior of the droplet in actual flow is more complicated than in this simplistic case, and the collision efficiency cannot simply be explained using just the definition of Stokes number, thus requiring the use of some sort of analytical and/or empirical formulations in order to calculate the overall collision efficiency. Presently, the overall collision efficiency formulation by Finstad et al. (Finstad et al., 1988a) is used in the ISO 12494 for calculation of α_1, which is itself based on the earlier parameterization by Langmuir and Blodgett (Langmuir and Blodgett, 1946). The key difference between these two models is a revision of droplet trajectories on a more modern machine, with more modern estimates of droplet drag coefficient, from experimental study of (Beard and Pruppacher, 1969). Moreover, Finstad simplified the elaborate scheme of Langmuir and Blodgett when it comes to correction of droplet's inertia parameter, due to non-Stokesian flow regime, which resulted in completely different parameterization for droplet collision efficiency (Finstad et al., 1988a).

In addition, the Finstad et al. model is one of the more complete models featuring parameterizations of local collision efficiencies, droplets impact velocities and maximum impingement angles. Furthermore, the model provides the way of calculating the ice shapes on iced cylinder under the assumption that developing ice layers will change the local collision efficiencies values and using variable ice density formulation of (Makkonen, 1984), however, those calculations are absent from final published version (Finstad et al., 1988a), which makes them somewhat preliminary in nature.

Finally, the model discusses more complete droplet trajectory equations, following approach of (Oleskiw, 1982), which may be useful when potential flow approximation is not valid and viscous and boundary layer effects may be of importance. The model validation for cylinders and airfoils was done as part of the doctoral thesis itself (Finstad, 1986), subsequently, the validation for cylinders was independently carried out by Makkonen and Stallabrass (Makkonen and Stallabrass, 1987), who recommended employing it over original Langmuir and Blodgett formulations in future studies. At present, this parameterization is the benchmark for calculation of droplet collision efficiencies on cylinders and it is an integral part of governing ISO standard – ISO 12494 "*Atmospheric Icing of Structures*" (ISO, 2001).

However, in order to better understand the need for the research, conducted in this work, as well as the limitations of the current understanding of the analytical parameterizations of the cloud impingement of the supercooled water droplets, a review of the already existing analytical models is necessary.

1.1.1 Analytical parameterizations of droplet collision efficiency

The purpose of this section is to provide a brief overview of the analytical collision efficiency parameterizations for the impinging droplets that have some "historic" value. Each model will be described briefly, in order to provide the general overview, such as, when the model in question was developed, what considerations the respective authors have been using, for what applications the model has been applied and what are the unique characteristics of it, etc.

Langmuir and Blodgett (LB) parameterization (1946). The Langmuir and Blodgett research (Langmuir and Blodgett, 1946) was mostly aimed at estimating the water droplet trajectories moving past infinitely long circular cylinder for cases, where Stokes' law is not applicable. Stokes law relates the drag force on the particle, acting on it as:

$$F_d = 6\pi\mu_f r_p v \tag{1.4}$$

where F_d is the drag (frictional) force, r_p is the particle radius, v is the relative droplet velocity, defined as:

$$v = \sqrt{u^2 - v^2} \tag{1.5}$$

in which u and v are the absolute air and droplet velocities, respectively. The Stokes' law is only valid for such a flow for which the droplet's Reynolds number $Re_d << 1$, meaning that the inertial effects are non-existent and only viscous effects are present. This is a flow at very low velocities, thus also called the *creeping flow*. It is worth mentioning that within the scope of this thesis it is assumed that the value

of Re_d is relative the *droplet's* Reynolds number *with respect to air*, unless explicitly mentioned otherwise. On the other hand, the (farfield) droplets' Reynolds number *Re* is calculated as:

$$Re = \frac{\rho_f d_p u}{\mu_f} \tag{1.6}$$

which is used in the calculation of the Langmuir parameter, ϕ, defined as:

$$\phi = \frac{Re^2}{K} \tag{1.7}$$

Langmuir and Blodgett used a General Electric developed analogue computer, called Differential Analyzer, to obtain the results for 61 droplet trajectories for the flow around cylinders, ribbons and spheres. The Langmuir and Blodgett model is one of the more complete models featuring parameterizations for overall and stagnation line collision efficiencies, maximum impingement angle and droplet's impact velocity, along with correction of overall collision efficiencies for low values of overall collision efficiency and different parameterization schemes for higher overall collision efficiency $E > 0.5$.

Moreover, Langmuir and Blodgett produced a series of plots for droplets' inertia and Langmuir parameter, *K*, and ϕ, respectively which may be used to obtain results graphically. The validation of results for cylinders was done in the original study, and it consisted of comparison with experimental data from Mt. Washington Observatory, obtained by few rotating cylinders, exposed to icing at various conditions (Langmuir and Blodgett, 1946), in addition to some experimental data, obtained by aircraft flying at 200 mph (miles per hour).

Lozowski et al. parameterization (1979). This parameterization is a part of the model, originally developed in 1979 by Lozowski, Stallabrass and Hearty (Lozowski et al., 1979), and published in 1983 (Lozowski et al., 1983a) for studying helicopter icing. This model includes the liquid water on the surface, known as "water runback" in it, due to the steady-state heat balance on the cylinder's surface, calculated using the Messinger's thermodynamic model (Messinger, 1953), which is the main innovation of this model. Messinger's thermodynamic model is also the thermodynamic model behind α_3 in the ISO 12494 model.

The parameterization of droplet trajectories is essentially similar to Langmuir and Blodgett approach, however slightly different empirical fit was used in order to avoid usage of Langmuir and Blodgett corrections for different ranges of overall collision efficiency *E*, thus attempting to use single parameterization scheme for entire range of *E*. Moreover, the model introduced an empirical formulation for local collision efficiencies β as function of impingement angle θ, which allows calculation of ice shapes, with limitation being assumed constant ice density of $\rho = 890$ kg/m^3 in their model. The experimental verification of model for cases of ice accretion on cylinders have been conducted by Lozowski et al. (Lozowski et al., 1983b), the verification for aircraft icing have been done independently by Bain and Gayet (Bain and Gayet, 1982).

Additionally, in 1977 Cansdale and McNaughtan (Cansdale and McNaughtan, 1977) developed the icing model for similar applications. Again, a slightly re-defined values of original Langmuir and Blodgett parameterization scheme was used by them for calculations of the droplet collision efficiency, in order to collapse it to single curve for entire range of *E*, which also differs from parameterization values those of Lozowski et al. (Lozowski et al., 1983a). However, Cansdale and McNaughtan model is more simplistic in its approach and only takes into account the flow near stagnation point.

Stallabrass parameterization (1980). This model was developed for studying icing of fishing trawlers (Stallabrass, 1980). The main difference in this model, when it comes to droplet collision efficiency parameterization, is an attempt to eliminate the use of multiple curves and droplet trajectory equations altogether for the estimation of the overall collision efficiency, and to collapse the parameterization to a single curve. As a result, the end formulae differs significantly from other models, which are based on derivation of original Langmuir and Blodgett formulations.

The Stallabrass model is also applicable to *rectangular* cross-sections, as opposed to previous models, which are only applicable to *circular* cross-sections. Model validation has been done in icing tunnel (Stallabrass, 1980), to demonstrate the effects of air temperature and cylinder diameter on ice formations, however, it should be noted that for icing trawlers the main ice accretion factor is expected to be sea spray, which can be characterized by large diameter of droplets. The heat balance calculation is also employed in this model, and it uses the Messinger thermodynamic model for calculation of steady-state heat balance.

Makkonen parameterization (1984). The Makkonen model was developed specifically for power cable icing (Lozowski and Makkonen, 2005). The model assumes cylinder being slowly rotating due to limited torsional stiffness, which results in uniform ice accumulation on the surface and no need for consideration of water runback. The model does not take into account such effects as maximum impingement angles or local collision efficiencies, thus being constrained to the flow near stagnation point, however, due to assumption of slow axial rotation, this should not be a limitation, provided adequate time stepping is used in calculations.

Two major innovations of this model are, estimation of conductor's diameter change due to continuous ice accretion and introduction of variable ice density, using Macklin parameter (Macklin, 1962) in the ice density empirical formulation. Additionally, the model takes into account boundary layer effects of the cylinder in calculation of the heat transfer coefficient (Makkonen, 1985) in addition to employing the Messinger model for heat balance calculation. Since the model is concerned with flow past stagnation line, the empirical parameterization follows that of Cansdale and McNaughtan, albeit with slightly different empirical fit and introduces separate two-point approximation of what Makkonen calls "real" collision efficiency, which is an attempt to collapse multiple curves of *E* for different droplet's sizes into one. The “real” overall collision efficiency *E*, in Makkonen model is calculated with following empirical fit (Makkonen, 1984):

$$E = 0.69E_m^{0.67} + 0.31E_m^{1.67} \tag{1.8}$$

The reason this parametrization is dubbed “real” overall collision efficiency is following. In his work, (Makkonen, 1984) correctly notes that in order to precisely estimate overall collision efficiency, the

formulation for E_m has to be applied for all droplet bins within the droplet distribution spectrum. However, since exact droplet distribution is typically not known, or, more commonly, only distribution MVD is known, it is not possible to recalculate the overall collision efficiency with full droplet distribution spectrum. Therefore, this simple linear parametric fit was developed in order to "emulate" the overall collision efficiency of full droplet distribution spectrum, to an extent.

As noted in (Lozowski and Makkonen, 2005), the model received limited experimental validation due to strict requirements on quality of experimental data it enforces, however, in cases where it has been tested, the agreement with experimental values was good.

Finstad parameterization (1986). The final parameterization approach is a parameterization developed by Finstad (Finstad, 1986). The key difference in this model is a revision of droplet trajectories on a more modern machine, with more modern estimates of droplet drag coefficient, from experimental study of (Beard and Pruppacher, 1969). Moreover, Finstad simplified the elaborate scheme of Langmuir and Blodgett when it comes to correction of droplet's inertia parameter, due to non-Stokesian flow regime, which resulted in completely different parameterization for droplet collision efficiency (Finstad et al., 1988a).

In addition, the model is one of the more complete models featuring parameterizations of local collision efficiencies, droplet impact velocities and maximum impingement angles. Furthermore, the model provides the way of calculating the ice shapes on iced cylinder under assumption that developing ice layers will change the local collision efficiencies values and using variable ice density formulation of (Makkonen, 1984), however, those calculations are absent from final published version (Finstad et al., 1988a), which makes them somewhat preliminary in nature.

Finally, the model discusses more complete droplet trajectory equations, following approach of (Oleskiw, 1982), which may be useful when potential flow approximation is not valid and viscous, and boundary layer effects may be of importance. The model validation for cylinders and airfoils was done as part of doctoral thesis itself (Finstad, 1986), subsequently, the validation for cylinders was independently carried out by Makkonen and Stallabrass (Makkonen and Stallabrass, 1987), who recommended employing it over original Langmuir and Blodgett formulations in future studies. At present, this parameterization is the benchmark for calculation of droplet collision efficiencies on cylinders and it is an integral part of governing ISO standard – ISO 12494 "*Atmospheric Icing of Structures*" (ISO, 2001).

1.1.2 Limitations of overall collision efficiency calculations for low values of *K*

As it was mentioned previously, the Finstad et al. model is valid for the range of the overall collision efficiencies $0.07 < E < 0.63$, as this was the range the model was tested against in the icing wind tunnel experiments of (Makkonen and Stallabrass, 1987). According to (Finstad et al. 1988a), they consider the lower limit of droplet inertia parameter being $K = 0.25$ in their model, below which Finstad et al. advise to "*recalculate the droplet trajectories using the appropriate drag coefficients for each droplet size in the spectra*". All the previous discussion and formulae, which uses droplet diameter d_p in them, assume and use a singular value – the Median Volume Diameter (MVD) of the spectrum. MVD is such

a value, for which half of the cloud droplet volume will be concentrated in droplets with larger or smaller diameters, respectively. The MVD of the spectrum is calculated as:

$$\mathrm{MVD} = \left(\frac{0.5 - w_{i-1}}{w_i - w_{i-1}} \times \left(d_i^4 - d_{i-1}^4\right) + d_{i-1}^4\right)^{0.25} \tag{1.9}$$

where w_{i-1} is a *cumulative* LWC fraction, such that $w_{i-1} < 0.5$ and w_i is a cumulative LWC fraction, such that $w_i > 0.5$, d_{i-1} and d_i are droplet diameters associated with w_{i-1} and w_i respectively. Subscripts i and i–1 correspond to the bins in the spectrum. What the Equation (1.9) does, is finding a "magic" bin in which the cumulative LWC is $w = 0.5$, *exactly*. The droplet diameter, associated with $w = 0.5$ is the MVD value of the *entire* droplet distribution spectrum. The principle behind Equation (1.9) can be used to calculate the MVD of any given droplet distribution spectrum, and also – to calculate the MVD values of each *bin* in the spectrum. In this case $w_{i-1} = 0$, $w_i = 1$, d_{i-1} and d_i are the smallest and the biggest droplet diameters in the bin (lower and higher bin bound).

The usage of MVD originated from (Langmuir and Blodgett, 1946) and as later showed by (Finstad et al., 1988b) it is an ideal single-valued approximation for droplet spectra. The reason for this assumption is the difficulty, associated with measurements of distribution of the micron-sized droplets in nature. However, Jones et al. has recently showed that MVD (Jones et al., 2014) approximation may not always be valid and in natural conditions such as on Mt. Washington Observatory (New Hampshire, USA), and the use of a droplet distribution spectrum can yield significantly better results over a monodisperse distribution when comparing ice accretion data on a multicylinder device. However, the issue with the calculations of the cloud impingement parameters, using the full droplet distribution spectrum, is that the droplet spectra information is typically unavailable, especially for the icing in natural conditions.

Another major difficulty with the calculation of the droplet trajectories "using the appropriate drag coefficients" is the trajectory equation itself in this case. This trajectory equation, following approach in (Oleskiw, 1982), in a non-dimensional vector form, with added buoyancy and gravitational effects, is given as (Oleskiw, 1982):

$$\frac{\mathrm{d}\overline{v_p}}{\mathrm{d}t} = \underbrace{\frac{2\left(\rho_\mathrm{p} - \rho_\mathrm{f}\right)}{\left(2\rho_\mathrm{p} + \rho_\mathrm{f}\right)}\overline{g}}_{\mathrm{I}} - \underbrace{\frac{3\rho_\mathrm{f}(C_D Re/24)}{4r_\mathrm{p}\left(2\rho_\mathrm{p} + \rho_\mathrm{f}\right)}\left|\overline{v_p} - \overline{v_f}\right|\left(v_p - v_f\right)}_{\mathrm{II}}$$
$$- \underbrace{\frac{9\rho_\mathrm{f}}{\left(2\rho_\mathrm{p} + \rho_\mathrm{f}\right)r_p}\sqrt{\frac{\mu_\mathrm{f}}{\pi\rho_\mathrm{f}}}\int_{-\infty}^{\mathrm{t}}\frac{\mathrm{d}\overline{v_p}}{\mathrm{d}\tau}\frac{\mathrm{d}\tau}{\sqrt{t-\tau}}}_{\mathrm{III}} \tag{1.10}$$

Where v_p is particle's (droplet's) velocity, r_p is the particles radius, v_f is the fluid (air) velocity and g is the gravitational acceleration. All quantities in this equation are non-dimensional and,

- I is the buoyancy and gravitational acceleration of the droplet;
- II is the steady viscous drag;
- III is the "history" term also known as the Basset force.

The “history term” aka. the Basset force and the history force is a kind of viscous force, which arises due to acceleration between continuous (fluid) and dispersed (particles, droplets) phases and the development of the boundary layer near the interfacial surface (*between the continuous and the dispersed phase*). The Basset force describes the force due to the lagging boundary layer development with changing relative velocity (acceleration) of bodies moving through a fluid. And due to this lagging, the relative velocities and the accelerations of bodies moving through a fluid at a time *t*, depend on *all* previous changes in velocities and accelerations. In short, the current velocities and accelerations depend on the *history* of velocities and accelerations, hence why the name “history term”. The Basset force is commonly neglected for practical reasons; however, it can be substantially important for particle motion when a high acceleration rate for the particle is encountered. During the process of particle acceleration, the total force acting on the particle can be many times that in the steady state.

The question is – how exactly important is the Basset force? Finstad et al., referring to Norment, suggest that history term becomes of importance in cases where:

$$N_A = d\left|\frac{\mathrm{d}u(\tau)}{\mathrm{d}\tau}\right|\frac{1}{v^2} > 0.01 \tag{1.11}$$

In which N_A is the acceleration modulus. If the acceleration modulus threshold is exceeded, it needs to be incorporated into the trajectory equation. How Finstad et al. writes: “*Numerical results from the trajectory integration model presented above show that N_A is well within this limit under most conditions of accretion on cylinders. However, for $K \leq 0.5$, N_A may reach values ≥ 0.01 just before impact, and for $K \leq 0.20$, the limit is exceeded as much as a few millimeters in front of the cylinder surface. For these small K values then, the effect of the history term is to decrease the droplet’s deceleration and increase both its total velocity near the surface and the resulting collision efficiency. Numerical integrations by Oleskiw (1982) for $K = 0.196$ and $\phi = 1000$ show an increase in E from 0.009 to 0.028, and in β_0 from 0.095 to 0.127 when the history term is included. This is an extreme example, however. At higher Reynolds numbers, the effect is smaller.*”

The Langmuir and Blodgett and, by extension, Finstad droplet trajectory equations are the simplified version of the Equation (1.10) and those can be written as (Oleskiw, 1982):

$$\frac{\mathrm{d}\overline{v_p}}{\mathrm{d}t} = \frac{3\rho_f(C_D Re/24)}{8\rho_p r_p}\left|\overline{v_p} - \overline{v_f}\right|\left(v_p - v_f\right) \tag{1.12}$$

where, r_p is particle radius. Finstad and Langmuir and Blodgett ignore the buoyancy and gravitational acceleration of the droplet (as it is a very small value; for example, for a 20 μm diameter droplet the terminal velocity in air is about 1.2 mm/s (Finstad et al., 1988a)); and during time of their publication (Langmuir and Blodgett, 1946) there was no way to approximate the history term. The reason for this is twofold.

First, the history term belongs to the group of integral equations called the Volterra integral equations. The Volterra integral equations concern themselves with solving for an unknown function *x*, while having a given function *f*. In the case of history term, the given function *f* is the droplet’s accelerations

while the unknown function x is the changes in the relative velocities due to the Basset force. It is not known how this unknown function x "looks" or "behaves" (which properties it posseses). Second, the Basset force contains the term $\sqrt{t-\tau}$ in the denominator of the integrand. During the integration when $\tau \rightarrow t$ the denominator turns to zero and the integrand is singular under integration. Thus, it is not possible to integrate the history term in the "standard" way and some mathematical manipulations and approximations are needed.

Technically, the trajectory equation of (Oleskiw, 1982), is a simplified version of another equation, called the Basset-Boussinesq-Oseen equation (BBO equation). The Basset–Boussinesq–Oseen equation describes the motion of – and forces on – a small particle in unsteady flow at low Reynolds numbers. The BBO equation is written as:

$$\frac{\pi}{6}\rho_p d_p^3 \frac{\mathrm{d}v_p}{\mathrm{d}t} = \underbrace{3\pi\mu d_p\left(v_f - v_p\right)}_{\mathrm{I}} - \underbrace{\frac{\pi}{6} d_p^3 \nabla p}_{\mathrm{II}} + \underbrace{\frac{\pi}{12}\rho_f d_p^3 \frac{\mathrm{d}}{\mathrm{d}t}\left(v_f - v_p\right)}_{\mathrm{III}} + \underbrace{\frac{3}{2} d_p^2 \sqrt{\pi\rho_f\mu} \int_{t_0}^{t} \frac{1}{\sqrt{t-\tau}} \left(v_f - v_p\right)\mathrm{d}\tau}_{\mathrm{IV}} + \underbrace{\sum_k F_k}_{\mathrm{V}} \tag{1.13}$$

The BBO equation is, in essence, the Newton's second law, in which the left-hand side is the rate of change of the particle's linear momentum, and the right-hand side is the summation of forces acting on the particle. Or in other words – it is a conservation of momentum equation. The terms on the right-hand side are, respectively, the:

- I – Stokes' drag, same as in Equation (1.4).
- II – Froude–Krylov force due to the pressure gradient in the undisturbed flow. The Froude–Krylov force is the force introduced by the unsteady pressure field generated by *undisturbed* waves. The Froude–Krylov force does, together with the diffraction force, make up the total non-viscous forces acting on a floating body in regular waves. The diffraction force is due to the floating body disturbing the waves.
- III – added mass. Added mass or virtual mass is the inertia added to a system because an accelerating or decelerating body must move (or deflect) some volume of surrounding fluid as it moves through it. Added mass is a common issue because the object and surrounding fluid cannot occupy the same physical space simultaneously. For simplicity this can be modeled as some volume of fluid moving with the object, though in reality *all* the fluid will be accelerated, to various degrees.
- IV – the history term aka. the Basset force.
- V – other forces acting on the particle, for example, gravity, etc.

The motion BBO equation describes is valid for any particle moving in any fluid, i.e., water droplet in air, sand particle in ocean, dust in air, etc. The issue with the BBO equation is term I, the Stokes drag. It makes it valid only for the droplet's Reynolds number $Re_d < 1$. A modification to the BBO equation, which makes it work with the flows, in which the droplet's Reynolds number $Re_d > 1$ is called a Maxey-Riley equation (MR-equation). It describes the same physical phenomena as the original BBO equation, however, as a result of its modification to work with any general flow it is more complicated.

Thus, the current state of analytical modeling of the in-cloud droplet impingement on structures is limited by the following factors:

- It is limited to simple geometries (circular and rectangular (Stallabrass, 1980) cylinders).
- The ISO 12494 model underestimates the accreted ice masses for the value of the overall collision efficiency $E < 0.10$ (ISO 12494, 2001), with the lower experimentally-verified limit being $E = 0.07$ (Makkonen and Stallabrass, 1987).
- The Finstad et al. parameterization is only applicable for the values of $K > 0.25$.
- Below this threshold, the calculation become cumbersome due to the presence of the Basset force and the need to know the full droplet distribution spectrum, which, in natural icing events, is typically unknown.
- The "fundamental" limit for the atmospheric ice accretion on structures is $K > 0.14$ (Finstad et al. 1988a) and $K_0 > 0.125$ (Langmuir and Blodgett (1946) and derivative works), below which the analytical calculations predict $E = 0$, i.e., no ice accretion occurs.

1.2 Aim and objectives

The primary aim of this work is to study the behavior of the current analytical model for the in-cloud droplet impingement of the ISO 12494 in the limit of the low values of the droplet's inertia parameter K, in addition to investigating the potential of its applicability in the modeling of such ice accretions. Furthermore, the main objectives of this thesis are:

- Study the ISO 12494/Finstad et al. analytical cloud impingement in order to circumvent the issue of underestimating the accreted ice masses for the cases when the overall collision efficiencies value are in the range of $E < 0.10$.
- Find a way to reasonably estimate the ice accumulation for the cases when $K < 0.25$ without the need to calculate the droplet trajectories.
- Study the potential issues with the overall collision efficiency reaching zero in the limit of the very low value of the droplet inertia parameter, i.e., – $E = 0$ if $K < 0.14$ (and/or $K_0 < 0.125$) (Finstad, 1986).
- Ascertain applicability of the modern CFD tools for modeling ice accretions for the cases with low values of K.

The reason for the latter point is as follows. Makkonen and Lozowski (2005) correctly mention that the usage of the CFD tools became more widespread in the years, following the publication of the Finstad et al. analytical parameterization model in the 1988. From that time the amount of available computational resources has grown exponentially and commercially available and experimentally-verified CFD packages, such as Ansys Fluent and FENSAP–ICE had appeared. However, to the best of the authors knowledge, these packages have not been tested or verified for such extreme conditions as $K \approx 0.25$. For example, the FENSAP–ICE CFD package was initially developed with the rotorcraft and aircraft icing in mind. Both of these applications are characterized by high operating wind speeds – and as a result high values of the droplet inertia parameter K. With the usage of CFD tools steadily growing over the years, one can wonder if they can be successfully applied for the type of the atmospheric ice accretion modeling, described in this work. Thus, it is deemed an important aim and objective to conduct within the scope of this work.

As for the rest of the aims and objectives, defined herein, Figure 3 illustrates the need and importance of this topic.

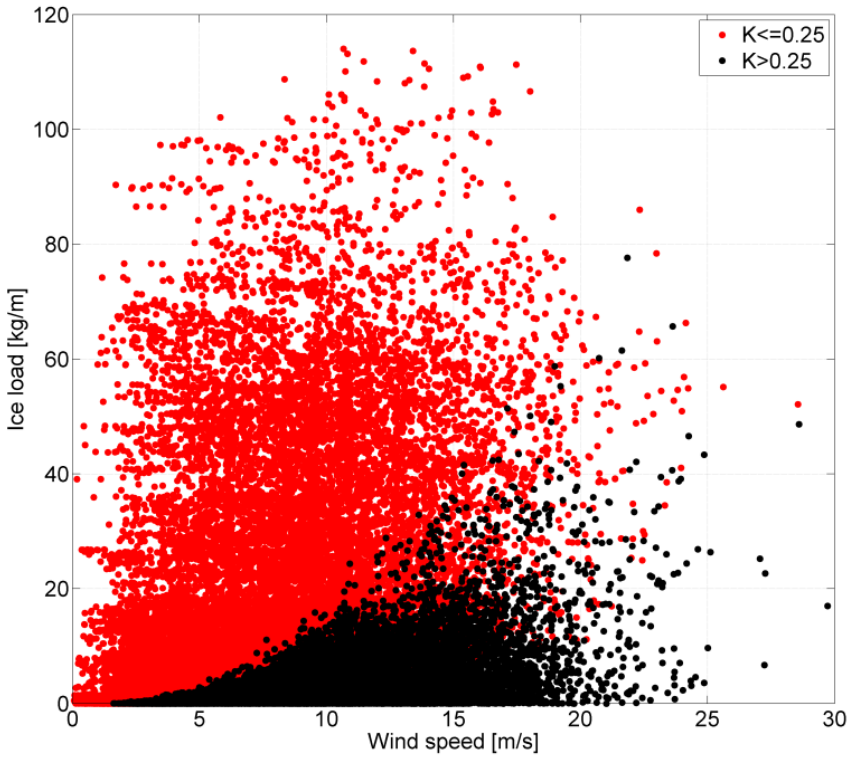

Figure 3 – Hourly data of modeled ice load and wind speed for the single conductor test span at Ålvikfjellet, 1085 m.a.s.l. Based on WRF data for the time period 1979 – 2017. Only points with LWC above 0.2 gm^{-3} are included. Red colors indicate when the Stoke's number falls below the critical limit of K ≤ 0.25. From (Nygaard et al., 2017).

From Figure 3 it can be seen that the absolute majority of the extreme ice loads occurs at the value of $K \leq 0.25$, exactly when the current analytical model of ISO 12494/Finstad et al. breaks down. Thus, for the purpose of the estimating the design loads for the power lines it is crucial to develop a better understanding of the analytical modeling of such extreme cases, without the need to employ the cumbersome trajectory calculation procedures and the need to know the full droplet distribution spectra, responsible for the icing events. In another words – what modifications to the current ISO 12494 can be done which will allow to model such ice accretions? Coupled with the point regarding the CFD usage – can the modern, commercially-available CFD tools be used in order to adequately model such extreme icing events?

In addition, since the continued ice accretions on circular cylinders will result in the time-dependent change of the iced diameters. This diameter change will increase the characteristic length of the cylinder, thus reducing the value of the droplet inertia parameter K, as it can be seen from the Equation (1.2), which may fall below the value $K \leq 0.25$. On the other hand, the increase in the iced diameter will increase the cross-sectional area of the cylinder, as evidenced by the Equation (1.1), effectively increasing the "catch area" of the cylinder. Proper handling of both these factors, which act to counteract one another is needed in the time-dependent analytical modeling of the in-cloud impingement on the circular cylinders.

1.3 Research questions addressed

Within the scope of this work following research questions have been addressed:

- Attempt at "definition" of "large diameter conductors". Since the current ISO 12494 is limited in the estimation of the accreted ice masses for the large iced cylinders/conductors, a better understanding of when the issues arise is crucial.
- As a result, the usage of Langmuir droplet spectra is proposed as a "way out" of MVD/full experimental droplet spectra, which should yield closer agreement with the available data for the low values of *K*. This is the primary objective achieved in this thesis.
- Furthermore, the usage of the constraint of the overall collision efficiency $E = 0.01$ for $K < 0.17$ is studied. While this constraint results in the non-zero accreted ice masses under any arbitrary icing conditions, this can be a conservative estimate with potential issues/limitations of it being overestimation of the ice masses.
- In the time-dependent cloud impingement modeling – the choice of density parameterization is crucial in the modeling of the accreted ice masses and iced diameters. An investigation into some empirical icing densities parameterizations has been carried out.
- Another assumption of the ISO 12494 standrad is the slowly rotating circular cylinder, which serves as a reference collector. In it, the slow rotation is assumed to be the result of the gravity and the (limited) torsional stiffness acting on the power line conductor. Modern CFD tools allow for "quantifying" the forces acting on the cylinder in attempt to verify the "slowly rotating" cylinder assumption. A test case has been studied within the scope of this thesis
- Finally, some brief discussion of the icing modeling on the bundled conductors is carried out, using the CFD tools along with some attention to the modeling of such icing cases under ISO 12494 analytical framework.

Each of these questions will be discussed and attempted to be addressed within the scope of this thesis, starting with the attempt at definition of the "large diameters circular conductors". This is of importance primarily due to two reasons – first, the ISO 12494 standard, specifies that the current analytical model tends to underestimate the accumulated ice masses for the values of the overall collision efficiency $E < 0.10$. Second, is the limitation of the $K \leq 0.25$ itself, below which the ISO 12494 breaks down. If the ISO 12494 model underestimates the accreted ice masses even above $K > 0.25$, then the results, obtained using it, can be unsatisfactory, when predicting extreme ice loads as given in Figure 3, even before the constraint of $K \leq 0.25$ is reached, and it can be potentially challenging if this threshold is crossed during actual accumulation event, as the iced diameter of the circular conductor growth under the influence of accumulation. Thus, in addition, overcoming the issues with underestimation of ice masses below the values of the overall collision efficiency $E < 0.10$ alone is not sufficient, and the changing conditions in the time-dependent in-cloud impingement has to also be ascertained.

These are primarily the functions of the (iced) cylinder diameters, which are the function of the accumulated ice masses and their densities. Thus, performing an investigation into the existing empirical parameterizations of the accreted ice densities is also important, in order to ascertain which empirical parameterization to choose, under which operating conditions, in order to represent the accreted ice densities and iced diameters (if known) with sufficient degree of accuracy as these values can be a key component in modeling long-term (continued icing accumulation over (several) icing events), which, in turn, are key factor in reproducing the extreme ice loads, as in Figure 3, especially under the condition of $K \leq 0.25$. An investigation into a few of these existing empirical accreted ice densities

parameterizations, available both for using with the analytical calculations and implemented in the commercially available CFD packages for the purposes of the numerical computations has been performed with the scope of this work.

As was mentioned previously, in the extreme cases ($K < 0.14$ (Finstad, 1986) and/or $K_0 < 0.125$ (Langmuir and Blodgett and derived works), the present analytical models for the in-cloud impingement on circular cylinders suggest zero accumulated ice masses ($E = 0$) which can be critical in modeling the in-cloud impingement on (very) large iced diameter cylinders. An example of such an event is given in Figure 4.

Figure 4 – Lønahorgi ice accretion event in Voss, Hordaland County, Norway, 1961 (photo: Olav Wist). According to Svein Fikke the measured iced diameters were in range of 1.1–1.4 meters with the accumulated ice masses per unit length were in the range of 301–305 kg/m. Figure taken from (IWAIS 2015).

Attempting to use any existing analytical impingement model, being it Finstad et al./ISO 12494 model or Langmuir and Blodgett and derived works, will result in giving the accumulated ice masses being zero, due to constraints of $K < 0.14$ and/or $K_0 < 0.125$ reached, especially at the "later stages" of the event. In addition, the existing experimental validation of the Finstad et al./ISO 12494 impingement parameterization was carried out only till 76 mm circular cylinders in diameter (Makkonen and Stallbrass, 1987).

Thus, an attempt of definition of what constitutes a "large diameter circular/cylinder" conductor was carried out within this thesis, in terms of the value of the droplet inertia parameter K, based on the

available experimental data from the (Makkonen and Stallabrass, 1987), which has been used to validate the present analytical impingement model itself; and the FRonTLINES project, which can be viewed as an "extension" of Makkonen and Stallabrass experiments for the range of $K \leq 0.25$. The primary importance of such definition and/or quantification is to ascertain when the existing analytical in-cloud impingement parameterizations will start to underestimate the accumulated ice masses and what modifications can be done to them, in order to "remedy" these potential issues.

Furthermore, ISO 12494 postulates a notion of the so-called "reference collector" which is a slowly rotating 30 mm diameter cylinder by 500 mm in length. The purpose of using a "reference collector" is the mapping and estimation of ice loads, for example the IceTroll sensor used by Kjeller Vindteknikk AS for the monitoring of ice loads on the Ålvikfjellet test span. The notion of using the rotating cylinder as a reference collector is two-fold – first, to keep the obtained results and subsequent modeling of the ice loads within the ISO 12494 framework; second, as noted in (Makkonen, 1984) majority of the icing events on the overhead power lines in natural conditions produce circular ice shapes. The circular ice shape is assumed to be the result of the limited torsional stiffness of the conductor resulting in the conductor slowly rotating during the ice accretion event. To verify this claim (Makkonen and Stallabrass, 1984) performed an experiment on "simulated" cable rotation under combined wind and ice load, which showed the "cable" to be slowly rotating under the combined wind and ice load, with the 1 cm diameter cable having a rotation rate of 223 °/hr and the 4 cm "cable" having a rotation rate of 65 °/hr. While, it is clear that it is possible that a slowly twistingly rotating cable could end up with a circular form of icing, it is not the central question in their experiments.

Several questions regarding the experimental setup of Makkonen and Stallabrass remain open. First, (Makkonen and Stallabrass, 1984) specify that their "cables", consisting of single, center steel core wire with 9 (for the 1 cm cable) and 27 (for the 4 cm cable) copper strands, woven around the steel core to be representative of the "power line cable in the middle of the transmission line" in terms of torsional rigidity. No other information is provided, in particular, the values of this torsional rigidity and the derivation/justification for it is not provided. The "cables" in the experiments were mounted in the center of an icing wind tunnel, attached to the springs, which, in turn, were mounted in the walls of the icing wind tunnel. The rotation was induced by "tapping" the bearing at the start of the experiment. The major open questions, therefore, are how (Makkonen and Stallabrass, 1984) can be sure that the torsional rigidity of their cables correspond to the actual power line conductors and how the usage of the spring-bearing mounting system (especially in the sense of the imposed boundary conditions) corresponds to the mounting of the conductors on the actual power lines. To the best of the author's knowledge, no other rigorous attempts to ascertain and quantify this phenomenon has been carried out. Thus, it is deemed important to ascertain the balance of aerodynamic and the gravity forces, acting on the circular cylinder and/or conductor in order to check and verify, if the gravitational force, as claimed by (Makkonen, 1984), would be responsible for the slow rotation of the overhead transmission lines conductors during the ice accretion events. An attempt of a such "quantification" has been carried within the scope of this thesis.

The purpose of this section is to provide a brief overview of the research questions answered within the scope of this work and the need behind them. The detailed description of the results, pertaining discussions and the summary of findings will be given later within this thesis. However, the author of

this work deems the most important contributions being achieved within the scope of Ph.D. work to be the “estimation” of what consititutes as the “large diameter conductors”, the investigation in the empirical accreted icing density parameterizations and the “modification” of the Finstad et al. model to carry out the calculations using the Langmuir droplet distribution spectra.

The latter is deemed to be the most important contribution of this work, as it “permits” the calculation of the overall collision efficiencies and the accreted ice masses for the range of $K \leq 0.25$ with acceptable accuracy of results, without the need to change the underlying equations in the analytical model of Finstad et al. This is achieved by performing “spectrum-averaging” calculations, in which the Finstad et al. model is applied to each droplet size bin in the spectra and then the results are averaged, using the LWC as a weighting factor. The results of the investigation into the empirical icing density parameterizations show that there are some fundamental limitations to the models, in the limit of low K value and low icing duration. This is primarily the result that said models “expect” the ice accretion to be represented by a uniform ice layer, while in reality, the ice accretion under such conditions can result in ice accretion in the shape of large individual beads. At this point, these empirical models produce unsatisfactory results. Finally, the results of “estimation” of what consititutes as the “large diameter conductors” show, based on the experimental data of Makkonen and Stallabrass, that the rough threshold for “large diameter conductor” is approximately 80 mm, under rather typical icing conditions, with the tendency to decrease with the decrease in the operating wind speed and/or MVD.

1.4 Thesis layout

This Ph.D. thesis structured in the following way. Chapter 1 contains the introduction, overview of the atmospheric ice accretion on structures, including the literature review into the existing analytical parameterizations of the in-cloud impingement on the circular cylinders and the overview of the current limitations of the analytical theory. In addition, Chapter 1 contains the aim and objectives of this thesis along with brief introduction on the research questions addressed.

Chapter 2 presents the methodology, used in this thesis, including the breakdown of the design of experiment along with the description of the main techniques used, those being the analytical calculation procedure, the CFD modeling setup and the descriptions of the experimental apparatuses, the results from which are used for the purposes of this work (where applicable).

Chapter 3 contains the results, discussion and main contributions of this work, including the summary of the results and findings, and incudes the highlight of main findings and contributions of this work. Potential applications of the results from this work are discussed. Furthermore, the summary of every published, paper under the scope of this work is given.

Chapter 4 presents the conclusions, drawn from this work and discusses possible further work and existing knowledge gaps.

Finally, bibliography and the research papers, as published, are attached.

2 Methodology

This section describes the design of experiment, used throughout this thesis, including the description of main techniques used, these being the analytical calculation procedure, the CFD modeling setup and the descriptions of the experimental apparatuses, the results from which are used for the purposes of this work (where applicable). Each of these techniques – the analytical calculation procedure; the CFD setup; and the description of the experimental apparatuses will be discussed in the relevant sub-sections. In addition, Figure 5 shows the flowchart of the "primary" calculation routine.

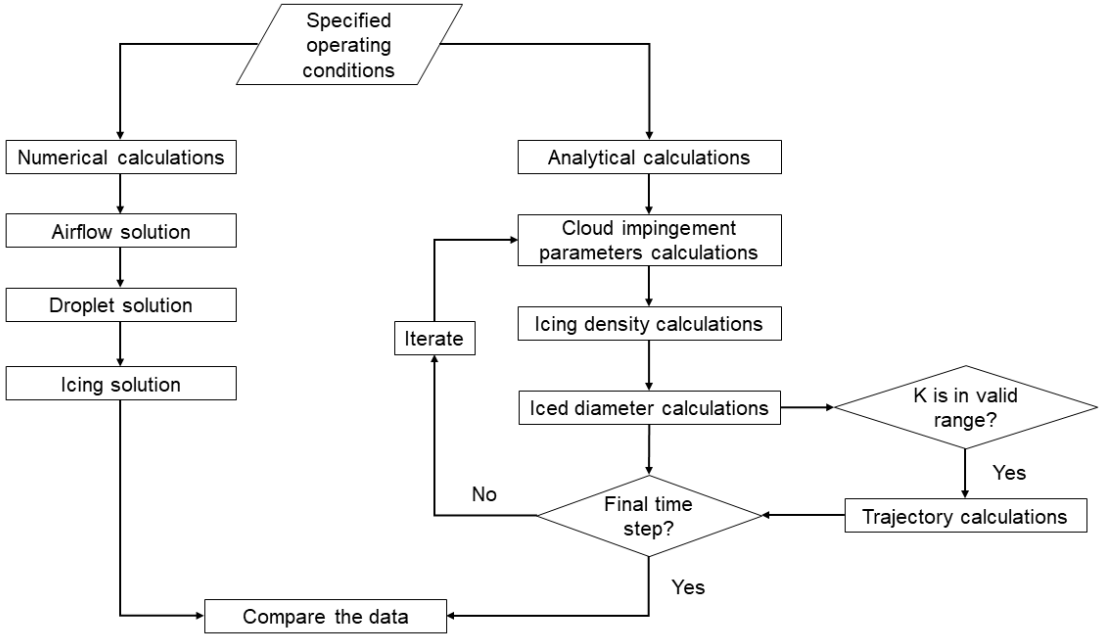

Figure 5 – Flowchart of the calculation routine.

2.1 Analytical calculation procedure

The purpose of this section is to describe the analytical calculation procedure, used in this work. Primarily, the analytical calculations are being carried out in two ways – one being the modified Finstad et al. analytical impingement model; and the seond being the trajectory calculations using the potential flow approximation. The later, in essence, is a repeat of the calculations of (Finstad, 1986), however, they will be shown in this work, for completeness and convenience sake. The main purpose of the trajectory calculations is to act as a validation/"sanity check" when comparing the obtained results between the modified Finstad et al. model and the analytical trajectory calculations.

2.1.1 Spectrum-averaging: the modified Finstad et al. model

From the known operating conditions – air temperature T and pressure p, calculate ambient parameters, namely, the air density, ρ_a, water density, ρ_w, and absolute viscosity of air, μ, using the ideal gas law for dry air, volumetric expansion for water, and Sutherland's law for viscosity, respectively, as follows:

$$\rho_a = \frac{p}{RT} \tag{2.1}$$

$$\rho_w = \frac{\rho_0}{1 + \gamma(T - T_0)} \tag{2.2}$$

$$\mu = \mu_{ref} \left(\frac{T}{T_{ref}} \right)^{\frac{3}{2}} \frac{T_{ref} + S}{T + S} \tag{2.3}$$

Where p is the pressure, R is the specific gas constant for the dry air, T is the absolute temperature, ρ_0 and T_0 are water density and the absolute temperature at 0 °C and γ is the volumetric expansion coefficient of water. The selected reference water density (ρ_0), corresponding to the water density at 0 °C, ensures that the Equation (2.2) would produce the correct water density at the temperature of +4 °C, with the error being of an order of 0.07% at +4 °C.

For Sutherland's law (which is also used by Ansys Fluent, as evidenced by the user manual), the reference values of absolute viscosity of air, absolute temperature and Sutherland's temperature, S are:

$$T_{ref} = 291.15 \text{ K} \qquad \mu_{ref} = 18.27 \text{ μPa·s} \qquad S = 120 \text{ K}$$

Calculate the time step from (if known) RPM of the cylinder as $dt = 60/\omega$, where ω is the rotational speed in RPM. This is so that the cylinder rotates 360° each time step. This is to ensure that the cylinder completes one full revolution per time step and one uniform ice layer is accreted in each time step. This approach follows that of (Makkonen, 1984).

However, the results will not change much if one would use a lower time step (for example $dt = 1$ s), however, it can be argued that the results may be "unphysical" – i.e., the cylinder diameter is updated before it finishes a revolution. If the RPM is unknown, some arbitrary value is assumed for the purposes of the calculations, with typical RPM being equal to 5.

If the MVD is known, and the "source" distribution is unknown, or, alternatively, it is not of importance, the calculations are performed using Langmuir distributions, given in Table 1.

Table 1 – Langmuir distributions given in terms of diameter ratios $(d/d_0)^n$. The value d_0 is the MVD value of the droplet distribution spectrum. Distribution A is monodispersed.

LWC fraction	***A***	***B***	***C***	***D***	***E***	***F***	***G***	***H***	***J***
0.05	1.00	0.56	0.42	0.31	0.23	0.18	0.13	0.10	0.06
0.1	1.00	0.72	0.61	0.52	0.44	0.37	0.32	0.27	0.19
0.2	1.00	0.84	0.77	0.71	0.65	0.59	0.54	0.50	0.42
0.3	1.00	1.00	1.00	1.00	1.00	1.00	1.00	1.00	1.00
0.2	1.00	1.17	1.26	1.37	1.48	1.60	1.73	1.88	2.20
0.1	1.00	1.32	1.51	1.74	2.00	2.30	2.64	3.03	4.00
0.05	1.00	1.49	1.81	2.22	2.71	3.31	4.04	4.93	7.34

The calculations are performed by simply multiplying the MVD value with the respective diameter ratios. All Langmuir distributions (from A to J) are calculated at once.

If the MVD value is unknown, but the source/experimental distribution is known, for example the one from the Cranfield University icing tunnel facility, given in Figure 6:

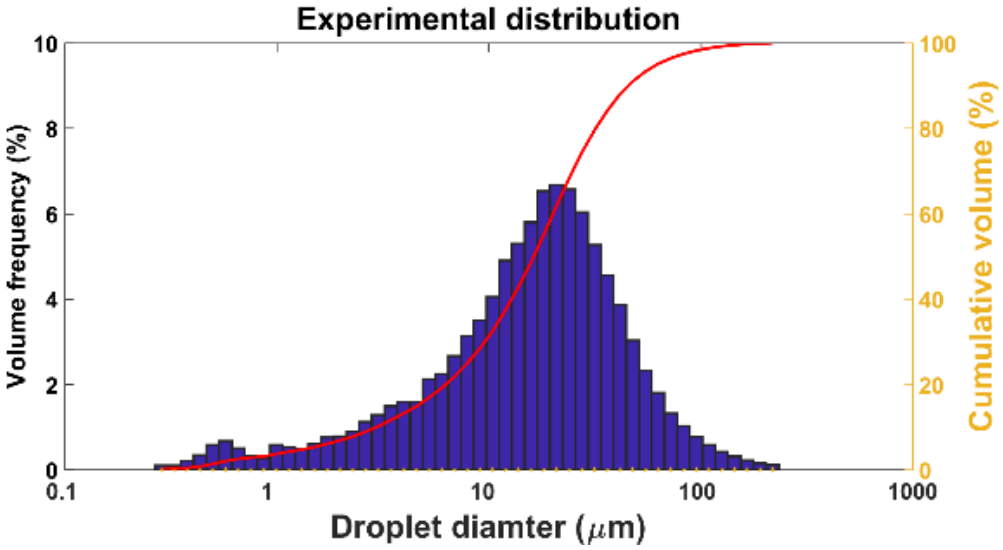

Figure 6 – Cranfield University icing tunnel droplet distribution spectrum.

Then the equation used for the calculation of the MVD is as follows:

$$\mathrm{MVD} = \left(\frac{0.5 - w_{i-1}}{w_i - w_{i-1}} \times \left(d_i^4 - d_{i-1}^4\right) + d_{i-1}^4\right)^{0.25} \tag{2.4}$$

The MVD values are calculated of each *bin* in the spectrum. In this case $w_{i-1} = 0$, $w_i = 1$, d_{i-1} and d_i are the smallest and the biggest droplet diameters in the bin. This calculation is repeated for all bins in the spectrum and then the Equation (2.4) is used once more to get the MVD value of the *spectrum* itself. Note, that while the MVD value of the spectrum is calculated, the following calculations *do not use it* in calculations of the cloud impingement parameters, as for the purposes of spectrum-averaging all necessary information is already known by using the MVD value of each individual bin in the spectrum. The spectrum MVD value is used only for verification of results and some other terms, primarily the Macklin parameter.

Next, calculate the droplet inertia parameter K_i, droplet's Reynolds number Re_i for each bin MVD value along with the Langmuir parameter ϕ, and spectrum-averaged inertia parameter K_{spec}:

$$K_i = \frac{\rho_w d_i^2 u}{18 \mu_a C} \tag{2.5}$$

$$Re_i = \frac{\rho_a d_i u}{\mu_a} \tag{2.6}$$

$$\phi = \frac{Re_i^2}{K_i} \tag{2.7}$$

$$K_{spec} = \sum_{i=1}^{N} w_i K_i = w_1 K_1 + w_2 K_2 + \ldots + w_{N-1} K_{N-1} + w_N K_N \tag{2.8}$$

where, d_i is a MVD of a bin i, u is the operating (freestream) wind speed, C is the characteristic length of an object, i.e., the circular cylinder. The value of cylinder radius R is used as the characteristic length C in the Equation (2.5). This is done in order to keep this value consistent between FENSAP–ICE and the calculations in this work. Second, while its is known that the Langmuir parameter ϕ is independent from the droplet diameter, it is still calculated in the same way as different parameters which *do* depend on droplet diameter. The reason for this is simply to err on the side of caution.

After calculating the droplet inertia parameter K_i for all bins in the spectrum, the check is performed in order to see, for which bin(s) the condition $K_i \leq 0.17$ is satisfied. If such bin(s) are present, the following values are assigned to them: $E = \beta_0 = \nu_0 = \theta = 0.01$. In another words, the overall (and stagnation line) collision efficiencies are limited to 0.01, the maximum impingement angle is limited to 0.01 radian (≈0.57°) and the impact velocity is 1% of the freestream velocity.

The physical explanation behind this is that what little ice is accreted is located around the stagnation line only. In nature, one can frequently find ice accretions on very large objects, like telecommunication masts or wind turbine towers, even though ISO 12494/Finstad et al. model will predict that such accretions are impossible (with the values of E, β_0, ν_0, θ all being less than zero or imaginary). Conversely, there is also a constraint implemented from the "other side": $E = \beta_0 = \nu_0 = \theta = 0.99$ for $K_i \geq 1000$, again, from (Finstad et al., 1988a) This constraint is obviously more physical (*very* high inertia) but insofar the author of this work has yet to encounter the flow conditions for which this can be enforced. The constraint of $K_i \leq 0.17$, combined with the droplet distribution spectra calculations is what allows to overcome the limitations of the ISO 12494/Finstad et al. model for $K < 0.25$, at least to some extent.

With everything in place, the cloud impingement parameters for the *current* time step are calculated, using the following expression:

$$\begin{aligned} X(K, \phi) = &\left[C_{X,1} K^{C_{X,2}} \exp\left(C_{X,3} K^{C_{X,4}}\right) + C_{X,5}\right] - \left[C_{X,6} (\phi - 100)^{C_{X,7}}\right] \\ &\times \left[C_{X,8} K^{C_{X,9}} \exp\left(C_{X,10} K^{C_{X,11}}\right) + C_{X,12}\right] \end{aligned} \tag{2.9}$$

with the values of constants of constants $C_1 - C_{12}$ given in Table 2.

Table 2 – Values of constant coefficients for the cloud impingement parameters calculations. Values are taken from (Finstad, 1986).

Coefficient	$X = \beta_0$	$X = \theta_{max}$	$X = E$	$X = \nu_0$
$C_{X,1}$	1.218	2.433	1.066	1.030
$C_{X,2}$	-6.70×10^{-3}	-4.70×10^{-3}	-6.16×10^{-3}	1.68×10^{-3}
$C_{X,3}$	–0.551	–0.375	–1.103	–0.796
$C_{X,4}$	–0.643	–0.576	–0.688	–0.780
$C_{X,5}$	–0.170	–0.781	–0.028	–0.040
$C_{X,6}$	3.05×10^{-3}	8.50×10^{-3}	6.37×10^{-3}	9.44×10^{-3}

$C_{X,7}$	0.430	0.383	0.381	0.344
$C_{X,8}$	2.220	1.757	3.641	2.657
$C_{X,9}$	–0.450	–0.298	–0.498	–0.519
$C_{X,10}$	–0.767	–0.420	–1.497	–1.060
$C_{X,11}$	–0.806	–0.960	–0.694	–0.842
$C_{X,12}$	–0.068	–0.179	–0.045	–0.029

This formula is valid for all cloud impingement parameters. One simply needs to select the constants depending on what is needed to be calculated. For example, if one is interested in the overall collision efficiency E, then the third column ($X = E$) is used, and the values of constants $C_1 – C_{12}$ are filled from it. However, in this work all four of these parameters, the stagnation line collision efficiency β_0, maximum impingement angle θ_{max}, the overall collision efficiency E, and the normalized impact velocity (by multiplying the result with the freestream wind speed U) V_0 are calculated at the same time.

With the overall collision efficiency E known, the thermodynamic surface balance for the dry growth is calculated using the Messinger model. In the case of dry growth, the surface temperature of the ice deposit can be obtained numerically as (Makkonen, 1984):

$$\frac{2}{\pi} Evw\left(L_f + c_w t_a - c_i t_s\right) = h\left[(t_s - t_a) + \frac{kL_s}{c_p p_a}(e_s - e_a) - \frac{rv^2}{2c_p}\right] + \sigma\alpha(t_s - t_a) \qquad (2.10)$$

where L_f and L_s are latent heats of fusion and sublimation respectively, c_w, c_i, and c_p are specific heats of water, ice and air respectively, p_a, e_s and e_a are air pressure, saturation water vapor pressures at surface and air temperatures respectively, h is the overall heat transfer coefficient, k = 0.62 (thermal conductivity of water in W/(m·K)), r is the recovery factor, with value of 0.79 being used for cylinder, t_s and t_a are surface and air temperatures in Celsius, σ is the Stefan-Boltzmann constant and $\alpha = 8.1 \times 10^7$ K^3. For the dry growth, a typical approximation of $t_a = t_s$ can be used, or, in another words, the surface temperature of ice deposit is equal to the operating temperature.

The recovery factor r can be explained as follows: at any given wind speed molecules of air collide with an object, with more molecules colliding at higher wind speeds. This causes a temperature rise of the object due to friction. Because the airflow is thought to be compressible and isentropic, which, by definition, is adiabatic and reversible, the equations for calculations of (adiabatic) wall temperatures do not take into account the friction (viscous) heating, as the viscous heating is caused by dissipation, which is irreversible. This is why the calculation of static air temperature requires the use of the recovery factor r to compensate for excess heat present in the system. This is the same recovery factor which needed to be specified in FENSAP–ICE ICE3D. The recovery factor r is not a constant but depends, in particular, on the character of the flow on the surface, the flow regime, and the thermal properties of the medium. For some simple cases, its value can be estimated as follows:

- At the front stagnation point of bodies in the flow, $r = 1$;
- In a laminar boundary layer on a plane plate, $r \approx \sqrt{Pr}$, $0.5 < Pr < 10$; where Pr is the Prandtl number.
- In a turbulent boundary layer on a plate, $r \approx \sqrt[3]{Pr}$, $Pr \approx 1$;
- For a circular cylinder, $r \approx 0.79$.

Returning to the Equation (2.10). The heat balance equation for the icing surface (the "*Messinger model*") is:

$$q_f + q_v + q_k + q_a = q_c + q_e + q_l + q_s + q_i \tag{2.11}$$

where:

- q_f is the latent heat released during freezing.
- q_v is the frictional (viscous) heating of air.
- q_k is the kinetic energy of the impinging water (droplets).
- q_a is the heat released in cooling the ice from its freezing temperature (0 °C) to the surface temperature t_s.
- q_c is the loss of sensible heat to air.
- q_l is the heat loss (gain) in warming (cooling) impinging water to the freezing temperature.
- q_s is the heat loss due to radiation.
- q_i is the heat loss into the ice due to conduction.
- The terms on the left hand side of the Equation (2.11) are heat sources (they generate/provide heat to the system), while the terms on the right hand side of the Equation (2.11) are sinks (they remove heat from the system). The Equation (2.11) is also a conservation of energy equation.

The terms in the Equation (2.11) can be parameterized as:

$$q_f = IL_f \tag{2.12}$$

where I is the intensity of accretion (mass per unit area per unit time, kg/(m^2·s)) and L_f is the latent heat of fusion at 0 °C;

$$q_v = \frac{hrv^2}{2c_p} \tag{2.13}$$

where h is the conductive heat transfer coefficient, r is the recovery factor for viscous heating (for circular cylinder $r = 0.79$ is assumed), v is the wind speed and c_p is the specific heat of air at constant pressure (meaning isobaric process); the kinetic energy of the droplets q_k can be safely ignored for most of the in-cloud icing events under natural atmospheric conditions (as $q_k = ½mv^2$ and $m = \rho V^3$ in which $V = 4/3\pi r_p^3$ and $O(r_p) = 10^{-6} – 10^{-5}$ m $\rightarrow$ $O(V) = 10^{-18} – 10^{-15}$ m^3 $\rightarrow$ $q_k \approx 0$);

$$q_a = Ic_i(0\ °\text{C} - t_s) \tag{2.14}$$

where c_i is the specific heat of ice and t_s is the temperature of the surface (°C);

$$q_c = h(t_s - t_a) \tag{2.15}$$

where t_a is the air temperature (°C);

$$q_e = \frac{hkL_e}{c_p p_a}(e_s - e_a) \tag{2.16}$$

where k = 0.62 (thermal conductivity of water), L_e is the latent heat of **e**vaporation (or **s**ublimation) at t_s, e_s and e_a are air pressure, saturation water vapor pressures at t_s and t_a, respectively and p_a is the (free) atmospheric pressure;

$$q_l = \frac{2}{\pi} Evwc_w(0\ °\text{C} - t_a) \tag{2.17}$$

where c_w is the specific heat of water, $2/\pi Evw$ is an impinging mass flux (can be recognized as $\alpha_1 vAw$ from the Equation (1.1) with $A = 2/\pi$, meaning the area of cylinder exposed to the icing and with the unit length) and it is assumed that the temperature of the droplets in the free stream is the same as that of air;

$$q_s = \sigma\alpha(t_s - t_a) \tag{2.18}$$

where σ is the Stefan-Boltzmann constant and $\alpha = 8.1 \times 10^7$ K^3. Equation (2.18) is obtained by linearizing the equation for the difference in the longwave radiation emitted by the icing surface and the fog. The heat conductivity of ice is sufficiently low that q_i on a slowly rotating cylindrical ice deposit can be neglected, except in the initial stage of icing, where the thickness of the ice layer is only a few (or a fraction of) millimeters.

In the wet growth process, the temperature of the surface t_s = 0 °C in the Equations (2.14) – (2.16) and (2.18). Therefore, q_a disappears and $e_s = e_0$ in the Equation (2.16) where e_0 is the saturation water vapor pressure over water at 0 °C. Then, using the Equation (2.11), neglecting q_k and q_i in it and solving for the icing intensity I yields:

$$I = hL_f^{-1}\left[-t_a + \frac{kL_e}{c_p p_a}(e_0 - e_a) - \frac{rv^2}{2c_p}\right] - L_f^{-1}\left(\frac{2}{\pi} Evwc_w + \sigma\alpha\right) t_a \tag{2.19}$$

On a cylindrical object the icing intensity I, i.e., the rate of increase in the mass of ice divided by the part of the surface area of the ice deposit that faces the wind (g/cm·h) can be calculated as:

$$I = \frac{2}{\pi} Envw \tag{2.20}$$

Combining the Equations (2.19) and (2.20) yields the expression for n:

$$n = \frac{\pi h}{2EvwL_f}\left[-t_a + \frac{kL_e}{c_p p_a}(e_0 - e_a) - \frac{rv^2}{2c_p}\right] - \frac{t_a}{L_f}\left(c_w + \frac{\pi\sigma\alpha}{2Evw}\right) \tag{2.21}$$

The equation for n is also the definition for the *freezing efficiency* α_3 and in the case of circular cylinder it is *exact*. For different geometry, the surface area that faces the wind has to be modified along with the recovery factor r. In addition, the FENSAP–ICE3D also calculates the thermodynamic balance on the wall, based on the Equations (2.11) and (2.21), as the physical principles behind the mechanism of freezing are the same.

While this subroutine is implemented in the calculations, it is typically not used. The main reason for it is that it is more computationally expensive than the rest of the cloud impingement calculations. In addition, since it is valid for the dry growth *only*, the typical assumption of the surface temperature t_s = air temperature t_a is used instead. The author of this work has carried out the calculations of the thermodynamic balance on the surface for the experimental cases in this work, using the formulae, discussed in this section. For all cases, the difference between the air and the surface temperature in the analytical calculations has been found not to exceed the threshold of 1 °C. This is deemed negligible, considering the significant reduction in the amount of calculations which are needed to be carried out for the analytical calculations of icing. Thus, for all subsequent calculaations, the assumption of equivalence between the air and the surface temperatures, $t_s = t_a$ is used.

Following that, the Macklin parameter and the density of the accreted ice are calculated as follows:

$$R_m = -\frac{V_0 d}{2t_s} \tag{2.22}$$

where d is the MVD in microns, V_0 is the impact velocity of the droplet in m/s and t_s is the surface temperature of the ice deposit in Celsius.

However, there is an important notion to mention about the Macklin parameter. The Macklin parameter does not accept the modification to it, in the same vein as the spectrum-averaged calculations, mentioned in previous steps. Thus, only the impact velocity is spectrum-averaged, and the MVD value of the entire spectrum is used in order to avoid this problem. Then, the accreted ice density is *typically* estimated as:

$$\rho_i = 378 + 425 \log_{10}(R_m) - 82.3\left(\log_{10}(R_m)\right)^2 \tag{2.23}$$

where, R_m is the Macklin density parameter. This empirical icing density parameterization, obtained by (Makkonen and Stallabrass, 1987) and based on the icing wind tunnel experiments, is the same equation as the so-called "*Macklin*" ice density model in the FENSAP–ICE3D. The only difference in the Equation (2.12), when compared to the one in the FENSAP–ICE manual, is that the Equation (2.23) is multiplied by a factor of 1×10^3 in order to convert the density from g/cm^3 to kg/m^3.

The idea to relate the accreted ice density to a set of parameters, measurable in the icing wind tunnel first came to (Macklin, 1962). However, the way they carried out the experiments drew a significant amount of criticism. From the viewpoint of the author of this work, the biggest issue is that the LWC range tested (and validated against) in the experiments, being w = 1.6 – 7.0 g/m^3, i.e., very high values of LWC. In any case, based on their icing wind tunnel testing (Makkonen and Stallabrass, 1984) have designed their empirical icing density formulation. Compared to (Macklin, 1962) they claim that it gives higher values of the accreted ice density, in no small factor being the uncertainty by Makkonen and Stallabrass of what sort of the droplet distribution they have actually measured in the icing wind tunnel (Makkonen and Stallabrass, 1984; Jones, 1990; Makkonen, personal communication, IWAIS 2019), however, in their work (Makkonen and Stallabrass, 1984) they attribute it to Macklin using the oil slide method for the purpose of the droplet size measurements, which is known for overestimating the MVD values.

Alternatively, the analytical calculations can also be carried out using the Jones empirical icing density parameterization. This is the formulation which FENSAP–ICE manual calls the "Jones (glaze)" icing formulation, while Jones herself refers to it as the "intermediate" version. The "intermediate" icing density formulation of (Jones, 1990) is given as (in g/cm^3).

$$\rho = 0.210 R_m^{0.53} \qquad R_m \leq 10$$

$$\rho = R_m/(1.15R_m + 2.94) \qquad 10 < R_m < 60$$

$$\rho = 0.84 \qquad R_m \geq 60$$

Jones has designed her icing density parameterization based on the Mt. Washington Observatory historical observations and the multicylinder device measurements in the "natural" conditions. This sets this model apart from majority of the empirical icing density parameterizations, which are developed based on the icing wind tunnel measurements. As noted in (Jones, 1990), when compared to the original empirical icing density formulation in (Macklin, 1962), the Jones ice density formulation should yield higher density values at lower values of the Macklin parameter R_m, and lower ice density values at high values of R_m. In addition, (Jones, 1990) notes several things about her "intermediate" empirical model (which FENSAP–ICE calls Jones (glaze)). Out of these, the first, is that the "Jones (glaze)" model only explains 50% of the icing density variance. And second, is that the *any* icing density formulation, based on the Macklin parameter tends to fail to give an explanation for the accreted icing density on the largest cylinder diameters, thus suggesting that there is a fundamental limitation in the Macklin parameter. Based on this (Jones, 1990), has devised a different empirical icing density parameterization, not dependent on the Macklin parameter. This formulation, known as the "final" version of the Jones model (or as FESNAP–ICE manual calls it – "Jones (rime)", model is given as (in g/cm^3)):

$$\begin{aligned}\rho = 0.249 &- 0.0840 \ln \pi_C - 0.00624\left(\ln \pi_\phi\right)^2 + 0.135 \ln \pi_K \\ &+ 0.0185 \ln \pi_K \ln \pi_\phi - 0.0339 (\ln \pi_K)^2\end{aligned} \tag{2.24}$$

where π_K is the droplet inertia coefficient, π_ϕ is the Langmuir parameter defined as (Langmuir and Blodgett, 1946):

$$\pi_\phi = \frac{18\rho_a^2 Dv}{\rho_d \mu_a} = \frac{Re^2}{K} \tag{2.25}$$

where Re is the droplet's Reynolds number. Finally, the term π_C is the ratio of the convective heat flux and the heat flux due to droplet freezing and is defined as:

$$\pi_C = \frac{k_a (-2T)/D}{wvL_f} \tag{2.26}$$

The "Jones (rime)" icing density formulation has two important properties – it is independent from the Macklin parameter formulation, thus making it applicable to the large cylinder diameters, i.e., the objects with large characteristic length, and it explains over 70% of variance of the accreted ice density (Jones, 1990).

However, the issue with this version of the Jones empirical icing density parameterization is that, based on the performed analytical and numerical calculations, using both the MVD approximation and the full droplet distribution spectra, it is struggling with the spectrum-averaged analytical calculations. With the spectrum-averaging calculations, the produced ice densities are overestimated, when compared to the measured values. The current assumed hypothesis behind this is that the Jones (rime) icing density parameterization was "fine-tuned" to the MVD approximation, as it operates with the values of K directly, and since with the change of distribution from the monodisperse one an incresease in the values of K is expected to happen, this will correspond to the increased ice denisties predicted by the model.

The main reasons behind discussing these particular empirical icing density parameterizations in detail are as follows: first, both the Makkonen and Stallabrass and the Jones (glaze) parameterizations both use the Macklin parameter in them, however, they use a different empirical fit (as seen from the preceding Equations in this section; and were derived based on the different operating conditions, i.e., – the icing wind tunnel data vs. the "natural" atmospheric ice accretions on the Mt. Washington); second, is the empirical icing density parameterization of Jones (rime), which, as it was mentioned previously, is one model, which is independent from the Macklin parameter; third, is the availability of all these aforementioned models – those being the Makkonen and Stallabrass (referred as "*Macklin*" in the CFD model), and both the intermediate and the final version of the Jones model (referred as "*Jones (glaze)*" and "*Jones (rime)*" in the CFD model) in both the analytical and the numerical models, which makes the comparison among them rather straightforward.

After calculating the accreted ice density, the iced diameter is calculated as:

$$D_i = \left[\frac{4(M_i - M_{i-1})}{\pi\rho_i} + D_{i-1}^2\right]^{1/2} \tag{2.27}$$

where M is the ice mass accretion per unit length, ρ is the accreted ice density and subscript i indicates the time step. Using the new value of D_i, the iced cylinder diameter is updated accordingly and the calculations are repeated as necessary, i.e., – the time limit for the icing duration is reached.

2.1.2 Analytical droplet trajectory calculations

The analytical calculations of water droplet trajectories for a circular cylinder, using the potential flow approximation, are, essentially, solving the following problem, given in Figure 7.

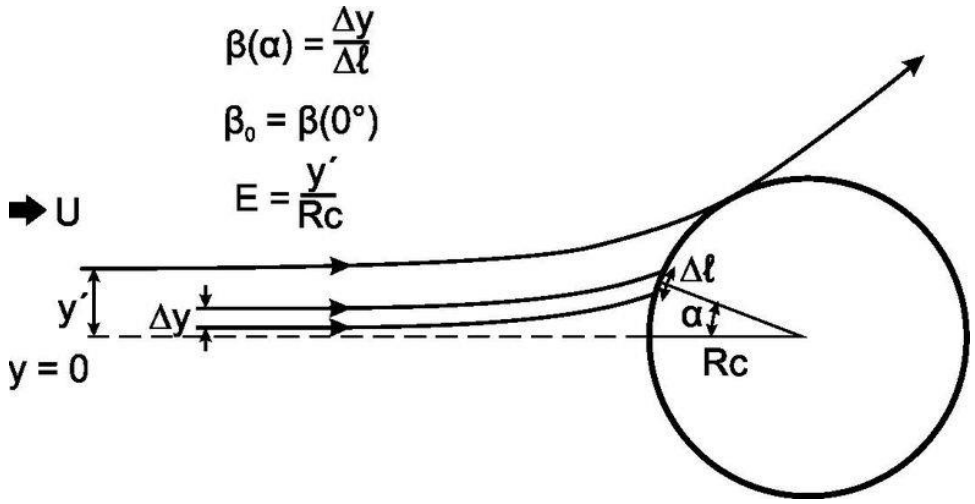

Figure 7 – Droplet trajectories impinging on a circular cylinder in cross section. The definitions of β(α), β_0 and E *are illustrated. On the accretion surface, α is the angle between the local surface normal and the free stream. The maximum impingement angle, corresponding to the "grazing trajectory" is designated α_{max}. Redrawn from (Finstad, 1986).*

In which, the β(α) is the ratio between the initial trajectory separation (Δy) to the final separation (on the cylinder wall; Δl), β_0 is the similar ratio, however it is valid for the trajectory originating at $y = 0$ (the stagnation line) and any droplet trajectory adjacent to it. For example, in this work the vertical separation, Δy = MVD is used. The overall collision efficiency E, is equal to the maximum vertical separation, y', the trajectory of which still collides with the cylinder. The associated angle is the maximum impingement angle, α_{max}, $\alpha_{max} = \text{asin}(l'/R)$, where R – cylinder radius.

As for the droplet calculations and the comparison between this approach and the modified Finstad et al. model, the calculations of the ambient operating conditions, such as air and water densities and absolute viscosity of air are identical to the calculations using the modified Finstad et al. formula.

The calculations of the time step, based on the RPM, are not carried out. The reason for this is the focus on pure trajectory calculations, for which small enough time steps are vital. While the Magnus effect and the Coriolis force do exist on the rotating cylinder, they are assumed to be negligible for a "slowly rotating" object. Instead, the time step is calculated as $dt = (1/1000) \times (D/U) = (1/500) \times (R/U)$, where D is the cylinder diameter, R is the cylinder radius and U is the freestream velocity. (Finstad, 1986) uses $dt = 0.0025(D/U) = (1/400) \times (D/U)$. The difference between the two different time step calculation methods on the final results of the trajectory calculations is negligible.

The calculations for the MVD/Langmuir spectra and the spectrum-averaging are performed not in the same way as with the modified Finstad et al. formula. While the calculations for the MVD and the LWC fractions for spectrum-averaging are carried out, the results using them, however, are obtained *after* the trajectory calculations.

For the calculations of the droplet trajectories themselves, the following is true:

First, the initial droplet coordinates, (x_0, y_0) are specified as: $x_0 = -10R$, $y_0 = 0 \ldots R$, Δy = MVD (note: the author of this work has performed calculations using multiple different starting x_0 values, for example,

using $x_0 = -10D$; the differences in the results were negligible, but it took twice as much time steps to finish the calculations).

Next, it is necessary to calculate the initial air and droplet velocity components. The air velocity components for the potential flow are:

$$u_x = U\left(1 + \left(\mathrm{R}^2 \frac{y^2 - x^2}{(x^2 + y^2)^2}\right)\right) \tag{2.28}$$

$$u_y = \frac{2xyRU}{(x^2 + y^2)^2} \tag{2.29}$$

where U is the freestream velocity, R is the cylinder radius and x and y are the horizontal and the vertical coordinate respectively. They are the same as the LB air velocity components in (Langmuir and Blodgett, 1946), but in dimensional form. The initial droplet velocity components v_x and v_y are the same as in (Finstad, 1986), and they are given as:

$$v_x(x_0, y_0) = u_x(x_0, y_0) \tag{2.30}$$

$$v_y(x_0, y_0) = 0.5u_y(x_0, y_0) \tag{2.31}$$

Following that, the droplet relative Reynolds number with respect to air as is calculated as:

$$Re_d = \frac{\rho_a \sqrt{(v_x - u_x)^2 + (v_y - u_y)^2}\, d}{\mu_a} \tag{2.32}$$

note that this is identical to the FENSAP–ICE, when it comes to the calculating the relative droplet Reynolds number in DROP3D.

Determine the droplet drag coefficient C_D, based on the relative Reynolds number as:

$(C_D Re/24) = 1 + 0.102Re^{0.955}$ for $0.2 \le Re \le 2.0$

$(C_D Re/24) = 1 + 0.115Re^{0.802}$ for $2.0 \le Re \le 21.0$

$(C_D Re/24) = 1 + 0.189Re^{0.632}$ for $21.0 \le Re \le 200.0$

$(C_D Re/24) = 1 + 0.197Re^{0.63} + 2.6\times10^{-4}Re^{1.38}$ for $Re > 200$

This empirical droplet drag coefficient formulation uses the combination of (Beard and Pruppacher, 1969) droplet drag coefficients for $Re \le 200$ and Langmuir and Blodgett droplet drag coefficient for $Re > 200$. FENSAP–ICE uses different empirical droplet drag parameterization for $Re \le 250$ (above that, FENSAP–ICE issues a warning that the droplet drag coefficient is no longer valid, as it is assumed that the particles cease to be spherical). The comparison between the analytical and the numerical droplet

drag coefficient for a spherical particle for the range $0 < Re_d < 150$ is given in Figure 8. This range of the droplet Reynolds number should be indicative of the all cases of interest of the in-cloud icing impingement modeling, considered in this work.

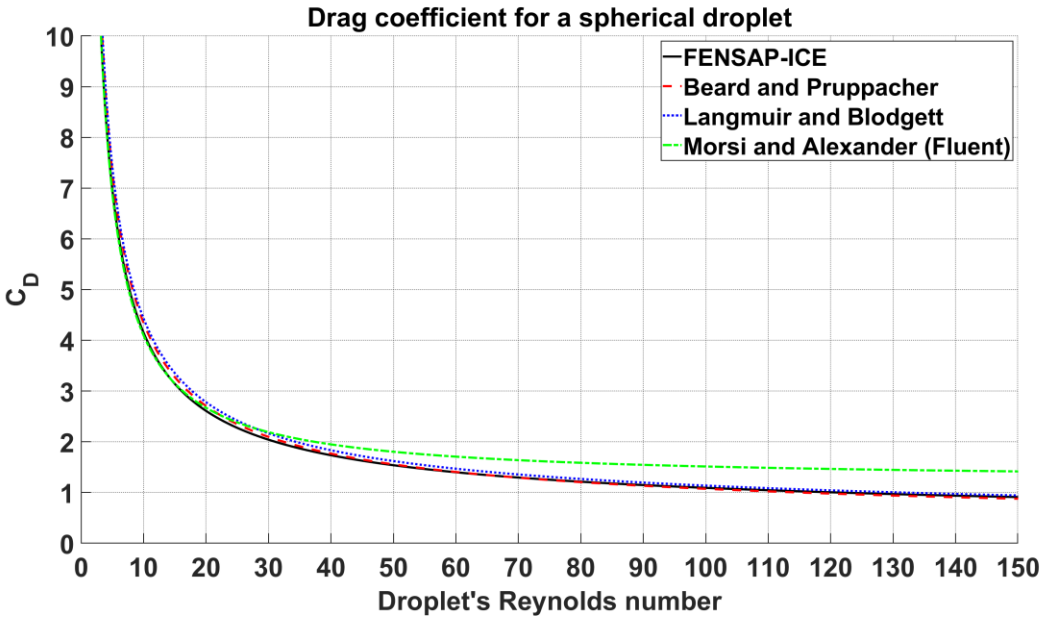

Figure 8 – Comparison of the analytical droplet drag coefficient used in the analytical modeling (Beard and Pruppacher; Langmuir and Blodgett) and the numerical modeling (FENSAP–ICE; Morsi and Alexander (Fluent)).

As it can be seen from Figure 8 – the correlation between the analytical expressions for the spherical droplet drag coefficient (Beard and Pruppacher, 1969; Langmuir and Blodgett, 1946) and the droplet drag coefficients, used in the modeling (FENSAP–ICE; Morsi and Alexander (Fluent), 1972) is good for the majority of the range of droplet Reynolds numbers considered. The only slight exception is the parameterization by the Morsi and Alexander, which is used by the Ansys Fluent, which displays slightly elevated values of the spherical droplet drag coefficient. In addition, it is also worth mentioning that the $(C_D Re/24) = 1$ for the Stokes flow, and $(C_D Re/24) > 1$ if not, which is reflected in the empirical drag coefficients above.

Next, the droplet accelerations are calculated as:

$$\frac{\mathrm{d}v_x}{\mathrm{d}t} = -\frac{(v_x - u_x)(UC_D Re_d)}{12DK} \tag{2.33}$$

$$\frac{\mathrm{d}v_y}{\mathrm{d}t} = -\frac{(v_y - u_y)(UC_D Re_d)}{12DK} \tag{2.34}$$

which, after some manipulation, can be rewritten as:

$$a_x = c\sqrt{(v_x - u_x)^2 + (v_y - u_y)^2}(v_x - u_x) \tag{2.35}$$

$$a_y = c\sqrt{(v_x - u_x)^2 + \left(v_y - u_y\right)^2}\left(v_y - u_y\right) \tag{2.36}$$

and the coefficient c is being equal to:

$$c = \frac{3\rho_a C_D}{4\rho_w d} \tag{2.37}$$

Followed by the calculations of the next step droplet speeds and positions:

$$v_x(i+1) = v_x(i) \; - a_x(i)\mathrm{d}t \tag{2.38}$$

$$v_y(i+1) = v_y(i) + a_y(i)\mathrm{d}t \tag{2.39}$$

$$x(i+1) = x(i) + \; v_x(\mathrm{i})\mathrm{d}t \; - \frac{a_x(i)\mathrm{d}t^2}{2} \tag{2.40}$$

$$y(i+1) = y(i) + v_y(i)\mathrm{d}t + \frac{a_y(i)\mathrm{d}t^2}{2} \tag{2.41}$$

Note the way in which the time step index (i) and (i+1) are written. Moreover, the Equations (2.38) – (2.41) are plain kinematics equations, which are technically, a single (Equations (2.38) and (2.39)) and double (Equations (2.40) and (2.41)) integral over the acceleration with dt as an integration variable.

Next is the calculation of the next step air speeds, droplet Reynolds number, drag coefficient and acceleration. This is done using the values from the previous step (Equations (2.38) – (2.41) and repeating the Equations (2.32) – (2.37).

After this is performed, iteration of calculations for next step of droplet speed and position, using averaged values of accelerations, is performed as:

$$v_x(i+1) = v_x(i) - \frac{(a_x(i) + a_x(i+1))\mathrm{d}t}{2} \tag{2.42}$$

$$v_y(i+1) = v_y(i) + \frac{(a_y(i) + a_y(i+1))\mathrm{d}t}{2} \tag{2.43}$$

$$x(i+1) = x(i) + v_x(i)\mathrm{d}t \; - \frac{(a_x(i) + a_x(i+1))\mathrm{d}t^2}{4} \tag{2.44}$$

$$y(i+1) = y(i) \; + v_y(i)\mathrm{d}t + \frac{(a_y(i) + a_y(i+1))\mathrm{d}t^2}{4} \tag{2.45}$$

The reason behind the previous two steps is simple. After calculating the droplet accelerations using the Equations (2.38) – (2.41), one has a rough idea how the droplet will behave itself during the next time step, however, it does not take into the account the effects of a different relative droplet Reynolds

number and how it affects the droplet acceleration, and thus – the velocities and position. Thus, one need to first calculate the estimate of the next time step droplet properties (position, velocity, acceleration, etc.), and then refine this estimate by iterating the calculations. This is a prediction-correction algorithm, and in this particular case – it is a finite difference, central differencing, one iteration scheme.

The droplet trajectories are iterated until the droplet reaches the cylinder, i.e., the condition $x^2 + y^2 \leq R^2$ is fulfilled. In this case, the droplet's final position is calculated using the quadratic equation for the slope with these final (x, y) coordinates and the ones in the preceding time step. Thus, the point of the impact is found. From the points of impact, the E, $\beta(\theta)$, β_0, θ and θ_{max} are found.

Note that, in the droplet trajectories calculations the droplet inertia coefficient, the Langmuir parameter, the Macklin parameter, the accreted ice density etc. are not calculated. In the droplet calculations the only things which are calculated are the trajectories and the behavior of the droplets, i.e., the distribution of the local collision efficiencies $\beta(\alpha)$. If the discrepancy between the modified Finstad et al. formula and the trajectory calculations becomes too large, the iced cylinder diameter will be modified in the trajectory calculations, based on the estimate from the modified Finstad et al. formula, as the iced cylinder diameter is the biggest factor behind the difference in values between these two methods.

In addition, the trajectory calculations method is notoriously poor in predicting the cloud impingement parameters for the low value of the droplet inertia parameter K, in particular in the (vicinity of) the limit $K \leq 0.25$. Moreover, unlike the modified Finstad et al. formula, there are no "easy" ways to correct or account for this. Thus, the question of the usability of the Finstad et al. trajectory calculations remain open in the range of $K \leq 0.25$. And the one way to do it is the evaluation of the "history term", discussed previously.

2.2 Numerical calculation procedure

For the numerical calculations within the scope of this work, Ansys FENSAP–ICE and Ansys Fluent commercial CFD packages are used. Out of these two, the FENSAP–ICE is used predominantly, and the Ansys Fluent is used primarily for the transient CFD simulations only (while the FENSAP–ICE is used for the remainder of the numerical simulations). In the FENSAP–ICE three separate modules are used for the purposes of the modeling atmospheric ice accretion. These are:

- **FENSAP**: 3D Finite Element Navier-Stokes Analysis Package.
- **DROP3D**: 3D finite element Eulerian water droplet impingement solver.
- **ICE3D**: 3D finite volume ice accretion and water runback solver.

FENSAP by itself is used to obtain the airflow solution, using the Reynolds-Avergaed Navier-Stokes equations. For convenience, these equations are given as:

$$\frac{\partial \rho_\alpha}{\partial t} + \vec{\nabla}\left(\rho_\alpha \overrightarrow{v_\alpha}\right) = 0 \tag{2.46}$$

$$\frac{\partial \rho_\alpha \overrightarrow{v_\alpha}}{\partial t} + \vec{\nabla}\left(\rho_\alpha \overrightarrow{v_\alpha}\ \overrightarrow{v_\alpha}\right) = \vec{\nabla}\cdot\sigma^{ij} + \rho_\alpha \vec{g} \tag{2.47}$$

$$\frac{\partial \rho_\alpha E_\alpha}{\partial t} + \vec{\nabla}\left(\rho_\alpha \overrightarrow{v_\alpha} H_\alpha\right) = \vec{\nabla}\left(\kappa_\alpha\left(\vec{\nabla} T_\alpha\right) + v_i \tau^{ij}\right) + \rho_\alpha \vec{g}\, \overrightarrow{v_\alpha} \tag{2.48}$$

where ρ is the density of air, *v* is the velocity vector, subscript α refers to the air solution, *T* refers to the air static temperature in Kelvin, σ^{ij} is the stress tensor and *E* and *H* are the total initial energy and enthalpy, respectively. The Equations (2.46) – (2.48) are the conservation of mass, momentum and energy equations, respectively. The stress tensor σ^{ij} is given as:

$$\sigma^{ij} = -\delta^{ij} p_a + \mu_a \left[\delta^{ijk} \nabla_k v^i + \delta^{ik} \nabla_k v^j - \frac{2}{3}\delta^{ij} \nabla_k v^k\right] = -\delta^{ij} p_a + \tau^{ij} \tag{2.50}$$

$$\tau^{ij} = \mu_a \left[\delta^{jk} \nabla_k v^i + \delta^{ik} \nabla_k v^j - \frac{2}{3}\delta^{ij} \nabla_k v^k\right] \tag{2.51}$$

Ansys FENSAP–ICE DROP3D, uses an Eulerian water droplet impingement solver. The existing analytical models of droplet behavior, for example, the ISO 12494/Finstad et al. solve droplet trajectories using Lagrangian particle tracking approach. The Eulerian method treats the particle phase as a continuum and develops its conservation equations on a control volume basis and in a similar form as that for the fluid phase. The Lagrangian method considers particles as a discrete phase and tracks the pathway of each individual particle. By studying the statistics of particle trajectories, the Lagrangian method is also able to calculate the particle concentration and other phase data. On the other hand, by studying particle velocity vectors and its magnitudes in Eulerian method, it is possible to reconstruct the pathways and trajectories of particles in a phase.

The general Eulerian two-phase model for viscous flow consists of the Navier-Stokes equations augmented by the droplets continuity and momentum equations:

$$\frac{\partial \alpha}{\partial t} + \vec{\nabla} \cdot \left(\alpha \overrightarrow{V_d}\right) = 0 \tag{2.52}$$

$$\underbrace{\frac{\partial\left(\alpha \overrightarrow{V_d}\right)}{\partial t} + \vec{\nabla}\left[\alpha \overrightarrow{V_d} \otimes \overrightarrow{V_d}\right]}_{\text{I}} = \underbrace{\frac{C_D Re_d}{24K} \alpha\left(\overrightarrow{V_a} - \overrightarrow{V_d}\right)}_{\text{II}} + \underbrace{\alpha\left(1 - \frac{\rho_a}{\rho_d}\right)\frac{1}{Fr^2}}_{\text{III}} \tag{2.53}$$

where the variables α and $V_{d,a}$ are mean field values of, respectively, the water volume fraction and droplet velocity.

The terms of this equation are, respectively, the:

- I – material derivative of acceleration.
- II – (steady-state) drag action the droplets of mean diameter *d*.
- III – buoyancy and the gravity forces.

The Equation (2.47) is a conservation of momentum equation (following the Newton's second law). It is peculiar to note that the FENSAP–ICE user manual specifies "droplets of mean diameter *d*" in connection to the Equation (2.47). To the author of this work it seems that this value is an actual MVD

value. In any case, the steady-state droplet drag is proportional to the relative droplet velocity, its drag coefficient C_D, and the droplets Reynolds number as follows:

$$Re_d = \frac{\rho_a d V_{a,\infty} \left\| \overrightarrow{V_a} - \overrightarrow{V_d} \right\|}{\mu_a} \tag{2.54}$$

and the droplet inertia parameter:

$$K = \frac{\rho_d d^2 V_{a,\infty}}{18 L_\infty \mu_a} \tag{2.55}$$

Where L_∞ is the characteristic length of the object. In case of the cylinder the characteristic length is cylinder radius.

The buoyancy and gravity forces are proportional to the local Froude number:

$$Fr = \frac{\left\| V_{a,\infty} \right\|}{\sqrt{L_\infty g_\infty}} \tag{2.56}$$

These governing equations describe the same physical droplets phenomenon as Lagrangian particle tracking approach. Only the mathematical form in which these equations are derived changes, using Partial Differential Equations instead of Ordinary Differential Equations. The droplet drag coefficient is based on an empirical correlation for flow around spherical droplets, or:

$C_D = (24/Re_d)\,(1 + 0.15\mathrm{Re}_d^{0.687})$ for $Re_d \leq 1300$

$C_D = 0.4$ for $Re_d > 1300$

In practice, the different droplet drag empirical correlations have a very good agreement among themselves for majority of possible droplet's Reynolds number ranges. The exceptions are very high values (Re_d > 200–250) or the Stokes flow (Re_d < 1). The local and overall collision efficiencies are calculated as follows:

$$\beta = -\frac{\alpha \overrightarrow{V_d} \cdot \vec{n}}{w V_\infty} \tag{2.57}$$

where α is the local volume fraction (kg/m^3) and $\vec{n}$ is the surface normal vector. It calculates it in a different way to the trajectory calculations in the Section 2.1 of this work. The way the FENSAP–ICE DROP3D solves it, is by comparing the normalized impact velocities times the local LWC fraction, to the total LWC fraction times freestream velocity. Since it does not track particles, it has to do it using the LWC and droplet velocity distributions. The overall collision efficiency is an integration of local collision efficiencies over surface area and is given as:

$$\beta_{tot} = \frac{\int \beta \, \mathrm{d}A}{L_\infty^2} \tag{2.58}$$

Which is a standard integral over the surface, and it is normalized by the characteristic length. However, one important point worth mentioning with the FENSAP–ICE DROP3D is the droplet momentum conservation equation, the Equation (2.53). Compare it to the trajectory equation by Oleskiw, the Equation (1.10), which, for convenience is presented in here as:

$$\underbrace{\frac{d\overline{v_p}}{dt}}_{\text{I}} = \underbrace{\frac{2\left(\rho_p - \rho_f\right)}{\left(2\rho_p + \rho_f\right)}\overline{g}}_{\text{II}} - \underbrace{\frac{3\rho_f (C_D Re/24)}{4r_p\left(2\rho_p + \rho_f\right)}\left|\overline{v_p} - \overline{v_f}\right|\left(v_p - v_f\right)}_{\text{III}} - \underbrace{\frac{9\rho_f}{\left(2\rho_p + \rho_f\right)r_p}\sqrt{\frac{\mu_f}{\pi\rho_f}}\int_{-\infty}^{t}\frac{d\overline{v_p}}{d\tau}\frac{d\tau}{\sqrt{t-\tau}}}_{\text{IV}} \tag{2.59}$$

where,

- I – the droplet acceleration;
- II – the buoyancy and gravitational acceleration of the droplet
- III – the steady viscous drag;
- IV – the "history" term.

Note, that there is one crucial term missing in the FENSAP–ICE DROP3D momentum equation (Equation (2.53)) compared to the analytical equation of Oleskiw (Equations (1.10) and (2.59)).

FENSAP–ICE DROP3D does not take into account the history term. In no way, shape or form. It completely ignores it. It partially makes sense, as the FENSAP–ICE was developed for the aerospace industry and in-flight icing. The normal operating conditions in these applications result in a quite high value of droplet inertia parameter *K*. Thus, the history term is simply not needed in those applications. In addition, the BBO equation, the MR equation etc., they all work under, and calculate the history term in the Lagrangian framework. It makes sense, as the term is dependent on the "history" of the particle and thus all its' previous positions, velocities, accelerations etc. Eulerian framework (to which FENSAP–ICE belongs to) cannot track it. It is simply not possible under the current Eulerian framework. Theoretically, it may be possible to devise such a numerical scheme, which can make some sort of an estimate based on the cell and node time-dependent values, but the memory and the CPU requirements would be exorbitant in this case.

Therefore, one can pose a question, what it is possible to do if issues with the FENSAP–ICE simulations are encountered for the values of *K*, below the threshold of $K \leq 0.25$ in connection with the cloud impingement parameters, such as ice masses, overall and local collision efficiencies, ice densities etc.? In another words – anything, which is controlled by the value of the droplet inertia parameter *K*. The most straightforward answer is to change the droplet distribution spectrum from, for example, Langmuir D to Langmuir E, while keeping the operating parameters constant. The change from the monodispersed distribution to the Langmuir distributions (and/or custom distributions) should lead to the increase of the "effective" value of the droplet's inertia parameter (for majority of cases with low enough values of the droplet's inertia parameter *K*). However, if the change from the monodispersed distribution to the Langmuir distributions fails to achieve the desired values of the overall collision efficiencies and the

accreted ice masses, there is very little one can hope to achieve further, as one cannot control directly how the FENSAP–ICE calculates the cloud impingement parameters. The alternatives will be running trajectory simulations in Fluent, using a Lagrangian tracking along with a number of user defined functions (UDFs) in order to approximate the history term itself. And since the history term is inherently unsteady, one needs to perform them in transient mode, which is very sensitive to the operating parameters. Or, alternatively, calculate the trajectories using an analytical model with the history term included.

Continuing with the discussion about analytical models when compared to the commercial CFD tools – the primary differences between them, when it comes to the cloud impingement parameters in the "dry growth" regime, can be summarized as follows, assuming an average "performance" over wide range of values of *K*. These are based on the author's experience in using both and are broadly summarized in the Table 3.

Table 3 – Comparison of the analytical modeling and the FENSAP–ICE numerical simulations in the terms of the in-cloud impingement parameters.

Parameter	***Comparison (Analytical vs. CFD)***
E	Typically, lower in the CFD. It becomes significantly lower at lower at low values of $K < 0.5$. Good agreement is found for $K > 1$ between analytical model and CFD results.
β_0	Largely the same behavior as above.
α_{max}	The maximum impingement angles are always almost the same, with the CFD reporting slightly higher values.
V_0	Lower in CFD across all ranges of *K*. The differences diminish with the increase in values of *K*.
M	Since it is a function of *E*, it has the same behavior as *E* for the dry growth conditions.
ρ_i	As it is a function of the V_0 it behaves in the same way. The author of this work agrees with Jones – during numerical calculations an abnormally high icing densities at large cylinder diameters ($D > 100$ mm) were observed. This suggests that there is a limitation in the Macklin parameter.
K	Its calculated in the same way between the analytical and the CFD model, as long as the iced diameters (in the steady-state mode) are not taken into the account.

However, the author of this work has never attempted a rigorous investigation as to why and how exactly the differences between the FENSAP–ICE and the analytical model arise. The current "suspicion" is that, those differences primarily arise due to the differences between the viscous flow versus the potential flow approximation. In the viscous flow there is a higher number of the physical phenomena, such as pressure gradients, viscous shear stresses, boundary layer response etc., acting against the droplet, which results in it slowing down and thus decreasing the value of *K*. These effects are not present in the potential flow approximation.

Finally, the ICE3D solves a system of two partial differential equations on all solid surfaces. The first equation expresses mass conservation:

$$\rho_f \left[\frac{\partial h_f}{\partial t} + \vec{\nabla} \cdot \left(\overline{V}_f h_f \right) \right] = V_\infty \mathrm{LWC} \beta - \dot{m}_{evap} - \dot{m}_{ice} \tag{2.60}$$

where the three terms on the right hand side correspond, respectively, to the mass transfer by water droplet impingement (source for the film), by evaporation and by ice accretion (sinks for the film). The second partial differential equation expresses conservation of energy:

$$\rho_f\left[\frac{\partial h_f c_f \tilde{T}_f}{\partial t}+\dot{\nabla}\left(\partial h_f c_f \tilde{T}_f\right)\right]=\left[c_f\left(\tilde{T}_\infty-\tilde{T}_f\right)+\frac{\left\|\vec{V}_d\right\|^2}{2}\right]V_\infty \mathrm{LWC}\beta - L_{evap}\dot{m}_{evap}$$
$$+\left(L_{fusion}-c_s\tilde{T}\right)\dot{m}_{ice}+\sigma\varepsilon\left(T_\infty^4\right)-T_f{}^4-c_h\left(\tilde{T}_f-\tilde{T}_{ice,rec}\right)+Q_{anti\text{-}icing} \quad (2.61)$$

where the first three terms on the right hand side model the heat transfer generated by the impinging supercooled water droplets, by evaporation and by ice accretion. The last three terms are the radiative, convective and 1D conductive heat fluxes.

The coefficients ρ_f, c_f, c_s, σ, ε, k_s, L_{evap}, L_{fusion} are physical properties of the fluid and of the solid, specified by the user. The reference conditions T_∞, V_∞, LWC are airflow and droplets parameters specified by the user. The local wall shear stress and the convective heat flux should be supplied by the flow solver. DROP3D provides local values of the collection efficiency β and droplets impact velocity V_d. The evaporative mass flux m_{evap} is recovered from the convective heat flux, using a parametric model.

Detailed mesh sensitivity analysis was carried out to accurately determine the boundary layer characteristics (shear stress and heat fluxes), a $y+$ values of less than 1 is used near the cylinder wall surface. Number of mesh elements and the $y+$ value was selected based upon the heat flux calculations, where a numerical check was imposed that the heat flux computed with the classical formulae dT/dn should be comparable with the heat flux computed with the Gresho's method.

FENSAP computes heat fluxes in two different manners: *Classical*, which is based on temperature gradients on the walls; *Gresho*, which is based on Gresho's Consistent Galerkin formulation (Gresho et al., 1987). Both Classical and Gresho fluxes are 2nd order accurate and should give very similar results (FENSAP–ICE User Manual). However, Gresho fluxes can exhibit some oscillations if the surface grid is uneven or coarse. For accurate heat fluxes, the recommended boundary layer grid spacing is: first element size 1×10^{-6} m, growth ratio 1.1.

Oftentimes the focal point of the analysis of a physical system is a derived quantity such as a flux, or force. In the corresponding numerical simulation the generation of such quantities directly from the solution can be plagued with accuracy and continuity problems. For example in deriving nodal fluxes related to a typical gradient transport phenomenon, a finite element representation of the solution leads to discontinuous nodal fluxes. The latter plus the superconvergence phenomena achieved in some problems on regular meshes has led to the common practice of using "Gauss-point" fluxes. However, various authors. For example, Gresho et al. and have suggested and employed an alternative technique, herein referred to as the consistent (flux) method, which can lead to more accurate results (Gresho et al., 1987).

An algorithmic way in which to view, (and perhaps implement), the consistent 'flux' method can be represented as (Gresho et al., 1987):

i. Initially, form *all* of the boundary nodal equations as if there were to be imposed the most general type of natural boundary condition at each node (for the Laplace operator considered thus far, it could be $\mathbf{n}\cdot\nabla T + h(T - T_0) + q = 0$, for example).

ii. Modify the boundary node equations for the particular problem at hand, e.g. for Dirichlet data, the nodal equation can be omitted entirely (after transposing the appropriate coupling information to the right-hand side), although it should also be "saved" for later use in step iv. For simpler natural boundary conditions, the proper deletions are made (e.g. h, T_0 or q in the current problem).

iii. Assemble and solve the conventional GFEM equations for the primary variables.

iv. Recall the nodal equation for which Dirichlet data are employed, simplify the general boundary condition to that relating the primary and derived variables ($q = -\mathbf{n}\cdot\nabla T$ for the current problem) in each equation, and solve for the consistently derived variables.

Finally, the calculation of $y+$ value is performed in the following way (White, 2002):

$$Re = \frac{\rho_f U_\infty L_\infty}{\mu_f} \tag{2.62}$$

$$C_f = \frac{0.026}{Re^{1/7}} \tag{2.63}$$

$$\tau_{wall} = \frac{C_f \rho_f U_\infty^2}{2} \tag{2.64}$$

$$U_{fric} = \sqrt{\frac{\tau_{wall}}{\rho_f}} \tag{2.65}$$

$$\Delta s = \frac{y^+ \mu_f}{U_{fric} \rho_f} \tag{2.66}$$

where ρ_f and μ_f are the density and dynamic viscosity of the continuous phase (air), U_∞ is the freestream velocity, L_∞ is the characteristic length, i.e., cylinder diameter, C_f is the skin friction coefficient, τ_{wall} is the shear stress at the wall, U_{fric} is the friction velocity and Δs is the wall spacing (first cell height). These computations are based on the flat-plate boundary layer theory from (White, 2002).

2.3 Description of the experimental apparatuses

Within the scope of this work, the results from three icing wind tunnels are used. While the author of this work has not performed some of the experiments themselves, it is deemed necessary to present the description of all the icing wind tunnel setups, the results from which has been used in this work.

2.3.1 VTT Technical Research Centre of Finland icing wind tunnel

The experiments were conducted in the VTT icing wind tunnel. This is an "open-loop" tunnel placed entirely inside a large cold room. The cross-section of the tunnel mouth is 0.7m by 0.7m. Ice was accumulated on 0.157 m long smooth aluminium cylinder, 30 – 170 mm in diameter, placed vertically

and rotated by a motor at a constant 5 RPM. The schematic of the icing wind tunnel is given in Figure 9. To rule out the effect of blockage, the cylinder was located in front of the exit of the tunnel. The temperature and wind speed in the test section were measured using calibrated sensors. The liquid water content (LWC) was calibrated for each wind speed and temperature pair by measuring the ice growth on a 30 mm cylinder and using the formulas defined in ISO 12494 (ISO 12494, 2001). Under the test conditions, LWC was 0.4 g/m^3. The air temperature was –5 °C and wind speed 4 and 7 m/s. The droplet size distribution in the icing tunnel has been calibrated by using The Cloud, Aerosol and Precipitation Spectrometer probe (CAPS), which can measure small particles between 0.61 and 50 µm by utilizing the light scattering principle (CAPS, Droplet Measurement Technologies, Boulder, Colorado, USA).

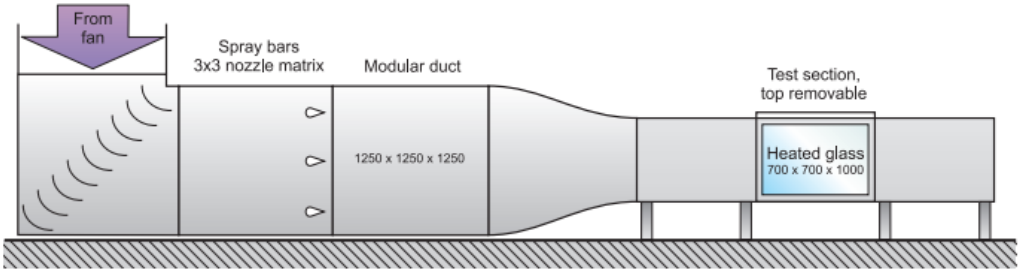

Figure 9 – VTT Technical Research Centre of Finland icing wind tunnel schematic. From (VTT, 2016).

The cylinder in the experiments was weighted using electronic scales with precision of ±0.001 gram. The diameter of the cylinder after the ice accretion was measured using cooled calipers. Those measurements were conducted every 30 minutes. An example of ice shape obtained from the icing tunnel experiments is shown in Figure 10.

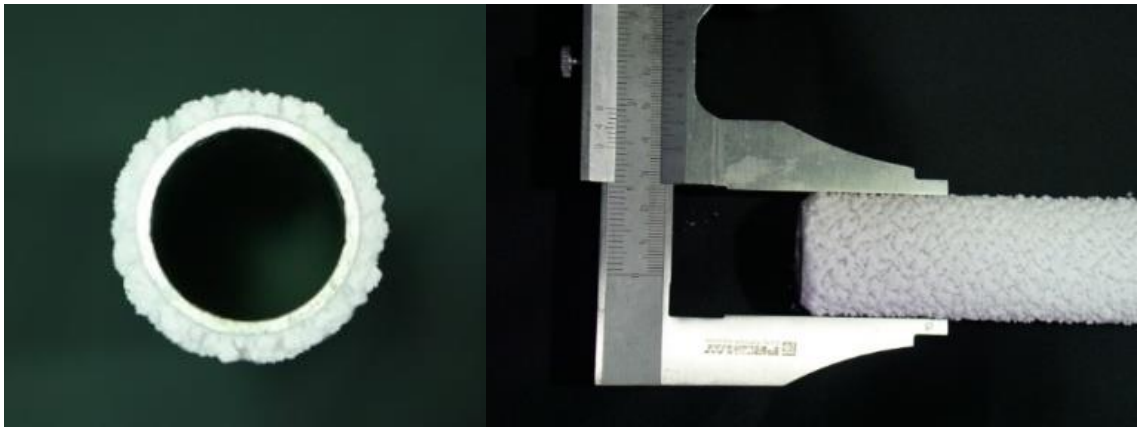

Figure 10 – Ice shape from the VTT Technical Research Centre of Finland icing wind tunnel experimentations for the 30 mm cylinder.

The test matrix for the experiments at the VTT Technical Research Centre of Finland is given in Table 4.

Table 4 – Operating conditions for the VTT Technical Research Centre of Finland icing wind tunnel studies.

Parameter	***Value***
Cylinder diameter (mm)	30, 50, 80, 100, 170

Air velocity (m/s)	4, 7
Air temperature (°C)	–5
Altitude (m.a.g.l)	0
Rotational Rate (Rpm)	5
MVD (µm)	18.73
Liquid Water Content (g/m^3)	0.4
Icing duration (min)	30
Cylinder length (mm)	157

2.3.2 Cranfield University icing tunnel

The icing tunnel experiments were conducted at Cranfield University icing tunnel facility. This is a "closed-loop" tunnel with 761 x 761 mm test section and is capable of operating wind speeds of Mach 0.1 to Mach 0.5, with wide range of possible droplet sizes and Liquid Water Content (LWC) due to flexible spray bars configuration. The schematic of the Cranfield University icing tunnel is given in the Figure 11.

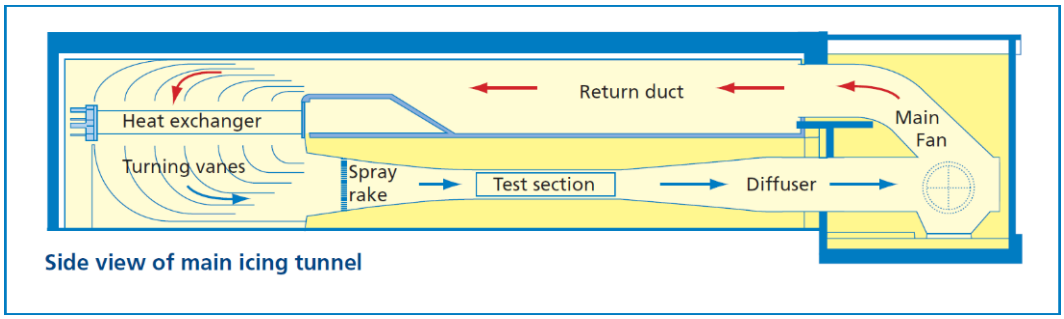

Figure 11 – Cranfield University icing tunnel schematic. From (Cranfield University, 2018).

The operating parameters used for the purposes this study are summarized in Table 5.

Table 5 – Operating conditions for the Cranfield University icing tunnel studies.

Parameter	***Value***
Cylinder diameter (mm)	20, 50.05, 80.25, 99, 149.5, 249, 298
Air velocity (m/s)	30
Air temperature (°C)	–25
Altitude (m.a.g.l)	0
Rotational Rate (RpM)	4
MVD (µm)	16.36
Liquid Water Content (g/m^3)	0.6
Icing duration (min)	20 (for 20 – 80 mm), 30 (for 99 – 298 mm diameter cylinders)
Cylinder length (mm)	50.04, 50, 67.85, 69.5, 83.5, 11.74, 50, 50

The choice of the operating air temperature is based on the need to maintain the "dry growth" regime during experimentation so that the sticking and accretion efficiencies, $\alpha 2 = \alpha 3 = 1$, respectively. The choice of LWC and MVD is based on the need to obtain a measurable ice thickness, while simultaneously keeping the small/low value of droplet inertia parameter *K*. The choice of wind speed corresponds to the minimum rated wind speed for the Cranfield University icing tunnel. During the experiments, the rotating multicylinder device, mounted in the center of the test section, was used. The

rotational velocity during the experiments was set to 4 RPM. Two cylinder configurations were tested – the configuration consisting of smaller cylinders, 20 – 80.25 mm in diameter, and a configuration, consisting of larger cylinders, 99 – 298 mm in diameter. The reason for testing two different configurations is that the used multicylinder device can only allow mounting of four cylinders at a time.The choice of only rotating cylinder is based on several considerations, primarily:

1. To keep the results strictly within ISO 12494 modeling framework.
2. According to the experiments of (Makkonen and Stallabrass, 1984) on wires, the rate of rotation was in between 65 and 223 °/hr, with large jumps in rotation occurring. This implies that for longer time period, of at least several hours of ice accretion, the resultant ice shape will be circular.
3. Moreover, (Makkonen, 1984) referencing Howe and Dranevic states that the ratio of the minor to the major axis on actual power line conductors is 0.88 for glaze and 0.82 for rime, on the average.
4. Following personal discussions with Bjørn Eigil Nygaard (Kjeller Vindteknikk AS, Norway) and, Egill Thorsteins (EFLA Iceland), it was noted that all significant ice accretions on simplex test spans are circular in nature.

To minimize the effect of blockage, the multicylinder device was mounted as close as possible to the center of the tunnel's test-section. The duration of the tests was chosen to give a measurable thickness of the ice deposit. Since the large cylinder configuration has significantly lower values of droplet inertia parameter and by extension – the overall collision efficiency, the test duration was increased to 30 min for large configuration in order to offset this. During the experimental runs the values for the pressure, air velocity and temperature in the plenum of the icing tunnel were constantly monitored and recorded. Subsequent analysis of this data has showed that these operating parameters (pressure, air velocity and temperature) didn't fluctuate by more than ±1% from the nominal (operating) values, prescribed in the experimental test matrix. Moreover, the cylinders were video recorded from multiple angles, in order to observe the ice growth in the details. Examples of final ice shapes from the experiments is given in Figure 12.

Figure 12 – Final ice shapes of the small (left) and large (right) cylinder configurations in the Cranfield University icing tunnel experiments.

Figure 13 shows intermediate ice shapes for the larger cylinder configuration during the experimentation with 5 min increments and the final ice shapes for the individual cylinders. The droplet distribution spectrum from the icing tunnel is given in Figure 6. The experimental droplet distribution spectrum is

measured using the laser diffraction method (based on the Fraunhofer diffraction). The MVD of this distribution is 16.36 μm.

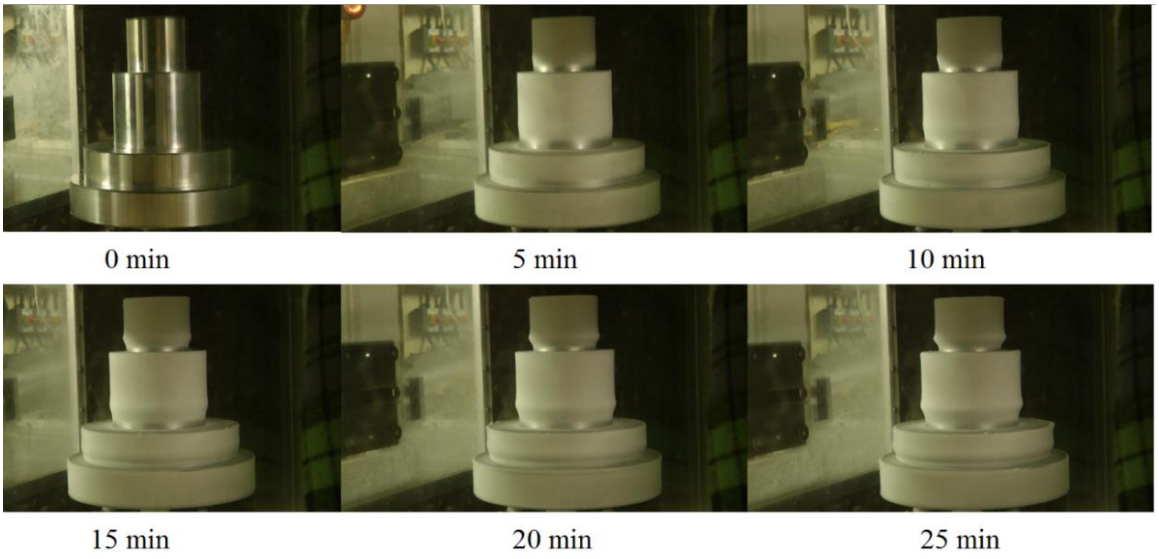

Figure 13 – Intermediate ice shapes for the large cylinder configuration in the Cranfield University icing tunnel experiments.

The droplet distribution spectrum was measured using laser diffraction methods, while (Makkonen and Stallabrass, 1984) measured their experimental droplet distribution spectra using Forward Scattering Spectrometer Probe (FSSP) in addition to the common oiled and soothed slides methods, and (Jones, 1990) estimates LWC, MVD and droplet distribution spectra based on the numerical fitting of accreted ice on the multicylinder device at Mt. Washington Observatory.

2.3.3 Makkonen and Stallabrass icing wind tunnel experiments

For the purposes of this work, a brief description of the Makkonen and Stallabrass (1984; 1987) icing wind tunnel experiments will be given. More detailed information about the experiments is available in (Makkonen and Stallabrass, 1984; 1987) and the description of the experimental facility is provided in detail in (Lozowski et al., 1983).

The icing experiments were made in the icing wind tunnel of the Low Temperature Laboratory, National Research Council of Canada. Icing tests were made on horizontally mounted rotating cylinders of four different diameters, 1.024, 3.183, 4.440 and 7.609 cm. The speed of rotation was 2 RPM. The experiments were conducted at two wind speeds – 20 and 36 m/s. The duration of the test runs were chosen to give a relatively small, yet measurable ice thickness. Thus, time of 30, 40 and 50 min were chosen for the 1.024, 3.183 and 4.440 cm diameter cylinders, respectively, giving ice thicknesses of between 1 and 3 mm. A 50-min duration was chosen for the 7.609 cm diameter cylinder also, resulting in slightly smaller ice thicknesses (i.e., between 0.6 mm and 2.5 mm).

The overall diameter of the ice deposits on the three smaller cylinders was measured with a cooled vernier caliper, while a micrometer was used for the largest cylinder. The ice mass was determined by weighing the central part of the cylinder together with its accumulated ice and subtracting the weight of

the cylinder. The three smaller cylinder were measured on a precision balance accurate to 1 mg. The largest cylinder was too heavy for this balance and was weighed on a balance scaled in 1 g increments, but visually interpolated to 0.1 g.

The experiments were conducted using three different droplet distribution spectra, with MVDs being 15.7, 13.4 and 12.2 μm for the distribution 1; 13.1 μm for distribution 2; and 17.1 and 14.4 μm for the distribution 3. Unfortunately, the exact information on the droplet distribution spectra for these experiments are no longer available (Makkonen, personal communication), which makes these experiments an excellent testbed for the usage of the Langmuir droplet distribution spectra.

2.3.4 Estimation of the cloud droplet sizes in the natural conditions

Unlike in the icing wind tunnels, the measurement of the droplet sizes and spectra in the natural conditions typically is not possible to be carried out using the same instrumentation as in the icing wind tunnels, for example using the Forward Scattering Spectrometer Probe, or any other methods, based on the laser diffraction and laser doppler velocimetry, primarily due to challenges with instrumentation icing, heating, and the stability of the operating conditions. Thus, other devices and techniques are used, for example the rotating (multi)cylinder device, used extensively by, for example, on the Mt. Washington Observatory (Jones, 1990), (Howe, 1990), in other conditions (Makkonen, 1992) or, a modified version of which is used for the measurements at the Ålvikfjellet test span.

A rotating multicylinder device (RMC) measurement provides ice weights on cylinders of known lengths and diameters. In the RMC method, the icing duration, wind speed, air temperature and air pressure are required. Ice thickness on the cylinders can also be used, but it's not required. The basis of this method lies in assumption that when MVD and LWC are known, the accurate time-dependent modeling of the ice accretion on the rotating cylinder (by using the ISO 12494), at a given ambient conditions is possible. This implies, that the reverse of this is true (and what is used in this method) – by "trial and error" such a combination of MVD and LWC can be found that the time-dependent numerical model predicts the accreted ice masses on the RMC. In theory, only two cylinders of sufficiently different diameters are needed, since there are two unknowns (LWC and MVD) in the system of equations to be solved. The accuracy of the method can be improved by inclusion of the additional cylinders. The block-scheme of RMC method is shown in Figure 14, for convenience.

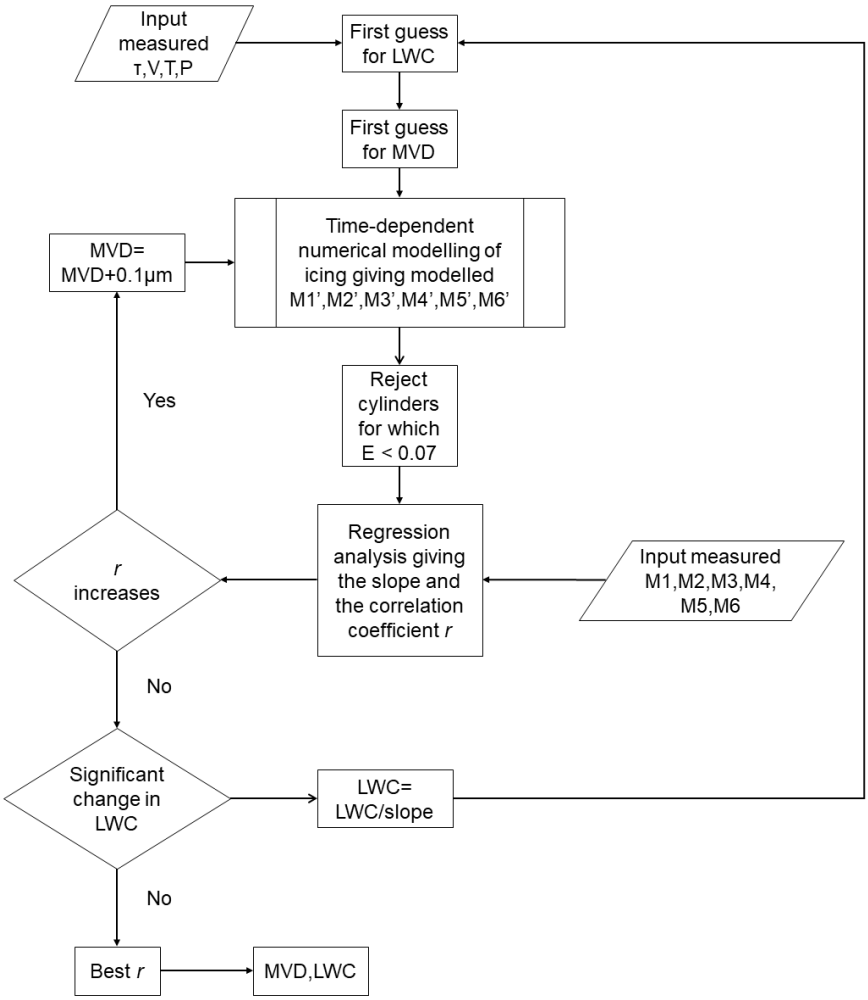

Figure 14 – Block diagram of the RMC method. Redrawn from (Makkonen, 1992).

The RMC method works as follows: the modeled ice masses at a given "guessed" MVD and LWC are compared to the measured ice masses by using the linear regression analysis and least-squares method. The linear regression correlation coefficient with respect to the regression line through the origin is then calculated. Next, the same procedure is then repeated for an MVD that is 0.1 μm larger than the "previous guess". This continues until the correlation coefficient is at maximum, meaning, until it starts to decrease. Then, the LWC value is "corrected" by calculating such a value that yields 1:1 line at the MVD with the highest correlation coefficient value. The calculation then repeats with the newly obtained MVD and LWC values as the new "guess". This continues till the values of the MVD and LWC are sufficiently stable (Makkonen, 1992).

While the RMC method cannot give adequate representation of the droplet distribution spectra (in practice; in theory it's possible, given sufficient, albeit large number of cylinders), it is a useful method for "correcting" LWC or MVD, when the estimate of one of these values is known with the sufficient accuracy. Also, unlike laser-based systems, this method is cheap and easy to implement in the natural icing conditions.

3 Results and Contributions

The purpose of this section is to provide detailed descriptions and discussion of the results, findings and highlights, obtained within the scope of Ph.D. work, primarily concerning the results concerning the calculation of the in-cloud droplet impingement parameters, particularly, for the values of K below 0.25, in order to bypass the limitations of the current Finstad et al./ISO 12494 model. In addition, the results of investigations into the empirical accreted ice densities and the aerodynamic forces acting on the (iced) circular cylinder will be presented. Furthermore, practical applications of the results and contributions from the current work will be discussed, along with the comparison of results and contributions versus some recent developments in the field of the modeling of the atmospheric ice accretion on objects.

3.1 Langmuir droplet distribution spectra and the low limit of *K*

3.1.1 Makkonen and Stallabrass experiments (1984)

This section describes the main results, findings and contributions, achieved within the scope studying the limitations of the current existing analytical parameterization, primarily for the cases when $K \leq 0.25$. The investigation and the analysis will start with the original experimental data of (Makkonen and Stallabrass, 1984; 1987), since this data was used in the validation of the in-cloud impingement parameterization of Finstad et al./ISO 12494 in the first place. Analyzing this data again may reveal some potential clues with regards to when the Finstad et al./ISO 12494 model may encounter issues with estimating the in-cloud impingement parameters, possibly in addition to the already postulated range of $0.07 < E < 0.63$. Table 6 shows the experimental test matrix of Makkonen and Stallabrass. In the Table 6 the value of K is calculated using the average diameter between the initial and the ultimate cylinder diameter using the MVD approximation, with the MVD values listed again in the Table 6.

Table 6 – Experimental test matrix in the Makkonen and Stallabrass (1984; 1987) experiments. The data for the droplet distribution spectrum category and the experimental and overall collision efficiency is omitted. The value of K is based on the calculation using the MVD approximation and the average diameter between the initial and the final cylinder diameters.

Test	***Initial Cylinder Diameter (cm)***	***Ultimate Cylinder Diameter (cm)***	***Test duration (min)***	***Wind Speed (m/s)***	***Air Temperature (°C)***	***LWC (g/m^3)***	***MVD (μm)***	***K***
1	1.024	1.55	30	20	–4.5	0.36	17.1	2.95
2	1.024	1.48	30	20	–4.5	0.35	14.4	2.15
3	1.024	1.42	30	20	–9.5	0.35	14.4	2.24
4	1.024	1.6	30	20	–19.3	0.35	14.4	2.16
5	1.024	1.43	31	20	–4.5	0.33	13.1	1.82
6	3.183	3.65	40	20	–4.5	0.36	17.1	1.11
7	3.183	3.54	40	20	–4.5	0.35	14.4	0.80
8	3.183	3.5	40	20	–9.5	0.35	14.4	0.82
9	3.183	3.7	40	20	–19.3	0.35	14.4	0.82
10	3.183	3.47	40	20	–4.5	0.33	13.1	0.67
11	4.44	4.85	50	20	–4.5	0.36	17.1	0.82
12	4.44	4.81	50	20	–4.5	0.35	14.4	0.58
13	4.44	4.82	50	20	–9.5	0.35	14.4	0.59

14	4.44	5.05	50	20	–19.5	0.35	14.4	0.60
15	4.44	4.71	50	20	–4.5	0.33	13.1	0.49
16	7.609	7.95	50	20	–4.5	0.36	17.1	0.49
17	7.609	7.98	50	20	–9.5	0.36	17.1	0.49
18	7.609	7.81	50	20	–4.5	0.35	14.4	0.35
19	7.609	7.89	50	20	–9.5	0.35	14.4	0.35
20	7.609	8.13	50	20	–19.3	0.35	14.4	0.36
21	7.609	8.13	50	20	–4.5	0.33	13.1	0.28
22	1.024	1.48	30	36	–4.9	0.15	15.7	4.61
23	1.024	1.4	30	36	–4.9	0.15	13.4	3.47
24	1.024	1.35	30	36	–4.9	0.14	12.2	2.93
25	3.183	3.6	40	36	–4.9	0.15	15.7	1.70
26	3.183	3.5	40	36	–4.9	0.15	13.4	1.26
27	3.183	3.45	40	36	–4.9	0.14	12.2	1.05
28	4.44	4.86	50	36	–4.9	0.15	15.7	1.24
29	4.44	4.75	50	36	–4.9	0.15	13.4	0.91
30	4.44	4.66	50	36	–4.9	0.14	12.2	0.77
31	7.609	7.91	50	36	–4.9	0.15	15.7	0.74
32	7.609	7.78	50	36	–4.3	0.15	13.4	0.54
33	7.609	7.77	50	36	–4.9	0.14	12.2	0.45

Complimentary to the Table 7, Figure 15 shows the values of the experimental overall collision efficiencies, E_{exp}, the theoretical overall collision efficiencies, as calculated by Makkonen and Stallabrass, using the full experimental droplet distribution spectra E_{theory}, and, the values of the overall collision efficiencies, calculated within the scope of this work, using the ISO 12494 analytical model, *ISO 12494*. In the Figure 15 the values of the overall collision efficiencies are plotted against the values of the droplet's inertia parameter, *K*, calculated from the experimental conditions in the Table 7.

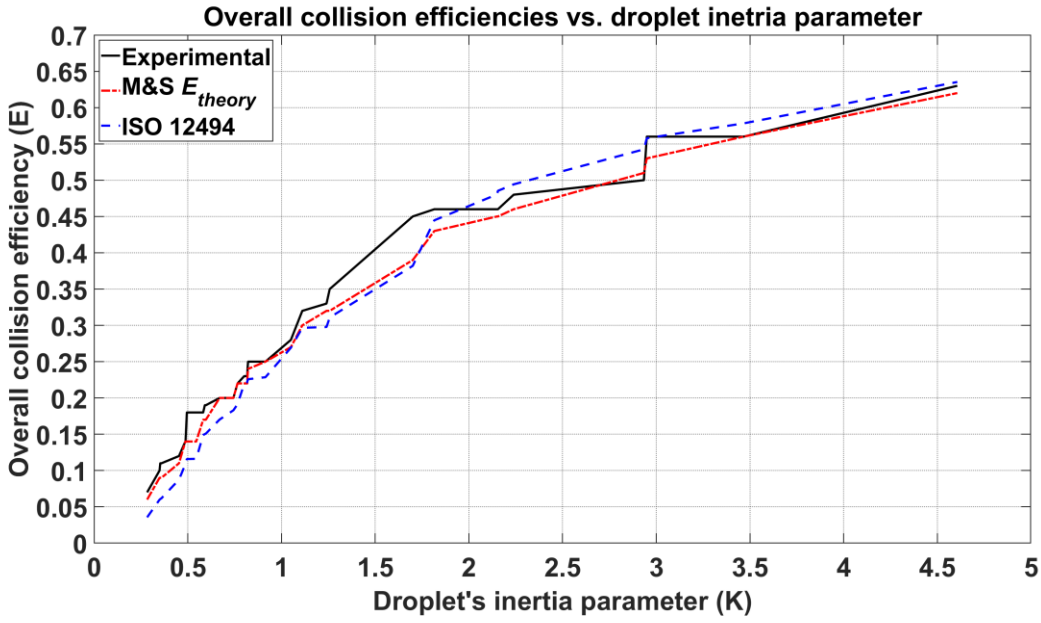

Figure 15 – Overall collision efficiencies versus the droplet inertia parameter in the Makkonen and Stallabrass experiments.

From Figure 15 it can be seen that the calculations by Makkonen and Stallabrass, using the full experimental droplet distribution spectra yield an acceptable agreement with the experimental data for the entire range of the droplet inertia parameter in the experiments. On the contrary, the results using the MVD approximation, do underestimate the overall collision efficiencies below the value of $K < 0.6 – 0.7$ in the Figure 15, which roughly corresponds to the value of $E < 0.10$. The calculations using the full experimental droplet distribution spectra yield good agreement up to the values of K of 0.25 – 0.3. It is also worth mentioning, Figure 15 suggests that the analytical model underestimates the overall collision efficiencies in the range of the values of K of 1.2 – 2, the explanation of it is the lack of data points in the Table 7 for this specific range of K.

In order to investigate the behavior of the analytical overall collision efficiency function of the Finstad et al./ISO 12494, the experimental data of the Makkonen and Stallabrass is tabulated using the Langmuir distributions from Table 1. The values are calculated for the experimental operating conditions in the Table 6. In the Table 7, the "#" column denotes the experimental droplet distribution spectra, for which, unfortunately information is unavailable. The purpose of this column is to serve as an additional reference point for the comparison of the results obtained using the Langmuir distributions. Again, it is worth mentioning that all results calculated with the Langmuir distributions have the same values of MVD as the experimental values, provided in the Table 6.

Table 7 – Experimental (E_{exp}), theoretical, based on the calculations using the full droplet distribution spectra by Makkonen and Stallabrass (E_{theory}), and the overall collision efficiencies, based on the ISO 12494 model calculation (ISO 12494). The columns A to J correspond to the results obtained using Langmuir distributions with the distribution A being monodispersed. Some discrepancies in the values are possible due to the rounding to the two significant digits. Red italic values refer to the closest fit with the theoretical values calculated by the Makkonen and Stallabrass and red bolded values denote the closest fit values with the experimental values. Note, that due to rounding in the original Makkonen and Stallabrass data to the two significant digits there are possible some small discrepancies and multiple "best fit" values per single row in the table.

Test	***A***	***B***	***C***	***D***	***E***	***F***	***G***	***H***	***J***	E_{exp}	E_{theory}	***ISO 12494***	***#***
1	**0.55**	0.54	*0.53*	*0.53*	0.52	0.51	0.51	0.51	0.50	**0.56**	**0.53**	**0.56**	**3**
2	**0.48**	0.47	**0.46**	**0.46**	**0.46**	**0.46**	0.45	**0.46**	*0.46*	**0.48**	**0.46**	**0.49**	**3**
3	0.48	0.47	**0.46**	**0.46**	**0.46**	*0.45*	*0.45*	*0.45*	**0.46**	**0.46**	**0.45**	**0.49**	**3**
4	0.48	0.47	**0.46**	**0.46**	*0.45*	*0.45*	*0.45*	*0.45*	*0.45*	**0.46**	**0.45**	**0.48**	**3**
5	**0.44**	0.43	*0.43*	0.42	0.42	0.42	0.42	*0.43*	*0.43*	**0.46**	**0.43**	**0.44**	**2**
6	*0.30*	*0.30*	*0.30*	*0.30*	0.31	**0.32**	0.33	0.34	0.35	**0.32**	**0.3**	**0.30**	**3**
7	*0.22*	*0.22*	0.23	0.24	**0.25**	0.26	0.27	0.29	0.31	**0.25**	**0.22**	**0.22**	**3**
8	0.22	0.22	***0.23***	0.24	0.25	0.26	0.27	0.29	0.31	**0.23**	**0.23**	**0.23**	**3**
9	*0.23*	*0.23*	*0.23*	**0.24**	0.25	0.26	0.27	0.29	0.31	**0.24**	**0.22**	**0.22**	**3**
10	0.18	***0.19***	***0.19***	0.21	0.22	0.23	0.25	0.26	0.29	**0.2**	**0.2**	**0.18**	**2**
11	0.22	0.22	**0.23**	*0.24*	0.25	0.26	0.27	0.28	0.31	**0.23**	**0.24**	**0.22**	**3**
12	0.15	0.15	*0.16*	*0.18*	**0.19**	0.21	0.22	0.24	0.27	**0.19**	**0.17**	**0.15**	**3**
13	0.15	*0.16*	*0.16*	***0.18***	0.19	0.21	0.22	0.24	0.27	**0.18**	**0.17**	**0.15**	**3**
14	0.15	0.16	*0.17*	0.18	**0.19**	**0.21**	0.22	0.24	0.27	**0.2**	**0.17**	**0.15**	**3**
15	0.12	0.12	***0.13***	***0.15***	0.16	0.18	0.20	0.21	0.24	**0.14**	**0.14**	**0.12**	**2**

16	0.11	0.12	0.13	*0.14*	0.16	**0.17**	**0.19**	0.21	0.24	**0.18**	**0.14**	**0.11**	**3**
17	0.11	0.12	0.13	*0.14*	0.16	0.18	**0.19**	0.21	0.24	**0.19**	**0.14**	**0.11**	**3**
18	0.06	0.07	0.08	***0.10***	0.12	0.13	0.15	0.17	0.20	**0.1**	**0.09**	**0.06**	**3**
19	0.06	0.07	*0.08*	***0.10***	**0.12**	0.13	0.15	0.17	0.20	**0.11**	**0.09**	**0.06**	**3**
20	0.06	0.07	*0.08*	*0.10*	**0.12**	0.14	0.15	0.17	0.20	**0.12**	**0.09**	**0.06**	**3**
21	0.04	0.05	*0.06*	***0.08***	0.10	0.11	0.13	0.15	0.18	**0.07**	**0.06**	**0.04**	**2**
22	**0.64**	***0.62***	0.61	0.60	0.59	0.58	0.57	0.57	0.55	**0.63**	**0.62**	**0.64**	**1**
23	0.57	0.56	0.55	0.54	0.54	0.53	0.52	0.52	0.51	**0.56**	**0.56**	**0.58**	**1**
24	0.54	0.53	0.52	*0.51*	**0.50**	**0.50**	**0.50**	0.49	0.49	**0.5**	**0.51**	**0.54**	**1**
25	0.38	0.38	0.37	0.37	0.38	0.38	0.38	*0.39*	**0.40**	**0.45**	**0.39**	**0.38**	**1**
26	0.31	0.31	0.31	0.31	*0.32*	**0.33**	**0.33**	0.34	0.36	**0.33**	**0.32**	**0.31**	**1**
27	*0.27*	*0.27*	*0.27*	**0.28**	0.29	0.30	0.30	0.31	0.33	**0.28**	**0.27**	**0.27**	**1**
28	0.30	0.29	0.30	0.30	0.31	*0.32*	*0.32*	0.33	**0.35**	**0.35**	**0.32**	**0.30**	**1**
29	0.23	0.23	0.23	0.24	***0.25***	0.26	0.28	0.29	0.31	**0.25**	**0.25**	**0.23**	**1**
30	**0.19**	**0.19**	*0.20*	0.21	0.22	0.24	0.25	0.26	0.29	**0.18**	**0.2**	**0.19**	**1**
31	*0.17*	*0.17*	0.18	0.19	0.21	**0.22**	0.23	0.25	0.27	**0.22**	**0.22**	**0.17**	**1**
32	0.12	0.12	***0.13***	***0.15***	0.16	0.18	0.19	0.21	0.24	**0.14**	**0.14**	**0.12**	**1**
33	0.09	0.09	***0.11***	0.12	0.14	0.15	0.17	0.19	0.22	**0.11**	**0.11**	**0.09**	**1**

Complimentary to the Table 8, Table 9 lists the values of the accreted ice masses with the Langmuir distributions for the experimental conditions in the Table 6.

Table 8 – Experimental (Exp), and theoretical accreted ice masses, based on the ISO 12494 model calculation (ISO 12494). The columns A to J correspond to the results obtained using Langmuir distributions with the distribution A being monodispersed. Some discrepancies in the values are possible due to the rounding to the two significant digits. Red italic values refer to the closest fit with the theoretical values calculated by the Makkonen and Stallabrass and red bolded values denote the closest fit values with the experimental values. Note, that due to rounding in the original Makkonen and Stallabrass data to the two significant digits there are possible some small discrepancies and multiple "best fit" values per single row in the table. In addition, in the original data, Makkonen and Stallabrass do not present the theoretical accreted ice masses, calculated using the experimental droplet spectra. Values are in g/10 cm.

Test	***A***	***B***	***C***	***D***	***E***	***F***	***G***	***H***	***J***	***Exp***	***ISO 12494***	***#***
1	**9.35**	9.10	8.92	8.78	8.65	8.54	8.45	8.40	8.34	**9.34**	9.30	**3**
2	7.69	**7.48**	7.36	7.29	7.25	7.20	7.18	7.22	7.25	**7.56**	7.66	**3**
3	7.79	7.59	7.46	7.40	7.36	7.31	**7.30**	7.33	7.38	**6.31**	7.61	**3**
4	7.97	**7.76**	7.64	7.58	7.54	7.49	7.48	7.53	7.58	**7.85**	7.94	**3**
5	6.73	**6.55**	6.47	6.45	6.44	6.43	6.46	6.52	6.61	**6.54**	6.70	**2**
6	17.56	17.31	17.39	17.83	18.21	**18.72**	19.26	19.83	20.83	**18.7**	17.58	**3**
7	12.53	12.52	12.87	13.47	**14.15**	14.84	15.52	16.26	17.73	**14.18**	12.53	**3**
8	**12.66**	12.65	13.00	13.60	14.29	14.97	15.66	16.41	17.88	**12.44**	12.68	**3**
9	12.93	12.92	**13.26**	13.86	14.54	15.23	15.93	16.67	18.16	**13.46**	12.93	**3**
10	9.65	9.75	**10.19**	10.89	11.61	12.33	13.10	13.93	15.39	**10.55**	9.64	**2**
11	21.99	22.00	22.62	**23.69**	24.90	26.12	27.34	28.65	31.26	**23.17**	22.00	**3**
12	14.50	14.90	15.80	**17.23**	18.64	20.09	21.73	23.32	26.12	**17.83**	14.46	**3**
13	14.68	15.08	15.97	**17.40**	18.82	20.27	21.91	23.51	26.33	**16.77**	14.67	**3**
14	15.07	15.44	16.33	17.76	**19.17**	20.61	22.25	23.87	26.72	**19.03**	14.97	**3**

15	10.55	11.12	**12.12**	13.54	14.95	16.59	18.16	19.71	22.45	**11.91**	10.52	**2**
16	18.35	19.41	21.22	23.78	26.36	**29.33**	32.20	35.01	40.04	**29.6**	18.26	**3**
17	18.62	19.66	21.46	24.02	26.57	29.54	**32.41**	35.24	40.28	**31.8**	18.55	**3**
18	9.74	11.29	13.24	**16.02**	18.81	21.66	24.48	27.31	32.49	**15.2**	9.69	**3**
19	9.96	11.49	13.42	**16.19**	18.99	21.85	24.67	27.50	32.70	**17.3**	9.88	**3**
20	10.41	11.88	13.80	16.54	**19.35**	22.21	25.05	27.88	33.09	**19.1**	10.21	**3**
21	5.85	7.59	9.61	**12.06**	14.58	17.20	19.84	22.51	27.49	**10.9**	5.54	**2**
22	7.72	7.54	**7.39**	7.25	7.09	6.96	6.86	6.77	6.60	**7.42**	7.73	**1**
23	6.88	6.70	6.57	6.46	**6.36**	6.27	6.20	6.15	6.07	**6.38**	6.81	**1**
24	5.90	5.75	5.64	5.56	5.49	5.43	**5.38**	5.36	5.33	**5.39**	5.84	**1**
25	16.76	16.42	16.29	16.38	16.48	16.57	16.79	17.07	**17.48**	**19.07**	16.79	**1**
26	13.46	13.26	13.29	**13.57**	13.82	14.14	14.51	14.90	15.55	**13.59**	13.46	**1**
27	10.80	10.69	10.81	**11.15**	11.48	11.88	12.29	12.72	13.51	**11.11**	10.80	**1**
28	22.33	22.03	22.13	22.66	23.14	23.74	24.41	25.12	**26.31**	**26.65**	22.34	**1**
29	17.01	16.98	17.37	**18.12**	18.92	19.78	20.64	21.54	23.34	**17.75**	17.01	**1**
30	**13.15**	13.25	13.76	14.56	15.47	16.36	17.26	18.28	20.13	**12.3**	13.16	**1**
31	21.43	21.73	22.72	24.26	25.95	**27.61**	29.29	31.23	34.65	**27.4**	21.40	**1**
32	14.44	15.13	**16.35**	18.20	20.03	22.09	24.18	26.24	29.93	**16.7**	14.44	**1**
33	10.19	10.99	**12.28**	14.01	15.91	17.93	19.91	21.87	25.43	**12.5**	10.17	**1**

The calculations in the Figure 15 and Tables 7 and 8 were carried out using the modified Finstad et al. calculation methodology, presented in the Section 2.1.1. Furthermore, the same calculations were repeated using the trajectory calculations methodology, presented in the Section 2.1.2. When it comes to the values of the overall collision efficiencies, both methodologies – the modified Finstad et al. formulae and the trajectory calculations method yield similar results. The difference in overall collision efficiency values obtained by both of these methods, using the Langmuir distributions, as shown in the Table 7, does not exceed 0.01. Therefore, for brevity, only results using the modified Finstad et al. formulae are presented in this work.

From Figure 15 and the Tables 7 and 8, the following conclusions can be drawn:

- The results obtained by Makkonen and Stallabrass using full experimental droplet distribution spectra adequately represent the experimental overall collision efficiencies, with some underestimation occurring for the 76 mm cylinder.
- The values of the overall collision efficiencies and the accreted ice masses, as a result, obtained with the MVD approximation using ISO 12494 unmodified formulae tend to overestimate, slightly, these values for the 1.024 cm cylinder, and underestimate those in more significant fashion, when compared to the results obtained by Makkonen and Stallabrss, using the full droplet distribution spectra, for the 7.609 cm cylinder.
- Calculations using the Langmuir droplet distribution spectra show that for experimental runs, performed at 20 m/s wind speed, the distributions C and D yield the best agreement, on average. This information suggests that the experimental droplet distribution spectra #2 and #3 are “narrow” and quite similar to each other.
- On the contrary, for the experimental runs performed at 36 m/s wind speed, the “wider” distributions, such as Langmuir E and F tend to produce better agreement with the experimental

values, which suggest that the distribution #1 in the Makkonen and Stallabrass data is a "wider" one, even potentially being bimodal.

- When comparing the results with the Langmuir distributions A – J, the results show significant spread in the values, ranging in the extreme case (experimental run #21, $E_{exp} = 0.07$, $K = 0.28$) from underestimating experimental overall collision efficiencies by ≈ 45%, to overestimating it by ≈ 155%, at the same operating conditions and the values of MVD.
- This spread of values becomes smaller with the increase in the values of the droplet inertia parameter K. At sufficiently high values, the trend in values "reverses" – i.e., the monodispersed distribution (Langmuir A) predicts the highest values of the overall collision efficiencies, while the "widest" Langmuir distribution (distribution J, which should estimate the properties of the bimodal/trimodal distributions) shows the lowest values of the overall collision efficiencies and the accreted ice masses.

The last two points worth more detailed attention. Recall, that the in-cloud impingement parameters are calculated as:

$$X(K, \phi) = \left[C_{X,1} K^{C_{X,2}} \exp\left(C_{X,3} K^{C_{X,4}}\right) + C_{X,5}\right] - \left[C_{X,6}(\phi - 100)^{C_{X,7}}\right] \times \left[C_{X,8} K^{C_{X,9}} \exp\left(C_{X,10} K^{C_{X,11}}\right) + C_{X,12}\right] \tag{3.1}$$

with the values of constants of constants $C_1 – C_{12}$ given in Table 2.

The droplet inertia parameter K_i, droplet Reynolds number Re_i for each bin MVD value along with the Langmuir parameter ϕ and spectrum-averaged inertia parameter K_{spec} are calculated as:

$$K_i = \frac{\rho_w d_i^2 u}{18 \mu_a C} \tag{3.2}$$

$$Re_i = \frac{\rho_a d_i u}{\mu_a} \tag{3.3}$$

$$\phi = \frac{Re_i^2}{K_i} = \frac{\left(\frac{\rho_a d_i u}{\mu_a}\right)^2}{\frac{\rho_w d_i^2 u}{18 \mu_a C}} = \frac{18 \mu_a C \rho_a^2 d_i^2 u^2}{\mu_a^2 \rho_w d_i^2 u} = \frac{18 C \rho_a^2 u}{\mu_a \rho_w} = 18 \frac{\rho_a^2}{\mu_a \rho_w} Cu = 9 \frac{\rho_a^2}{\mu_a \rho_w} Du = cDu \tag{3.4}$$

$$K_{spec} = \sum_{i=1}^{N} w_i K_i = w_1 K_1 + w_2 K_2 + \ldots + w_{N-1} K_{N-1} + w_N K_N \tag{3.5}$$

where, d_i is a MVD of a bin i, u is the operating (freestream) wind speed, C is the characteristic length of an object, i.e., the circular cylinder and c is the proportionality constant. The value of cylinder radius R is used as the characteristic length C in the Equations (3.2) and (3.4). From the Equation (3.4) it follows that the Langmuir parameter ϕ is independent from the droplet diameter, and, disregarding the differences in the iced cylinder diameters, it can be assumed to be almost constant for different Langmuir droplet distribution spectra under same operating conditions.

However, since the value of the droplet inertia parameter K in the Equation (3.2), and as the result – its' spectrum-averaged values K_{spec} in the Equation (3.5) are dependent on the values of the per-bin median volume diameter d_i.

In order to give an example of the calculation of the droplet inertia parameter – consider the following example of calculations of K_{spec} using the Langmuir D distribution:

$$K_{spec} = \sum_{i=1}^{7} w_i K_i = 0.05K_1 + 0.1K_2 + 0.2K_3 + 0.3K_4 + 0.2K_5 + 0.1K_6 + 0.05K_7 \tag{3.6}$$

where $K_1 - K_7$ are the values of the droplet inertia parameter for bins 1 – 7 and values 0.05, 0.1, 0.2 and 0.3 are LWC fractions of the respective bin. To give a further example, suppose one wants to find a value of K_{spec} for Langmuir D distribution, when compared to the monodispersed one (Langmuir A). Since the only difference in this case is the ratio of diameters, the K_{spec} value for the Langmuir D distribution can be found as:

$$\begin{aligned} K_D = \sum_{i=1}^{7} w_i K_i &= 0.05K_1 + 0.1K_2 + 0.2K_3 + 0.3K_4 + 0.2K_5 + 0.1K_6 + 0.05K_7 \\ &= 0.05\times 0.31^2\times K + 0.1\times 0.52^2\times K + 0.2\times 0.71^2\times K + 0.3\times 1^2\times K \\ &\quad + 0.2\times 1.37^2\times K + 0.1\times 1.74^2\times K + 0.05\times 2.22^2\times K \\ &= 0.0048K + 0.0270K + 0.1008K + 0.3K + 0.3754K + 0.3028K + 0.2464K = 1.3572K \end{aligned} \tag{3.7}$$

where K is the droplet inertia parameter value of the monodispersed distribution. In another words, for Langmuir D distribution the spectrum-averaged value of the droplet inertia parameter is approximately 1.36 times larger than the monodispersed distribution. Under the *same* operating conditions. At the *same value of (spectrum) MVD*. The same is also true for the numerical CFD calculations using the FENSAP–ICE and DROP3D.

This is the main reason why the change of droplet distribution spectrum works when simulations or calculations fail to give the correct ice mass, thickness, shape or density. Since all of these parameters are controlled by the value of K and *changing* this K will change *everything* else in turn. And the way it works is by giving a high "weight" to the contribution of the largest droplets in the spectrum, even when their LWC fraction (relative to the others) is small. That is also the reason why one should be ***extremely*** careful when selecting the droplet distribution spectrum for use in calculations or simulations. In addition, in the author's opinion this is entirely *physical* as for each and every icing event be it in-cloud, precipitation, etc., there is *always* a distribution of droplet sizes. It is the monodispersed approximation which is *unphysical* while being *mathematically* correct.

In order to illustrate this concept further, Table 9 shows the values of the droplet inertia parameter K calculated with the Langmuir distributions A – J for the experimental conditions in the Table 6.

Table 9 – Droplet inertia parameter K values calculated using the Langmuir distributions for the experimental operating conditions in the Makkonen and Stallabrass experiments (1984). The value Exp denotes the experimental value of the droplet inertia parameter, reverse calculated from the experimental operating

conditions, overall collision efficiencies and ice masses, using the MVD approximation, and the mean cylinder diameter (half value of the sum of the initial and the ultimate cylinder diameters) in their experiments.

Test	***A***	***B***	***C***	***D***	***E***	***F***	***G***	***H***	***J***	***Exp***
1	2.95	3.16	3.48	4.03	4.80	5.90	7.42	9.58	16.80	**2.95**
2	2.14	2.29	2.53	2.93	3.48	4.27	5.37	6.92	12.11	**2.15**
3	2.14	2.29	2.52	2.92	3.47	4.26	5.35	6.90	12.08	**2.24**
4	2.15	2.30	2.54	2.94	3.49	4.28	5.38	6.94	12.14	**2.16**
5	1.80	1.93	2.12	2.46	2.92	3.58	4.50	5.79	10.13	**1.82**
6	1.12	1.19	1.31	1.52	1.80	2.21	2.77	3.57	6.22	**1.11**
7	0.80	0.86	0.94	1.09	1.30	1.59	1.99	2.56	4.46	**0.80**
8	0.81	0.87	0.95	1.10	1.31	1.60	2.01	2.58	4.49	**0.82**
9	0.83	0.88	0.97	1.12	1.33	1.63	2.05	2.63	4.58	**0.82**
10	0.67	0.72	0.79	0.91	1.09	1.33	1.67	2.14	3.73	**0.67**
11	0.82	0.87	0.96	1.11	1.32	1.62	2.03	2.60	4.54	**0.82**
12	0.59	0.63	0.69	0.80	0.95	1.16	1.46	1.87	3.26	**0.58**
13	0.59	0.63	0.70	0.81	0.96	1.17	1.47	1.89	3.29	**0.59**
14	0.61	0.65	0.71	0.83	0.98	1.20	1.50	1.93	3.36	**0.60**
15	0.49	0.52	0.58	0.67	0.80	0.97	1.22	1.57	2.72	**0.49**
16	0.49	0.53	0.58	0.67	0.80	0.98	1.23	1.59	2.76	**0.49**
17	0.50	0.53	0.59	0.68	0.81	0.99	1.25	1.61	2.79	**0.49**
18	0.35	0.38	0.42	0.49	0.58	0.72	0.90	1.15	1.98	**0.35**
19	0.36	0.38	0.43	0.49	0.59	0.72	0.91	1.16	2.00	**0.35**
20	0.37	0.39	0.44	0.51	0.61	0.74	0.93	1.19	2.05	**0.36**
21	0.29	0.32	0.35	0.41	0.49	0.60	0.75	0.96	1.65	**0.28**
22	4.65	4.98	5.49	6.36	7.57	9.30	11.71	15.12	26.57	**4.61**
23	3.43	3.67	4.05	4.69	5.58	6.85	8.62	11.12	19.51	**3.47**
24	2.89	3.10	3.41	3.95	4.70	5.77	7.26	9.36	16.40	**2.93**
25	1.71	1.83	2.01	2.32	2.76	3.38	4.25	5.48	9.58	**1.70**
26	1.26	1.34	1.48	1.71	2.03	2.48	3.12	4.02	7.01	**1.26**
27	1.05	1.12	1.23	1.43	1.69	2.07	2.61	3.36	5.85	**1.05**
28	1.25	1.33	1.46	1.69	2.01	2.46	3.09	3.98	6.95	**1.24**
29	0.91	0.98	1.07	1.24	1.48	1.81	2.27	2.92	5.09	**0.91**
30	0.76	0.81	0.90	1.04	1.23	1.51	1.90	2.44	4.25	**0.77**
31	0.75	0.80	0.88	1.02	1.21	1.48	1.86	2.39	4.18	**0.74**
32	0.55	0.58	0.64	0.75	0.89	1.09	1.37	1.76	3.06	**0.54**
33	0.45	0.49	0.54	0.63	0.74	0.91	1.15	1.47	2.56	**0.45**

From Table 9 it can be seen that the values of the droplet inertia parameter K always increase with the increase in the "width" of the Langmuir distribution, meaning that the values of K increases as the ratios of the per-bin MVD values $(d/d_0)^n$ increases. In the Table 9, the value of the spectrum-averaged droplet inertia parameter K_{spec}, at maximum, using the distribution Langmuir J, can exceed the same value for the Langmuir A distribution (monodispersed distribution) by as much as 450–500%.

However, the same increase in the values of the droplet inertia parameter does not necessarily equate to the similar increase in the values of the overall collision efficiencies *E*. Indeed, consider the following example, given in the Table 10:

Table 10 – Values of the overall collision efficiency (E) as a function of the droplet's inertia parameter K and the Langmuir parameter ϕ. The value ΔE shows the change of the overall collision efficiency compared to the previous calculation/row in the table.

K	***ϕ***	***E***	***ΔE (%)***
0.25	100	0.033	100.0
0.5	100	0.153	363.6
1	100	0.326	113.1
2	100	0.507	55.6
4	100	0.663	30.8
8	100	0.780	17.7
16	100	0.862	10.5
32	100	0.915	6.2
64	100	0.948	3.6
128	100	0.967	2.0
0.25	1000	0.025	100.0
0.5	1000	0.118	372.0
1	1000	0.260	120.3
2	1000	0.424	63.1
4	1000	0.579	36.6
8	1000	0.707	22.1
16	1000	0.803	13.6
32	1000	0.870	8.3
64	1000	0.915	5.2
128	1000	0.944	3.2
0.25	10000	0.012	100.0
0.5	10000	0.066	450.0
1	10000	0.163	147.0
2	10000	0.300	84.1
4	10000	0.454	51.3
8	10000	0.598	31.7
16	10000	0.715	19.6
32	10000	0.804	12.5
64	10000	0.868	8.0
128	10000	0.911	5.0

In the Table 10, the value of the droplet inertia parameter *K* doubles in each subsequent/following row, unless the value of the Langmuir parameter ϕ changes. Under the same operating conditions, with only variable being the value of the MVD itself, the doubling of the value of the droplet inertia parameter *K* means that the (per-bin) droplet MVD value increase as a factor of $\sqrt{2}$ – i.e., meaning 5 μm droplet becomes 7.07 μm droplet, 10 μm droplet becomes 14.14 μm droplet, 20 μm droplet becomes 28.28 μm droplet and so forth.

From the Table 10 it can be seen that the change in the overall collision efficiency values ΔE occurs in the non-linear fashion when cross-checked with the change of the droplet inertia parameter K. For example, changing the droplet inertia parameter from $K = 0.25$ to $K = 0.5$ results in the increase of the overall collision efficiencies by more than 300%; doubling the droplet inertia parameter from 0.5 to 1 results in the increase of the overall collision efficiencies by more than 100%. On the other hand, increasing the value of K from $K = 32$ to $K = 64$, or from $K = 64$ to $K = 128$ yields an increase in the overall collision efficiencies values of an order of a few percent.

This mechanism explains the behavior of the Langmuir distributions from the Tables 7 and 8. In the lower limit of the droplet inertia parameter, changing the K value significantly leads to a large increase in the overall collision efficiencies. The effect diminishes as the value of K increases. Since the change in the droplet distribution spectra for the Langmuir distributions always results in the increase in the values of K (when changing distributions from A to J) at sufficiently high values of K this change, and the corresponding per-bin values of K_i will yield a relatively small increase in the overall collision efficiencies. And since these "wider" distributions are "top heavy" meaning that the larger bins are responsible for majority of the performance increase, this effect gets "diluted" at high values of K. However, since the monodispersed distribution has only one diameter in it, corresponding to the value of the entire spectrum MVD, it is much less affected by this mathematical manipulation. Such behavior of Langmuir distributions was initially noted by the (Langmuir and Blodgett, 1946) and Tables 7, 8 and 10 are in accordance with their predictions. In essence, this is a "self-limiting" mechanism which does not allow for the Langmuir distributions to significantly overestimate the values of the overall collision efficiencies and the accreted ice masses at high values of the droplet's inertia parameter K.

3.1.2 FRonTLINES project experimental cases (2017)

Having established the behavior of the Langmuir distributions and the (modified) Finstad et al. analytical parameterization for the experimental data of (Makkonen and Stallabrass, 1984), which served as the baseline for the validation of the Finstad et al. model for the range of the overall collision efficiencies of $0.07 < E < 0.63$, it is necessary now to analyze the available experimental data for the range of overall collision efficiencies and the droplet inertia parameter values, for which the Finstad et al./ISO 12494 model underestimates the accreted ice masses/breaks in its current iteration. This corresponds to the values of $E < 0.10$ and $K \leq 0.25$, respectively. For this purpose, the experimental data from the FRonTLINES project is used, which was specifically performed in order to obtain some experimental evidence for these extreme values of K and E. These experiments were performed at the VTT Technical Research Centre of Finland, Espoo, Finland, and the description of the experimental apparatus and conditions is given in Section 2.3.1 of this work. For convenience, the experimental test matrix of the FRonTLINES experiments is given in the Table 11.

Table 11 – Experimental test matrix of the FRonTLINES experiments. The value E_{exp} is the experimental collision efficiencies. The value of K_{exp} is based on the calculation using the MVD approximation and the initial cylinder diameter, as the final diameter of the iced cylinders in the experiment is unknown.

Test	***Cylinder Diameter (mm)***	***Test Duration (min)***	***Wind Speed (m/s)***	***Air Temperature (°C)***	***LWC (g/m^3)***	***MVD (μm)***	***Ice Mass (g)***	***E_{exp}***	***K_{exp}***
1	30	30	4	–5	0.4	18.73	1.163	0.086	0.346

2	50	30	4	–5	0.4	18.73	0.722	0.032	0.208
3	80	30	4	–5	0.4	18.73	0.743	0.021	0.130
4	100	30	4	–5	0.4	18.73	0.77	0.017	0.104
5	170	30	4	–5	0.4	18.73	0.812	0.011	0.061
6	30	30	7	–5	0.4	18.73	4.211	0.018	0.606
7	100	30	7	–5	0.4	18.73	4.754	0.036	0.182

Moreover, unlike the experiments of the Makkonen and Stallabrass, the experimental droplet distribution spectrum is known for the FRonTLINES experiments. However, due to some confusion VTT has specified the following information regarding the experimental droplet distribution spectra:

- A monodispersed distribution with the MVD value of 20 µm.
- An experimental distribution with the MVD value of 18.73 µm, given in Figure 16 and Table 12, respectively.

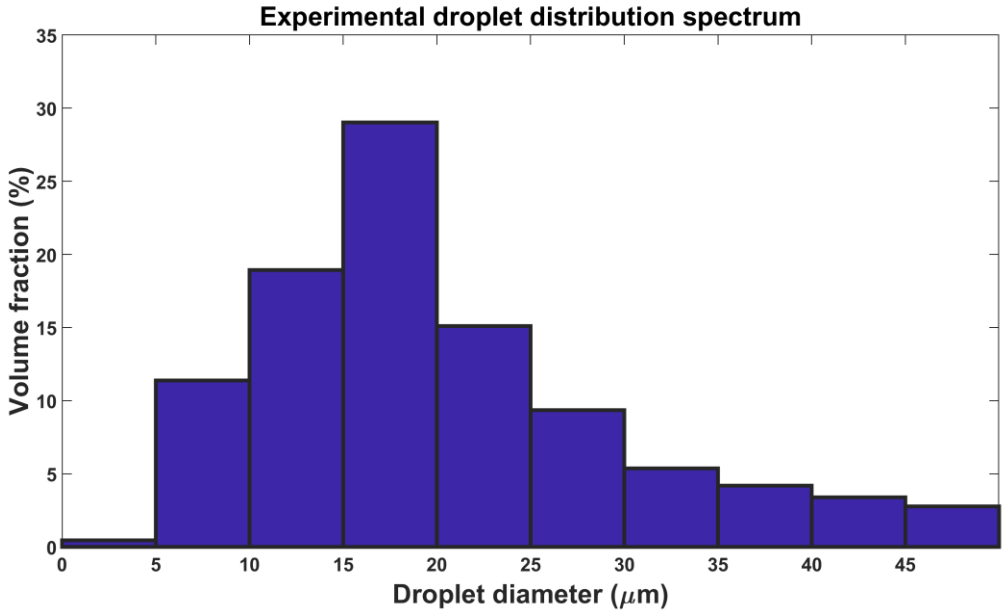

Figure 16 – VTT experimental droplet distribution spectrum with the MVD value of 18.73 µm.

Table 12 – VTT experimental droplet distribution spectrum with the MVD value of 18.73 µm. The LWC fraction is given as a normal fraction with its cumulative sum corresponding to unity.

Bin (µm)	***Bounds (µm)***	***LWC fraction***
5	0.61 – 5	0.0045
10	5 – 10	0.1138
15	10 – 15	0.1893
20	15 – 20	0.2902
25	20 – 25	0.1510
30	25 – 30	0.0935
35	30 – 35	0.0537
40	35 – 40	0.0419
45	40 – 45	0.0339

50	45 – 50	0.0277
Σ	**18.73**	**1**

The calculations of the operating parameters, including the value of the K_{exp} in the Table 11 is carried out using the full experimental droplet distribution spectrum.

As with the Makkonen and Stallabrass experimental data, Table 13 lists the values of the overall collision efficiencies using the Langmuir distributions and the experimental distribution. The assumed MVD for this Table is 18.73 µm, which was based on the available information from the VTT at the point when this data was tabulated. The monodispersed distribution with the value of MVD of 20 µm is not used.

Table 13 – Overall collision efficiencies in the FRonTLINES experiments in the analytical calculations. The values in "Exp" column denotes the experimental values, and the "VTT" column denotes the results of calculations using the experimental droplet distribution spectrum. Red bolded values denote the closest fit values with the experimental values across all distributions tested.

Test	***A***	***B***	***C***	***D***	***E***	***F***	***G***	***H***	***J***	***VTT***	***Exp***
1	0.057	0.070	**0.086**	0.105	0.124	0.144	0.162	0.181	0.213	0.114	**0.086**
2	0.010	0.023	**0.035**	0.050	0.066	0.084	0.102	0.120	0.155	0.058	**0.032**
3	0.010	0.011	0.016	**0.024**	0.036	0.050	0.066	0.082	0.116	0.031	**0.021**
4	0.010	0.010	0.012	**0.018**	0.026	0.037	0.051	0.066	0.098	0.023	**0.017**
5	0.010	0.010	0.010	**0.011**	0.014	0.020	0.028	0.037	0.063	0.013	**0.011**
6	0.148	0.153	0.164	**0.180**	0.195	0.211	0.228	0.245	0.272	0.191	**0.177**
7	0.010	0.016	0.026	**0.038**	0.052	0.068	0.084	0.101	0.135	0.045	**0.036**

In addition, Table 14 lists the experimental accreted ice masses, calculated accreted ice masses using the Langmuir and the experimental distributions.

Table 14 – Accreted ice masses in the FRonTLINES experiments in the analytical calculations. The values in "Exp" denotes the experimental values, and the "VTT" column denotes the results of calculations using the experimental droplet distribution spectrum. Red bolded values denote the closest fit values with the experimental values across all distributions tested. Values are in grams.

Test	***A***	***B***	***C***	***D***	***E***	***F***	***G***	***H***	***J***	***VTT***	***Exp***
1	0.772	0.952	**1.168**	1.437	1.702	1.968	2.225	2.478	2.930	1.564	**1.163**
2	0.226	0.529	**0.795**	1.138	1.509	1.908	2.315	2.734	3.525	1.325	**0.722**
3	0.362	0.398	0.575	**0.871**	1.307	1.818	2.377	2.980	4.198	1.115	**0.743**
4	0.453	0.453	0.545	**0.813**	1.164	1.692	2.315	3.005	4.456	1.022	**0.770**
5	0.769	0.769	**0.769**	**0.855**	1.077	1.560	2.170	2.885	4.811	0.975	**0.812**
6	3.566	3.694	3.947	**4.338**	4.708	5.115	5.531	5.931	6.621	4.609	**4.211**
7	0.793	1.308	2.048	**3.038**	4.151	5.387	6.689	8.055	10.723	3.559	**2.853**

From Tables 13 and 14 it can be seen that as with the experiments of the Makkonen and Stallabrass different droplet distribution spectra show significant spread in predicted overall collision efficiencies and the accreted ice masses, and in the worst cases they can either underestimate these by about 70% or overestimate by nearly 500%.

Furthermore, note that in the Table 13 there are multiple entries for which the overall collision efficiencies are the same and are equal to the value of $E = 0.01$. The reason for this is the enforced constraint of $E = 0.01$ for $K \leq 0.17$ for each bin in the spectra. Since the summation of the spectrum-averaged values is based on the per-bin values using the LWC fraction as the weighting coefficient, it follows that the $E_{spec} = 0.01$ for $K_{spec} \leq 0.17$ is also true.

While this constraint allows for the droplets to "impinge" on the circular cylinders even in the range of very low K values and may be useful for the purposes of the extreme value analysis it has certain potential limitations. First, since the droplet's "behavior" is governed by the value of K, which shows the balance of inertia and the drag, acting on it, all droplets, for which the constraint of $X(K, \phi) = 0.01$ for $K \leq 0.17$ is true, where X is a cloud impingement parameter, which is a function of K, for example – the overall collision efficiency, "behave" in the same way. This means that their impact velocities, angles, collision efficiencies etc. are equal, irrespective of the actual size of the droplet. This means this analytical calculation procedure will show the same values of the in-cloud impingement parameters for 5, 10, 20 or 50 μm droplet as long as the constraint of $X(K, \phi) = 0.01$ for $K \leq 0.17$ is enforced.

Conversely, the same applies to the cylinder diameters. Note that in the Table 13, the 50, 80, 100 and 170 mm cylinders all have the same overall collision efficiencies (with respect to the monodispersed distribution) due to this constraint being enforced for all of them. The cylinder diameter can be arbitrarily high – for example, 1000 mm, and the overall collision efficiencies still will be 0.01. Since the accreted ice mass is a function of the characteristic length, it being a cylinder diameter, on (very) large conductors this constraint can potentially result in a sever overestimation of the accreted ice masses.

Finally, the constraint of $E = 0.01$ for $K \leq 0.17$ may explain why in the Tables 13 and 14 the experimental distribution overestimates the overall collision efficiencies and the accreted ice masses when compared with the experimental values for the tests 1 – 5, which all have low values of the droplet inertia parameter, $K < 0.35$. In order to confirm or deny this hypothesis an alternative method is needed (as the trajectory calculations, using the methodology presented in the Section 2.1.2 of this work are not suitable for the values of $K \leq 0.25$). Thus, the usage of the numerical CFD simulations will be employed, in particular Ansys FENSAP–ICE, which is free of this constraint.

For this purpose, the numerical CFD simulations of the FRonTLINES experimental data has been carried out using the FENSAP–ICE. Due to the fact that FENSAP–ICE only natively supports Langmuir A – E distributions (the remaining distributions can be used if inputted as "custom distribution" provided the MVD of it is known) the numerical CFD simulations are constrained to these only. In addition, due to provided information by the VTT at the point when these CFD simulations were carried out, the operating assumption was that the MVD of it is 20 μm. Thus, the numerical simulations with the Langmuir spectra has been carried out at this value of MVD. The numerical calculations were carried out in accordance with the presented CFD numerical simulations setup, described in the Section 2.2. The results of the numerical simulations for the FRonTLINES experimental test cases is given in the Tables 15 and 16 for the overall collision efficiencies and the accreted ice masses, respectively.

Table 15 – Overall collision efficiencies in the FRonTLINES experiments in the numerical calculations. The values of Exp denotes the experimental values, and the VTT column experimental droplet distribution. Red bolded values denote the closest fit values with the experimental values across all distributions tested.

Test	*A*	*B*	*C*	*D*	*E*	*VTT*	*Exp*
1	0.054	0.067	**0.083**	0.102	0.121	0.091	**0.086**
2	0.010	0.021	**0.034**	0.050	0.066	0.046	**0.032**
3	0.003	0.005	0.011	0.027	0.036	**0.024**	**0.021**
4	0.001	0.002	0.006	**0.013**	0.022	**0.013**	**0.017**
5	0.000	0.001	0.001	0.003	**0.015**	0.004	**0.011**
6	0.146	0.149	**0.176**	0.196	0.243	0.197	**0.177**
7	0.006	0.013	0.023	**0.036**	0.050	0.034	**0.036**

Table 16 – Accreted ice masses efficiencies in the FRonTLINES experiments in the numerical calculations. The values of Exp denotes the experimental values, and the VTT column experimental droplet distribution. Red bolded values denote the closest fit values with the experimental values across all distributions tested. Values are in grams.

Test	*A*	*B*	*C*	*D*	*E*	*VTT*	*Exp*
1	0.736	0.906	**1.129**	1.382	1.637	1.234	**1.163**
2	0.234	0.475	**0.770**	1.122	1.500	1.043	**0.722**
3	0.103	0.182	0.409	0.976	1.306	**0.878**	**0.743**
4	0.066	0.104	0.264	0.568	0.998	**0.605**	**0.770**
5	0.030	0.040	0.073	0.223	**1.191**	0.287	**0.812**
6	3.465	3.548	**4.182**	4.660	5.764	4.672	**4.211**
7	0.484	1.028	1.823	**2.834**	3.993	2.675	**2.853**

The results from the numerical CFD simulations show similar trend in values as the results obtained with the analytical calculations for the FRonTLINES experimental cases – large spread in the values of the overall collision efficiencies and the accreted ice masses, in addition to the increase in these values, associated with the change of the Langmuir distributions, from "narrower" to "wider", for example, changing from the distribution B to E.

Note that despite performing the CFD simulations at higher value of MVD (20 μm in the numerical calculations versus 18.73 μm in the analytical calculations, with the exception of the experimental droplet distribution spectrum) the results from the CFD simulations for the overall collision efficiencies and the accreted ice masses in the Tables 15 and 16, respectively, show lower values than the same entries for the analytical calculations, given in the Tables 13 and 14, respectively. There are a few possible explanation for this, primarily, the aforementioned analytical constraint of the $X(K, \phi) = 0.01$ for $K \leq 0.17$ in the analytical calculations, to which the numerical CFD simulations are not subject to, as evidenced from the very low values of the overall collision efficiencies for the monodispersed distribution in the Table 15.

In particular, for the 170 mm cylinder the value of the overall collision efficiency is zero due to rounding to the three significant digits. This experimental case, which has the value of the droplet inertia parameter $K_{exp} = 0.06$ can be considered the limit of applicability of the CFD simulations (with the monodispersed distribution). With the exception of this case, the CFD simulations can adequately represent the overall collision efficiencies and the accreted ice masses with the experimental distribution along with the Langmuir C and D distributions. The good performance of the Langmuir C and D distribution is also present in the analytical calculations, for the both FRonTLINES and the Makkonen

and Stallabrass experiments. Thus, these distributions (Langmuir C and D) are recommended for the "first guess" usage for the modeling of the dry ice growth on the circular structures, in the range of the low values of *K*.

Furthermore, in order to give a quantitative estimate in the performance of both the analytical and numerical model in comparison with the experimental results, the overall collision efficiencies were obtained in both numerical and analytical calculations using the monodispersed distribution with the value of MVD of 18.73 μm. In addition, the analytical calculations were performed according to the Finstad et al./ISO 12494 formulae, meaning that the constraint of the $E = 0.01$ for $K \leq 0.17$ in the analytical calculations is not enforced this time. The reason for this is to keep the results from both the analytical and the numerical calculations as close as possible to the ISO 12494 modeling guidelines (while keeping in mind the possible underestimation of the overall collision efficiencies for the range of $E < 0.10$).

Table 17 – Overall collision efficiencies in the FRonTLINES experiments in the numerical and the analytical calculations obtained using the monodispersed distribution with the 18.73 μm MVD. No constraints are used in the analytical model, in order to make the results ISO 12494 compliant. The relative error values are given with respect to the experimental overall collision efficiencies.

Test	*Experiment*	*MVD Analytical*	*MVD CFD*	*Error Analytical (%)*	*Error CFD (%)*
1	0.086	0.057	0.037	–33.7	–57.0
2	0.032	0.002	0.007	–93.8	–78.1
3	0.021	0.000	0.002	–100.0	–90.5
4	0.017	0.000	0.001	–100.0	–94.1
5	0.011	0.000	0.000	–100.0	–100.0
6	0.177	0.148	0.120	–16.4	–32.2
7	0.036	0.000	0.004	–100.0	–88.9

From Table 17 it can be seen that the results obtained using both the analytical and the numerical calculations with the monodispersed distribution agree poorly with the experimental values. In fact, the agreement is so poor, that the analytical results for the FRonTLINES experimental cases 2 – 5 and 7 are negative ($E < 0$, the values have been rounded to $E = 0$ for these cases in the Table 17). The CFD results in the Table 17 also fare poorly and therefore both methodologies (numerical and analytical) are not suitable for modeling such in-cloud impingement cases using the monodispersed distribution.

On the other hand, Tables 18 and 19 list the comparison of overall collision efficiencies and ice masses, respectively, using the experimental distribution with both analytical and numerical results, calculated based on the procedure, discussed previously in Section 2 of this thesis, for both of them.

Table 18 – Overall collision efficiencies in the FRonTLINES experiments in the numerical and the analytical calculations obtained using the experimental droplet distribution spectrum with the 18.73 μm MVD. The constraint of $E_i = 0.01$ for $K_i \leq 0.17$ is used in the analytical calculations. The relative error values are given with respect to the experimental overall collision efficiencies.

Test	*Experiment*	*Analytical*	*Numerical*	*Error Analytical (%)*	*Error Numerical (%)*
1	0.086	0.114	0.091	32.6	5.8
2	0.032	0.058	0.046	81.3	43.8
3	0.021	0.031	0.024	47.6	14.3

4	0.017	0.023	0.013	35.3	-23.5
5	0.011	0.013	0.004	18.2	-63.6
6	0.177	0.190	0.197	7.3	3.7
7	0.036	0.045	0.034	25.0	-5.6

Table 19 – Accreted ice masses in the FRonTLINES experiments in the numerical and the analytical calculations obtained using the experimental droplet distribution spectrum with the 18.73 μm MVD. The constraint of $E_i = 0.01$ for $K_i \leq 0.17$ is used in the analytical calculations. The relative error values are given with respect to the experimental overall collision efficiencies.

Test	***Experiment (g)***	***Analytical (g)***	***Numerical (g)***	***Error Analytical (%)***	***Error Numerical (%)***
1	1.163	1.560	1.234	34.1	6.1
2	0.722	1.321	1.043	83.0	44.5
3	0.743	1.112	0.878	49.7	18.12
4	0.770	1.020	0.605	32.5	-21.4
5	0.812	0.973	0.287	19.8	-64.7
6	4.211	4.600	4.672	9.3	1.6
7	2.853	3.549	2.675	24.4	-6.2

From the Tables 18 and 19 it can be seen that the use of full droplet distribution spectrum produces significantly better results than the monodisperse distribution. In addition, the experimental distribution has a lower value of MVD, being equal to the 18.73 μm, than the initially assumed monodisperese distribution with MVD value of 20 μm, while typical assumption from Finstad et al./ISO 12494 theory would suggest that the higher values of MVD would produce correspondingly higher values for overall collision efficiencies and ice masses. While it may not be always the case, this can be explained as follows.

The overall collision efficiency E depends on the droplet inertia parameter K, and Langmuir parameter ϕ. Since ϕ is independent from the droplet diameter, and depends only on the operating conditions, as it was mentioned previously, it can be said that the overall collision efficiencies E_i of different droplet bins depend only on the droplet inertia parameter K_i values of bins. Those dependences are not linear - the K_i depends on a square of d_i, while in turn the E_i has exponential dependence on K_i. This, in turn will lead to the fact that dependence of E_i on K_i is highly non-linear and complex.

Moreover, since Finstad et al./ISO 12494 model parameterization for overall collision efficiency was developed with monodisperse distribution in mind, and therefore it is intrinsically "fine-tuned" to the monodisperse distribution, which may result in that the values, obtained with full distribution spectrum show higher values of overall collision efficiencies in the analytical model calculations for the low values of droplet inertia parameter, as the change of the droplet distribution spectra will change the spectrum-averaged droplet inertia parameter value K_{spec}. Furthermore, the imposed constraint of $E_i = 0.01$ for $K_i \leq 0.17$ may lead to further increase in values of overall collision efficiency in analytical calculations.

As a result, the values of the overall collision efficiency values tend to scale somewhat "aggressively" for the very low values of droplet inertia parameter K, and can lead to some degree of overestimation in values of overall collision efficiencies for those very low values of K, as it can be seen from the analytical

model results in Tables 25 – 27, as for majority of the FRonTLINES experimental cases the analytical model results tend to overestimate the overall collision efficiencies values, when compared to experimental results. However, when comparing the respective results from the Tables 17 – 19, the analytical results with full the distribution spectrum in use, while somewhat overestimating the values of overall collision efficiencies in experiments are, in general, considerably closer to experimental results, than the results, obtained with monodisperse distribution. Furthermore, it can be argued that usage of a few different constraints for E_i, depending on the value of K_i, as opposed to use of a singular constraint of $E_i = 0.01$ for $K_i \leq 0.17$ can yield better results. Overall, the approach used in analytical calculations in this section and discussed in details in the Section 2.1.1, is deemed useful for estimating "worst-case" ice loads, for example in extreme value analysis, as some degree of consistent overestimation of the results, based on the comparison with experimental data can be treated as sort of "safety margin" in terms of loading, produced by those masses.

When comparing the results from the Tables 17 – 19, it can be seen that the CFD model with full distribution used matches the experimental results significantly better, when compared to monodisperse distribution. The only cases where the relative error between CFD simulations and experimental results is large are cases 2, 4, and 5, i.e. – 50, 100 and170 mm rotating cylinders at 4 m/s wind speed, respectively. The under estimation of ice masses for 170 mm cylinder at 4 m/s wind speed can be explained by very low value of K for this case ($K \approx 0.25$), as the CFD simulations do not employ the same constraint of $E_i = 0.01$ for $K_i \leq 0.17$, and as a result, E_i can be significantly lower than 0.01 for smallest bins in the distribution in the CFD simulations. By extension, this can also explain why the CFD results when compared with analytical results are consistently lower in terms of overall collision efficiencies and ice masses, as no sort of minimum overall collision efficiency value is enforced in CFD simulations, with obvious exception of E_i being non-negative in CFD simulations. Finally, the relatively poor agreement for the test case 2, i.e., the rotating 50 mm cylinder at 4 m/s wind speed cannot be easily explained, as analytical results also significantly overestimate the overall collision efficiency and the accreted ice mass for this particular case. Overall, CFD simulations are well suitable for modeling ice accretion process for low K cases, with possible exceptions of cases with extremely low values of K, such as, for example, the case of 170 mm cylinder at 4 m/s wind speed.

Furthermore, based on the comparison of experimental, analytical and numerical results with the usage of full droplet distribution spectra and spectrum weighting of distributions, presented in this work, makes the method of using Langmuir droplet distribution spectra (in particular, the Langmuir C and D distributions) with the constraint of $X(K, \phi) = 0.01$ for $K \leq 0.17$ much more suitable for estimating ice loads, than the typical MVD approximation in particular at conditions, corresponding to low values of K. The analytical model results tend to overestimate the overall collision efficiencies and total ice masses, possibly due to the nature of overall collision efficiency values scaling with different bin sizes, as opposed to the monodisperse distribution, to which the Finstad et al./ISO 12494 model is intrinsically tuned to and the use of strict constraint of $E_i = 0.01$ for $K_i \leq 0.17$.

On the contrary, CFD simulations tend to underestimate the overall collision efficiencies values, especially for very low values of K. Consequently, the usage of both analytical and CFD results can give an "upper" and "lower" estimation of ice load intensities, with combined results being sufficiently accurate, at least for the experimental cases discussed in here. Therefore, for modeling ice accretions in

situations where it is expected to have the values of K in the range of $K < 0.6 – 0.7$ (which corresponds to the "limit" of the "large diameter circular conductors" as based on the analyzing of the results of the experiments Makkonen and Stallabrass), the usage of both analytical and CFD results is recommended along with calculations with full droplet distribution spectrum (or gamma distributions), as opposed to calculations with MVD approximation.

3.1.3 Droplet distribution spectra effects for the in-cloud impingement on the circular cylinder

As it was mentioned previously, the analytical calculations using the full (be it experimental or Langmuir) droplet distribution spectra tend to overestimate the values of the overall collision efficiencies when compared to the numerical CFD results and some FRonTLINES experimental cases. While the main assumption of this is the enforced constraint of the on the cloud impingement parameters, this constraint being $X(K, \phi) = 0.01$ for $K \leq 0.17$, however, as discussed in (Yoon and Ettema, 1993), this may also result from the usage of the inviscid, irrotational, potential flow approximation in the analytical model. In the modern CFD solvers, such as Ansys FENSAP–ICE and Fluent, the Reynolds-Averaged Navier-Stokes (RANS) equations are used for the flow solution. Thus viscous and rotational effects, such as boundary layer response, vorticity and vorticity shedding in the wake of the circular cylinder are present, and they may affect the resultant multiphase flow significantly. In order to investigate the potential implications of the viscous flow effects on the dry impingement on cylinders, one of the FRonTLINES cases has been selected for the deeper investigation within both the analytical and the numerical modeling. The test case in question is the 30 mm cylinder at 4 m/s wind speed. This choice is governed by two primary reasons – first, is the value of the droplet inertia parameter K which is calculated to be 0.35, which gives a value just above the current limitation of K, and similar values of K can be found in the Makkonen and Stallabrass experiments.

Second, is the good agreement obtained between the results, for this particular case, among the analytical, numerical and the experimental results. For convenience, the operating conditions for this test case are given in the Table 20.

Table 20 – Operating conditions for the droplet distribution spectra effects on the dry impingement on the circular cylinder investigation.

Parameter	***Value***
Cylinder diameter (mm)	30
Air velocity (m/s)	4, 7
Air temperature (°C)	–5
Altitude (m.a.g.l)	0
Rotational Rate (Rpm)	5
MVD (μm)	18.73
Droplet Distribution Spectra	Langmuir A – J, experimental droplet distribution spectra
Liquid Water Content (g/m^3)	0.4
Icing duration (min)	30
Cylinder length (mm)	157

The main focus in this subsection is to demonstrate the effect of the droplet distribution spectrum on cloud impingement parameters using the analytical and the numerical procedure. The comparison is done using a series of graphs and tables, which show the average value for each parameter, using

algebraic value of all time steps. The purpose of this is to take into account the effect of the continued ice accretion process on respective values.

3.1.3.1 Analytical Analysis

Figure 17 shows the values for inertia parameter (*K*), normalized impact velocities at stagnation line in m/s (V_0), stagnation line local collision efficiencies (β_0), maximum impingement angles (θ) and overall collision efficiencies (*E*), respectively for all distributions. The "*spectrum averaged*" graphs present the spectrum averaged values of the respective parameter and how much each distribution contributes towards the average value with the exception of maximum impingement angles. The color code of the Figures 17 and 18 should be read as follows: each unique color represents a single bin from any given distribution used from Figure 16 or Table 12. The right-hand side of Figures 17 and 18, shows the "spectrum-averaged" values in a "stacked" way, i.e., it "stacks" the individual values of each bin, weighted by its respective LWC in order to obtain the "spectrum-averaged" values, where again, each unique color represents the contribution of individual bin towards the final value of a given cloud impingement parameter. Note, that the maximum impingement angles in the Figures 17 and 18 are not "spectrum-averaged" as in the authors opinion it does not make physical sense to average the "maximum impingement angles", which correspond to the "grazing" trajectory angle.

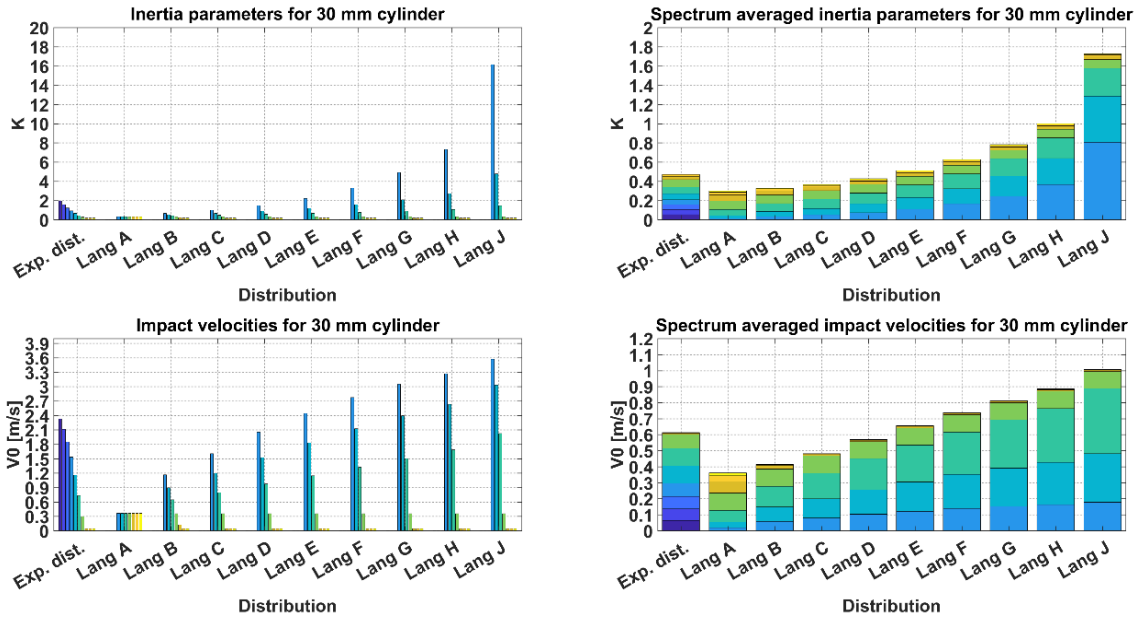

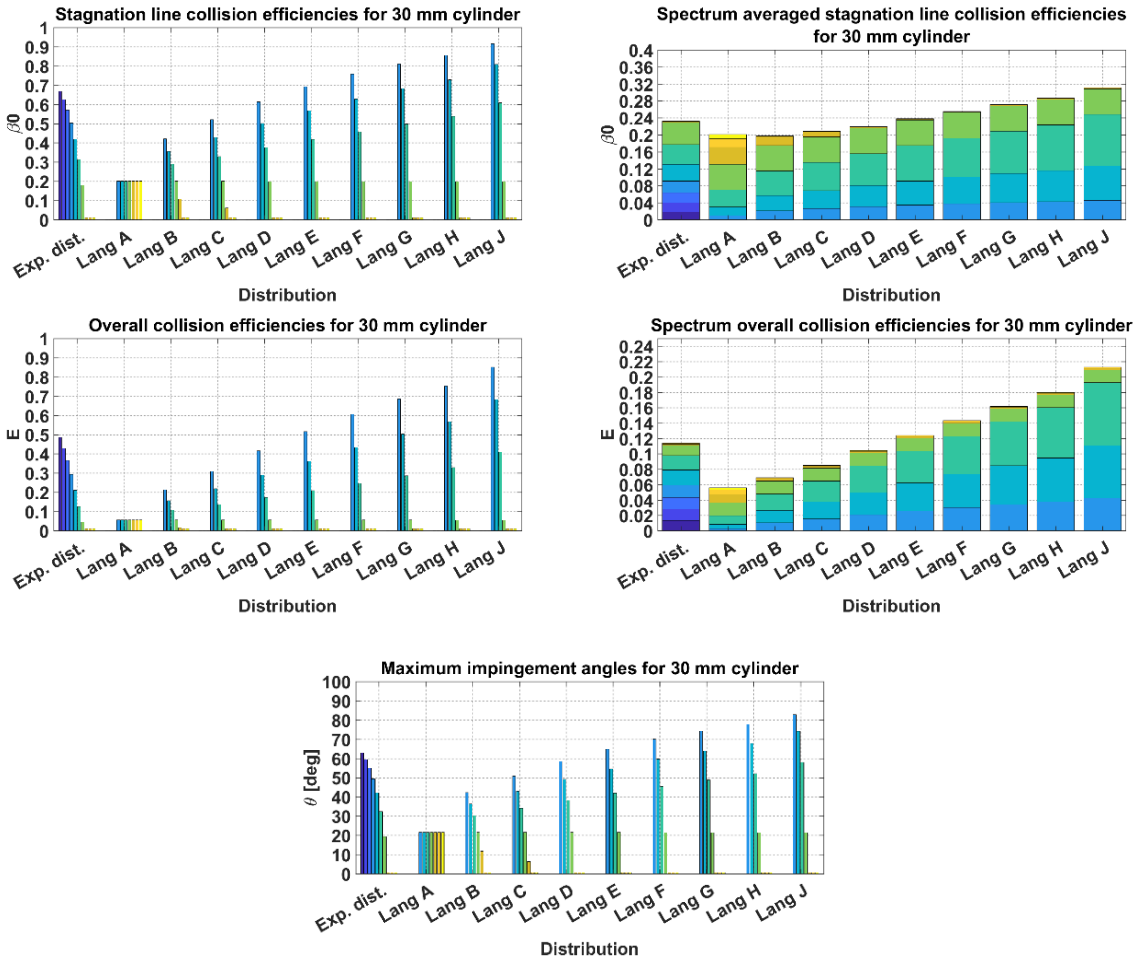

Figure 17 – The values of cloud impingement parameters in the analytical model on per-bin basis (left) and spectrum-averaged values (right).

While it may be hard to estimate the change of any of the respective parameters during the process from the figures, the typical observed differences between start and end values for all parameters are within 2–3% for the ice accretion process under operating conditions from Table 20. However, for bins with smaller diameters, the limit of $K = 0.17$ is quickly reached and for distribution D and above, the three smallest bins are consistently below the constraint value, meaning that limits of $E = \beta_0 = \nu_0 = \theta = 0.01$ are enforced and there is virtually no distinction between. Furthermore, the change in parameters of interest between larger droplet diameters in these distributions, when compared to the MVD value of 18.73 microns is of considerably larger magnitude, which smooths the impact of the constrained values to a large extent. In order to investigate the differences in values of cloud impingement parameters in a more concise manner, Table 21 lists the results of analytical calculations for all cloud impingement parameters with distributions from Figure 16 and Table 12 for MVD of 18.73 micron. In the Tables 21 and 22, the "*VTT*" row refers to the results obtained using the experimental distribution from the Figure 12, while the "*Experiment*" row refers to the experimentally measured values.

Table 21 – Spectrum weighted parameters values in analytical model.

Distribution	***Parameter***							
	K	V_0 *(m/s)*	β_0	θ *(°)*	*E*	*M (g)*	ρ *(kg/m^3)*	*D (mm)*
A	0.302	0.362	0.201	21.6	0.056	0.768	305.9	30.3
B	0.327	0.416	0.198	42.3	0.069	0.948	332.8	30.4
C	0.365	0.481	0.209	50.8	0.085	1.165	360.8	30.4
D	0.428	0.572	0.220	58.4	0.105	1.433	392.5	30.5
E	0.512	0.657	0.238	67.7	0.124	1.698	417.3	30.5
F	0.627	0.737	0.256	70.0	0.143	1.964	437.8	30.6
G	0.784	0.813	0.272	74.3	0.162	2.221	454.7	30.7
H	1.002	0.885	0.287	77.8	0.180	2.474	469.2	30.7
J	1.725	1.008	0.312	82.8	0.213	2.926	490.8	30.8
VTT	0.471	0.612	0.232	62.9	0.114	1.560	405.3	30.5
Experiment	0.458	–	–	–	**0.086**	**1.163**	–	–

As it is seen from Table 21, all cloud impingement parameters increase in their respective values with the increase of value in the droplet inertia parameter *K*, associated with change of the droplet distribution spectrum. The primary reason for the increase in the values of *K* is the significantly larger contribution to the spectrum-averaged values of droplet inertia parameter of individual bins with large droplet sizes, as it is seen from Figure 17. The resultant increase in values of the cloud impingement parameters is non-linear, primarily due to the structure of the equation for the calculation of the cloud impingement parameters $X(K, \phi)$ itself, and secondly, due to non-linear increase in the values of *K* associated with the change of the droplet distribution spectrum.

3.1.3.2 Numerical Analysis

The numerical simulations results for all distributions and bins are given in Figure 18, following the same methodology as was used in presenting the analytical results in Figure 17.

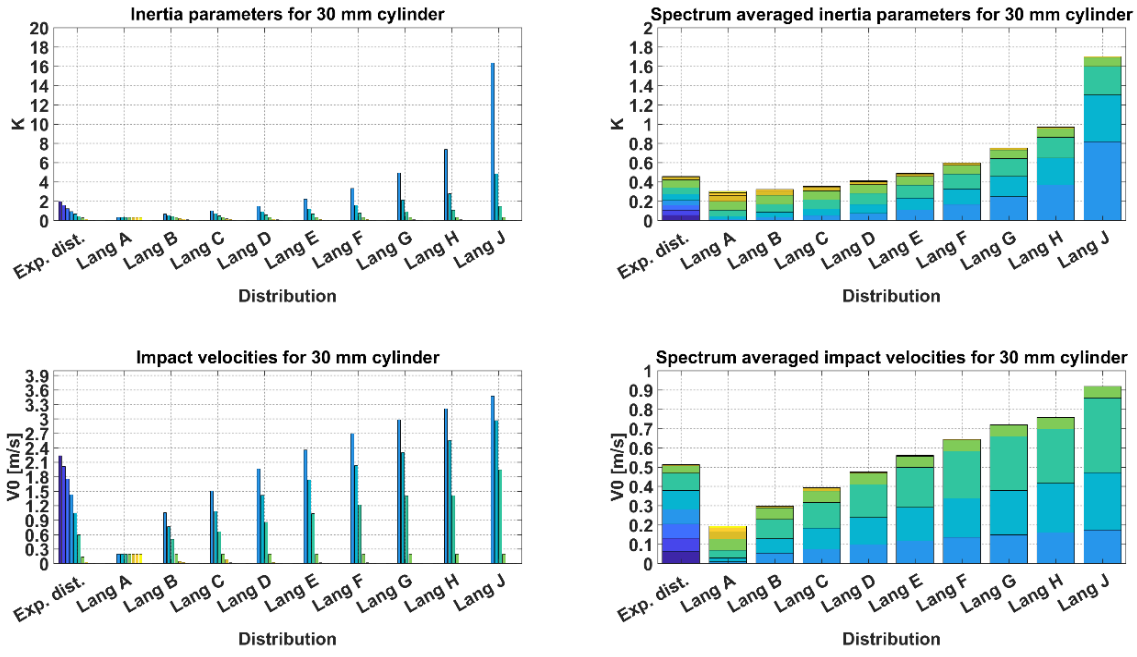

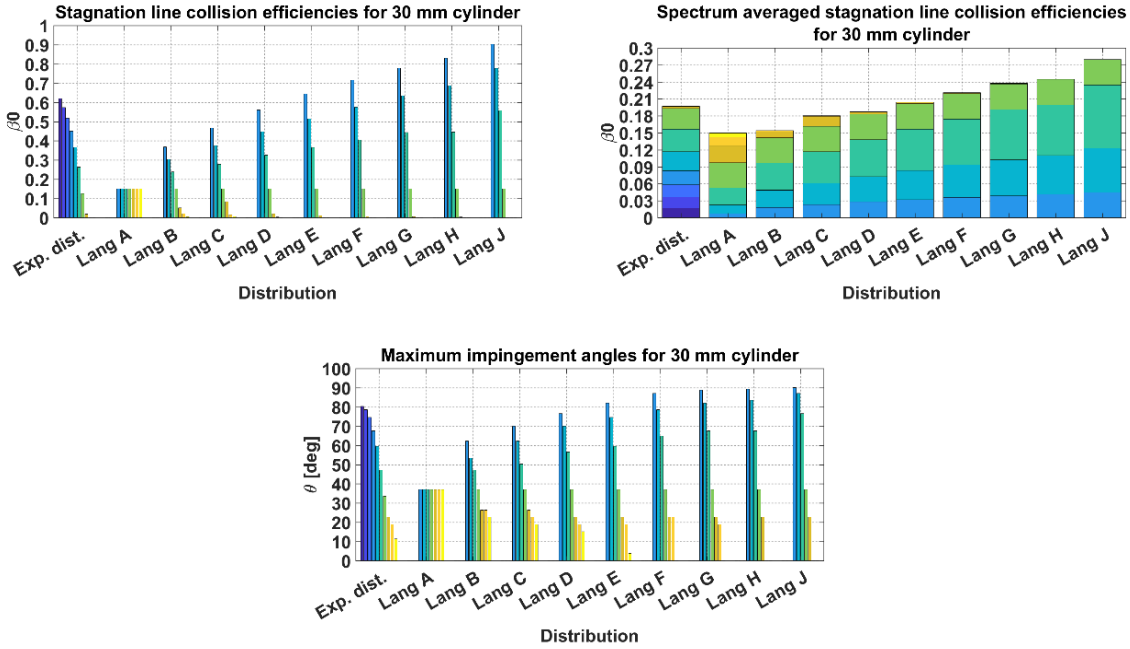

Figure 18 – The values of cloud impingement parameters in the numerical model on per-bin basis (left) and spectrum-averaged values (right).

Numerical analysis shows that in Figure 18, the maximum impingement angle remains unchanged for some droplets with different diameters, typically pertaining to smaller bins. The reason for this is that simulation data is output in terms of discrete "nodes" with coordinates and values of the respective parameter of that node, meaning that the precision is inherently limited to the quality of the mesh and the discretization in the CFD simulations, which controls the amount of the cylinder nodes in the simulation, as if any given property reaches value of zero in-between the nodes, it will be rounded-up to the coordinates of the closest node. Furthermore, observe that in some of the cases in the Figure 18, the reported value of the stagnation line collision efficiency is zero, while the impingement angle is not. The reason for this is the rounding the collision efficiencies to the three significant digits. In addition, since the values of inertia parameter in numerical simulations are not restricted in the same manner as in the analytical model, the values of impingement parameters can be significantly below 0.01. Observe, that in numerical simulations the stagnation line collision efficiency and maximum impingement angles are equal to zero only for very small droplets, typically of the diameter of 5 μm or less, which gives a rough value of inertia parameter of 0.03. This differs from the assumptions of (Langmuir and Blodgett, 1944) and (Finstad, 1986) that those respective values can be equal to zero in cases of $K < 0.125$ and $K < 0.14$ respectively. Moreover, the impact velocities in the numerical simulations are never equal to zero. The total ice masses and the overall collision efficiency values after 30 minutes of ice accretion along cylinder with spectrum weighted data from Figure 18 are given in Table 22.

Table 22 – Spectrum weighted parameters values from numerical simulations.

Distribution	***Parameter***					
	K	V_0 (m/s)	β_0	θ (°)	E	M (g)
A	0.304	0.198	0.150	37.1	0.037	0.506
B	0.320	0.299	0.154	62.3	0.053	0.713

C	0.356	0.382	0.169	70.0	0.067	0.915
D	0.412	0.474	0.187	76.6	0.086	1.163
E	0.489	0.560	0.204	82.0	0.104	1.415
F	0.599	0.643	0.221	87.1	0.123	1.674
G	0.753	0.720	0.238	88.7	0.142	1.928
H	0.971	0.758	0.245	89.3	0.153	2.073
J	1.700	0.921	0.280	90.0	0.195	2.641
VTT	0.458	0.534	0.198	81.1	0.095	1.286
Experiment	0.458	–	–	–	**0.086**	**1.163**

Summarizing the results in Tables 21 and 22, the rotating cylinder in the CFD simulations, for all tested distributions, exhibits smaller values in impact velocities, stagnation line and overall collision efficiencies, and by extension, – the total accreted ice masses, while the values of maximum impingement angle are larger than in the analytical model, even considering the potential impact of cylinder surface discretization and resultant nodes placement impact on maximum impingement angle in numerical simulations. Moreover, the use of modern CFD tools allows for in-depth investigation of a several concepts, not covered within the scope of the ISO 12494 model, such as viscous and boundary layer effects, liquid water content and droplet concentrations, vorticity and vorticity shedding, etc. As an example, Figure 19 shows droplet velocity magnitudes, impingement angles and local collision efficiencies for a few selected distributions.

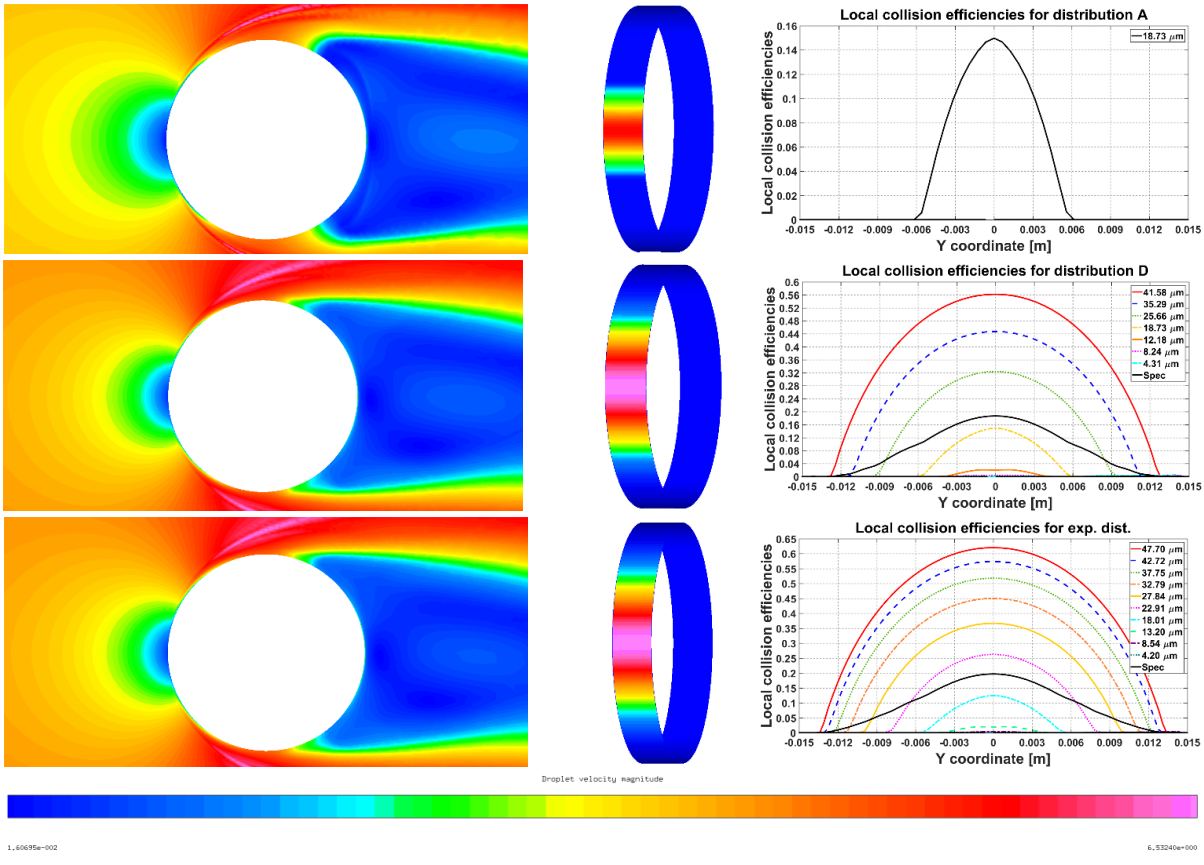

Figure 19 – Droplet velocity magnitude (left), impingement angles (middle) and local collision efficiencies (right) for monodisperse (top), Langmuir D (middle) and experimental (bottom) distributions.

Figure 19 shows that the droplet behavior changes extensively, depending on the droplet distribution spectrum used. Observe the significant difference in the maximum impingement angles, local collision efficiencies, and much more "intricate" structure of the local collision efficiencies values, which directly correspond to the spectrum-weighted collision efficiencies, denoted as solid black line in Figure 19. Moreover, the maximum impingement angles seem to coincide well with the velocity minima from the velocity magnitude plots. In addition, the flow separation is much more clearly observed in the plots for experimental and Langmuir D distributions.

This, coupled with the values of the stagnation line impact velocities and collision efficiencies and the maximum impingement angles, suggest that there is a potential impact of the viscous effects in the boundary layer, pushing the inflowing droplets away from the stagnation line in the CFD simulations. This hypothesis is primarily made by observing the behavior of the expression for the droplet drag coefficient between the analytical and the numerical calculations in the Figure 8. For the specified range of the droplet Reynolds number in the Figure 8, which is $0 < Re_d < 150$ the value of the C_D is almost identical between the two models. This suggest that there must be an additional physical mechanism, acting on the droplets and slowing them down before the impact in the numerical simulations (thus explaining the lower values of the stagnation line impact velocities and collision efficiencies), while simultaneously pushing them away from the stagnation line (thus explaining higher maximum impingement angles in the CFD simulations when compared to the analytical results).

Note, that this difference cannot being explained by the balance of the drag and inertia, acting on the droplet (which is the physical definition of K), as the droplet's inertia parameter is calculated in the similar fashion between the analytical and the numerical models, as discussed in the Section 2, which shows the detailed description of both models used in this work.

Furthermore, this difference cannot be caused by the "history" term also, as the FENSAP–ICE does not take it into the account at all, due to it being an Eulerian solver, while the analytical calculations were carried without the "history" term incorporated. In fact, the Basset force will cause the *opposite* effect, if it is taken into the account – it serves to decrease the droplet deceleration before the impact, thus permitting its impact at higher impact velocities and collision efficiencies. Thus, it is deemed that the viscous effects in the CFD simulations are the primary driver between the differences in the analytical and the numerical calculations.

From Tables 21 and 22, the analytical model tends to predict higher values of the stagnation line droplet collision efficiencies and impact velocities and as a result, – the accreted ice masses. Contrary, the numerical results have higher values of the maximum impingement angles. Moreover, the relative increase in the values of the stagnation line collision efficiency and impact velocity, the overall collision efficiency and the total accreted ice mass, arising with the change of droplet distribution spectrum is also higher in the numerical results, while the relative increase in the values of the maximum impingement angle is higher in the analytical results.

In comparison, the experimental accreted ice mass is 1.163 g, which results in an overall collision efficiency of 0.086. When comparing with analytical and numerical results from Tables 29 and 30 respectively, the closet fit distributions are distribution C, for the analytical results, and distribution D

for the numerical results, respectively, with values of total ice mass and overall collision efficiency of 1.165 g, 0.085 and 1.163 g and 0.086, respectively. This matches experimental results within the margin of error, considering the rounding-up in calculations. This also supports previous conclusions in this work, based on the suitability of the Langmuir distributions C and D for the modeling of the in-cloud impingement on cylinders, based on the analysis on the experimental data of the Makkonen and Stallabrass and the FRonTLINES project experiments.

Slightly unexpectedly, the experimental distribution tends to produce higher values of overall collision efficiency and total ice mass in both analytical and numerical results, being 0.114 and 1.560 g, respectively, for the analytical results, and 0.095 and 1.286 g, for the numerical results, respectively. At least some of this difference can be explained by restricting the inertia parameter in the analytical model, and the overestimation of overall collision efficiency by the potential flow theory limitations, as was discussed in (Yoon and Ettema, 1993) and the viscous effects in the CFD simulations, as was discussed previously.

Furthermore, from the Tables 21 and 22, it can be seen that results from monodisperse distribution are unsatisfactory when compared to the experimental values. Monodispersed distribution failed to reproduce experimental values, both in analytical and numerical calculations, and gave the lowest values for all parameters across all distributions. Based on the experimental verification of the Finstad et al. model done by (Makkonen and Stallabrass, 1987), along with discussion on the droplet distribution spectra properties done by (Langmuir and Blodgett, 1946) and also carried within this work, coupled with recent investigation of droplet spectra effects by (Jones et. al., 2014) for the icing events in the natural conditions at the Mt. Washington Observatory, suggests that this unsatisfactory performance of the monodispersed distribution primarily applies to cases with low values of inertia parameter only.

In addition, the governing theory from the ISO 12494 standard does not focus directly on the aspects of different cloud impingement parameters on ice accretion process, other than the overall collision efficiency. While, as was discussed previously, the ISO 12494 theory and conducted experimental verification, such as in (Makkonen and Stallabrass, 1987), make the theory well developed and understood for the majority of typical icing situations and related engineering applications, especially those at higher wind speeds, for long-term or extreme icing events the impact of those parameters, associated with the droplet distribution spectrum may be important, in order to properly estimate the extreme or long term loads such icing conditions can exert on cylindrical structures, such as power lines or masts. Moreover, other factors, not accounted for in this study, such as surface roughness, sublimation and deposition, viscous and boundary layer effects may become prominent in cases where the inertia parameter is sufficiently low. However, the usage of the CFD tools as with this work, in addition to some recent results (Makkonen et al., 2018), shows that the CFD simulations are well suited for modeling of the ice accretion at the low values of K.

In particular, the Langmuir D distribution yields good agreement with the experiment for the analytical case, and matches it exactly in the CFD simulations, while in the analytical results, obtained with the Langmuir distribution C, is the results are very close to the experimental value of overall collision efficiency. The experimental distributions for both cases tends to overestimate the value of overall collision efficiency, however, for the CFD results the absolute error is approximately 0.01. Overall, the

numerical simulations are well suited for detailed studies of the droplet distribution spectrum effects and the ice accretion modeling in general, as multiple different cloud impingement parameters can be investigated and compared in detailed manner, which is not possible using analytical approach. In addition, the usage of the Langmuir D distribution as a sort of a "first guess" distribution is recommended, as it is typically and successfully employed for aircraft icing studies (Bidwell, 2012; Papadakis et. al, 2007; Wright, 2008).

3.2 Investigation into the empirical icing density parameterizations

While performing the analysis of the droplet distribution spectra effects, detailed in the preceding section, one particular issue became of interest in the analytical results. As it can be seen from the analytical results in the Table 21, while the analytical calculations predict the overall collision efficiencies and the accreted ice masses correctly (depending on the source droplet distribution used), for all cases the end iced cylinder diameter is less than 1 mm greater than the original, uniced cylinder diameter. Furthermore, the accreted ice densities can be classified as "soft rime" as per ISO 12494 classification (ISO 12494, 2001), which is expected, based on the choice of the experimental conditions and the expected results from the design of the experiments in the FRonTLINES experiments.

The need to explain and understand these values resulted into performing the investigation into the empirical accreted icing density parameterizations. All analytical calculations in the Section 3.1 were carried out using the Makkonen and Stallabrass empirical icing density parameterization, which is an empirical fit obtained by Makkonen and Stallabrass (Makkonen and Stallabrass, 1984) to the original empirical icing density parameterization by Macklin (Macklin, 1962).

Thus, in order to investigate the behavior of this parameterization the experimental data of Makkonen and Stallabrass has been analyzed and the analytical calculations were carried out for the end iced cylinder diameters and the accreted ice densities, given in Tables 23 and 24, respectively, in the same fashion as the calculations for the overall collision efficiencies and the accreted ice masses, carried out previously. The values of the iced cylinder diameters and the accreted ice densities were carried out using Langmuir A – J droplet distribution spectra, with the constraint of $X(K, \phi) = 0.01$ for $K \leq 0.17$ enforced, where applicable.

Table 23 – Experimental (Exp), and analytical, end iced cylinder diameters in the Makkonen and Stallabrass experiments (1984). The columns A to J correspond to the results obtained using Langmuir distributions with the distribution A being monodispersed. Red bolded values denote the closest fit values with the experimental values. Note, that due to rounding in the original Makkonen and Stallabrass data to the two significant digits there are possible some small discrepancies and multiple "best fit" values per single row in the table. Values are in cm.

Test	*A*	*B*	*C*	*D*	*E*	*F*	*G*	*H*	*J*	*Exp*
1	1.59	1.58	1.57	1.56	1.56	**1.55**	**1.55**	**1.55**	1.54	**1.55**
2	1.52	1.51	1.50	1.50	1.50	**1.49**	1.49	1.50	1.50	**1.48**
3	1.57	1.56	**1.55**	**1.55**	**1.55**	**1.55**	**1.55**	**1.55**	**1.55**	**1.42**
4	1.65	1.64	**1.63**	**1.63**	**1.63**	**1.63**	**1.63**	**1.63**	**1.63**	**1.6**
5	1.47	1.46	**1.46**	**1.46**	**1.46**	**1.46**	**1.46**	**1.46**	1.47	**1.43**
6	3.62	3.61	3.61	3.62	3.63	3.64	**3.65**	3.67	3.69	**3.65**
7	3.52	3.52	3.53	**3.54**	3.55	3.57	3.59	3.60	3.63	**3.54**

8	**3.57**	**3.57**	3.58	3.59	3.61	3.63	3.64	3.66	3.70	**3.5**
9	3.65	3.65	3.66	3.68	**3.70**	3.72	3.74	3.76	3.79	**3.7**
10	3.45	3.46	**3.47**	3.48	3.50	3.52	3.54	3.55	3.59	**3.47**
11	**4.85**	**4.85**	4.86	4.88	4.90	4.92	4.94	4.96	5.00	**4.85**
12	4.74	4.75	4.76	4.79	**4.81**	4.84	4.86	4.89	4.93	**4.81**
13	4.79	4.80	**4.82**	4.85	4.87	4.90	4.93	4.96	5.01	**4.82**
14	4.89	4.90	4.92	4.95	4.98	5.01	**5.04**	5.07	5.12	**5.05**
15	4.67	4.68	**4.70**	4.73	4.75	4.78	4.81	4.83	4.88	**4.71**
16	7.84	7.85	7.87	7.90	7.92	**7.95**	7.98	8.01	8.06	**7.95**
17	7.88	7.90	7.92	7.95	**7.98**	8.01	8.04	8.07	8.12	**7.98**
18	7.75	7.77	7.79	**7.82**	7.85	7.88	7.91	7.94	7.99	**7.81**
19	7.79	7.82	7.84	**7.88**	7.91	7.94	7.97	8.00	8.06	**7.89**
20	7.88	7.90	7.93	7.96	8.00	8.04	8.07	**8.11**	8.17	**8.13**
21	7.71	7.73	7.76	7.78	7.81	7.84	7.87	7.90	**7.95**	**8.13**
22	1.49	**1.48**	1.47	1.46	1.46	1.45	1.44	1.44	1.43	**1.48**
23	1.45	1.44	1.43	1.43	1.42	1.42	1.42	**1.41**	**1.41**	**1.4**
24	1.40	1.39	1.39	1.38	1.38	1.38	1.38	1.38	**1.37**	**1.35**
25	3.57	3.56	3.56	3.56	3.57	3.57	3.57	3.58	**3.59**	**3.6**
26	3.51	**3.50**	3.51	3.51	3.52	3.52	3.53	3.54	3.55	**3.5**
27	**3.45**	**3.45**	**3.45**	3.46	3.47	3.48	3.49	3.50	3.51	**3.45**
28	4.82	4.82	4.82	4.83	4.84	4.85	**4.86**	4.87	4.89	**4.86**
29	**4.75**	**4.75**	4.76	4.77	4.78	4.79	4.81	4.82	4.85	**4.75**
30	**4.69**	**4.69**	4.70	4.71	4.73	4.74	4.76	4.77	4.80	**4.66**
31	7.84	7.85	7.86	7.87	7.89	**7.90**	**7.92**	7.94	7.97	**7.91**
32	**7.78**	**7.78**	7.80	7.82	7.83	7.85	7.87	7.89	7.93	**7.78**
33	7.74	7.75	**7.76**	**7.78**	7.80	7.82	7.84	7.86	7.89	**7.77**

Table 24 – Experimental (Exp), and analytical, accreted ice densities in the Makkonen and Stallabrass experiments (1984). The columns A to J correspond to the results obtained using Langmuir distributions with the distribution A being monodispersed. Red bolded values denote the closest fit values with the experimental values. Note, that due to rounding there are possible some small discrepancies and multiple "best fit" values per single row in the table. Values are in kg/m^3.

Test	***A***	***B***	***C***	***D***	***E***	***F***	***G***	***H***	***J***	***Exp***
1	**809**	807	805	803	802	800	799	797	796	**870**
2	**783**	781	779	777	776	774	773	773	772	**840**
3	**703**	700	698	696	694	692	691	690	689	**820**
4	**611**	607	604	602	600	598	597	596	595	**670**
5	**767**	764	762	761	760	758	758	758	757	**840**
6	760	758	757	758	758	759	761	762	**765**	**830**
7	714	713	714	716	719	722	725	728	**735**	**750**
8	620	618	619	622	626	629	633	637	**644**	**740**
9	516	**513**	514	518	522	526	530	534	543	**480**
10	683	682	685	689	694	699	703	**708**	716	**710**
11	732	730	731	734	737	740	743	746	**752**	**780**
12	**673**	**673**	678	685	691	697	703	709	719	**670**
13	571	572	577	585	592	599	**607**	614	625	**610**

14	**459**	**459**	464	473	482	489	498	506	519	**420**
15	**632**	635	642	652	661	671	679	687	699	**630**
16	659	662	670	680	689	**699**	707	715	726	**700**
17	556	559	568	580	591	601	612	621	**635**	**680**
18	562	574	592	612	**631**	646	659	670	687	**630**
19	443	457	478	**501**	522	539	554	568	588	**500**
20	**319**	333	355	380	403	423	440	455	478	**300**
21	**484**	512	540	569	593	612	628	642	663	**460**
22	**849**	848	847	845	844	842	841	840	837	**880**
23	**832**	830	829	827	825	824	823	822	820	**890**
24	**820**	818	817	815	814	812	811	810	809	**880**
25	**818**	816	815	814	814	813	813	813	814	**850**
26	788	786	785	786	786	787	788	789	**791**	**820**
27	768	766	765	767	768	769	771	773	**776**	**810**
28	799	797	797	797	798	799	800	801	**803**	**840**
29	763	761	762	764	766	769	771	774	**779**	**790**
30	736	735	737	741	745	749	752	756	**763**	**800**
31	753	**752**	755	759	764	768	772	776	783	**740**
32	712	714	720	729	736	744	751	**758**	768	**760**
33	**654**	660	669	682	693	705	714	723	736	**650**

From the Tables 23 and 24 a few interesting observations can be made. First, is that with the exception of the test 3, the analytical calculations of the end iced cylinder diameters, across all tested Langmuir distributions show good agreement with the experimental values, with eror not exceeding a few percent. Second, is that the calculations of the accreted ice densities, using the Makkonen and Stallabrass own empirical icing density fit, against their own data, result in some underestimation of the accreted ice densities, mostly for the cases with higher values of the droplet inertia parameter *K*. This primarily can be explained due to the fact that, according to the Makkonen and Stallabrass, there was a certain uncertainty regarding the droplet sizes measurements, based on the disagreement in the measurements made by the FSSP and the oil slide method (Makkonen and Stallabrass, 1984). The matter is further complicated by the fact that the experimental distribution information is no longer available (Makkonen, personal communication). Nonetheless, the obtained data suggests that, where its applicable, the empirical icing density parameterizations of Makkonen and Stallabrass performs well, in terms of both end iced cylinder diameters and the accreted ice densities, although the latter is underestimated to a small extent.

Having established the performance of the Makkonen and Stallabrass empirical icing density parameterizations in the benchmark cases, these being their own data, the same empirical icing density parameterization will be used for the calculations of other available experimental data – this being the FRonTLINES project test cases. While, unfortunately, the precise experimental values for the end iced diamaters, and thus – accreted ice densities are unknown, the analysis of this data is still valuable in order to test the predictions of the empirical icing density parameterizations in the range of low *K* values. For this purpose, Tables 25 and 26 list the calculated end iced cylinder diameters and the accreted ice densities, using the Makkonen and Stallabrass fit to the Macklin icing density parameterization. In

addition, Tables 25 and 26 list the values of the experimental values of the end iced cylinder diameters and the experimental accreted ice densities. However, since the experimental end iced cylinders and the accreted ice densities are unknown, these values has been interpolated from the visual data (e.g. photos of the iced cylinder and interpolated to the nearest millimeter) and the accreted ice masses.

Table 25 – End iced cylinder diameters in the FRonTLINES experiments in the analytical calculations. The columns A to J correspond to the results obtained using Langmuir distributions with the distribution A being monodispersed, and the VTT column denotes the experimental droplet distributions spectrum in the experiments. Values are in mm.

Test	***A***	***B***	***C***	***D***	***E***	***F***	***G***	***H***	***J***	***VTT***	***Exp***
1	30.3	30.4	30.4	30.5	30.5	30.6	30.7	30.7	30.8	30.5	**37**
2	50.2	50.4	50.4	50.4	50.4	50.5	50.5	50.6	50.7	50.4	**58**
3	80.2	80.2	80.3	80.4	80.4	80.4	80.4	80.5	80.5	80.4	**87**
4	100.2	100.2	100.2	100.3	100.5	100.4	100.4	100.4	100.5	100.4	**N/A**
5	170.2	170.2	170.2	170.2	170.3	170.4	170.5	170.4	170.4	170.2	**N/A**
6	30.9	30.9	30.9	31.0	31.1	31.2	31.2	31.3	31.4	31.1	**39**
7	100.3	100.4	100.4	100.4	100.5	100.5	100.6	100.7	100.9	100.4	**114**

Table 26 – Accreted ice densities in the FRonTLINES experiments in the analytical calculations. The columns A to J correspond to the results obtained using Langmuir distributions with the distribution A being monodispersed, and the VTT column denotes the experimental droplet distributions spectrum in the experiments. Values are in kg/m^3 and the lower bound of the accreted ice density of 100 kg/m^3 is enforced in the calculations, where applicable.

Test	***A***	***B***	***C***	***D***	***E***	***F***	***G***	***H***	***J***	***VTT***	***Exp***
1	305	331	359	391	416	436	453	468	489	404	**20**
2	100	100	179	248	299	339	370	397	435	277	**7**
3	100	100	100	100	179	243	292	331	388	140	**5**
4	100	100	100	100	101	183	244	292	360	100	**N/A**
5	100	100	100	100	100	100	109	170	276	100	**N/A**
6	549	550	556	565	574	581	590	598	609	573	**55**
7	100	138	233	308	362	405	439	467	507	336	**13**

From Tables 25 and 26 it can be seen that there are three primary conclusions to be drawn: first, that for all the cases in the analytical calculations the end iced cylinder diameters exceed the initial ones by less than 1 mm, which is rather expected, as the analytical model suggests that a uniform layer of ice must be form and be present in the calculations. Second, for majority of cases the lower bound of the accreted ice density of 100 kg/m^3 in the analytical calculations is quickly reached. This lower bound was put into the analytical calculations as a sort of a lower "physically meaningful" constraint on the density of the accreted ice in a layer. Lastly, and most importantly, the calculated experimental ice densities are significantly below the minimum constraint of 100 kg/m^3 (as this results from the calculations using the interpolated end iced diameters which are significantly higher than those predicted by the analytical model). As a result, this suggests that the uniform ice layer does not form in the experiments, and the accreted icing is mostly in the form of individual large beads. Indeed, Figure 20 shows some examples of the accreted ice shapes in the FRonTLINES experiments.

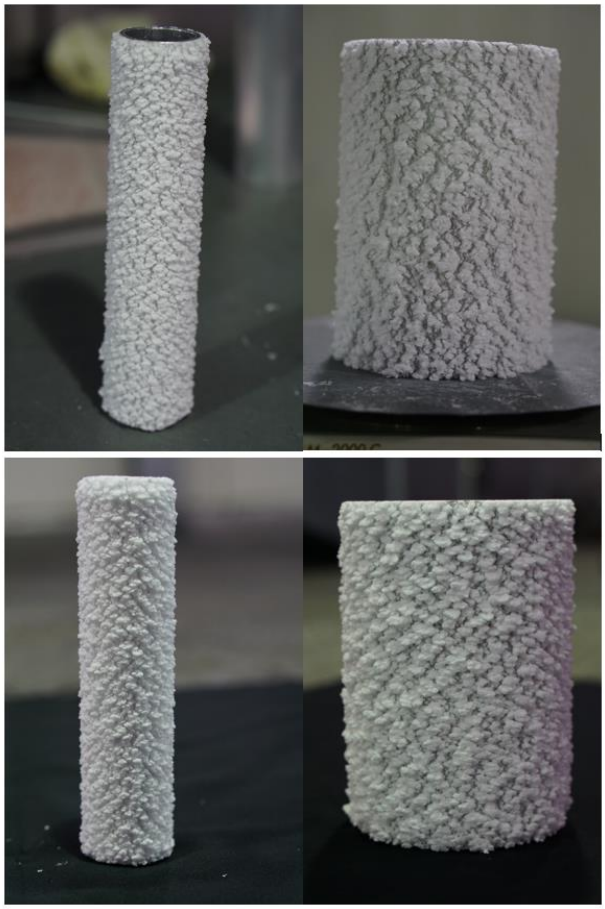

Figure 20 – Examples of the accreted ice shapes in the FRonTLINES experiments, for the 30 mm diameter cylinder (left) and 100 mm diameter cylinder (right) for the 4 m/s wind speed (top row) and 7 m/s wind speed (bottom row).

As it can be seen from the Figure 20 the accreted ice does not form a uniform ice layer and instead the accreted ice shape represents a collection of individual large beads. While the Figure 20 shows examples from four experimental test cases, similar ice shapes to those in the Figure 20, were present in all experimental cases with the rotating cylinders. Such ice shapes can be explained as the tendency of the impinging droplet to collide with the (or nearby) already impinged and frozen droplets, which may suggest that the already impinged droplets act as individual icing collectors, which is postulated by the ISO 12494 to be one of the potential reasons behind the underestimation of the accreted ice masses for cases, when the overall collision efficiencies are below the value $0.10 < E$. However, to the best of the authors knowledge, no rigorous investigation into this claim has ever been made, as the underlying assumptions (micron-sized frozen droplet deforming the surface of the cylindrical object and affecting the multiphase flow in vicinity of them) make the testing of this hypothesis difficult both in the analytical and the experimental calculations.

Indeed, one can wonder how well the CFD simulations can predict the ice shapes and densities, such as in the Figure 20 and the Table 26. For this purpose, Tables 27 and 28 show the end iced cylinder diameters and the accreted ice densities in the numerical simulations, using the distributions A – E and the experimental distribution.

Table 27 – End iced cylinder diameters in the FRonTLINES experiments in the numerical calculations. The columns A to J correspond to the results obtained using Langmuir distributions with the distribution A being monodispersed, and the VTT column denotes the experimental droplet distributions spectrum in the experiments. Values are in mm.

Test	***A***	***B***	***C***	***D***	***E***	***VTT***	***Exp***
1	30.1	30.1	30.2	30.2	30.2	30.2	**37**
2	50.0	50.0	50.1	50.1	50.1	50.1	**58**
3	80.0	80.0	80.0	80.0	80.0	80.0	**87**
4	100.0	100.0	100.0	100.0	100.0	100.0	**N/A**
5	170.0	170	170.0	170.0	170.0	170.0	**N/A**
6	30.5	30.5.0	30.6	30.7	30.8	30.8	**39**
7	100.0	100.0	100.1	100.1	100.2	100.1	**114**

Table 28 – Accreted ice densities in the FRonTLINES experiments in the numerical calculations. The columns A to J correspond to the results obtained using Langmuir distributions with the distribution A being monodispersed, and the VTT column denotes the experimental droplet distributions spectrum in the experiments. Values are in kg/m^3.

Test	***A***	***B***	***C***	***D***	***E***	***VTT***	***Exp***
1	917	917	917	917	917	917	**20**
2	917	917	917	917	917	917	**7**
3	917	917	917	917	917	917	**5**
4	917	917	917	917	917	917	**N/A**
5	917	917	917	917	917	917	**N/A**
6	917	917	917	917	917	917	**55**
7	917	917	917	917	917	917	**13**

From Tables 27 and 28 it can be seen that the agreement between the CFD simulations and the experimental values of the end iced cylinder diameters and the accreted ice densities is very poor. In the similar vein to the analytical model, the CFD simulations predict an almost uniform and very thin ice layer present. Despite beading being activated in the numerical calculations, the difference in the ice thicknesses in the (adjacent) nodes on the cylinder surface in the CFD simulations are of an order of a fraction of a millimeter. Furthermore, note that in the Table 28 the accreted ice densities are of a constant value of 917 kg/m^3 which is the upper value in the Makkonen and Stallabrass empirical icing density parameterization (although FENSAP–ICE refers to it as "*Macklin*"). One can wonder about the applicability of the CFD simulations in such situations where a uniform icing layer does not form, as the "mechanism" of "origin" and the growth of the ice beads in such cases (where subsequent particles ten to impinge close to initial droplet striking positions) makes this process rather "Lagrangian" in nature, which may be difficult to resolve in the CFD simulations in the Eulerian framework as the ice growth in those depends on the thermodynamics and liquid water content in the cells, adjacent to the surface of the cylinder. Thus, one would expect from these a uniform layer of ice accretion, in case of the rotating cylinder, in similar fashion as the analytical model suggests.

Nonetheless, despite the apparent failure of both the analytical and the numerical models to predict the correct accreted ice densities and the end iced diameters in the FRonTLINES experiments, it is still important to carry out the investigation into the empirical accreted icing density formulations for a few reasons. First, one needs to keep in mind that not all ice accretions in nature result in the formation of

the individual ice beads, where uniform ice layers do not form, as the resultant ice shapes. Moreover, as noted in (Makkonen, 1984) the resultant ice accretions on the actual overhead transmission lines are almost always perfectly circular in shape.

Second, while at the initial stages of the ice accretion one might expect an ice accretion in the form of individual beads (whether or not it is a function of the droplet inertia parameter *K* alone or some other operating values is not precisely known) the end result, over longer periods of time (hours and days), and over multiple individual icing events (as expected to happen on the overhead transmission lines in the remote areas) will result in the circular end ice shape. Moreover, estimating the accreted ice masses from the (assumed or interpolated) ice densities and iced diameters is a rather common practice.

Furthermore, when dealing with ice densities one has to keep in mind how the empirical icing formulation(s) for the particular parameterization(s) were derived. For example, the original empirical icing density parameterization by Macklin (Macklin, 1962), on the basis on which the Macklin parameter itself was derived, was obtained from the wind tunnel tests of the 1, 6 and 14 mm cylinder, rotating at 30 RPM and at the LWC concentrations being, w = 1.6 – 7.0 g/m^3, i.e., very high values of LWC. Obviously, one expects that under such operating conditions a uniform ice layer will be accreted. However, the experiments of (Macklin, 1962) drew some criticism and questions and over the years, researchers attempted to recreate the Macklin experiments or to carry out the experiments on their own. As a result, a significant number an empirical icing density formulations have appeared, those being briefly summarized in (Jones, 1990). The available icing density parameterizations, based on the discussion in (Jones, 1990) can be broadly classified into two categories:

- Those that use the Macklin parameter in them. The models which utilize the Macklin parameter are the most numerous ones. The primary difference in these is the empirical fit, which utilizes the Macklin parameter (even though its definition remains constant). As it follows from (Jones, 1990) majority of these empirical icing density parameterizations were derived as the result of the icing wind tunnel (or similar testing in the laboratory).
- Those that do not use the Macklin parameter in them. To the best of the author's knowledge, currently only the model of (Jones, 1990) is only such widely used empirical icing density formulation.

For the comparison purposes of the performances of these models, the data from the Cranfield University icing tunnel experiments has been used. Those experiments were conducted on the lower air temperature (–25 °C), higher wind speeds (30 m/s) and a larger spread in the circular cylinder diameter (20 – 298 mm) when compared to the FRonTLINES experiments. The description of the experimental apparatus along with the operating conditions in this study is given in the Section 2.3.2 of this work, while Table 29 lists the values of the initial and the ultimate cylinder diameters, along with the experimental values of the droplet's inertia parameter *K*, calculated based on the ISO 12494 (meaning that the monodispersed distribution with the MVD value of 16.36 μm was used for the calculations).

Table 29 – Cranfield University icing tunnel experiments initial, uniced, end, iced cylinder diameters and the calculated value of the droplet inertia parameter K_{exp} in the experiments.

Cylinder #	***Initial Cylinder Diameter (mm)***	***End Iced Cylinder Diameter (mm)***	K_{exp}
1	20	32.30	2.153
2	50.05	60.45	1.011
3	80.25	87.57	0.666
4	99	113.72	0.525
5	149.5	155.36	0.366
6	249	254.06	0.222
7	298	307.06	0.185

From Table 29 it follows that the experimental spread in terms of the droplet inertia parameter is quite large – the values of it tend to be well within the values within Makkonen and Stallabrass experiments, based on which the current ISO 12494 model was verified, to cases with values of the droplet inertia parameter being low enough to fit within the FRonTLINES experiments. Moreover, Tables 30 and 31 list the values of the droplet inertia parameter, end iced cylinder diameters and the accreted ice densities, in the analytical and the numerical calculations, respectively, for the Makkonen and Stallabrass and both the intermediate and the final version of the Jones empirical icing density model, calculated both using the full droplet distribution spectra and the MVD approximation.

Table 30 – Cranfield University icing tunnel experiments initial, uniced, end, iced cylinder diameters and the calculated value of the droplet inertia parameter K_{exp} in the experiments in the analytical calculations.

Full experimental droplet distribution spectra

D *(mm)*	*K*			*D_{end} (mm)*				*ρ (kg/m^3)*		
	M&S	Jones (glaze)	Jones (rime)	M&S	Jones (glaze)	Jones (rime)	***Exp.***	M&S	Jones (glaze)	Jones (rime)
20	9.623	9.188	10.069	29.70	32.39	27.34	***32.30***	636.9	495.8	856.0
50.05	4.317	4.316	4.499	57.37	60.37	55.72	***60.45***	590.6	416.2	770.8
80.25	2.871	2.821	2.890	86.25	89.28	85.10	***87.57***	554.5	366.2	690.3
99	2.328	2.280	2.342	107.08	111.55	105.74	***113.72***	534.3	341.3	645.2
149.5	1.586	1.566	1.590	156.02	160.27	160.30	***155.36***	488.5	293.7	545.9
249	0.989	0.982	0.988	253.87	257.60	257.58	***254.06***	415.1	234.4	399.6
298	0.840	0.836	0.839	302.38	305.83	302.91	***307.06***	384.3	214.2	342.9
	MVD Approximation									
D *(mm)*	*K*			*D_{end} (mm)*				*ρ (kg/m^3)*		
	M&S	Jones (glaze)	Jones (rime)	M&S	Jones (glaze)	Jones (rime)	***Exp.***	M&S	Jones (glaze)	Jones (rime)
20	2.239	2.174	2.257	29.72	32.10	30.07	***32.30***	649.0	521.1	641.1
50.05	1.042	1.028	1.038	56.09	58.83	57.82	***60.45***	575.2	394.5	451.6
80.25	0.672	0.669	0.670	84.34	86.91	86.85	***87.57***	502.3	308.3	313.9
99	0.545	0.542	0.540	103.92	107.41	108.39	***113.72***	455.8	265.9	241.0
149.5	0.366	0.367	0.362	152.6	155.07	159.36	***155.36***	329.2	184.9	100.0
249	0.221	0.224	0.225	251.06	251.06	251.06	***254.06***	100.0	100.0	100.0
298	0.185	0.187	0.188	300.06	300.06	300.06	***307.06***	100.0	100.0	100.0

Table 31 – Cranfield University icing tunnel experiments initial, uniced, end, iced cylinder diameters and the calculated value of the droplet inertia parameter K_{exp} in the experiments in the numerical calculations.

Full experimental droplet distribution spectra

D *(mm)*	*K*			*D_{end} (mm)*				*ρ (kg/m^3)*		
	M&S	Jones (glaze)	Jones (rime)	M&S	Jones (glaze)	Jones (rime)	***Exp.***	M&S	Jones (glaze)	Jones (rime)
20	4.747	6.683	9.427	79.68	50.80	30.19	***32.30***	40.7	111.1	473.8
50.05	4.308	4.040	4.349	59.78	67.06	58.74	***60.45***	376.4	202.3	425.1
80.25	2.799	2.694	2.819	88.80	95.35	87.57	***87.57***	333.8	181.9	392.9
99	2.320	2.216	2.276	104.92	114.50	108.85	***113.72***	425.9	233.0	376.7
149.5	1.560	1.525	1.540	153.77	160.77	157.69	***155.36***	444.6	246.9	343.8
249	0.945	0.936	0.940	251.75	256.37	254.55	***254.06***	444.7	246.9	295.0
298	0.792	0.786	0.787	299.70	304.36	302.87	***307.06***	440.5	243.7	276.9
	MVD Approximation									
D *(mm)*	*K*			*D_{end} (mm)*				*ρ (kg/m^3)*		
	M&S	Jones (glaze)	Jones (rime)	M&S	Jones (glaze)	Jones (rime)	***Exp.***	M&S	Jones (glaze)	Jones (rime)
20	2.133	1.859	2.226	32.44	40.17	30.25	***32.30***	374.1	201.1	473.8
50.05	1.054	1.014	1.047	56.11	60.28	56.74	***60.45***	471.9	270.1	425.1
80.25	0.677	0.662	0.678	84.93	88.76	84.70	***87.57***	373.4	200.7	392.9
99	0.555	0.548	0.552	102.58	105.06	103.60	***113.72***	486.4	283.9	376.7
149.5	0.372	0.371	0.371	150.99	152.02	151.65	***155.36***	494.6	292.2	342.8
249	0.225	0.224	0.224	249.33	249.56	249.53	***254.06***	481.4	278.9	295.0
298	0.188	0.188	0.188	298.26	298.56	298.45	***307.06***	473.5	271.5	276.9

Note that despite similar way of calculating the droplet inertia parameter *K* between the analytical and the numerical model, there are differences in values between these two, in addition to the differences between the values calculated using the full droplet distribution spectra and the MVD approximation. This difference is caused by the values of the end iced cylinder diameters. Furthermore, the results from the Tables 30 and 31, show that Makkonen and Stallabrass ice density formulation tends to have good agreement with the smaller cylinders, while it tends to underestimate the icing thicknesses for the larger cylinder diameters. On the other hand, the Jones ice density formulation shows consistently better results for almost all tested cases and especially for the larger cylinder diameters. Both versions of the Jones icing density formulation (the intermediate and the final one) show close agreement in the results for majority of cases, however, the issue with the final version of the Jones empirical icing density parameterization is that, based on the performed analytical and numerical calculations, using both the MVD approximation and the full droplet distribution spectra, is that it is struggling with the spectrum-averaged analytical calculations. With the spectrum-averaging calculations, the produced ice densities are overestimated, when compared to the measured values.

This issues with the final version of the Jones empirical icing density model can be explained by the fact that it operates with the droplet inertia parameter values directly. As the values of it change significantly, when changing from the monodispersed distribution to the full droplet distribution spectra, as evidenced by the Tables 30 and 31, this will cause the value of *K* to become significantly higher when

using the full droplet distribution spectra. As noted in (Jones, 1990) this formulation is very sensitive to the MVD value and using the higher value of K with the spectra is effectively is equivalent to "increasing" the value of MVD (due to the change to the value of K).

Moreover, in the Cranfield University icing tunnel experiments a uniform ice layer was observed for all tested cases and cylinders. This suggests that the "bead-shaped" ice accretions in the FRonTLINES experiments is the function of the wind speed, primarily, in conjunction with the low values of K, although, the potential effects of the low operating temperature in the Cranfield University experiments cannot be ruled out safely at this stage. Furthermore, based on the underestimation of the accreted ice thicknesses for the largest cylinders in these experiments along with the issues regarding estimation of the accreted ice densities for the largest three cylinder diameters on the Mt. Washington Observatory, as discussed in (Jones, 1990) coupled with the rather underwhelming performance of Makkonen and Stallabrass empirical icing density parameterization in predicting the accreted ice densities and cylinder diameters for the FRonTLINES cases, lead the author of this work to the same conclusion as in (Jones, 1990) – that there is a fundamental limitation to the Macklin parameter, primarily in the low wind speed and droplet inertia parameter settings.

Thus, in the analytical calculations, the author recommends to use the Jones (rime) icing density formulation, if and only if, there is a need to calculate cloud impingement parameters using MVD approximation (Langmuir A distribution) *only*. For the rest of cases. the author uses either Makkonen and Stallabrass (aka. Macklin in the FENSAP–ICE) or the Jones (glaze) formulation. The choice depends, based on the operating conditions – if it is an icing wind tunnel data, the author will normally use Makkonen and Stallabrass icing density formulation, otherwise – Jones (glaze).

3.3 Applications of the research work

This subsection focuses on presenting and discussing some potential practical applications for the working methodology, presented in this thesis, be it either the analytical calculation procedure, the numerical CFD simulations or both. The comparisons with other recent developments in the field of the atmospheric icing will be discussed, if applicable.

3.3.1 Comparison with the Volume Weighted Diameter (VWD) approach

As it was mentioned in the ISO 12494 itself (ISO 12494, 2001), the analytical model of in-cloud impingement of Finstad et al./ISO 12494 tends to underestimate the accreted ice masses for cases when $E < 0.10$, in addition to the fundamental constraint in terms of the droplet's inertia parameter $K \leq 0.25$. These limitations have drawn some researchers in the field of the atmospheric icing to improve the applicability of the existing analytical icing parameterization to cover such potential ice accretions.

Recently, Zhang et al. (Zhang et al., 2018) have proposed a novel droplet parametric size in order to evaluate overall collision efficiency for cases with the low K value. While strictly adhering to Finstad et al./ISO 12494 standard model in order to evaluate the overall collision efficiency itself, Zhang et al. (Zhang et al., 2018) substitute the MVD with Volume Weighted Diameter (VWD) defined as:

$$\mathrm{VWD} = \sum x_i d_i \tag{3.8}$$

where x_i is fractional volume of the bin i of the droplet distribution spectrum and d_i is the MVD value of bin i of the droplet distribution spectrum. Note the similarity of VWD and the spectrum-averaging formulation, discussed in the Section 2.1. The usage of VWD formulation should give higher value for droplet diameter, and as a result – the overall collision efficiency will be increased when compared with MVD approximation due to usage of large value of droplet diameter in the calculation. Indeed, for the Langmuir distributions A – J, with the distribution A being monodispersed, the following ratios of droplet diameters were obtained using the VWD calculations, when compared to the MVD approximation.

Table 32 – Droplet diameter ratios using the Volume Weighted Diameter for the Langmuir distributions A – J when compared with the Median Volume Diameter approximation. Distribution A (monodispersed) serves as a reference point and the value of it is equal to unity.

Distribution	***A***	***B***	***C***	***D***	***E***	***F***	***G***	***H***	***J***
VWD	1	1.009	1.030	1.068	1.117	1.180	1.258	1.357	1.613

As it can be seen from the Table 32 different droplet distribution spectra when calculated with the VWD approximation will have the different value of the MVD, compared to the monodispersed distribution. In essence, it will result in the increase in the droplet's inertia parameter value K as it's a function of the droplet diameter as d^2. Thus, the VWD concept will have a higher value of the droplet's inertia parameter, when compared to the MVD approximation, however, the question remains how high this increase will be, compared to the usage of Langmuir spectra. Fortunately, this is rather easy to test as, essentially, the VWD approximation is a monodipsrsed distribution, albeit with the higher value of the MVD.

The VWD concept and its results will be compared against MVD approximation and spectrum-averaged results, based on full droplet distribution spectrum. For this purpose, some selected cases from Makkonen and Stallabrass experimental data will be used. Furthermore, to add data points to the comparison, the cylinder diameters from the FRonTLINES and the Cranfield Unviersity icing tunnel experiments will be used. In order to streamline the comparison, only some droplet distributions will be tested, namely, the Langmuir A, D and E distributions are selected. The reasons for this particular choice being that the Langmuir A distribution is the MVD approximation itself; Langmuir D distribution has been showed to be a good "first guess" distribution, based on its performance in both Makkonen and the Stallabrass and the FRonTLINES experiments, both in the analytical and the numerical calculations; and, finally, Langmuir E was deemed to be a good "test distribution", being "wider" than the distribution E, but not as wide as, for example, distributions G – J.

Overall, Table 33 lists the operating conditions for this comparison.

Table 33 – Operating conditions for the comparison of the MVD, VWD and the Langmuir distribution approaches. The values are valid for both the analytical and the numerical calculations.

Parameter	***Value***
Cylinder diameter (mm)	10.24, 20, 30, 50, 76.09, 80, 100, 149.5, 170, 249, 298
Cylinder length (m)	0.1
Air velocity (m/s)	20
Air temperature (°C)	–4.5

Icing duration (min)	30
LWC (g/m^3)	0.36
MVD (micron)	17.1
Rotational speed (RPM)	2

The comparison of the MVD, VWD and the Langmuir distributions are given in terms of the overall collision efficiencies, as shown in Table 34.

Table 34 – Comparison of the overall collision efficiencies among the MVD approximation (denoted "Mono"), the VWD approximation (denoted "VWD") and the using the Langmuir spectra (denoted "Lang") in the analytical ("A") and the numerical ("N") calculations. Langmuir distributions A (in the MVD columns), D and E are used. In the analytical model the constraint of $E_i = 0.01$ for $K_i \leq 0.17$ is enforced for all droplet bins, meeting the criteria.

D (mm)	***Mono N***	***Mono A***	***VWD D N***	***VWD D A***	***VWD E N***	***VWD E A***	***Lang D N***	***Lang D A***	***Lang E N***	***Lang E A***
10.24	0.562	0.554	0.592	0.581	0.61	0.598	0.533	0.525	0.526	0.518
20	0.386	0.414	0.419	0.445	0.439	0.465	0.380	0.401	0.383	0.402
31.83	0.249	0.303	0.278	0.334	0.296	0.354	0.261	0.306	0.270	0.312
50	0.171	0.196	0.199	0.224	0.217	0.243	0.194	0.216	0.208	0.229
76.09	0.081	0.111	0.101	0.133	0.114	0.150	0.116	0.143	0.116	0.158
80	0.082	0.102	0.096	0.124	0.109	0.139	0.117	0.135	0.125	0.151
100	0.051	0.067	0.067	0.085	0.079	0.098	0.088	0.104	0.104	0.121
149.5	0.015	0.022	0.022	0.033	0.028	0.042	0.045	0.060	0.058	0.074
170	0.009	0.012	0.022	0.021	0.028	0.029	0.038	0.048	0.058	0.062
249	0.003	0.010	0.004	0.010	0.005	0.010	0.017	0.027	0.025	0.038
298	0.002	0.010	0.002	0.010	0.003	0.010	0.011	0.020	0.017	0.029

Furthermore, the comparison from the Table 34 is given visually in Figure 21.

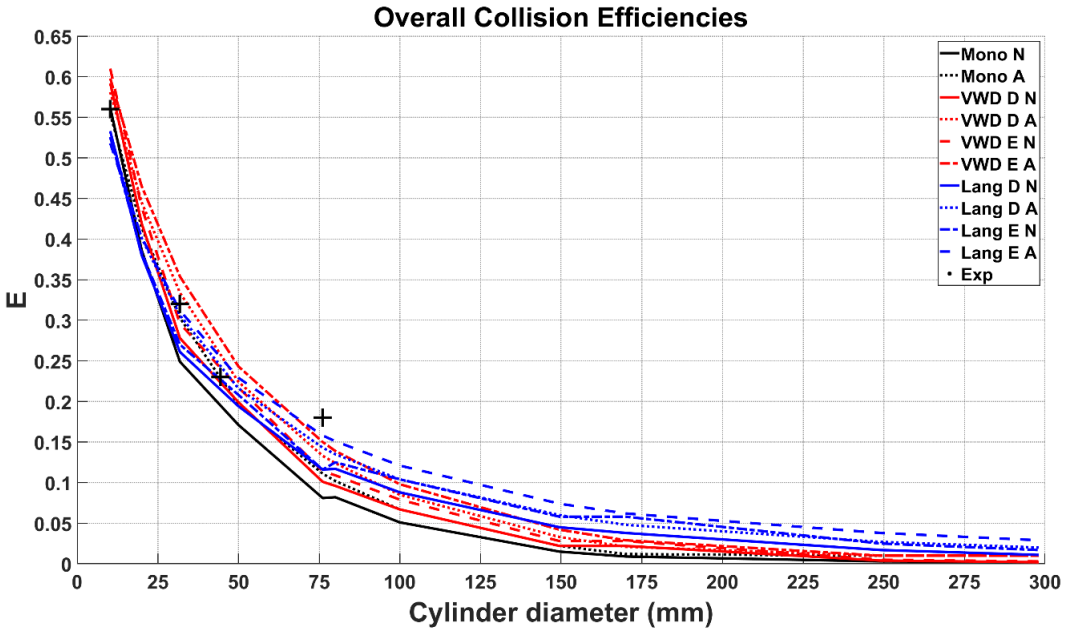

Figure 21 – Overall collision efficiencies for the cases from the Table 34. The black crosses represent experimental values from the (Makkonen and Stallabrass, 1987) experiments. Letters "A" and "N" indicate the analytical and the numerical results, respectively.

From Table 34 and the Figure 21 it follows that for higher values of the droplet inertia parameter, $K > 0.5$, the VWD approximation tends to yield higher values of the overall collision efficiencies for all tested distributions. Furthermore, observe that for very high value of $K > 1.5$, corresponding to cases of 10.24 and 20 mm cylinders, the Langmuir distributions are giving the smaller values of E than the monodisperse distributions. This property of the Langmuir distribution has been discussed in the Section 3.1 of this work. However, since the VWD approximation is a monodisperse distribution, the similar behavior does not apply to it, so the values of the overall collision efficiency will continue to increase with the increase of K.

For the ranges of $0.4 < K < 0.75$, corresponding to the 50 – 100 mm cylinders, both the VWD and the spectrum-averaged values are in relatively good agreement. In general, the VWD approximation is more sensitive to the change in droplet distribution spectrum than the spectrum-averaging procedure for the higher values of K. However, for the cases of 149.5 – 298 mm cylinders, which corresponds to the value of $K < 0.25$ the situation reverses, and the spectrum-averaged results show higher values of overall collision efficiencies and bigger changes arising with the change of distribution.

Furthermore, the behavior of both spectrum-averaging and VWD approximations in the CFD simulations is relatively the same as in case with analytical modeling, thus the preceding discussion and its conclusions do apply for numerical modeling also, however, some of the obtained values in CFD when compared to analytical results are somewhat different and thus need explanation.

First, observe that for majority of cases tested the CFD values show lower overall collision efficiencies. This can be explained by the viscous treatment of the flow in the CFD models, as it was discussed in the Section 3.1.3. This effect becomes more significant with the increase of cylinder's diameter as it can be inferred from the results for the monodispersed case. Second, observe significantly lower values for the larger cylinder diameters, in particular 249 and 298 mm one, in the CFD simulations. The reason for this is that the constraint of $X(K_i, \phi)_i = 0.01$ for $K_i \leq 0.17$ is not employed in the numerical simulations, thus the overall collision efficiency can be an arbitrary small positive value much less than 0.01. Therefore, based on these results, the CFD modeling can be used for both the spectrum-averaging and the VWD approximation approaches, and as with the VWD approach itself, the best results are reached for the cases with $K > 0.5$.

3.3.2 Practical application: Empirical k-factor relating ice accretion on the wind turbine blade to the reference collector

The ISO 12494 standard "*Atmospheric Icing on Structures*" is not limited to circular cylinders alone, and its application can extend to any geometry/structure which can be reasonably approximated by a circular geometry, such as overhead transmission lines, or ice accretions on airfoils for the aircraft/wind power industry, rotorcraft icing etc.

When it comes to the ice accretions on airfoils one common notion is characterizing the characteristic length of the airfoil as the value of the leading edge radius or diameter. Thus, the droplet inertia parameter becomes:

$$K = \frac{v\rho_w d^2}{18\mu R} = \frac{v\rho_w d^2}{9\mu D} \tag{3.9}$$

where R is the leading edge radius and D is the leading edge diameter, respectively.

The interest in modeling the atmospheric ice accretion on the wind turbine blades primarily comes from the estimation and mitigation of the ice shedding events and estimating the losses in the wind power production due to accreted icing disrutpting the performance of the airfooils. Other possible applications involve studying aeroacoustic problems for the purposes of generated noise, and aeroelasiticity in the estimating the negative impacts that the atmospheric ice accretion on blades can cause, such as increased fatigues, mechanical shocks etc. However, direct measurements of ice load on wind turbines are difficult, if not impossible, and therefore some simplifications and empirical relations can be employed. In 2013, VTT technical research center of Finland proposed to use a so-called "*k*–factor" (Turkia et al., 2013), a constant conversion ratio of an order of k = 20 at 85% of blade length deemed to be a representative value for wind turbine ice accretion.

The practical meaning of *k*–factor is a ratio of ice mass accreted on a reference collector, i.e. a slowly rotating cylinder 30 mm in diameter by 500 mm in length, mounted on a met mast to the ice mass accreted on a rotating wind turbine blade profile section in question. The *k*–factor 20 means that rotating wind turbine blade profile, in general, will accrete 20 times more ice in the same time under same operating conditions than a reference collector. However, the VTT model does not explicitly states for what icing conditions it is applicable, as it is expected that reference collector and wind turbine might have differences in ice accretion processes, primarily due to the fact that under ISO 12494 model, it is assumed that velocity vector is normal to the object, i.e., the reference collector, while for wind turbine the velocity vector would not be normal to the blade as the true air speed of the turbine blade is a function of normal velocity caused by the wind and tangential velocity as function of blade rotation. However, the precise extent of those possible differences on ice accretion process is not known as to the best of author's knowledge, and there are no experimental investigations being done for objects rotating in such a way.

In addition, the impact of the airfoil geometry on the ice accretion can be underestimated, especially, in the analytical model, as under the framework of ISO 12494, as long as the characteristic dimension is the same across two objects (provided that other operating conditions are kept constant) the resultant ice accretions can be the same. Fortunately, since the CFD simulations are not bound to such limitations, they can be used to ascertain the possible effects of the airfoil geometry on the resultant ice accretions (and the *k*–factor values).

For this purpose, a few airfoils have been selected for this study and they are: NACA 0012, 4412, 6412, 23012 and N-22, all having the same leading edge radius of 15 mm and maximum thickness of 12 cm. The choice of airfoils has been governed by the need to select a "type" of airfoils having same leading edge radius, thickness and chord length, differing only in the geometric shape and symmetry in order to see if those geometric features have an impact on *k*–factor or not. The remainder of the operating parameters for this study is summarized in the Table 35.

Table 35 – Operating conditions for the empirical k–factor study.

Parameter	***Value***
Cylinder radius [leading edge radius of airfoil] (mm)	15
Air velocity (m/s)	7 (cylinder), 60 (airfoil)
Air temperature (°C)	–5
Altitude (m.a.g.l)	10 (cylinder), 80 (hub)
MVD (micron)	20
Liquid Water Content (g/m^3)	0.4
Icing duration (min)	60
Chord length (m)	1
Droplet distribution	Langmuir A – E

The choice of 7 m/s wind speed is deemed to re representative of the typical icing conditions on the reference collector, mounted on the 10 m.a.g.l. mast, while the 60 m/s wind speed is deemed to be representative of the wind turbine blade speed at 85% of the chord length. This also give the tip speed ratio (TSR) (discounting the hub height factor effect) of about 8.5 – 8.6.

Using these operating conditions, the analytical and the numerical calculations have been carried out. Table 36 shows the values of the overall collision efficiencies in the CFD simulations for the different airfoils at 7 and 60 m/s wind speed conditions along with the reference values obtained from the analytical calculations, under the same operating conditions, and the calculated values of the *k*–factor.

Table 36 – CFD simulations results of the overall collision efficiencies for the different airfoils and the circular cylinder for the 7 and 60 m/s wind speed conditions for the different airfoils in this study, using the Langmuir A – E distributions. The reference values from the analytical calculations are also provided. Since in the analytical calculations the geometry does not impact the end result, as long as the operating conditions are identical, the analytical reference values show the calculated values for the reference collector – i.e., the circular cylinder. The k–factor values are tabulated as the ratio of the overall collision efficiencies, obtained at 60 m/s wind speed, divided by the overall collision efficiencies, obtained at 7 m/s wind speed calculations.

Distribution Airfoil	***Langmuir A***	***Langmuir B***	***Langmuir C***	***Langmuir D***	***Langmuir E***
			Wind speed = 60 m/s		
Reference (Analytical)	0.613	0.600	0.589	0.580	0.570
			CFD - 60 m/s		
Cylinder	0.519	0.508	0.501	0.494	0.488
NACA 0012	0.581	0.587	0.602	0.631	0.670
NACA 4412	0.588	0.586	0.598	0.627	0.662
NACA 6412	0.609	0.604	0.622	0.654	0.690
NACA 23012	0.568	0.579	0.591	0.616	0.641
N-22	0.586	0.586	0.604	0.633	0.663
			Wind speed = 7 m/s		
Reference (Analytical)	0.179	0.182	0.191	0.206	0.220
			CFD - 7 m/s		
Cylinder	0.146	0.151	0.176	0.196	0.243
NACA 0012	0.043	0.060	0.079	0.104	0.135
NACA 4412	0.048	0.067	0.083	0.105	0.136
NACA 6412	0.065	0.076	0.090	0.112	0.143

NACA 23012	0.055	0.070	0.088	0.112	0.137
N-22	0.057	0.070	0.087	0.112	0.141
			k–*factor values*		
NACA 0012	34.13	33.27	29.29	27.57	23.64
NACA 4412	34.55	33.24	29.09	27.38	23.36
NACA 6412	35.78	34.26	30.28	28.56	24.35
NACA 23012	33.33	32.85	28.74	26.90	22.61
N-22	34.43	33.26	29.40	27.62	23.42

From Table 36 it follows that the *k*–factor is not constant and its value varies, depending on the droplet distribution spectrum used and, to lesser, extent, the airfoil used in the calculations. Furthermore, in all cases in the Table 45, the calculated value of the *k*–factor exceeds the value $k = 20$, although it can be explained by the choice in the operating conditions. For consistency purposes, the values of the "pseudo" *k*–factor were calculated for the operating conditions, given in (Turkia et al., 2013) and the obtained results show that for those conditions it varies in the range of 19.4 – 21.4, depending on the droplet distribution used.

The "pseudo" *k*–factor is defined as:

$$\gamma = v_r E_r \tag{3.10}$$

where v_r is the wind speed ratio (the TSR) between the reference collector and the wind turbine blade at 85% of the chord, and the E_r is the overall collision efficiencies ratio between the reference collector and the wind turbine blade. Furthermore, for the operating conditions in the Table 44, an analysis was carried out in order to study the potential sensitivity of the ("pseudo") *k*–factor values, depending on the MVD. This analysis was carried out using the same operating conditions, as in the Table 35, but the MVD value of the spectra were varied in the increment of 5 μm, in the range of $15 \leq \text{MVD} \leq 50$ μm. The obtained results from this study are given in the Table 37.

Table 37 – Values of the "pseudo" k–factor values, using the analytical conditions, under the operating conditions from the Table 35.

Distribution	***A***	***B***	***C***	***D***	***E***
MVD (micron)					
15	59.98	50.08	41.55	33.96	28.63
20	29.35	28.26	26.33	24.00	21.94
25	20.86	20.74	20.19	19.22	18.31
30	17.03	17.14	17.00	16.55	16.09
35	14.89	15.06	15.07	14.90	14.63
40	13.55	13.73	13.80	13.77	13.63
45	12.63	12.81	12.91	12.94	12.90
50	11.97	12.14	12.25	12.32	12.35

The main conclusion from the Table 37 is that the values of the ("pseudo") *k*–factor do not depend only on the droplet distribution spectrum uses, but also vary significantly, depending on the MVD of the droplet distribution spectrum. This, coupled with the results from the Table 36, suggests that the *k*–

factor value is not a constant $k = 20$ and it can vary significantly, based on the number of factors, these primarily being:

- The droplet distribution used.
- The value of median volume diameter.
- Wind speed ratio and TSR.
- Airfoil geometry.

3.3.3 Practical application: Aerodynamic forces acting on the circular cylinder for the dry growth ice accretion

Another interesting notion of the ISO 12494 is the usage of the rotating "reference collector", this being a circular cylinder, 30 mm in diameter, by 500 mm in length, slowly rotating around its principal axis. The notion of using the reference collector originates from (Makkonen, 1984), who notes, based on the referenced observations therein, that majority of ice accumulation events on wire-shaped structures in nature (including the overhead transmission lines) are circular in shape. The main hypothesis, proposed for this, and also used in the ISO 12494 standard, is of continued slow rotation of the collector/conductor, due to the limited torsional stiffness and the influence of gravitational force.

From the viewpoint of the analytical model, using the inviscid, potential flow approximation this makes sense, as for a circular shape in it, one expects the total sum of aerodynamic forces on it to be equal zero, meaning that the $C_D = C_L = 0$, and thus the gravitational force is the only remaining major force. Again, the CFD simulations are not a subject to such limitations and therefore the numerical CFD simulations were carried out in order to check what sort of an aerodynamic forces act on the lightly iced cylinder, and how well these aerodynamic forces will correspond to each other in the case of a non-rotating cylinder, at different angles of attack being checked against same forces, acting on the rotating and uniced cylinder.

For the purposes of this study and as a baseline for comparison, the case no. 2 from (Fu et al., 2006) has been selected. This particular choice was governed by several reasons, namely the need to select the case with known experimental ice shape, under "dry growth" conditions, and with the cylinder diameter, which is representative of a diameter of a power line conductor. In particular, having the information on the experimental ice shape allows for an ease of validation of the numerical results, while operating with the "dry growth" conditions reduces the amount of variables that can influence the ice growth. The operating conditions for this study are given in Table 38. Since the droplet distribution spectrum information was not provided in (Fu et al., 2006), the simulations were performed using Langmuir D distribution, as it is a common distribution in the in-flight icing studies (Bidwell, 2012;Papadakis et. al, 2007;Wright, 2008).

Table 38 – Operating conditions for the numerical CFD simulations in the study of the aerodynamic forces acting on the circular cylinder for the dry growth ice accretion. The values for different angles of attack were selected to provide a decent coverage in one quadrant and the non-zero angle of attack simulations in CFD were performed by rotating the inflow angle by a specified angle of attack.

Parameter	***Value***
Air speed (m/s)	5
Temperature (°C)	–15

MVD (micron)	35
Cylinder diameter (mm)	35
LWC (g/m^3)	1.2
Icing duration (min)	30
Angle of attack	0°, 30°, 60°, 90°

The steady-state numerical simulations of the atmospheric ice accretion were carried out using the Ansys FENSAP–ICE. However, the transient airflow simulations of the cylinders were performed using Ansys Fluent. The reason for selecting the Fluent and transient simulations is that it is deemed that the transient CFD simulations will give a better "description" of the airflow, acting on the cylinders, as such phenomena as vorticity shedding, wake behavior, etc. are better resolved using the transient CFD techniques, as opposed to the steady-state simulations, which tend to "smooth" the unsteady airflow effects and primarily recover the mean values of the flow.

The time step chosen for the transient simulations in Ansys Fluent is 0.7071 ms. The choice of time step is based on the assumption of Strouhal number being equal to 0.2 for cylinder for the value of cylinder Reynolds number range, as calculated from the operating conditions in the Table 38. Thus by reverse calculation, the frequency of flow has been found and from there the time step has been obtained. The amount of iterations per time step has been set to 50, with 7500 total time steps, as this particular combination has been found to provide good convergence along with parameters of interest reaching the "steady-state". Thus, the total transient simulation time was approximately equal to 5.3 seconds.

The transient airflow simulation results are presented in terms of combined plots of several parameters of interest, namely the drag, lift and moment coefficients, combined pressure and viscous force (denoted as force) as well as the Strouhal number. These plots are given in Figure 22 and show the transient curves for the last 1.3s of the flow, which corresponds to approximately last 2000 time steps. To avoid cluttering multiple different curves on a single plot, any given parameter of interest is presented by two subplots – first showing the values for the cases at different angles of attack (AOAs), and second showing the values for the benchmark cases. In order to keep the comparison visually simple, the black curve, corresponding to 0° AOA case is presented in all subplots and the axis limits are kept consistent between the respective subplots.

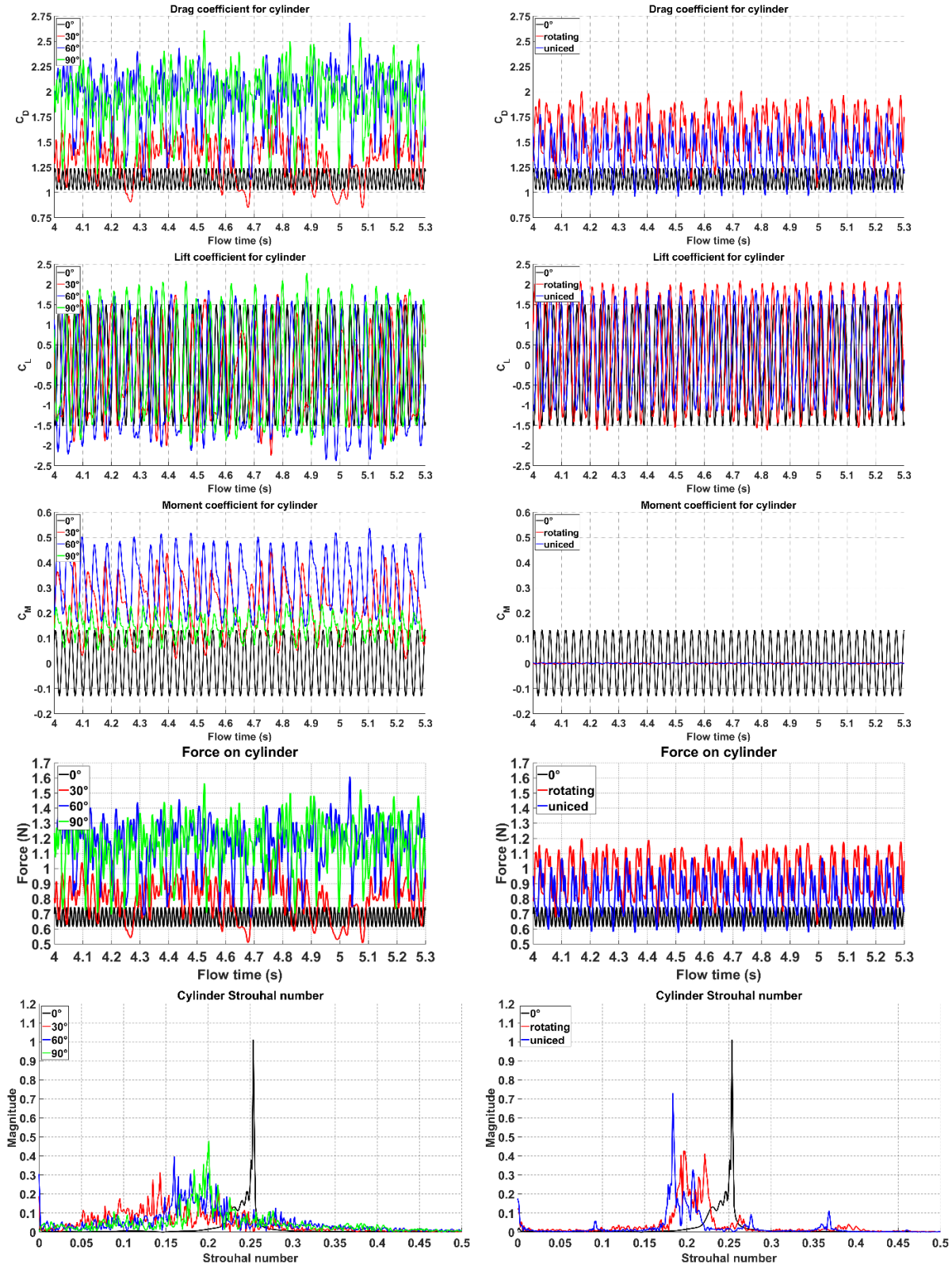

Figure 22 – Drag coefficient, lift coefficient, moment coefficient, combined viscous and pressure force and the Strouhal number values in the transient CFD simulations for the 0°, 30°, 60°, 90° AOA, rotating iced and benchmark uniced cylinders.

Table 39 shows the mean values of C_D, C_L, C_M and total pressure and viscous force F, while the Strouhal number given in it corresponds to the value associated with the maximum magnitude. The mean values reported in the Table 48 were taken from the last 2000 time steps of the airflow simulations, in order to avoid possible skewing of the resulting from taking into account the values at the beginning of the simulations, where results may not yet be converged.

Table 39 – Drag coefficient, lift coefficient, moment coefficient, combined viscous and pressure force and the Strouhal number values in the transient CFD simulations for the 0°, 30°, 60°, 90° AOA, rotating iced and benchmark uniced cylinders.

Variable	***0°***	***30°***	***60°***	***90°***	***Rotating***	***Uniced***
C_D	1.13	1.34	1.93	1.93	1.58	1.38
C_L	–0.01	–0.21	–0.37	–0.03	0.26	0.27
C_M	0.00	0.21	0.32	0.15	0.00	0.00
F	0.68	0.79	1.16	1.15	0.95	0.83
Strouhal	0.25	0.14	0.16	0.20	0.20	0.18

The results from benchmark cases for the drag coefficient and Strouhal number compare favorably with the results of Relf and Simmons, as reported by (Tanida et al, 1973) and (Gerrard, 1961), with C_D values in this work being slightly higher than these experimental values, possibly due to higher turbulence intensity in the numerical simulations in this work. Moreover, the C_D values of uniced and 90° AOA match closely those in the numerical simulations of (Keyhan, 2012) for the 5 m/s wind speed cases, and the C_D values with respect to angle behave in a similar trend, as in (Rossi et al, 2020), even if their C_D values are different, due to different Reynolds number and the ice shapes. Moreover, the behavior of C_D and C_L curves and values, follows closely the ones in the (Selvam, 1997) for the unicied cylinder at $Re = 10^4$ who used Large Eddy Simulation (LES) in their study, contrary to the Unsteady Reynolds Averaged Navier-Stokes (URANS) in this work.

One interesting result, as inferred from the Figure 22 and Table 39 is that the iced cylinders at 0° and 30° AOA has smaller values of the drag and total pressure and viscous force, when compared to the rotating iced and uniced cylinder benchmarks. The accreted iced cylinder shapes, primarily for the 0° AOA case, are rather streamlined, which may result in flow separation to be more gradual when compared to rotating and/or uniced cylinder. Second, is the airflow behavior around the cylinder, as discussed in the previous section. In addition, since all numerical simulations have used Shin et al. surface roughness model, the actual effect of iced surface roughness for the iced cases can be underestimated when compared to the uniced cylinder.

The cylinder at 30° angle of attack also experiences lower average values of the drag coefficient and force when compared to the uniced and rotating cylinder, however, the amplitude of fluctuation of C_D and F is higher than in benchmark cases. As for the 60° and 90° AOA cases, they exhibit an “expected” behavior, i.e., higher values of all the parameters of interest and higher amplitude of fluctuations. This suggests that the cylinder in these cases experiences higher aerodynamic loads than the reference cases of rotating and uniced cylinders. Furthermore, the moment coefficient is higher in the cases of 30° and 60° AOA, as compared to 90° AOA. A possible explanation here is that the 90° AOA is a mostly “symmetric” situation, with this sort of symmetry naturally reducing the C_M value, also indicated by the

C_L value being zero for this case, as expected from the "symmetric" situation (the positive moment convention in the numerical simulations is the counter-clockwise). On the other hand, the C_M value for the 0° AOA is expectedly zero, however, the amplitude of fluctuation of it is not, thus indicating that this configuration is prone to oscillation around $y = 0$ line.

However, several peculiarities have been observed in the results in Figure 22 and Table 39. First, the similarity in the amplitude of C_L values in the results for all tested configurations. While the maximum C_L oscillations do increase with change of configuration, for example, changing from 0° to 90° AOA, the magnitude of the fluctuations is not nearly as close as amplitude fluctuations in C_D values. This indicates that while configurations at extreme AOAs are more aerodynamically loaded, in absolute terms, they are just marginally more loaded in C_L terms. Second, is the non-zero C_L values for the uniced and the rotating cylinders, with the C_L being equal to 0.27 and 0.26, respectively. This may indicate possible asymmetry of the flow separation from the cylinder edges. When comparing these C_L values with available results for the circular cylinder at the Reynolds number $Re = 10^4$ the results in this study for the circular cylinders are on the low range of the C_L values as measured in experiments by (Gopalkrishnan, 1992) with mean value of stationary circular cylinder C_L being 0.38.

Finally, the Strouhal number values, obtained from the C_L oscillations show a wide range of values, from 0.14 for the 30° AOA case to the 0.25 for the 0° AOA case. From reverse calculation, the frequency values of 36, 18, 19, 24, 25 and 26 Hz for the lift force oscillations were obtained, for the 0° – 90° AOA, rotating and uniced cylinder, respectively, and twice the indicated frequencies for the drag force oscillations. Therefore, the cylinder at 0° AOA tends to have higher frequency of vortex shedding at smaller amplitudes, while 30° and 60° AOA cylinder have considerably higher amplitudes at smaller frequency. The 90° AOA and the benchmark cases fall in-between, and thus, the rotating cylinder "equivalence" assumption compares favorably.

Summarizing, since the cases with the 0° and 30° AOA are less aerodynamically loaded, while the 60° and 90° AOA cases are more aerodynamically loaded than the benchmark cases of the rotating and the uniced cylinder. It suggests that the "averaged" values across all 0 – 90° AOA cases should be comparable to the benchmark, and thus the "rotating" assumption should be mostly equivalent. To illustrate this, Figure 23 shows the averaged values of total pressure and viscous force vs. benchmark cases. The total pressure and viscous force has been chosen as a parameter to compare, as it is independent of reference length and area in the numerical simulation, thus being the most "direct" way of comparing the results.

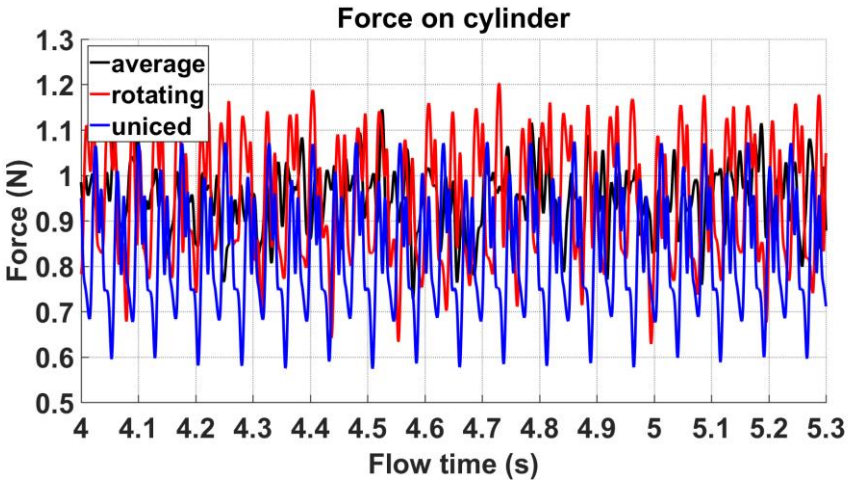

Figure 23 – Averaged values of the combined viscous and pressure force in the transient CFD simulations for the 0°, 30°, 60°, 90° AOA, compared to the benchmark cases of the rotating iced and uniced cylinders.

The results from Figure 23 tend to support this previous assumption, as the combined *F* curve lies mostly on the rotating cylinder *F* curve in the steady state range, with mean value of *F* for the "averaged" curve being 0.95, which matches the value for rotating case from Table 39 within the rounding error. Thus, from the viewpoint of total aerodynamic force, acting on the cylinder, the rotating cylinder is equivalent to the "averaged" case of 0° – 90° AOA.

3.3.4 Practical application: Study of dry ice growth on duplex cylinders

Another practical application of the methodology, described in this work, is the modeling of the atmospheric ice accretions on the bundled conductors. A significant proportion of the overhead transmission lines consists of the bundled conductors; those being arranged in the duplex/triplex/quadruplex/etc. configurations. However, the ISO 12494 does not provide necessary guidelines on how to model the ice accretions in such cases, and utilizing the inviscid, potential flow approximation, as used in the analytical model can be detrimental, as it does not take into account any sort of disturbances of the flow, caused by the windward conductor in the bundle, including the potential wake effects.

Thus, one can apply the CFD methods in order to model such ice accretions. Indeed, such works has been carried out by (Wagner, 2010) and (Qing et al., 2018). Unfortunately, to the best of the author's knowledge, the available works on the topic are limited to the aforementioned studies, and there are some limitations to them. In case of (Wagner, 2010), they do not attempt to "quantify" the resultant ice accretions, only referring to them as "full", "partial", and "no ice accretion" (on the leeward conductor, compared to the windward conductor). The methodology of (Qing et al., 2018) is questionable, in particular in their CFD governing equations and the droplet drag coefficient formulations. The available information in the original source makes it nigh impossible to reproduce their study in detail.

Therefore, during this work a study of dry ice growth on duplex cylinders has been carried out in order to "close the gaps" in the results of (Wagner, 2010) and (Qing et al., 2018) and to attempt to apply the commercial CFD tools in order to obtain the "preliminary quantification" of the overall collision

efficiencies and the accreted ice masses on the cylinders in the duplex configuration for the case of the dry ice growth.

Table 40 shows the operating conditions in this study with Figure 24 giving a schematic overview of the duplex bundled cylinders setup.

Table 40 – Operating conditions for the duplex cylinder configuration study of the dry ice growth on cylinders.

Parameter	***Value***
Cylinder diameter (mm)	30
Air velocity (m/s)	4, 7, 10, 20
Air temperature. (°C)	–5
Altitude (m.a.g.l)	10
Median Volume Diameter (µm)	15, 20, 25, 30, 40
Liquid Water Content (g/m^3)	0.4
Icing duration (min)	30
Cylinder separation (mm)	500
Droplet distribution spectrum	Monodisperse

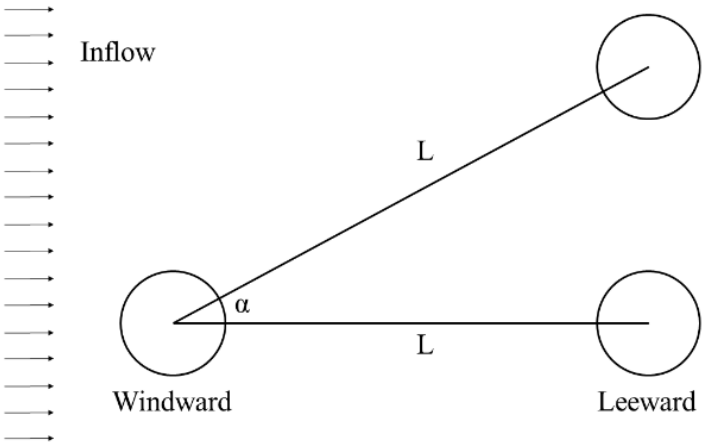

Figure 24 – Schematic overview of the duplex cylinder configuration.

The choice of cylinder diameter and separation is deemed to be representative of an actual diameter and separation of a typical duplex conductor bundle. The range of air velocities in this study is deemed representative of simulating in-cloud icing in typical conditions, and the choice of Median Volume Diameters (MVDs) should also be sufficient to represent the naturally-occurring variation, without going into the Supercooled Large Droplet (SLD) size ranges, thus introducing potential issues with splashing and bouncing of the droplets.

Furthermore, the case of a cylinder bundle being exposed to icing at operating wind speed of 10 m/s and MVD of 20 µm was selected for further investigation of the effect of an angle/vertical separation on the icing on bundled conductors. The vertical separations chosen are one cylinder radius (15 mm; ≈1.7° angle), one cylinder diameter (30 mm; ≈3.4°), two cylinder diameters (60 mm, ≈6.8°) and 129.4 mm, corresponding to the angle of 15° exactly. This range of vertical separations fits in between the

simulation cases, performed at different angle by (Wagner, 2010) and (Qing et al., 2018). The reason for performing numerical simulations at different angles is to simulate the gradual sag of the conductor bundle (1.7° – 6.8° angles) and extreme sag due to significant ice accretion (15° angle). Larger angles are not considered in this study as its assumed that the leeward conductor would not be "shielded" by a windward one past this point and thus the flow conditions and the ice accretion on both of them would be almost identical, as covered by (Qing et al., 2018).

Tables 41 and 42 show the overall collision efficiencies (*E*) and their ratios between the windward and the leeward cylinders respectively for all test cases from the Table 40.

Table 41 – Overall collision efficiencies on the windward (W) and leeward (L) cylinders.

MVD	***15***		***20***		***25***		***30***		***40***	
V	*W*	*L*	*W*	*L*	*W*	*L*	*W*	*L*	*W*	*L*
4	0.005	0.007	0.057	0.054	0.140	0.122	0.224	0.186	0.371	0.277
7	0.052	0.045	0.154	0.122	0.256	0.193	0.347	0.242	0.490	0.298
10	0.103	0.077	0.223	0.150	0.330	0.204	0.421	0.238	0.557	0.278
20	0.233	0.095	0.372	0.139	0.479	0.163	0.563	0.181	0.679	0.209

Table 42 – Overall collision efficiencies ratios of leeward to windward cylinders.

MVD	***15***	***20***	***25***	***30***	***40***
V					
4	121%	94%	87%	83%	75%
7	87%	79%	75%	70%	61%
10	75%	67%	62%	57%	50%
20	41%	37%	34%	32%	31%

Since for the "dry growth" regime the sticking and freezing efficiencies, $\alpha_2 = \alpha_3 = 1$ respectively, the accreted ice mass ratios between the windward and the leeward cylinders will be identical to overall collision efficiencies ratios from Table 42. Visually, the ratio from Table 42 is given in Figure 25.

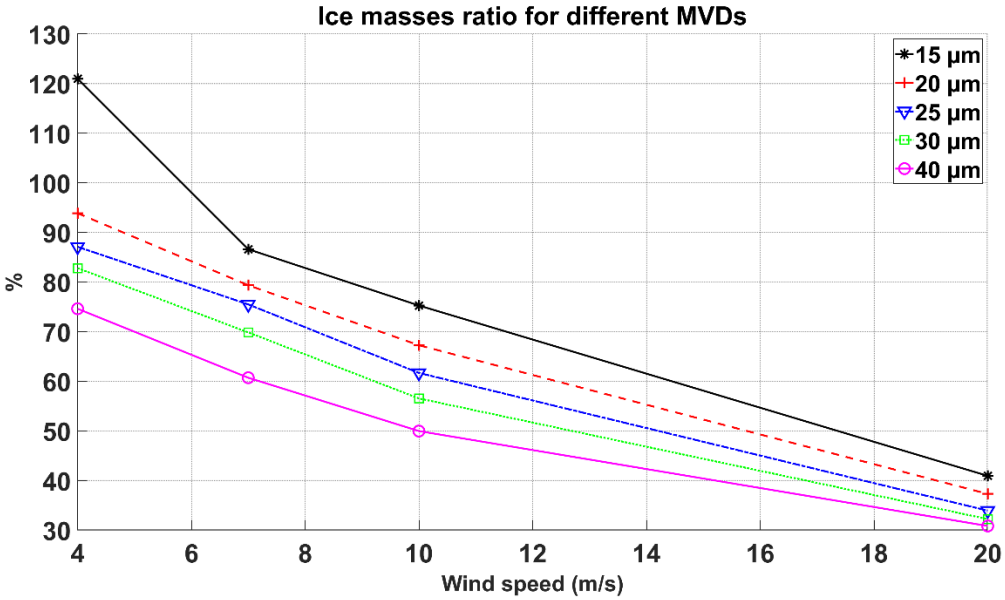

Figure 25 – Overall collision efficiencies for bundled cylinders in this study.

From Table 42 and the Figure 25 the conclusion that can be made is that with the increase in the MVD and/or wind speed values, the ratio of overall collision efficiencies between the leeward and the windward cylinder decreases from "full accretion" to a "partial accretion" of an around 31%. The decrease in the overall collision efficiencies is more "steeper" for smaller MVDs. This decrease can be directly correlated to the increase in the droplet inertia parameter *K*, and to lesser extent – the Langmuir parameter ϕ.

The physical explanation behind the decrease of the accreted ice mass ratios, associated with the increase in values of *K* and ϕ is two-fold. First, with the increase of droplet inertia, associated with the increase of MVD and/or wind speed, the inertia will be dominating the droplet movement and thus the characteristic time for the droplet to adapt to the new conditions will increase. For example, the increase in the wind speed will result in shorter "time window" for the droplet, passing over the windward cylinder, to adjust to new trajectory, such that allows for the collision with the leeward cylinder, at a given separation. In addition, higher wind speeds result in the wake effects being prominent, potentially affecting the ice accretion of the leeward conductor.

Furthermore, Figure 26 shows the overall collision efficiencies ratio from Table 42 compared to the value of the droplet inertia parameter *K*.

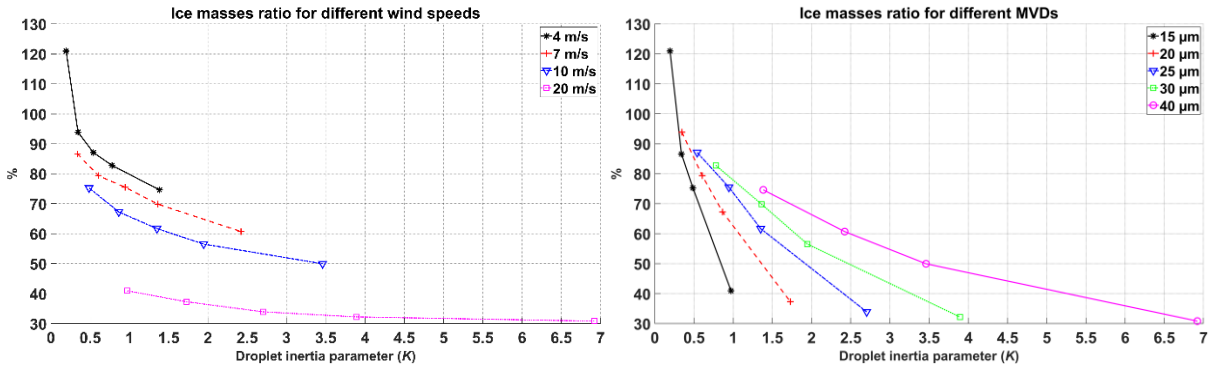

Figure 26 – Accreted ice masses ratio versus the droplet inertia parameter K for different wind speeds (left) and MVDs (right). Each marker in the plot corresponds to one pair of wind speed and MVD values from the Table 51.

Figure 26 shows that the accreted ice masses ratio decreases in the similar fashion for all combinations of wind speeds and/or MVDs with the increase in the value of *K*. Moreover, the curves, featuring inherent larger changes in values of *K*, for example, at 4 m/s wind speed or at MVD of 15 µm tend to decrease the accreted ice masses ratio faster. This is in agreement with the results of (Wagner, 2010), especially for the curve dividing "full" and "partial" accretion, as in that plot the higher values of *K* are towards upper right of the plot. Unfortunately, it is not possible to quantify the results further, as (Wagner, 2010) haven not presented the overall collision efficiencies or the accreted ice masses ratios in their work.

However, for the test case of the bundled conductors at 4 m/s wind speed and 15 µm MVD, the droplet inertia parameter *K* value is below the critical value of 0.25. As with was discussed in the Section 2.2, detailing the numerical setup, the FENSAP–ICE lacks the term pertaining to the calculation of the "history term", which for the cases of $K < 0.25$ can make significant difference, when it comes to the overall collision efficiencies, as discussed in the (Finstad et al., 1988). As such, the "physical meaning" of the simulation results at 4 m/s wind speed and MVD of 15 µm, which results in the accreted ice masses ratio of 121% can be questioned.

Figure 27 shows the accreted ice masses for all operating conditions in this study plotted against the droplet inertia parameter *K*. In addition, a curve has been added, corresponding to the analytical calculations for the accreted ice mass on the windward conductor, carried out using ISO 12494 formulae/trajectories calculation method. The value of the droplet inertia parameter *K* was estimated using standard ISO 12494 formulae and uniced diameters.

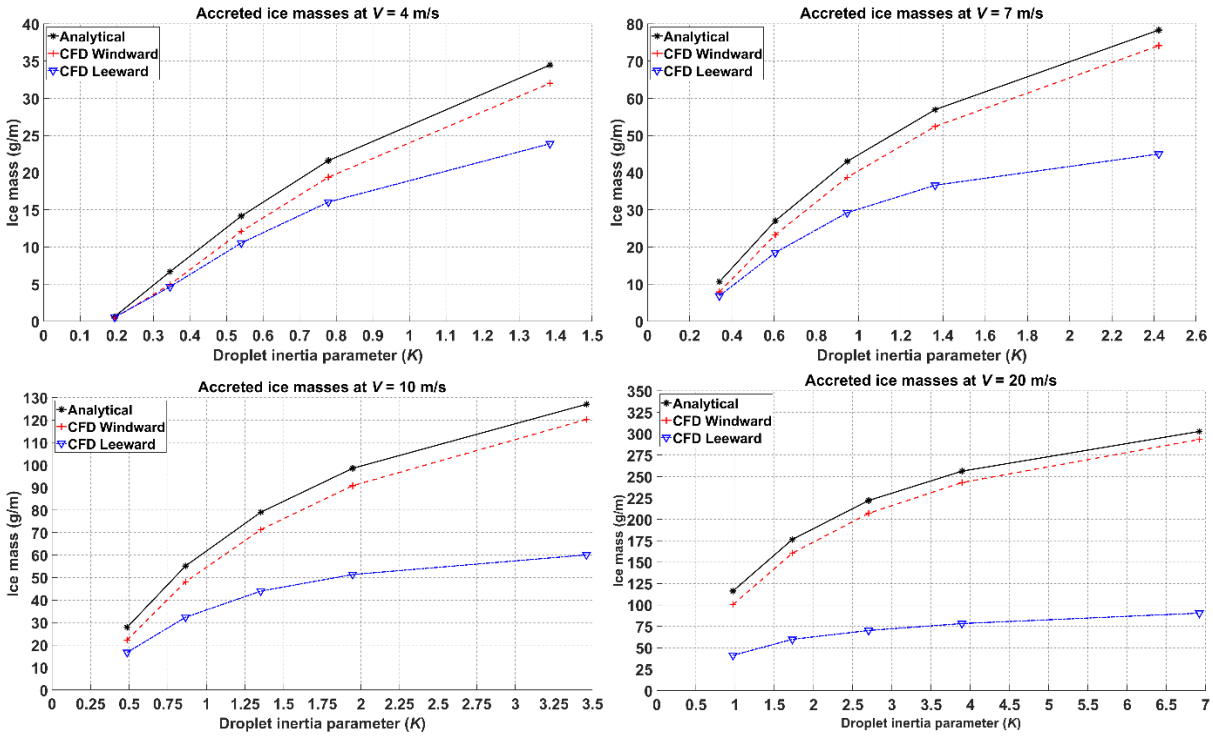

Figure 27 – Accreted ice masses versus the droplet inertia parameter K for different wind speeds. Each marker in the plot corresponds to one MVD value from the Table 42.

From Figure 27 it can be seen that the analytical and the CFD results for the windward conductor agree well. On the contrary, the leeward conductor behaves rather differently from the windward conductor in the CFD and the analytical model, with an interesting tendency of "flat lining" in terms of accreted ice masses for the values of $K > 4$.

For the purpose of studying the effect of the angle on the atmospheric ice accretion on the bundled cylinders one test case was selected from the Table 40, having the MVD value of 20 μm and the wind speed value of 10 m/s. As with all cases the distance between cylinders is held constant at 500 mm and the desired angle is achieved by manipulating the horizontal and the vertical separation distances. The results from the ice accretion simulations on the angled bundle are given in terms of the overall collision efficiencies, their ratios and the accreted ice masses, and they are given in Table 43. As with all test cases in this study, the "dry growth" icing conditions are maintained in the CFD simulations, therefore, the accreted ice mass ratios are identical to the overall collision efficiencies ratios.

Table 43 – Overall collision efficiencies, ratios and accreted ice masses on the angled cylinders.

Vertical separation (mm)	***Angle***	***Overall Collision Efficiency***		***Accreted Ice Mass (g/m)***		***Overall Collision Efficiency Ratio***
		W	*L*	*W*	*L*	
15	1.7°	0.22	0.14	47.3	31.3	66%
30	3.4°	0.22	0.24	47.8	52.5	110%
60	6.8°	0.22	0.24	47.7	50.9	107%
129.4	15°	0.21	0.22	45.6	46.7	103%

Figure 28 shows the distribution of local collision efficiencies for the angled bundle configuration. For the dry growth conditions, the distribution local collision efficiencies is also representative of the accreted ice shapes.

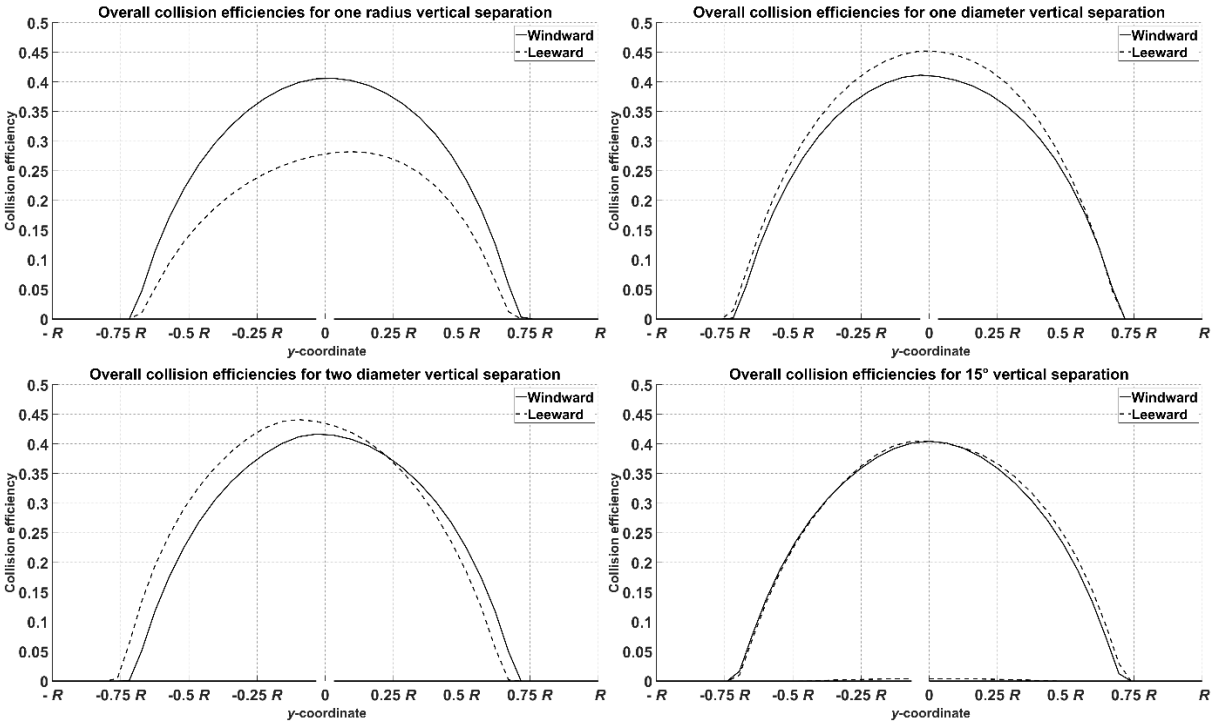

Figure 28 – Local collision efficiencies of the angled cylinders configuration. The vertical separations are 15 mm (one cylinder radius; top left); 30 mm (one cylinder diameter; top right); 60 mm (two cylinder diameters; bottom left); and 129.4 mm, corresponding to the angle of 15° (bottom right).

Figure 29 shows the accreted ice masses and their ratios for the angled bundle configuration.

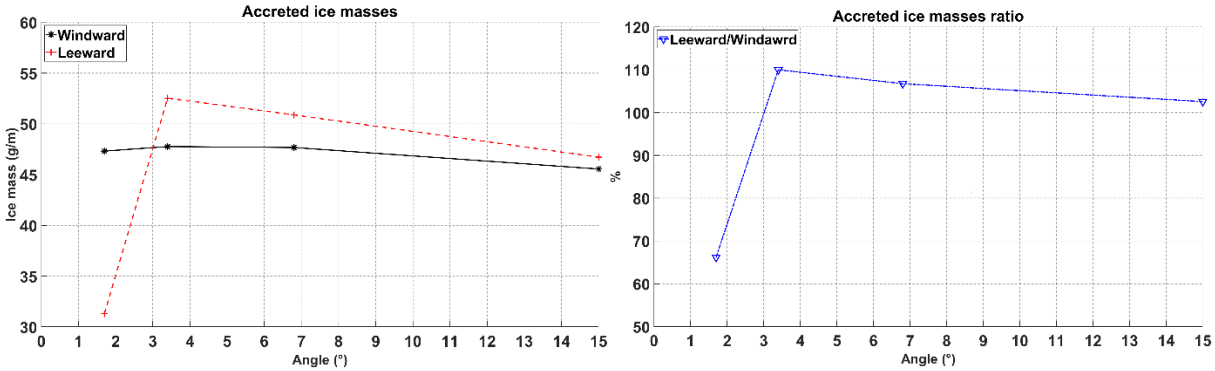

Figure 29 – Accreted ice masses (left) and their ratios (right) for the angled cylinders configuration.

From Table 43 and Figures 28 and 29, it can be seen that at vertical separation of 15 mm, equal to the one cylinder radius, the "shielding" effects from the windward cylinder are very pronounced, limiting the amount of accumulated ice mass on the leeward cylinder at 67%, compared to the windward cylinder. This value is almost identical to the corresponding case from the Table 42 simulated at 0°

incidence. At the vertical separations of 30 and 60 mm, equal to the one and two cylinder diameters respectively, the ice accretion on the leeward cylinder "normalizes", becoming equal and even slightly higher than on the windward cylinder. This is more pronounced for the leeward conductor at one cylinder diameter vertical separation, which accretes approximately 10% more ice mass. This increased accretion can be explained by part of the multiphase flow, carrying significant LWC concentration at high speed being redirected from the top edge of windward cylinder onto the leeward one. The effect dissipates with the increase of vertical separation, as evidenced from the results at 15° angle, corresponding to the vertical separation of 129.4 mm which is slightly more than four cylinder diameters. In this case both cylinders accrete almost identical ice masses, within 3% of each other.

These results tend to agree well with the ones from (Wagner, 2010), who notes that for the angle of twist of 1.91°, corresponding to the vertical separation of 13.33 mm, the leeward conductor accreted 86% ice mass, compared to the windward conductor. For the angle of 2.86° (vertical separation of 19.96 mm) the accreted ice mass ratio is almost 100%. However, some discrepancies between results of (Wagner, 2010) and this work are present. For the angle of 0.96° (6.7 mm), their leeward conductor accretes only 11% mass, and for the conductor at 0° Wagner writes that "*the downstream cable without any ice deposit*". Contrary, in this work the conductor at 0° incidence accretes 67% ice mass. When comparing the operating conditions of (Wagner, 2010) with this work, the values of the droplet inertia parameter K and the Langmuir parameter ϕ are different, being $K = 0.87$ and $\phi = 273.8$ for this work and $K = 1.27$ and $\phi = 365.1$ in (Wagner, 2010), along with the ratio of the cylinder separation L to the diameter D. In this work $(L/D) = 16.67$ and for Wagner it is $(L/D) = 10$. The windward cylinders Reynolds number are 2.3×10^4 and 3.1×10^4, respectively.

The practical meaning of this phenomenon for the ice accretions on actual power lines with bundled conductors is, when the windward conductors accretes enough ice mass in order to sag sufficiently enough to no longer "shield" the leeward conductor, the ice accretions on the both conductors in the bundle will be almost equal, and thus they can be modeled using simplex configuration in CFD along with the formulae of ISO 12494, if desired. This does not take into account the possibility and potential implications of vibrations or rotations of the conductors, due to fluid-structure interaction. It is assumed that these interactions can cause the windward conductor to no longer "shield" the leeward conductor at even earlier point in time during an icing event. However, these potential effects are not within the focus of current study and will not be ascertained here.

3.3.5 Practical application: Modeling of the extreme ice loads on the overhead transmission lines

Another practical calculation of the calculation methodology, presented in this work is the estimation of the icing intensities on the Ålvikfjellet test span. Currently, the icing intensity on the conductor(s) is estimated using the monodispersed distribution, with the values of the MVD and LWC estimated from the rotating reference collector, in similar fashion to the methodology of (Makkonen, 1992) using the rotating multicylinder device, meaning the MVD and LWC combinations for a given event are estimated from the accreted ice masses on the collector under known operating conditions.

A change has been made, based on the results within this work, and the MVD approximation was substituted with the Langmuir D distribution, based on its satisfactory performance in modeling the

results of the Makkonen and Stallabrass and the FRonTLINES experiments in both the analytical and the numerical models. Figure 30 shows the observed icing intensities, and those obtained via analytical modeling, using the MVD approximation and the Langmuir D distribution, respectively.

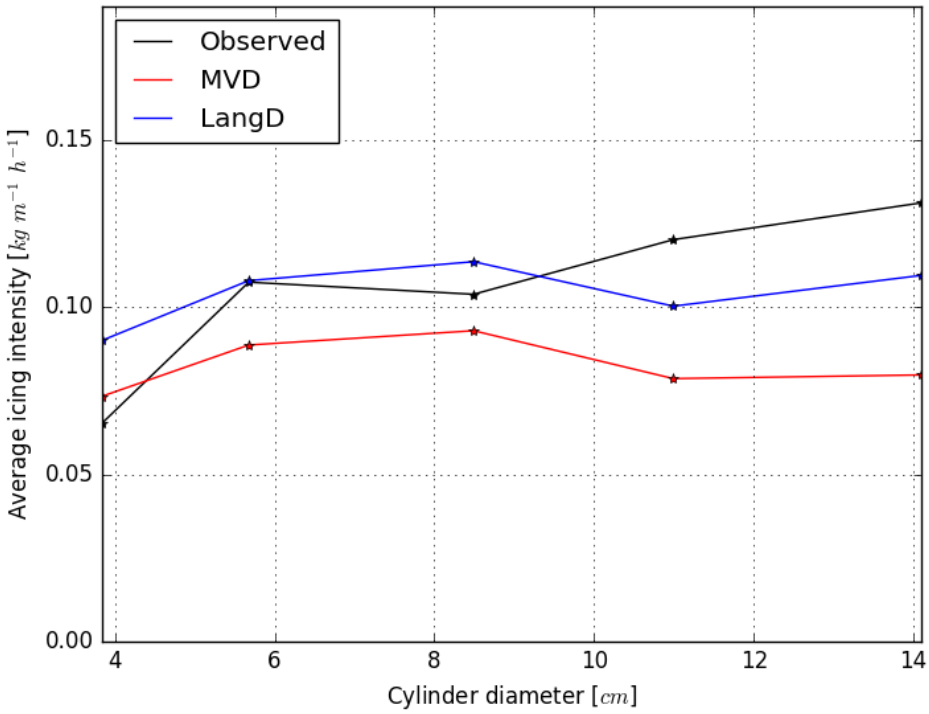

Figure 30 – Observed and modeled icing intensities on the simplex conductor on the Ålvikfjellet test span (Ingvaldsen et al., 2019).

From Figure 30 it is clear that the usage of the Langmuir D distribution provides better fit with the observed icing intensities for all ranges of the cylinder diameter than the MVD approximation. The agreement between the observed icing intensities and those modeled using the Langmuir D distribution is satisfactory for majority of the range of the cylinder diameter values, with exception of the range above approximately 11 cm. This, however, can be explained by not forcing a constraint on the overall collision efficiency of $E = 0.01$ for $K \leq 0.17$ and the lower limit of E for the ice intensities in the Figure 30 is $E = 0.005$. Thus using the constraint of $E = 0.01$ for $K \leq 0.17$ will improve the agreement for the extreme iced diameters, at the potential cost of overestimation of the icing intensities for smaller values of the cylinder diameter, however, it is not known by how much these values will be overestimated.

3.4 Summary of published papers

This section presents the summary of the published (and if applicable – under review as of writing of this work) scientific papers within the scope of this Ph.D. thesis. The background and major conclusions/findings of each of these papers will be given in the subsequent subsection below. For convenience, Table 44 lists the papers which has been published under the scope of this thesis.

Table 44 – Overview of published papers within the scope of this thesis.

No.	*Title*	*Authors*	*Journal/ Conference*	*Publication Status*	*Year*
Paper 1	Analytical parametrizations of droplet collision efficiency on cylinders – A review study	P. Sokolov M. S. Virk	Cold Regions Science and Technology	Accepted	2018
Paper 2	Accreted ice mass ratio (k-factor) for rotating wind turbine blade profile and circular cylinder	P. Sokolov J. Y. Jin M. S. Virk	Wind Energy	Accepted	2019
Paper 3	Droplet distribution spectrum effects on dry ice growth on cylinders	P. Sokolov M. S. Virk	Cold Regions Science and Technology	Accepted	2019
Paper 4	An investigation into empirical ice density formulations for dry ice growth on cylinders	P. Sokolov M. S. Virk	Cold Regions Science and Technology	Accepted	2019
Paper 5	Modelling of dry ice accretion on cylinders- a case study of present analytical state	P. Sokolov M. S. Virk	18th International Workshop of Atmospheric Ice Accretion on Structures (IWAIS 2019)	Accepted	2019
Paper 6	Aerodynamic Forces on Iced Cylinder for Dry Ice Accretion – A Numerical Study	P. Sokolov M. S. Virk	Wind Engineering & Industrial Aerodynamics	Accepted	2020
Paper 7	Study of Dry Ice Growth on Duplex Cylinders	P. Sokolov M. S. Virk	Cold Regions Science and Technology	Under review	N/A

In addition, the final, pre-print versions of published papers from Table 44 are attached with this thesis.

3.4.1 Analytical parametrizations of droplet collision efficiency on cylinders – A review study

Within the scope of this work, several major ice accretion parameterizations have been investigated, staring from the original Langmuir and Blodgett work on the water droplet trajectories, up to and including the Finstad et al., mathematical model of overall collision efficiency parameterization, which is part of current governing ISO standard, thus covering a timeframe of several decades of investigation in icing modeling. The paper provides a general and mathematical overview of those parametrizations, presents necessary formulae for calculations of overall collision efficiency, starting with trajectory evaluation, and discusses underlying assumptions and approximations made by respective authors in those models, as well as includes discussion and comparison with some of the newer concepts in ice modeling, such as Volume Weighted Diameter (VWD) and makes use of CFD simulations to estimate feasibility of using the CFD tools to simulate ice accretion at low values of the droplet's inertia parameter *K*.

As an application example, two experimental datasets have been used for overall collision efficiency calculations and comparison of parameterizations. Those experiments span large amount of operating conditions, thus giving the droplet's inertia parameter range $0.1 < K < 4.6$, and overall collision efficiencies range of $0.01 < E < 0.63$ which should cover majority of possible icing conditions. The results show several important points, namely, that for higher ranges of droplet inertia, approximately $K > 0.8$, the monodisperse droplet distribution yields good agreement with the experimental values, however, for values of K below that, as droplet's inertia decrease further and characteristic length of the object increases, the monodisperse droplet distribution approximation tends to underestimate the overall collision efficiencies when compared to the experimental and spectrum calculated values. In those cases, the empirical fit of Makkonen (Makkonen, 1984) for the calculation of overall collision efficiency produces better results, than Finstad et al. model (Finstad et al., 1988a) with MVD approximation, as parameterization by Makkonen was developed with the purpose of collapsing the different droplet spectrum collision efficiencies into a single curve.

However, for very low values of K and E, roughly corresponding to the $K \leq 0.3$ and $E \leq 0.07$, respectively, the MVD approximation, using any present model in this study tends to underestimate the overall collision efficiency significantly. For those cases the recalculation of droplet trajectories using full spectrum is recommended. However, due to extensive work needed to carry this analysis, a simplified approach using, full droplet distribution, if available, with the Finstad et al. model, using the constraint of $E = 0.01$ for $K < 0.17$ is suggested as an alternative, and in general this yields good agreement with experimental results, though, as it has been shown this approach may have overestimate the overall collision efficiency. As was discussed, the reason for this overestimation is primarily due to potential flow approximation, flow disturbances (Yoon and Ettema, 1993) and constraint of $E = 0.01$ for $K \leq 0.17$.

The numerical results obtained with modern CFD software show good potential of modeling in-cloud icing at low values of K, with possible exception of extremely low values of K, granted if the full droplet distribution spectrum is used in the simulations. The results with the MVD approximation for those cases show even lower values than analytical parameterizations, which already tend to underestimate the overall collision efficiency values. Moreover, the CFD results tend to produce lower values than analytical parameterizations for all tested droplet size parameters, namely MVD, VWD and spectrum-averaged values, however, again, this comes to usage of potential flow theory in analytical parameterizations over viscous flow in CFD results, and the results are in line with experimental observations of (Yoon and Ettema, 1993). Alternatively, the history term can be included in CFD simulations, as it has been shown to produce excellent agreement with experimental results (Makkonen et al., 2018).

If actual droplet distribution spectrum is not available, it is recommended to carry out the analysis using Langmuir distributions, such as widely used Langmuir D distribution and to check the results against different Langmuir distributions and Makkonen two-point approximation in order to obtain rough estimate of overall collision efficiency. While Volume Weighted Diameter (VWD) concept also aims to solve the issue of underestimating the overall collision efficiency at low values of K, in order to use it the full droplet distribution spectrum should be known, at which case the spectrum-averaging using the full droplet distribution spectrum may produce better results.

3.4.2 Droplet distribution spectrum effects on dry ice growth on cylinders

Within the scope of this paper a detailed analytical study along with a series of numerical simulations were performed for experimental data of ice accretion on a 30 mm circular cylinder. Results show that the droplet distribution spectrum change has a significant effect on the overall and local collision efficiencies, maximum impingement angles, droplet impact velocities, ice densities and ice mass accretion. The associated changes in the results are significant enough to cause the theory to either underestimate, be within the margin of error, or significantly overestimate experimental results, depending on the droplet distribution chosen. Moreover, the numerical and analytical results tend to have some differences in the results, with tendency towards better agreement in the results of wider distributions with higher value of inertia parameter. This shows that care is needed when dealing with droplet distributions even with matching MVDs as those distributions do not have the same value of droplet inertia parameter. The reported results are deemed valid for low values of droplet inertia parameter *K*.

Some of those differences can be explained using viscous, boundary layer and surface roughness effects, however, due to limitations of existing theory, in particular, when it comes to the inviscid flow assumption of the ISO model, further investigation in those aspects necessitates more experimental evidence in carefully controlled conditions, as it has been shown how a change in droplet distribution spectrum affects ice accretion on the cylinders, at lower values of droplet inertia. Overall, the further experimental, analytical and numerical investigations into those aspects at lower values of the droplet inertia parameter are deemed necessary in order to expand the understanding of connected terms on ice accretion process and performance of current icing theory in cases with low values of droplet inertia parameter. Out of those, the CFD simulations show good results for the low values of *K*, and as it has been shown in this work, allow for studying the variety of different parameters and their effect on the ice accretion process. For the low values of *K*, which correspond to the values of *E* being 0.10 or less the usage of the full droplet spectrum is recommended in calculations. In addition, based on the results of this and previous works the Langmuir D distribution is recommended as a first guess distribution.

Summarizing, the numerical model results produce the best agreement with the experimental results for narrower distributions B – E, while wider distributions tend to overestimate the accreted ice values. The analytical results tend to match experimental results well for distributions B – D, however, in general they tend to overestimate the accreted ice more than the numerical results, in particular for wider distributions F – J, however, this property can be exploited in the extreme value analysis of the icing events and ice maps generation.

3.4.3 An investigation into empirical ice density formulations for dry ice growth on cylinders

In this paper the investigation into several empirical accreted ice density formulations have been conducted, with the main goal of assessing how well the empirical formulations can capture the accreted ice thicknesses. The practical purpose of it is to use the accreted ice thickness as a sort of icing severity estimate in modeling of the long-term icing events, if the accreted ice mass is an unknown value. The icing modeling in this study was done by using both the analytical modeling and the CFD simulations,

in order to compare two most likely approaches of the modeling of the long term icing events. The obtained icing thicknesses were than compared to experimentally measured values.

The obtained results show that both the analytical and the numerical models can adequately estimate end iced cylinder diameters for majority of the tested cylinder diameters in this study. In particular, while the Makkonen and Stallabrass empirical icing density formulation tends to have good agreement with the smaller cylinder configuration, it tends to underestimate the icing thicknesses for the larger cylinder configuration. On the other hand, the Jones formulations show consistently better results for almost all tested cases, and especially, for the larger cylinder configuration. However, all formulations tend to underestimate the icing thicknesses for the largest cylinders, 249 and 298 mm in diameter.

These results were obtained using the full droplet distribution spectrum from the Cranfield University icing tunnel. In order to keep the results consistent with the framework of ISO 12494 icing theory, the matching set of values, using the monodisperse droplet distribution with the equivalent value of the MVD was obtained. The results with the MVD approximation show good agreement mainly for smaller cylinder configuration, 20 – 80 mm in diameter, and the agreement for the larger cylinder diameter is unsatisfactory, primarily due to low values of droplet inertia parameter *K* for these cases, which puts the results using the MVD approximation outside of the verified range of the current icing theory. Thus, calculations with the full droplet distribution spectrum are recommended. Summarizing the findings of the validation section, both tested formulations based on Macklin parameter, i.e., the numerical fit by Makkonen and Stallabrass, and the intermediate version of Jones formulation have showed better agreement than the final version of Jones formulation, however, as noted in the original work (Jones, 1990) there are several reasons for this discrepancy.

3.4.4 Accreted ice mass ratio (k–factor) for rotating wind turbine blade profile and circular cylinder

In this paper the investigation into *k*–factor, describing the ratio of ice accretion on reference collector and wind turbine blade has been carried out by performing a series of numerical simulations using modern CFD software and analytical calculations within the framework of the existing ice accretion theory (ISO 12494, 2001). The results show that *k*–factor is not equal to the constant value of $k = 20$, contrary to currently postulated assumption, and it can vary to a significant degree, depending on a number of different parameters not accounted in present model for it. These factors include the effect of object's geometry on ice accretion, droplet overall collision efficiencies, droplet distribution spectrum and median volume diameter under significantly different ambient conditions, pertaining to wind speed and tip speed ratios experienced by both the reference collector and wind turbine blade. While the results presented in this paper can be considered somewhat simplistic, the explanation of *k*–factor variance is established based on effects of MVD, droplet distribution spectrum, tip speed ratios and geometry effects. However, further numerical experimentations and experimental validation are necessary, in particular, when it comes to the ice accretions on different airfoils under different operating conditions. Despite this, the obtained results still show the shortcomings of current implementation for empirical *k*–factor ratio and as a result modifications and improvements for this ratio are needed. Considering the complexity of the process in question, there is a significant chance that ice accretion on a wind turbine, when compared to ice accretion of reference collector cannot be explained using simple, constant, dimensionless ratio.

3.4.5 Modeling of dry ice accretion on cylinders – a case study of present analytical state

In this work the detailed comparison between the "spectrum-averaging" procedure and the Volume Weighted Diameter (VWD) has been performed for the wide range of cylinder diameters in order to test the applicability and performance of both concepts over a wide range of values of the droplet inertia parameter K. Results show that for the value of $K > 0.5$ both approaches tend to be in good agreement with each other and the experimental results, however, for the very high values of $K > 1.5$, the behavior of VWD approximation does not change in the same vein as with the spectrum-averaged values. In general, for the values of $K > 0.5$ the VWD approximation is very sensitive towards the source distribution(s). For the range of the values of K corresponding to $0.3 < K < 0.5$, the agreement between spectrum-averaged results and the VWD approximation is somewhat worse and depends, in large, on the source distribution(s) used, with wider distributions producing worse agreement. Finally, for the values of $K < 0.25$, the VWD approximation produces significantly lower values of the overall collision efficiencies, albeit, still higher than the MVD approximation, which can potentially be detrimental in designing for and estimating icing loads in such conditions, such as, long-term accretion of power lines, power line and communication towers etc.

Fundamentally, while VWD approximation does alleviate some issues of the MVD approximation, for the low values of K, such as $K < 0.25$, it does not achieve much added performance when it comes to estimating the overall collision efficiencies, while, simultaneously, and, on the other hand, for the very high values of K it can overestimate the overall collision efficiency. Ultimately, its lesser complexity when compared to the spectrum-averaging does not warrant the use in these sort of conditions, while for higher values of K, i.e., $0.3 < K < 0.7$ its usage may be warranted over the MVD approximation to produce higher estimates of the overall collision efficiency.

3.4.6 Aerodynamic forces on iced cylinder for dry ice accretion – A numerical study

Within the scope of this work numerous CFD simulations of the atmospheric ice accretion and the transient airflow behavior over iced cylinder with different angles of attack were performed. The objective was to investigate how the commonly postulated assumption of slow, continuous rotation on a reference collector and/or power line (ISO 12494, 2001;Makkonen, 1984) compares with non-rotating iced cylinder at different angles of attack, which is deemed to be representative of very slow and/or spontaneous rotation. For the basis of comparison several flow parameters have been chosen in order to ascertain similarity, namely, ice shapes, maximum ice thicknesses and iced areas, accreted ice mass, ice densities, overall collision efficiencies, drag, lift and moment coefficients, pressure and viscous force, velocity magnitudes and pressure distributions.

The obtained results compare favorably for the hypothesis of rotating cylinder being "equivalent" to the series of non-rotating cylinder at different angles of attack. In particular, the results tend to agree very well for the comparison of ice accretion parameters, where all cases, with the exception of the 90° angle of attack case, compare well to the rotating cylinder benchmark. The discrepancy in the 90° AOA case can be explained by the deficiencies in the numerical setup.

The comparison of the aerodynamic forces suggests that the benchmark cases of rotating and uniced cylinders, do have "similar" aerodynamic loads when compared to the "averaged" AOA simulations results, namely, when it comes to the values of total pressure and viscous force, which for the "averaged" case matches the rotating one within the rounding error. However, on individual basis the difference in the airflow regime between AOA cases and the benchmark cases can be significant, particularly, if checking the instantaneous values for the velocity magnitudes and pressure distributions in the transient airflow separation. In particular, the results from small AOA simulations (0° and 30°) show that the cylinder is less aerodynamically loaded than the benchmark cases. On the other hand, the results from simulations at large AOA (60°and 90°) produced "expected" results, as the cylinder in these configurations is significantly more aerodynamically loaded than the reference cases. However, as it was discussed previously, given sufficient enough time frame for continued ice accretion, the gravity force, exerted by the accreted ice deposit, will, eventually, be the dominating force, however, the exact situation will depend on the operating conditions and the shape of the developing ice deposit.

The comparison of the results from this work with the results of numerical simulations of (Keyhan, 2012) and experimental data of (Demartino et al., 2013) shows good agreement, where applicable, however, one apparent trend in both (Keyhan, 2012) and (Demartino et al., 2013) is that the resultant aerodynamic loads are not only a function of Reynolds number but the accreted ice shape as well.

3.4.7 Study of dry ice growth on duplex cylinders

Within this work a series of CFD simulations have been performed on the bundled cylinders under the dry ice growth regime. The primary interest of modeling of such geometric configurations comes from the need of modeling the ice accretion on bundled conductors on the power lines. First, is to "fill the gaps" in the works of (Wagner, 2010) and (Qing et al., 2018), mostly, in an attempt to "expand" the work by (Wagner, 2010), by presenting the accreted ice mass ratios for the simulations within this study, in attempt to further quantify the "partial ice accretion on downstream conductor" statement. Second, is to ascertain the viability of the commercial CFD package in the modeling of the dry ice accretion on the bundled conductor, as opposed to creating the in-house code. If such ice accretions can be viably modeled by a commercial CFD software, then it would be readily possible to extend this work further, in an attempt to produce the accreted ice masses ratio between the windward and the leeward conductor as a function of the operating conditions.

For this purpose, a circular cylinder is considered an acceptable approximation. The performed simulations cover a wide range of possible icing conditions by varying the operating wind speed, from 4 to 20 m/s and MVDs from 15 to 40 μm respectively. The obtained results for the 0° angle of incidence show that the overall collision efficiencies and accreted ice mass ratios between the leeward and the windward cylinders varies from ≈100% to ≈30%. This ratio decreases with the increase in the values of the operating wind speed and/or median volume diameter. This can be explained by the increase in the droplet inertia, corresponding to the increase of droplet inertia parameter *K*, as a function of droplet size and wind speed. Specifically, with the increase in the operating wind speed, the droplets have less "window time" to adapt to the flow conditions past the windward conductor and move into a trajectory which allows a collision with the leeward cylinder.

For the comparison with the experimental data, the CFD simulations have a good agreement in terms of the accreted ice masses ratio for the 4 and 7 m/s wind speed conditions; acceptable agreement at 10 m/s wind speed, and rather poor agreement at 20 m/s. The latter is believed to be primarily the factor of the changes in the wake behavior at this wind speed, with the significant vortex shedding present. As a result, a significant portion of the droplets is entrained in the vortices. Overall, the CFD simulations tend to underestimate the accreted ice masses in the experiment, to an extent, particularly, for the monodispersed distribution, and the monodispersed distribution consistently shows the higher ratio of the accreted ice masses. This "feature" is believed to be again the primary impact of the droplet inertia parameter K on the accreted ice masses ratio. For full droplet distribution spectrum, the "spectrum-average" results depend significantly on the larger droplets in the spectrum, which, by the nature of them being of the larger diameter, have higher value of K, when compared to the rest of the droplet sizes and/or the monodispersed distribution. The monodispersed distribution, featuring only one droplet size, is lacking this "feature".

For a case of bundled cylinders at 10 m/s wind speed and 20 μm MVD, the angle of incidence was varied from 0° to 15°, and angles corresponding to the vertical separations being equal to one cylinder radius and one and two cylinder diameters, respectively. This was primarily done in order to ascertain the effects of an angle and potential sag, due to accreted ice on the power line. For the cases with non-zero angle of incidence, the simulated overall collision efficiencies and accreted ice masses are approximately equal, with the leeward cylinder accreting slightly more ice, as soon as the angle of incidence is large enough to introduce a vertical separation equal or greater of one cylinder diameter. This can be explained by leeward cylinder being no longer "shielded" by the windward one and thus the effects of perturbed airflow past the windward cylinder are no longer significantly affect the leeward cylinder. In such cases it is deemed possible to model the resulting ice accretion on the bundled cylinders using simplex configuration and ISO 12494 analytical modeling framework.

4 Conclusions and Future Work

This thesis within the programme of Engineering Science at the UiT – The Arctic University of Norway concerns itself with the in-cloud atmospheric icing accretion on the circular cylinders for the "dry growth" conditions. The study of the atmospheric ice accretion has attracted some attention from the scientific community prior, with the available knowledge spanning from the works of the Langmuir and Blodgett (1946) on the Mt. Washington Observatory till the analytical parameterization of the Finstad et al. (1988), with the latter being the current analytical benchmark and the integral part of the ISO 12494 "*Atmospheric Icing on Structures*", which serves as a current guideline for the analytical estimation of the ice loads on structures. A detailed literature review of the present and past analytical parameterizations of the analytical parameterizations of the in-cloud impingement on cylinders is carried out as a part of this thesis.

As a result, based on the findings within this work, some potential changes and modifications to the existing analytical framework have been carried out within the scope of this work, with the primary aim of application for the analytical modeling of the in-cloud impingement on the circular cylinders for the low values of the droplet inertia parameter K. The proposed changes do show some promise in the modeling of the atmospheric ice accretion for such cases, when compared to the existing analytical framework of the ISO 12494 standard. In addition, the usage of modern, commercial CFD tools have been employed in order to investigate the suitability of these tools for the modeling of atmospheric ice accretions for the low values of K. While there can be some potential limitations to those, as was discussed within the framework of this work, the usage of the CFD tools is deemed promising. The primary achievement of this work is the introduction of the spectrum-weighted calculations using the Langmuir distributions. The usage of the spectrum-weighted calculations and the Langmuir distributions are deemed to be sufficient, at this stage, to "overcome" the issues with the underestimation of the overall collsion efficiencies in the rnage of $K \leq 0.25$, although the employed constraint in the analytical calculations of $X(K, \phi) = 0.01$ for $K \leq 0.17$ can result in the overestimation of the accreted ice masses in the extreme cases.

4.1 Concluding remarks

Based on the available knowledge, one of the major limitations of the Finstad et al. parameterization is its applicability for the range of the overall collision efficiencies of $0.07 < E < 0.63$, resulting from the experimental verification of parameterization by Makkonen and Stallabrass (1987). Furthermore, ISO 12494 standard states that the current model underestimates the accreted ice masses for the collision efficiencies values below $E < 0.10$ and the Finstad et al. themselves postulate that they consider the lower limit of droplet inertia parameter being $K = 0.25$ in their model, below which Finstad et al. advise to "*recalculate the droplet trajectories using the appropriate drag coefficients for each droplet size in the spectra*". As evidenced by the available data from the test span measurements at the Ålvikfjellet test span in Norway, the majority of the extreme ice loads occur for the value of K below the critical value of 0.25. Thus, there is a need for a method which allows for better prediction and estimation of ice loads for such conditions, with one of the primary applications being modeling of extreme value loads on the overhead power lines for the purposes of the ice maps generation and ice load guidelines.

However, when considering the statement of Finstad et al. regarding calculation of the droplet trajectories using the appropriate drag terms in the analytical calculations, one term in the droplet's equations of motions becomes an issue. This term, known as the "history" term (or the Basset force), which is a non-steady state drag coefficient, which needs, ideally, to be taken into account in the modeling of the atmospheric ice accretion for the cases when $K < 0.25$, poses some challenges in the handling and approximation of it in the analytical calculations. This term depends on the previous positions, velocities and accelerations of the inflowing particle (hence why it is called the "history" term), thus necessitating the evaluation of these. In addition, in the "classical" formulation this term is singular under the integration.

However, instead of the evaluating and approximating this term the other potential solution, which involves the usage of the "idealized" Langmuir distributions is suggested, those originally proposed by (Langmuir and Blodgett, 1946) and (Howe, 1990). Those distributions have the same values of the MVD as the typically postulated assumption of the monodispersed distribution from the ISO 12494, which makes them suitable under the framework. One major advantage of using the Langmuir distributions is that they effectively have a higher value of the droplet inertia parameter *K*, due to the nature of the "spectrum-averaging" procedure, when compared to the simple monodispersed distribution, while maintaining all other parameters, primarily the MVD and the LWC constant.

Within the scope of this work this analytical calculation procedure, using the Langmuir distribution spectra for both the analytical formulae of (Finstad et al., 1988) and the (Finstad, 1986) droplet trajectory equations is presented. The usage of the Langmuir distributions is primarily proposed to be "easier to use" alternative to the trajectory calculations, thus simplifying the calculations in such applications, for example, as ice load maps generation and the extreme value analysis, thus enabling one to perform these in more efficient manner, at least when it comes to the needed time and computations. The "spectrum-averaging" analytical calculation procedure is the major contribution of this work.

The performed validation of the modified calculation procedure was done using both the original (Makkonen and Stallabrass, 1984) data and the FRonTLINES ("Frost and rime icing impact on overhead transmission lines") project, with the experimental data of latter dealing almost exclusively for the dry ice growth accretions for the limit of $K \leq 0.25$. The obtained results, using both the analytical and the numerical tools, indicate that the usage of the Langmuir droplet distribution spectra can result in large variance of the overall collision efficiencies and, as a result, the accreted ice masses, even under the same operating conditions, due to the way the distributions change the value of the droplet inertia parameter *K*.

The conducted analytical and numerical calculations along with analysis of the available experimental data suggest that the Langmuir distributions C and D are consistently good in estimation of both the Makkonen and Stallabrass and the FRonTLINES experimental data. In addition, the available experimental distribution for the FRoNTLINES test cases has a tendency of slight overestimation of the results for the overall collision efficiencies and the accreted ice masses using the analytical calculations. The reason for this is believed to primarily be the constraining the cloud impingement parameters to 0.01 for the values of $K < 0.17$, with this constraint being used following the recommendations of (Finstad et al., 1988). While this constraint allows analytical model to predict non-zero ice masses under

any arbitrary conditions, it can result in the overestimation of the accreted ice masses, however, it may not be sufficiently detrimental for the purposes of the extreme value analysis.

For the CFD calculations of the same results the absolute error is approximately 0.01, while using the experimental distribution, and Langmuir C and D distributions yield very close agreement with the obtained results. Overall, the numerical simulations are well suited for the detailed studies of the droplet distribution spectrum effects and the ice accretion modeling in general, as multiple different cloud impingement parameters can be investigated and compared in detailed manner, which is not possible using the current analytical approach. In addition, the usage of the Langmuir D distribution as a sort of a "first guess" distribution is recommended, as it is typically and successfully employed for aircraft icing studies (Bidwell, 2012;Papadakis et. al, 2007;Wright, 2008). However, other factors, not accounted in the analytical part for in this work, such as surface roughness, sublimation and deposition, viscous and boundary layer effects may become prominent in cases where the droplet inertia parameter is sufficiently low, although modern CFD tools might be able to capture those.

While performing analytical calculations for the FRonTLINES experiments, it was noted that the empirical icing density parameterization used (Makkonen and Sallabrass fit to the Macklin equation) resulted in the end cylinder diameters to be a fraction of a millimeter larger than the initial, uniced cylinder diameters, while the accreted ice densities were in the "expected range" based on the ISO 12494 classification of those. The analytical calculations using the same empirical icing density parameterization against the original data (that being Makkonen and Stallabrass experiments) showed that the end cylinder diameter values calculated using the analytical model match experimental results well, while the accreted ice density is underestimated slightly. These results necessitated the investigation into the available empirical icing density parameterizations.

The obtained results suggest that there are fundamental limitations with the empirical icing density parameterizations based on the so-called Macklin parameter, in the analytical calculations as the obtained results with it for the low values of K ($K \approx 0.25$) show that the end cylinder diameters barely change from the initial ones, while the density values quickly reach the lower constraint of the 100 kg/m^3 employed in the analytical calculations. Based on the available experimental evidence, using the FRonTLINES data and the data from the Cranfield University, experiments show that this primarily happens when the accreted ice shapes on the rotating cylinders are no longer can be considered to be a "uniform ice layers", meaning that instead of such a layer, large individual beads are present, as is the case with the accreted ice shapes, obtained in the FRonTLINES experiments. For such cases, the existing empirical icing density models which expect the formation of the "uniform ice layer" may not be applicable. This is another important finding of this work.

Based on the conducted analysis with the Langmuir droplet distribution spectra, some possible applications and comparisons of the methodology presented within this work are discussed. First, the comparison with other recent advances in the field of the analytical modeling of the atmospheric ice accretion on structures is performed – namely, the comparison with the Volume Weighted Diameter (VWD) approach by the (Zhang et al., 2018). The results of comparison suggest that the methodology, derived within this work compares favorably to the available experimental evidence when compared to the VWD approximation.

Moreover, since the presented methodology is not only applicable to the power line conductors alone and it can be extended to any structure which characteristic length can be reasonably approximated by a circular cylinder, another possible application is demonstrated – the investigation into the empirical *k*–factor for the ice accretion on the wind turbines, postulated by (Turkia et al., 2013), which relates the icing on the wind turbine blade to the reference collector from the ISO 12494 standard as a constant factor $k = 20$. The results, obtained in this work, show that the *k*–factor does not equal to the constant value $k = 20$ and can vary to a significant degree.

Furthermore, modern CFD tools allow for the in-depth investigation of the multiphase flow behavior. This advantage allows for the modeling of the atmospheric ice accretions and the connected phenomena, which would not be possible using the current existing analytical framework. These applications are namely being the modeling of the (unsteady) aerodynamic forces, acting on the iced cylinders and the study of the dry ice accretion on the bundled (duplex) cylinder configuration. There is a practical need in better understanding how to model such atmospheric ice accretions, for example – it is widely known that significant number of ice accretion events in nature on the overhead transmission lines results in the circularly shaped ice accretion, yet the precise mechanism behind those is not precisely known. It is postulated by (Makkonen, 1984) that this is a result of the limited torsional stiffness of the conductor and the gravitational force, acting on the (iced) conductor. Modeling of the ice accretion on the bundled conductors, is also of importance, as a significant portion of the overhead transmission bundles is arranged in the bundled configuration with different geometric properties, such as vertical and horizontal separations, number of conductors in the bundle, conductor diameters etc. The applications of the modern CFD tools to such applications are presented and discussed in this thesis.

Lastly, some potential applications of the current methodology are presented within the scope of the modeling of the icing intensities and extreme ice loads on the overhead transmission lines following the available data from the Ålvikfjellet test span.

4.2 Future work

Unfortunately, it is not possible to cover all existing questions under the scope of one work and thus there are existing knowledge gaps.

4.2.1 The history term

The primary of these, being the challenges associated with the "history" term and the need to incorporate it in the analytical and the numerical calculations. As was mentioned before, this term is singular under integration and thus numerical schemes need to be employed in order to evaluate it. Furthermore, the term itself is rather cumbersome to calculate, even if these schemes are employed.

For example, when it comes to the droplet trajectory calculations, using the Equation (1.10) one problem in approach of (Oleskiw, 1982) is apparent. Oleskiw uses the Lagrange polynomials in order to approximate the effect of history term, however, the exact form of calculation methodology is not clearly defined in (Oleskiw, 1982), thus making it difficult to implement. On the other hand, the problem of estimating the "history term", is not only limited to the field of atmospheric icing, and extends to the multiphase flows in general. Therefore, significant amount of knowledge has been accumulated on the

problem. Following the (Moreno-Casas and Bombardelli, 2015) the methods of approximating the "history terms" can be broadly classified as follows:

- Modifying the kernel in the history term in the Equation (1.10) in order to avoid singularity and make it applicable to use with finite Reynolds number (Mei and Adrian, 1992).
- Numerical approximations to the history term, such as open-quadrature formulas, semi-derivative approaches, trapezoidal-based methods, etc. (van Hinsberg et al., 2011).
- Transforming the droplet trajectory equation, given in the Equation (1.10) into higher-order Ordinary Differential Equation (ODE), explicit in velocity (Michaeldis, 1992;Vojir and Michaelides, 1993).

In the current work, the issue with the calculation of the "history" term has been "avoided" by using the Langmuir spectra and the use of the constraint for the in-cloud impingement parameters of $X(K, \phi) = 0.01$ for $K \leq 0.17$. However, for "physical" reasons a better "parameterization" of this term is necessary, possibly with the implementation of "cascading" constraint (meaning multiple threshold values) instead of one singular value of $X(K, \phi) = 0.01$ for $K \leq 0.17$. Furthermore, as was discussed, the existing 3D CFD solvers, such as FENSAP–ICE, operating using the Eulerian formulation, do not take this term into account, though it may be possible to incorporate it using User Defined Functions (UDF). Further investigations into this are warranted, provided there exists more experimental data points for validation of such concepts, as the current experimental data for the ice accretions in the range of $K \leq 0.25$ to the best of the author's knowledge is limited to the FRonTLINES experimental cases.

4.2.2 Other important questions

Furthermore, current existing analytical icing models only cover the impingement of the supercooled water droplets on the structures, and thus limited to ice accretion only. As evidenced by the available data on the Ålvikfjellet test span periods of ice accretions are followed by ice shedding and ablation on the test span, yet no model, including the one in this work, takes shedding and/or ablation into the account. This may be of importance for the application purposes of the transmission tower design, estimating ice loads and extreme value analysis. In addition, the effects of sublimation, deposition and the accreted ice surface roughness, where roughness elements may act as individual ice collectors and the effects of this roughness may play a role in the underestimation of the ice loads within the framework of the ISO 12494 (ISO 12494, ISO, 2001) for the cases with the values of the overall collision efficiencies $E < 0.10$. Again, the current model does not take these into the account, and, it may be challenging to take such effects into the account, for example if the iced surface roughness is large enough (of an order of a few percent of the uniced diameter) – one can ask what would be the calculation procedure/numerical simulation setup for modeling ice accretions under such conditions. And on the topic of the surface roughness – as it was shown in this work, *any* tested icing density formulation, based on the Macklin parameter, tends to fail to give an explanation for the accreted icing density on the largest cylinder diameters, thus suggesting that there is a fundamental limitation in the Macklin parameter. This limitation is theorized to be the result of the uniform ice layer failing to form under the given operating conditions and instead ice deposit is represented by the collection of the individual large beads. More information about such ice accretions and shapes is needed to either confirm or deny this hypothesis, and if necessary – develop a new empirical icing density parameterization, aimed at providing "reasonable" accreted icing densities estimates under extreme operating conditions.

Moreover, there is a need to better understand the underlying mechanics behind the ice accretions on the power lines for the cases of circular ice shapes, caused by the conductor rotation and the ice accretion and shedding on the bundled conductors. While the hypothesis of (Makkonen, 1984) regarding slow conductor rotation under the influence of the limited torsional stiffness and gravity was tested, to a degree, in this work (by studying the forces acting on the iced conductor, disregarding its torsional stiffness) the understanding of these mechanical factors, primarily – the values and effects of the torsional stiffness needs to be better ascertained. In addition, one cannot simply disregard possible influences from the vibrational motion of the conductor, under the influence of the cross-wind, including its torsional motion and galloping. In the author's opinion there is limited knowledge regarding this topic is available, especially for the iced conductors.

The effects of (vibrational) motion and torsional stiffness of the iced conductors in a bundle may affect the ice accretions in such cases, if the mentioned motion causes the bundle configuration to (frequently) change its geometrical properties. This may affect the accreted ice masses on the individual conductors in the bundle, and thus presents a challenge for the purposes of the estimation of the design loads. While some numerical simulations have been carried out with regards to dry ice growth on the bundled conductors in this work, they only cover a limited amount of operating conditions and configurations. Therefore, more work is needed within this topic.

Finally, as was discussed within this work, there are limitations in the existing analytical icing framework, resulting from the usage of the inviscid, potential flow approximation in it. Such approximations make the existing framework largely applicable to the circular shapes only; they completely disregard any potential viscous effects in the flow, by the nature of being inviscid, and cannot be used for the analytical estimation of the aerodynamic forces acting on conductor. Thus, there may be a need to develop a completely new analytical parameterization of the ice accretion on structures, which is based on the more "physically complete" models than the potential and the inviscid flow approximation, used currently. Such models may address the issues of the underestimation of the accreted ice loads for the values of the overall collision efficiencies below $E < 0.10$ and the limitation of the droplet inertia parameter $K \leq 0.25$ in a more efficient way. However, implementing the analytical calculation procedure using the Navier-Stokes equation (for the airflow solution) and the Maxey-Riley equation (for the droplet motion; Maxey and Riley, 1983) may be (very) challenging. Therefore, questions about practical applications of such models and possible improvements and gains from implementing them remain open.

Paper 1. Analytical Parametrizations of Droplet Collision Efficiency on Cylinders – a Review Study

Pavlo Sokolov and Muhammad Shakeel Virk

Cold Regions Science and Technology, 2018, Volume 155. pp. 119 – 127.

DOI: 10.1016/j.coldregions.2018.08.015

Author's Contribution

Pavlo Sokolov has contributed substantially in the proposal of research idea, literature review, modelling, computing, analytical and numerical analysis, and writing of the paper.

Analytical Parametrizations of Droplet Collision Efficiency on Cylinders – a Review Study

Sokolov Pavlo*, Muhammad Shakeel Virk

Institute of Industrial Technology

University of Tromsø – The Arctic University of Norway,

*Email: pavlo.sokolov@uit.no

Abstract

Within the scope of this work several major ice accretion parameterizations has been investigated, staring from original Langmuir and Blodgett work (Langmuir and Blodgett, 1946) on the water droplet trajectories, up to and including the Finstad et al., model (Finstad et al, 1988a) of overall collision efficiency, which is part of current governing ISO 12494 standard (ISO, 2001), thus covering a timeframe of several decades of investigations in icing modeling. This paper provides a general and mathematical review of those parameterizations, includes necessary formulae for calculations of droplet overall collision efficiency, starting with trajectory evaluation, and discuses underlying assumptions and approximations made by respective authors. This discussion might be of interest to icing modelers who wish to obtain more general understanding of icing modeling. As an application example, two experimental datasets have also been used for droplet overall collision efficiency calculations and comparison. These experiments span large amount of operating conditions, thus covering significant range of the droplet's inertia parameter range, *K*, and overall collision efficiency, *E*, values which should cover majority of possible icing conditions. The results show that for higher values of droplets inertia (K), the monodisperse distribution yields good agreement with the experimental values, however, with gradual decrease in values of droplet's inertia parameter, the MVD approximation tends to underestimate the overall collision efficiency when compared with the experimental and spectrum-averaged values. Moreover, for very low values of *K* and *E*, roughly corresponding to the limits provided in ISO 12494, the MVD approximation tends to underestimate the overall collision efficiency significantly. For those cases the recalculation of droplet trajectories using full spectrum is recommended. If actual droplet distribution spectrum is not available, it is recommended to carry out the analysis using Langmuir distributions, such as widely used 'Langmuir D' distribution (Wright, 2008), (Bidwell, 2012), (Papadakis et al., 2007).

Keywords: Droplet collision efficiency; MVD[1]; Cylinder diameter; Analytical; CFD; Experiment.

[1]Median Volume Diameter

1 Introduction

Atmospheric icing of structures, is a hazardous phenomenon which may lead to undesirable effects.

To properly estimate the potential hazards of atmospheric icing, a good understating of ice accretion process is needed. Presently, the aggregated knowledge on modeling of atmospheric icing and its effects is governed by ISO standard, ISO 12494 *"Atmospheric Icing of Structures"*. Most importantly, the main equation in the icing modeling, which describes the rate of icing per unit time is given as (ISO, 2001):

$$\frac{\mathrm{d}m}{\mathrm{dt}} = \alpha_1 \alpha_2 \alpha_3 wAv \tag{1}$$

In this equation, otherwise known as "Makkonen model" (Makkonen, 2000), A is the cross-sectional area of the object (*with respect to the direction of the particle velocity vector v*), α_1 (also referred as E in literature) is the collision efficiency, α_2 is the sticking efficiency, α_3 is the accretion efficiency. The correction factors α_1, α_2 and α_3 represent different processes that may reduce dm/dt from its maximum value wAv. These correction factors vary between 0 and 1.Factor α_1 represents the efficiency of collision of the droplets, i.e. is the ratio of the flux density of the droplets that hit the object to the maximum flux density, which is a product of the mass concentration of the droplets, w, and the velocity, v, of the droplets with respect to the object.

Consequently, the collision efficiency α_1 is reduced from one, because small droplets tend to follow the air streamlines and may be deflected from their path towards the object, as shown in Figure 1.

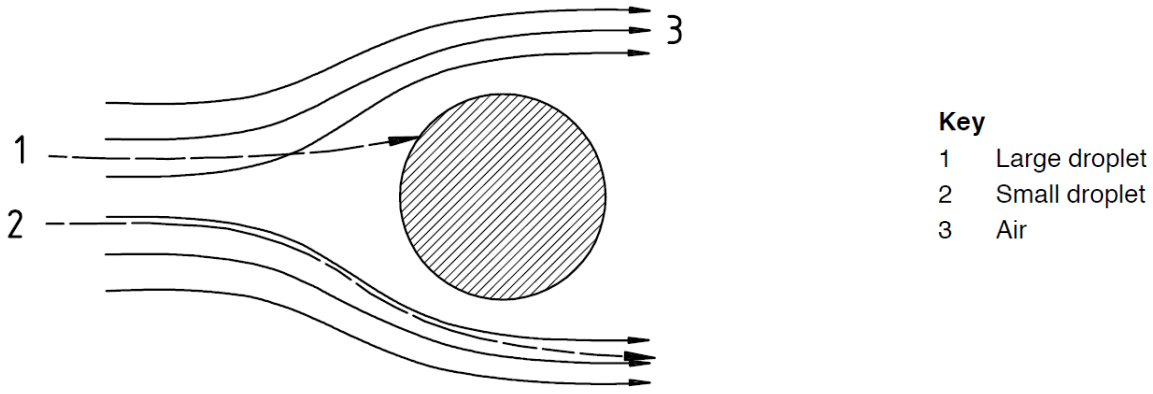

Figure 1 – Air streamlines & droplet trajectories around a cylindrical object (ISO, 2001).

In the broadest case of a given fluid flow, the "behavior" of water droplets can be explained using the definition of the Stokes number:

$$Stk = \frac{t_0 u}{L} \tag{2}$$

where L is the characteristic length of the obstacle and t_0 is the relaxation time of the particle, which describes its exponential velocity decay due to influence of drag and it is defined as:

$$t_0 = \frac{\rho_p d_p^2}{18\mu_f} \tag{3}$$

in which ρ_p is the particles density, d_p is the particle's diameter and μ_f is the absolute viscosity of the fluid. A particle with a low Stokes number follows fluid streamlines (*perfect advection*), while a particle with a large Stokes number is dominated by its inertia and continues along its initial trajectory, thus colliding with the object. As it can be seen from eqs. (2) and (3), larger particles, or those moving at higher velocities, will have higher Stokes number and thus – higher possibility of collision with the object, hence defining physical meaning of the collision efficiency.

However, in reality, the behavior of the droplet in actual flow is much more complicated than in this simplistic case, and the collision efficiency cannot simply be explained using just the definition of Stokes number, thus requiring the use of some sort of analytical and/or empirical formulations in order to calculate the overall collision efficiency. Presently, the overall collision efficiency formulation by Finstad et al. (Finstad et al., 1988a) is used in the ISO 12494 for calculation of α_1, which is itself based on the earlier parameterization by Langmuir and Blodgett (Langmuir and Blodgett, 1946).

While Finstad et al. model is the standard model in icing studies, based on the experimental results of (Makkonen and Stallabrass, 1987), arguments and comparison provided by (Finstad et al., 1988a), extensive work on "standard" icing model by (Makkonen, 2000), in which Finstad et al. parametrization is one of the core concepts, which ultimately led to its inclusion in governing ISO 12494 standard (ISO, 2001)he overview of other historical models, developed prior to it, might be useful for icing modelers, as majority of those models are based on similar concepts and share core assumptions, applications and limitations.

Broader understanding of those historical models as well as current model of Finstad et al might be useful in conducting experimental, numerical and analytical analyses, especially, when there is a need of modeling of ice accretion in extreme cases, close to the limits of applicability, as given in ISO 12494 (ISO, 2001) and therefore, the review study of said models is the main scope of this work. The analytical parameterizations being investigated within the scope of present study are the original Langmuir and Blodgett parameterization (Langmuir and Blodgett, 1946), as well as parameterizations derived by Cansdale and McNaughtan (Cansdale and McNaughtan, 1977), Stallabrass (Stallabrass, 1980), Lozowski et al. (Lozowski et al., 1983a), Makkonen (Makkonen, 1984), Finstad (Finstad, 1986) and its'presentversion by Finstad et al. (Finstad et al., 1988a).

2 Analytical Parameterizations of Droplet Collision Efficiency

The purpose of this subsection is to provide a brief overview of the droplet analytical collision efficiency parameterizations, which are within the scope of this study. Each model will be described briefly, in order to provide the general overview, such as, when the model in question was developed, what considerations the respective authors have been using, for what applications the model has been applied and what are the unique characteristics of it, etc. The proper references are provided in each respective paragraph, however, for brevity, the specific equations will be given later.

Langmuir and Blodgett (LB) parameterization (1946). The Langmuir and Blodgett research (Langmuir and Blodgett, 1946) was mostly aimed at estimating the water droplet trajectories moving past infinitely long circular cylinder for cases, where Stoke's law is not applicable. Langmuir and Blodgett used a General Electric developed analogue computer, called Differential Analyzer, to obtain the results for 61 droplet trajectories for the flow around cylinders, ribbons and spheres.

The Langmuir and Blodgett model is one of the more complete models featuring parameterizations for overall and stagnation line collision efficiencies, maximum impingement angle and droplet's impact velocity, along with correction of overall collision efficiencies for low values of overall collision efficiency and different parameterization schemes for higher overall collision efficiency $E > 0.5$.

Moreover, Langmuir and Blodgett produced a series of plots for droplets' inertia and Langmuir parameter, K, and ϕ respectively which may be used to obtain results graphically. The validation of results for cylinders was done in the original study, and it consisted of comparison with experimental data from Mt. Washington Observatory, obtained by few rotating cylinders, exposed to icing at various conditions (Langmuir and Blodgett, 1946), in addition to some experimental data, obtained by aircraft flying at 200 mph.

Lozowski et al. parameterization (1979). This parameterization is a part of the model, originally developed in 1979 by Lozowski, Stallabrass and Hearty (Lozowski et al., 1979), and published in 1983 (Lozowski et al., 1983a) for studying helicopter icing with inclusion of liquid water on the surface, known as “water runback” in it, due to the steady-state heat balance on the cylinder's surface, calculated using Messinger's thermodynamic model (Messinger, 1953), which is the main innovation of this model.

The parameterization of droplet trajectories is essentially similar to Langmuir and Blodgett approach, however slightly different empirical fit was used in order to avoid usage of Langmuir and Blodgett corrections for different ranges of overall collision efficiency E, thus attempting to use single parameterization scheme for entire range of E. Moreover, the model introduced an empirical formulation for local collision efficiencies β as function of impingement angle θ, which allows calculation of ice shapes, with limitation being constant ice density of $\rho = 890$ kg/m^3 being used in their model. The experimental verification of model for cases of ice accretion on cylinders have been conducted by Lozowski et al. (Lozowski et al., 1983b), the verification for aircraft icing have been done independently by Bain and Gayet (Bain and Gayet, 1982).

Additionally, in 1977 Cansdale and McNaughtan (Cansdale and McNaughtan, 1977) developed the icing model for similar applications, again, using slightly re-defined values of original Langmuir and Blodgett parameterization scheme for droplet collision efficiency, in order to collapse it to single curve for entire range of E, which also differs from parameterization values those of Lozowski et al. (Lozowski et al., 1983a). It is deemed appropriate to include both parameterizations in this study to observe the differences in droplet collision efficiency values between two similar models, developed roughly at the same time and for similar applications. However, Cansdale and McNaughtan model is more simplistic in its approach and only takes into account the flow near stagnation point.

Stallabrass parameterization (1980). This model was developed for studying icing of fishing trawlers (Stallabrass, 1980). The main difference in this model, when it comes to droplet collision efficiency

parameterization, is an attempt to eliminate the use of multiple curves and droplet trajectory equations altogether for estimation of overall collision efficiency, and collapse the parameterization to a single curve. As a result, the end formulae differs significantly from other models, which are based on derivation of original Langmuir and Blodgett formulations.

The Stallabrass model is also applicable to rectangular cross-sections, as opposed to previous models, which are only applicable to circular cross-sections. Model validation has been done in icing tunnel (Stallabrass, 1980), to demonstrate the effects of air temperature and cylinder diameter on ice formations, however, it should be noted that for icing trawlers the main ice accretion factor is expected to be sea spray, which can be characterized by large diameter of droplets. The heat balance calculation is also employed in this model, and it uses the Messinger thermodynamic model for calculation of steady-state heat balance.

Makkonen parameterization (1984). The Makkonen model was developed specifically for power cable icing (Lozowski and Makkonen, 2005). The model assumes cylinder being slowly rotating due to limited torsional stiffness, which results in uniform ice accumulation on the surface and no need for consideration of water runback. The model does not take into account such effects as maximum impingement angles or local collision efficiencies, thus being constrained to the flow near stagnation point, however, due to assumption of slow axial rotation this should not be a limitation, provided adequate time stepping is used in calculations.

Two major innovations of this model are, estimation of conductor's diameter change due to continuous ice accretion and introduction of variable ice density, using Macklin parameter (Macklin, 1962) in the ice density empirical formulation. Additionally, the model takes into account boundary layer effects of the cylinder in calculation of the heat transfer coefficient (Makkonen, 1985) in addition to employing Messinger model for heat balance calculation. Since the model is concerned with flow past stagnation line, the empirical parameterization follows that of Cansdale and McNaughtan, albeit with slightly different empirical fit and introduces separate two-point approximation of what Makkonen calls "real" collision efficiency, which is an attempt to collapse multiple curves of E for different droplet's sizes into one.

As noted in (Lozowski and Makkonen, 2005), the model received limited experimental validation due to strict requirements on quality of experimental data it enforces, however, in cases where it has been tested the agreement with experimental values was good.

Finstad parameterization (1986). The final parameterization approach is a parameterization developed by Finstad (Finstad, 1986). The key difference in this model is a revision of droplet trajectories on a more modern machine, with more modern estimates of droplet drag coefficient, from experimental study of (Beard and Pruppacher, 1969). Moreover, Finstad simplified the elaborate scheme of Langmuir and Blodgett when it comes to correction of droplet's inertia parameter, due to non-Stokesian flow regime, which resulted in completely different parameterization for droplet collision efficiency (Finstad et al., 1988a).

In addition, the model is one of the more complete models featuring parameterizations of local collision efficiencies, droplets impact velocities and maximum impingement angles. Furthermore, the model

provides the way of calculating the ice shapes on iced cylinder under assumption that developing ice layers will change the local collision efficiencies values and using variable ice density formulation of (Makkonen, 1984), however, those calculations are absent from final published version (Finstad et al., 1988a), which makes them somewhat preliminary in nature.

Finally, the model discusses more complete droplet trajectory equations, following approach of (Oleskiw, 1982), which may be useful when potential flow approximation is not valid and viscous and boundary layer effects may be of importance. The model validation for cylinders and airfoils was done as part of doctoral thesis itself (Finstad, 1986), subsequently, the validation for cylinders was independently carried out by Makkonen and Stallabrass (Makkonen and Stallabrass, 1987), who recommended employing it over original Langmuir and Blodgett formulations in future studies. At present, this parameterization is the benchmark for calculation of droplet collision efficiencies on cylinders and it is the integral part of governing ISO standard - ISO 12494 "*Atmospheric Icing of Structures*" (ISO, 2001).

2.1 Mathematical Overview

The mathematical overview of the presented parameterizations of droplet overall collision efficiencies will start with the trajectory equations of the water droplet in the potential flow, as all models, based on the original Langmuir and Blodgett model, use or assume the same trajectory equations. Those equations in dimensionless form are (Langmuir and Blodgett, 1946):

$$Kv_x \frac{\mathrm{d}v_x}{\mathrm{d}s} = (C_D Re/24)(v_x - u_x) \tag{4}$$

$$Kv_y \frac{\mathrm{d}v_y}{\mathrm{d}y} = -(C_D Re/24)\left(v_y - u_y\right) \tag{5}$$

$$\mathrm{d}x/\mathrm{d}t = -v_x \tag{6}$$

$$\mathrm{d}y/\mathrm{d}t = v_y \tag{7}$$

$$(Re/Re_\infty)^2 = (v_x - u_x)^2 + \left(v_y - u_y\right)^2 \tag{8}$$

where the air velocity components for the potential flow around cylindrical objects are given as:

$$u_x = 1 + \left(y^2 - x^2\right)/\left(x^2 + y^2\right)^2 \tag{9}$$

$$u_y = 2xy/\left(x^2 + y^2\right)^2 \tag{10}$$

In the equations above, x and y are horizontal and vertical distances respectively, with origin taken from cylinder axis, where radius is equal to unity, quantities v_x and v_y denote horizontal and vertical component respectively of droplet velocity, u_x and u_y are horizontal and vertical component of air velocity respectively, Re_∞ denotes droplets Reynolds number at freestream velocity, ($C_D Re$/24) is the

droplet drag coefficient, which is equal to unity, if Stokes law is obeyed, and greater than unity otherwise, and finally, K is the droplet's inertia parameter, defined as:

$$K = \frac{2\rho_p r_p^2 u}{9\mu_f C} = \frac{\rho_p d_p^2 u}{18\mu_f C} \tag{11}$$

In which C is the characteristic length of the object, in case of cylinder $C = R$, where R is the cylinder radius. The droplet inertia parameter, K, can be recognized as the Stokes number from eq. (3), and, furthermore, with some manipulation it can be re-written as:

$$K = \frac{\rho_p d_p^2 u}{18\mu_f C} = \frac{t_0 u}{L} = \frac{\lambda_s}{L} \tag{12}$$

The quantity $\lambda_s = t_0 u$ can be interpreted as the droplet's "range", i.e., the range which the droplet of the size d_p, released as projectile in the still air at velocity u would have before coming to rest, assuming Stokes' law is valid. If the Stokes flow is not valid, i.e., $(C_D Re/24) > 1$, the definition of the range parameter would not be valid, as higher droplet drag in ultra-Stokesian regime would reduce the actual value of droplet's range λ from that of λ_s for the case when Stokes' law is being valid. Therefore, a non-Stokesian drag correction factor has to be introduced, defined as "range parameter" λ/λ_s in (Langmuir and Blodgett, 1946). Assuming Mach number much less than unity, the λ/λ_s ratio is calculated as:

$$\lambda/\lambda_s = \frac{1}{Re_\infty} \int_0^{Re_\infty} \frac{d\boldsymbol{Re}}{(C_D \boldsymbol{Re}/24)} \tag{13}$$

in which, the $(C_D \boldsymbol{Re}/24)$ is the droplet drag coefficient as function of Re, and the integration variable $\boldsymbol{Re}$ is taken as relative droplet's Reynolds number with respect to the freestream. In their work, Langmuir and Blodgett used following empirical fit for $(C_D Re/24)$:

$$(C_D Re/24) = 1 + 0.197 Re^{0.63} + 2.6\times10^{-4} Re^{1.38} \tag{14}$$

Having determined the λ/λ_s ratio, it is now possible to evaluate "modified" inertia parameter K_0 with the λ/λ_s ratio included. Following Langmuir and Blodgett approach this is done as:

$$K_0 = \left(\lambda/\lambda_s\right)\left(K - \frac{1}{8}\right) + \frac{1}{8} \tag{15}$$

which is used in all subsequent calculations in Langmuir and Blodgett model (Langmuir and Blodgett, 1946), and its derivatives in place of K. Upon closer inspection two potential issues are apparent.

First, is that the integral equation, from which the λ/λ_s ratio is obtained is not a straightforward calculation, usually requiring some approximations to it in order to be easily available, which may be valid only for certain ranges of droplet's Reynolds number Re. Some discussion about those approximations is given in, for example (Ruff, 1985), (Finstad, 1986) and (Anderson, 2004).

Second that any sort of relation obtained as a result from the λ/λ_s integral calculation is intrinsically bound to the approximation for droplet drag coefficient ($C_DRe/24$) used, and thus, in return, depends on accuracy of experimental data and fits to it. The change of droplet drag coefficient ($C_DRe/24$) parameterization was the major keystone of the (Finstad, 1986) and (Finstad et al., 1988a) works, which, in essence, are a repeat of Langmuir and Blodgett calculations on more modern machine and with updated droplet drag coefficient expressions. For comparison purposes, those expressions are given as in (Finstad, 1986):

$$(C_DRe/24) = 1 + 0.102Re^{0.955} \qquad \text{for } 0.2 \le Re \le 2.0$$

$$(C_DRe/24) = 1 + 0.115Re^{0.802} \qquad \text{for } 2.0 \le Re \le 21.0$$

$$(C_DRe/24) = 1 + 0.189Re^{0.632} \qquad \text{for } 21.0 \le Re \le 200.0$$

which is noticeably different from the empirical relation for ($C_DRe/24$) used by Langmuir and Blodgett, and, as a result, part of the reason why overall collision efficiency parameterization of Finstad et al., is markedly different from the rest of the models. Speaking about overall collision efficiency parameterizations, the overall collision efficiency parameterizations of the analytical models, discussed in previous subsection, are summarized in Table 1.

Table 1 – Parameterizations of droplet collision efficiency by different researchers (Finstad, 1986).

Author(s)	***K_0***	***Overall collision efficiency***	***Validity Range***
Finstad/ ISO	K	$E = A–0.028–C(B–0.0454)$	$K > 0.25$ $10^2 \le \phi \le 10^4$
Langmuir and Blodgett	$K_0 = 0.125 + \dfrac{K - 0.125}{1 + 0.0967Re^{0.6367}}$	$E = 0.466[\log_{10}(8K_0)]^2$	$0.125 < K_0 < 1.1$
		$E = \dfrac{K_0}{K_0 + \frac{\pi}{2}}$	$K_0 > 1.1$
		$E = \dfrac{K}{K + \frac{\pi}{2}0.112Re^{0.63} + 0.75\times10^{-4}Re^{1.38}}$	$E > 0.5$
Lozowski et al.	$K_0 = 0.125 + \dfrac{K - 0.125}{1 + 0.0967Re^{0.6367}}$	$E = 0.489[\log_{10}(8K_0)]^{1.978}$	$0.125 < K_0 < 0.9$
		$E = \dfrac{K_0}{K_0 + \frac{\pi}{2}}$	$K_0 > 0.9$
Cansdale and McNaughtan	$K_0 = \dfrac{K}{1 + 0.087Re^{0.76Re^{-0.027}}}$	$E = 0.53[\log_{10}(8K_0)]^{1.8}$	$0.125 < K_0 < 1.1$
		$E = \dfrac{K_0^{1.1}}{K_0^{1.1} + 1.223}$	$K_0 > 1.1$
Makkonen	$K_0 = \dfrac{K}{1 + 0.087Re^{0.76Re^{-0.027}}}$	$E_m = 0.5[\log_{10}(8K_0)]^{1.6}$	$0.125 < K_0 < 1.1$
		$E = \dfrac{K_0^{1.1}}{K_0^{1.1} + 1.426}$	$K_0 > 0.8$
Stallabrass	$\xi = v^{0.6}d^{1.6}\mathrm{D}^{-1}$	$E = 0$	$\xi < 3200$
		$E = \dfrac{\xi - 3200}{\xi - 27000}$	$\xi > 3200$

where approximations for the modified inertia parameter K_0 are as given by (Finstad, 1986), and constants *A*, *B*, and *C* are defined as:

$$A = 1.066K^{-0.00616}\exp(-1.103K^{-0.688}) \tag{16}$$

$$B = 3.641K^{-0.498}\exp(-1.497K^{-0.694}) \tag{17}$$

$$C = 0.00637(\phi - 100)^{0.381} \tag{18}$$

and ϕ is the dimensionless Langmuir parameter, sometimes also referred as impingement parameter and is given as:

$$\phi = \frac{Re^2}{K} \tag{19}$$

As it can be seen from Table 1, expectedly, different overall collision efficiency formulations have different parameterizations. However, it is interesting to note that models, which employ the same parameterization for modified inertia parameter K_0 has different parameterization expression for α_1, for example, parameterizations by Langmuir and Blodgett, compared to Lozowski et al., and Cansdale and McNaughtan compared to Makkonen. This can be explained by the fitting schemes employed, in addition to considerations respective authors employ when developing the empirical fit. For example, Lozowski et al., uses their formulation for all possible ranges of overall collision efficiencies, while Langmuir and Blodgett switch to different parameterization scheme for higher values of overall collision efficiencies, in addition to using a correction table for low values of collision efficiency. Same argument can be said when comparing parameterizations by Cansdale and McNaughtan and Makkonen. While the overall collision efficiency formulation look closely related the "real" overall collision efficiency *E*, in Makkonen model is calculated with following empirical fit (Makkonen, 1984):

$$E = 0.69E_m^{0.67} + 0.31E_m^{1.67} \tag{20}$$

The reason this parametrization is dubbed "real" overall collision efficiency is following. In his work, (Makkonen, 1984) correctly notes that in order to precisely estimate overall collision efficiency, the formulation for E_m has to be applied for all droplet bins within the droplet distribution spectrum. However, since exact droplet distribution is typically not known, or, more commonly, only distribution MVD is known it is not possible to recalculate the overall collision efficiency with full droplet distribution spectrum. Therefore, this simple linear parametric fit was developed in order to "emulate" the overall collision efficiency of full droplet distribution spectrum, to an extent. This equation will be used in all subsequent calculations of overall collision efficiency which use Makkonen model, in addition to respective formulae from table 1.

2.2 Limitations of overall collision efficiency parameterizations for lower values of *K*

The main purpose of this subsection is to discuss the theoretical limitations of droplet overall collision efficiency parameterizations, as described by respective authors, for the cases of low values of droplet's

inertia parameter *K*. Those limitations are expected to happen when modeling the ice accretion at lower wind speeds and/or droplet sizes for larger objects. All subsequent discussion within this subsection is based on theoretical derivations and assumptions of each respective model.

According to the relevant theoretical discussions in (Finstad et al. 1988a), they consider the lower limit of droplet inertia parameter (*K*) being $K = 0.25$ in their model, below which Finstad et al. advise to recalculate the droplet trajectories using the appropriate drag coefficients for each droplet size in the spectra. All the previous discussion and formulae, which uses droplet diameter d_p in them assume a median volume diameter (MVD) of the spectrum. MVD is such a value, for which half of the cloud droplet volume will be concentrated in droplets with larger or smaller diameters, respectively.

The usage of MVD originated from (Langmuir and Blodgett, 1946) and as later showed by (Finstad et al., 1988b) it is an ideal single-valued approximation for droplet spectra. The reason for this assumption is the difficulty, associated with measurements of distribution micron-sized droplets in nature. In such cases, where overall collision efficiency has to be evaluated with entire droplet spectrum, the overall collision efficiency of entire spectrum can be evaluated as:

$$E_{spec} = \sum w_i E_i \tag{21}$$

Where w_i is fractional volume of LWC of *i*th bin in the distribution, and E_i is overall collision efficiency of *i*th bin, evaluated from formulae in Table 1, where instead of spectrum MVD d_p, the MVD of *i*th bin, d_{pi} is used. In addition, it is also possible to evaluate spectrum-averaged local collision efficiencies and impact velocities, β and v_0 respectively, using the same procedure.

Moreover, it can be seen from expression for *K*, that each bin will have its own value of *K*, as function of dp_i, and, at least for some of those bins, the value of inertia parameter K_i can be below 0.25. In those cases, again, recalculation of droplet trajectories is needed, or alternatively, the values of overall and local collision efficiencies, impact velocities and maximum impingement angles can be constrained, i.e. $E = \beta_0 = v_0 = \theta = 0.01$, for $K_i \leq 0.17$, as per (Finstad et al., 1988a), however, this approximation can only provide rough estimates, with another possibility being reading the values for those parameters from proper *K* and ϕ curves, as given by (Finstad et al., 1988a).

However, if higher accuracy in calculation is needed, there is no way around of calculating droplet trajectories for cases of interest. Moreover, in such cases the overall collision efficiency parameterization by Finstad et al. cannot be readily used, and one would need to find the value of *E*, based on the discussion in preceding section, or, following geometric interpretation of *E*, given by (Finstad et al., 1988a).

As discussed previously, Finstad uses drag coefficient values reported by Beard and Pruppacher (Beard and Pruppacher, 1969) over the original Langmuir and Blodgett empirical formulation for drag coefficient, while keeping the trajectories equations consistent with (Langmuir and Blodgett, 1946). Therefore, one can assume that solutions should match, provided the Langmuir and Blodgett model is modified with Beard and Pruppacher's drag coefficient, however such modification is left outside the scope of this work. Furthermore, (Finstad et al., 1988a) argue that buoyancy and gravitational effects on

drag can be ignored, the vorticity diffusion from accelerating droplets' surface and the induced mass increase of the droplet due to accelerating air in immediate surroundings are important factors of non-steady state drag term, and are represented in the model by so-called "history" term, following approaches of (Pearcey and Hill, 1956) and (Landau and Lifshitz, 1959), in the equations of motion of linearly accelerating particle in the flow. This term is defined as:

$$F = -\frac{18\rho_f}{\left(2\rho_p + \rho_f\right) d}\left(\frac{\mu}{\pi\rho_f}\right)^{\frac{1}{2}} \int_{-\infty}^{t} \frac{\mathrm{d}u(\tau)}{\mathrm{d}\tau} \frac{\mathrm{d}\tau}{\sqrt{t-\tau}} \tag{22}$$

where ρ_p and ρ_f are particle and fluid densities, respectively, and $u(\tau)$ is droplet's absolute velocity. Finstad et al., referring to Norment, suggest that history term becomes of importance in cases where:

$$N_A = d\left|\frac{\mathrm{d}u(\tau)}{\mathrm{d}\tau}\right| \frac{1}{v^2} > 0.01 \tag{23}$$

Where N_A is acceleration modulus. If the acceleration modulus threshold is exceeded, it needs to be incorporated into the trajectory equation. This trajectory equation, following (Oleskiw, 1982) in non-dimensional vector form with added buoyancy and gravitational effects, is given as (Oleskiw, 1982):

$$\frac{\mathrm{d}\overline{v_p}}{\mathrm{d}t} = \frac{2\left(\rho_p - \rho_f\right)}{\left(2\rho_p + \rho_f\right)}\bar{g} - \frac{3\rho_f (C_D Re/24)}{4r_p\left(2\rho_p + \rho_f\right)}\left|\overline{v_p} - \overline{v_f}\right|\left(v_p - v_f\right) - \frac{9\rho_f}{\left(2\rho_p + \rho_f\right) r_p}\sqrt{\frac{\mu_f}{\pi\rho_f}} \int_{-\infty}^{t} \frac{\mathrm{d}\overline{v_p}}{\mathrm{d}\tau} \frac{\mathrm{d}\tau}{\sqrt{t-\tau}} \tag{24}$$

Where v_p is particle's (droplet's) velocity, r_p is the particles radius, v_f is the fluid (air) velocity and g is the gravitational acceleration. All quantities in this equation are non-dimensional and the first term on the right hand side is the buoyancy and gravitational acceleration of the droplet, second term is the steady viscous drag and the third term can be recognized as history term. The Langmuir and Blodgett droplet trajectory equations are the simplified version of the preceding equations and those can be written as (Oleskiw, 1982):

$$\frac{\mathrm{d}\overline{v_p}}{\mathrm{d}t} = \frac{3\rho_f (C_D Re/24)}{8\rho_p R_p}\left|\overline{v_p} - \overline{v_f}\right|\left(v_p - v_f\right) \tag{25}$$

where, R_p is particle radius. Therefore, for the cases of $K < 0.25$, the most accurate solution would be the recalculation of water droplet trajectories, using full spectra, with the trajectory equations of (Oleskiw, 1982), if non-steady state drag terms and/or larger droplets, with possibly have large buoyancy and gravitational drift are present, or (Langmuir and Blodgett, 1946) equations, if this is not the case. Finally, if the Langmuir's parameter of the flow is not in range of $10^2 \leq \phi \leq 10^4$ the usage of constants in the Finstad et al. formulation of overall collision efficiency should follow that of (Finstad, 1986), instead of those in Table 1, as the constants from Table 1 were derived specifically for those range, to provide better fit with the data. (Finstad, 1986) argues that Langmuir's parameter range of $10^2 \leq \phi \leq 10^4$ covers majority of possible icing conditions, so deviation from it are expected to be infrequent.

The limitation of $K_0 < 0.125$ for the (Langmuir and Blodgett, 1946) model arises from the theoretical derivations in said work, in which case the droplet should follow the streamlines exactly, thus having the perfect advection, and, therefore, no ice accretion can occur. Other authors, who base their models on the Langmuir and Blodgett model didn't try to ascertain this assumption in more detail, instead focusing on overall collision efficiency parameterization, and thus they all share the same lower limit of *K*. However, the lower limit of $K_0 < 0.125$, to the best of authors' knowledge, has not been tested experimentally, nor how it would change, if at all, if the different drag terms were inserted in the trajectory equations. Finally, in case of (Stallabrass, 1980) model the lower range of $\xi < 3200$ is mentioned explicitly, as a result of dimensional analysis from the previous work, and it is easy to see from the equations in Table 1 that no deposition can occur for cases $\xi < 3200$.

Recently, Zhang et al. (Zhang et al., 2018) have proposed a novel droplet parametric size in order to evaluate overall collision efficiency for cases with the low *K* value. While strictly adhering to Finstad et al./ISO 12494 standard model in order to evaluate the overall collision efficiency itself, Zhang et al. (Zhang et al., 2018) substitute the MVD with Volume Weighted Diameter (VWD) defined as:

$$\mathrm{VWD} = \sum x_i d_i \tag{26}$$

where x_i is fractional volume of the bin *i* of the droplet distribution spectrum and d_i is the MVD value of bin *i* of the droplet distribution spectrum. Note the similarity of VWD and E_{spec} formulation from eq. (21). The usage of VWD formulation should give higher value for droplet diameter, and as a result – the overall collision efficiency will be increased when compared with MVD approximation due to usage of large value of droplet diameter in the calculation. The VWD concept and its results will be compared against MVD approximation and spectrum-averaged results, based on full droplet distribution spectrum, in subsequent section of this study.

3 Mathematical Analysis & Comparison with Experimental Data

For the purpose of this study, two data sets of experimental results have been used – the experiments of (Makkonen and Stallabrass, 1987) and FRonTLINES project experimental cases, done by VTT.

The main reason of choosing two experimental data sets to conduct further investigation is as follows. The experiments of (Makkonen and Stallabrass, 1987) established the validity of basic theory of collision efficiency of cloud droplets in the range of $0.07 < E < 0.63$, in addition to arguing for validity of said theory for the range $E > 0.63$. However, as was discussed in (Makkonen and Stallabrass, 1987), at lower values of *E* several factors, such as air turbulence, surface roughness and electrical forces may became much more significant. The FRonTLINES project test cases were specifically conducted for the conditions which may result in overall collision efficiency to be of an order of $E = 0.07$ or lower. Moreover, for majority of FRonTLINES cases the droplets inertia parameter is expected to be of an order $K = 0.3$ or lower, which allows for observations of theoretical limitations, as discussed in respective section.

The experiments of Makkonen and Stallabrass were conducted at Low Temperature Laboratory, National Research Council of Canada. The experiments employed a single atomizing spray nozzle at the centerline of 30.5 cm × 30.5 cm test section. Due to expected tunnel blockage effects for some test cases, plenum chambers with perforated walls were installed in place of test section floor and ceiling in order to achieve porosity of test section of 10%. Icing tests were made on horizontally mounted rotating cylinders of 1.024, 3.183, 4.440 and 7.609 cm in diameter. The speed of rotation was 2 RPM.

A water micromanometer was used to measure the dynamic pressure in the tunnel test section. The total temperature of the tunnel air was controlled and measured by a thermostat. The static temperature in the test section (as listed in Table 2) was lower than the total temperature, due to the adiabatic expansion of the air accelerating within the contraction. LWC was measured using the single rotating cylinder method while droplet size measurements were done with the Forward Scattering Spectrometer Probe (FSSP). Measurements of the droplet size distributions (listed in the Table 2 as "droplet size distribution category") were made at four wind velocities and nozzle settings. More information about experimental setup is available in the original source (Makkonen and Stalabrass, 1987), while the experimental test matrix for (Makkonen and Stallabrass, 1987) experiments is given in Table 2. Unfortunately, due to the passage of time the information on droplet distributions in those experiments is no longer available (Makkonen, personal communication), so it is not possible to recalculate the results with full distribution spectrum for those experiments, in order to directly compare the results.

Table 2 – Makkonen and Stallabrass experimental test matrix.

Test	***Initial cylinder diameter (cm)***	***Ultimate cylinder diameter (cm)***	***Test duration (min)***	***Wind velocity (m/s)***	***Air temperature (°C)***	***Liquid water content (g/m^3)***	***Median volume diameter (μm)***	***Droplet size distribution category***	***Ice mass (g/10 cm)***
1	1.024	1.55	30	20	–4.5	0.36	17.1	3	9.34
2	1.024	1.48	30	20	–4.5	0.35	14.4	3	7.56
3	1.024	1.42	30	20	–9.5	0.35	14.4	3	6.31
4	1.024	1.60	30	20	–19.3	0.35	14.4	3	7.85
5	1.024	1.43	31	20	–4.5	0.33	13.1	2	6.54
6	3.183	3.65	40	20	–4.5	0.36	17.1	3	18.70
7	3.183	3.54	40	20	–4.5	0.35	14.4	3	14.18
8	3.183	3.50	40	20	–9.5	0.35	14.4	3	12.44
9	3.183	3.70	40	20	–19.3	0.35	14.4	3	13.46
10	3.183	3.47	40	20	–4.5	0.33	13.1	2	10.55
11	4.440	4.85	50	20	–4.5	0.36	17.1	3	23.17
12	4.440	4.81	50	20	–4.5	0.35	14.4	3	17.83
13	4.440	4.82	50	20	–9.5	0.35	14.4	3	16.77
14	4.440	5.05	50	20	–19.5	0.35	14.4	3	19.03
15	4.440	4.71	50	20	–4.5	0.33	13.1	2	11.91
16	7.609	7.95	50	20	–4.5	0.36	17.1	3	29.6
17	7.609	7.98	50	20	–4.5	0.35	17.1	3	31.8
18	7.609	7.81	50	20	–9.5	0.35	14.4	3	15.2
19	7.609	7.89	50	20	–19.3	0.35	14.4	3	17.3
20	7.609	8.13	50	20	–4.5	0.33	13.1	3	19.1

21	7.609	7.80	50	20	–4.5	0.36	17.1	2	10.9
22	1.024	1.48	30	36	–4.9	0.15	15.7	1	7.42
23	1.024	1.40	30	36	–4.9	0.15	13.4	1	6.38
24	1.024	1.35	30	36	–4.9	0.14	12.2	1	5.39
25	3.183	3.60	40	36	–4.9	0.15	15.7	1	19.07
26	3.183	3.50	40	36	–4.9	0.15	13.4	1	13.59
27	3.183	3.45	40	36	–4.9	0.14	12.2	1	11.11
28	4.440	4.86	50	36	–4.9	0.15	15.7	1	26.65
29	4.440	4.75	50	36	–4.9	0.15	13.4	1	17.75
30	4.440	4.66	50	36	–4.9	0.14	12.2	1	12.30
31	7.609	7.91	50	36	–4.9	0.15	15.7	1	27.4
32	7.609	7.78	50	36	–4.3	0.15	13.4	1	16.7
33	7.609	7.77	50	36	–4.9	0.14	12.2	1	12.5

The experiments for FRonTLINES project were conducted using the VTT icing wind tunnel. The tunnel is an "open-loop" tunnel placed entirely inside a large cold room. The cross-section of the tunnel mouth is 0.7 m by 0.7 m. Ice was grown on 0.157m long smooth aluminum cylinders, 30, 50, 80, 100 and 170 mm in diameter, placed vertically and rotated by a motor at 5 rotations per minute (RPM). The schematic of the icing wind tunnel is given in Figure 2.

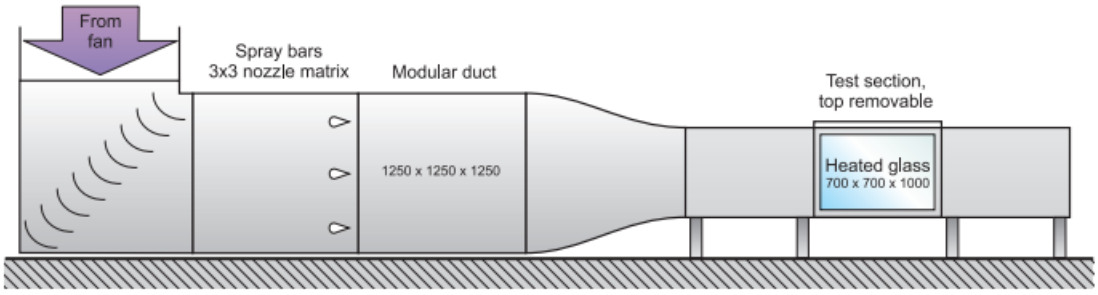

Figure 2 – Icing wind tunnel schematic (VTT, 2016).

To rule out the effect of blockage the cylinders were located in front of the exit of the tunnel. To ensure uniform ice growth on the cylinder and minimize border effects, the cylinders were placed between two thin metal sheets. The temperature and wind speed in the test section were measured using calibrated sensors. The liquid water content (LWC) was calibrated for each wind speed and temperature pair by measuring the ice growth on a 30 mm cylinder and using the formulas defined in ISO 12494 (ISO, 2001). Under the test conditions, LWC was 0.4 g/m^3. Air temperature was –5 °C and wind speed either 4 or 7 m/s, depending on the test case. The droplet size distribution in the tunnel has been calibrated by using The Cloud, Aerosol and Precipitation Spectrometer probe. CAPS allows for measuring of small particles, between 0.61 and 50 µm by utilizing light scattering principle (CAPS, Droplet Measurement Technologies, Boulder, CO, USA). This droplet distribution is given in the Table 3. The calculated MVD of this distribution is 18.73 microns. The MVD calculation procedure follows that of (Finstad et al., 1988b).

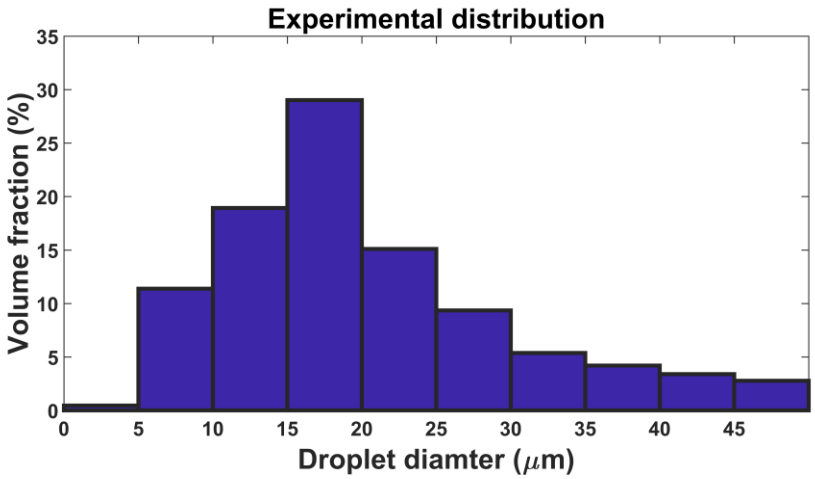

Figure 3 – Experimental distribution.

Table 3 – Experimental distribution.

Bin (μm)	***Bounds (μm)***	***LWC fraction***
5	0.61-5	0.0045
10	5 - 10	0.1138
15	10 - 15	0.1893
20	15 - 20	0.2902
25	20 - 25	0.1510
30	25 - 30	0.0935
35	30 - 35	0.0537
40	35 - 40	0.0419
45	40 - 45	0.0339
50	45 - 50	0.0277

The cylinders in the experiments were weighted using electronic scales with precision of ±0.001 gram. The diameter of the cylinder after the accretion was measured using cooled calipers. Those measurements were conducted for each 30 minutes. An experimental test matrix with ice accretions after 30 minutes is given in Table 4. For all FRonTLINES experimental cases the LWC was 0.4 g/m^3 and air temperature was –5 °C. As was discussed previously, the MVD value of 18.73 microns is used in calculations of the FRonTLINES test caes.

Table 4 – VTT icing tunnel experimental cases.

Test	***Cylinder Diameter (mm)***	***Wind speed (m/s)***	***Total ice mass (g)***
1	30	4	1.163
2	50	4	0.722
3	80	4	0.743
4	100	4	0.770
5	170	4	0.812
6	30	7	4.211

7	100	7	2.853

As it can be seen from Tables 2 and 4, the experimental case presented in this study have a broad range of conditions, which will, in turn, correspond to broad range of inertia parameter *K* in those experiments. The wide range of *K* allows for better relative comparison among the overall collision efficiency parameterizations, discussed in this study, as it covers wide range of possible icing conditions.

All calculations are performed assuming altitude of 10 meters above sea level (m.a.s.l.).The choice of altitude is based on reporting by Finstad, that the pressure difference between ground level and Mt. Washington caused about 0.5% difference in collision efficiency values (Finstad et al., 1988a). Based on values of ambient temperature in Tables 2 and 4, the assumption of "dry growth" regime is made, and hence the freezing fraction of impinging droplets $n = 1$, (Makkonen, 1984), therefore $\alpha_2 = \alpha_3 = 1$, which means that all impinging droplets will stick and freeze immediately after impact. This leaves the overall collision efficiency α_1 as the only unknown constant in the governing equation of icing rate, which is simplified to:

$$\frac{\mathrm{d}m}{\mathrm{d}t} = \alpha_1 w A v \tag{27}$$

For the purpose of this study, the MVD approximation will be used with MVDs listed in Tables 2 and 4. Thus, some difference in values in this paper is expected to occur, when compared to values of (Makkonen and Stallabrass, 1987), when it comes to theoretical overall collision efficiency values, as (Makkonen and Stalabrass, 1987) present their theoretical results using full droplet spectrum distribution.

Moreover, in order to streamline the calculations, the λ/λ_s ratio won't be calculated in derivation of modified inertia parameter K_0. Instead, the K_0 approximations by (Finstad, 1986) from Table 1 are used for calculations of modified inertia parameter. Finally, after determining all necessary parameters' values, the overall collision efficiency α_1 are calculated using formulae from Table 1, with exception of Makkonen parameterizations which will be, in addition, calculated using eq. (20), in order to see how two different empirical fits in said model compare with each other.

3.1 Numerical simulations

With the development of modern computational resources and computational fluid dynamics (CFD) software, the usage of such software for modeling atmospheric icing steadily increases (Lozowski and Makkonen, 2005). While primarily used for modeling of in-flight icing, the modeling on in-cloud icing can also be done with modern CFD software.

For purposes of this paper a series of numerical CFD simulations were performed in order to compare the analytical and experimental results with numerical results. The CFD simulations were performed for FRonTLINES cases only, as for those cases the exact droplet distribution is known. The CFD simulations were performed for MVD approximation, VWD approximation and using full droplet distribution spectrum.

The multiphase CFD based numerical simulations were carried out using ANSYS FENSAP-ICE, which uses Eulerian water droplet impingement solver. The existing analytical models of droplet behavior such and Langmuir and Blodgett, Finstad et al. etc. solve droplet trajectories using Lagrangian particle tracking approach. The Eulerian method treats the particle phase as a continuum and develops its conservation equations on a control volume basis and in a similar form as that for the fluid phase. The Lagrangian method considers particles as a discrete phase and tracks the pathway of each individual particle. By studying the statistics of particle trajectories, the Lagrangian method is also able to calculate the particle concentration and other phase data. On the other hand, by studying particle velocity vectors and its magnitudes in Eulerian method, it is possible to reconstruct the pathways and trajectories of particles in a phase.

4 Results and Discussion

The comparison of different overall collision efficiency parameterizations are done in a series of tables. Tables 5 and 6 show the overall collision efficiencies values for the Makkonen and Stallabrass and FRonTLINES experimental cases respectively. For convenience, Table 5 lists the results of theoretical collision efficiency calculations performed by (Makkonen and Stallabrass, 1987) under E_{theory} column. However, unlike the rest of the results in Table 5, the theoretical results of Makkonen and Stallabrass were obtained using spectrum-averaged values of overall collision efficiency, based on the distribution spectra, as opposed to the monodisperese approximation results, which were calculated in this study.

Moreover, Tables 5 and 6 also list values of inertia parameter K for the both sets of experimental cases, in order to allow quick estimation of performance of overall collision efficiency parameterizations, when compared to experimental results, at different values of K. The values of K presented are calculated using eq. (11) and represent the inertia parameter K and not modified inertia parameter K_0 which is used in some overall collision efficiency parameterizations. The reason for it, is that K_0 formulation tend to differ to certain extent, as evident from Table 1, while inertia parameter K used to calculate K_0 is the same for all the parameterizations.

Table 5 – Comparison of overall collision efficiencies parameterizations for (Makkonen and Stallabrass, 1987) experiments.

Test	**K**	***Experimental***	***Finstad***	***Langmuir and Blodgett***	***Lozowski et al.***	***Cansdale and McNaughtan***	***Makkonen-Em***	***Makkonen- E***	$\mathbf{E_{theory}}$
1	2.944	0.560	0.557	0.680	0.522	0.578	0.540	0.567	0.53
2	2.146	0.479	0.485	0.493	0.456	0.505	0.466	0.501	0.46
3	2.230	0.410	0.493	0.505	0.463	0.513	0.474	0.508	0.47
4	2.138	0.475	0.478	0.481	0.449	0.496	0.457	0.493	0.45
5	1.812	0.434	0.444	0.436	0.422	0.463	0.427	0.465	0.43
6	1.109	0.317	0.297	0.272	0.266	0.266	0.271	0.323	0.30
7	0.799	0.251	0.221	0.200	0.191	0.187	0.198	0.254	0.22
8	0.816	0.222	0.225	0.203	0.194	0.190	0.201	0.257	0.23
9	0.815	0.233	0.222	0.199	0.190	0.185	0.196	0.252	0.22
10	0.668	0.200	0.183	0.159	0.155	0.149	0.162	0.219	0.20

11	0.816	0.231	0.219	0.196	0.187	0.180	0.191	0.247	0.24
12	0.581	0.184	0.148	0.129	0.124	0.112	0.126	0.182	0.17
13	0.589	0.172	0.150	0.130	0.125	0.113	0.127	0.183	0.17
14	0.592	0.191	0.149	0.128	0.123	0.110	0.124	0.180	0.17
15	0.486	0.131	0.116	0.095	0.096	0.083	0.096	0.150	0.14
16	0.487	0.176	0.108	0.087	0.088	0.070	0.083	0.135	0.14
17	0.486	0.189	0.108	0.087	0.088	0.070	0.082	0.134	0.14
18	0.354	0.094	0.061	0.047	0.050	0.030	0.039	0.080	0.09
19	0.362	0.106	0.063	0.048	0.051	0.030	0.039	0.081	0.09
20	0.283	0.116	0.035	0.028	0.031	0.012	0.017	0.045	0.09
21	0.492	0.071	0.110	0.089	0.090	0.072	0.084	0.137	0.06
22	4.597	0.610	0.635	0.707	0.593	0.653	0.617	0.638	0.62
23	3.459	0.542	0.578	0.667	0.537	0.592	0.555	0.581	0.56
24	2.928	0.501	0.542	0.643	0.504	0.556	0.517	0.547	0.51
25	1.697	0.434	0.381	0.352	0.355	0.354	0.349	0.394	0.39
26	1.255	0.314	0.310	0.281	0.275	0.272	0.276	0.327	0.32
27	1.048	0.277	0.269	0.243	0.233	0.227	0.235	0.289	0.27
28	1.238	0.354	0.296	0.268	0.259	0.252	0.258	0.311	0.32
29	0.912	0.238	0.228	0.201	0.192	0.182	0.193	0.249	0.25
30	0.764	0.179	0.191	0.162	0.158	0.145	0.158	0.215	0.20
31	0.742	0.218	0.170	0.144	0.139	0.121	0.134	0.190	0.22
32	0.544	0.134	0.116	0.092	0.093	0.071	0.084	0.136	0.14
33	0.452	0.108	0.087	0.070	0.070	0.047	0.058	0.105	0.11

Table 6 – Comparison of overall collision efficiencies parameterizations for FRonTLINES experiments.

Test	**K**	***Experimental***	***Finstad***	***Langmuir and Blodgett***	***Lozowski et al.***	***Cansdale and McNaughtan***	***Makkonen-Em***	***Makkonen- E***	***Stallabrass***
1	0.303	0.086	0.057	0.049	0.052	0.050	0.061	0.109	0.145
2	0.182	0.032	0.010	0.008	0.009	0.002	0.004	0.016	0.056
3	0.114	0.021	0.010	0.000	0.000	0.000	0.000	0.000	0.000
4	0.091	0.017	0.010	0.000	0.000	0.000	0.000	0.000	0.000
5	0.054	0.011	0.010	0.000	0.000	0.000	0.000	0.000	0.000
6	0.531	0.177	0.151	0.137	0.132	0.134	0.147	0.204	0.218
7	0.159	0.036	0.010	0.003	0.003	0.000	0.000	0.000	0.010

Table 7 shows comparison of overall collision efficiencies between analytical and numerical results for FRonTLINES experimental cases, for the MVD, VWD approximations and spectrum-averaged values.

Table 7 – Overall collision efficiency comparison among MVD, VWD and spectrum-averaged values for FRonTLINES test caes.

Test	***Experimental***	***Monodisperse Analytical***	***Spectrum Analytical***	***VWD Analytical***	***Monodisperse CFD***	***Spectrum CFD***	***VWD CFD***
1	0.086	0.057	0.114	0.092	0.037	0.091	0.067
2	0.032	0.010	0.058	0.020	0.007	0.046	0.014

3	0.021	0.010	0.031	0.010	0.002	0.024	0.003
4	0.017	0.010	0.023	0.010	0.001	0.013	0.002
5	0.011	0.010	0.013	0.010	0.000	0.004	0.000
6	0.177	0.151	0.190	0.199	0.120	0.165	0.164
7	0.036	0.010	0.045	0.010	0.004	0.034	0.008

The calculations of experimental collision efficiency for Tables 5–7 is based on approach of Makkonen and Stallabrass (Makkonen and Stallabrass, 1987):

$$E_{exp} = \frac{M}{vwDLt} \tag{28}$$

where E_{exp} is the experimental collision efficiency, M is the total ice mass accreted during the test, v is the wind speed, w is the LWC, L is the cylinder length, t is the test duration and D is the cylinder diameter.

Makkonen and Stallabrass data has also been recalculated using the expression for E_{exp} in order to provide more "precise" comparisons among the models, as original values, given in (Makkonen and Stallabrass, 1987) only show values of E_{exp} up to two decimal places. Moreover, in calculations for Makkonen and Stallabrass experimental cases, the mean cylinder diameter has been used, while for FRonTLINES experimental data, only initial cylinder diameter was used, as the end cylinder diameter is unknown. Thus, for FRonTLINES experimental cases, the “real” experimental collision efficiencies will be lower than the ones in presented in Table 5. In addition, observe the large difference between “Finstad” column in Table 5 and “E_{theory}” column in (Makkonen and Stallabrass, 1987). The reason for this is that in (Makkonen and Stallabrass, 1987) the theoretical collision efficiency is calculated using full droplet distribution spectra, present in icing tunnel during experimentation, and denoted "Droplet size distribution category" 1, 2 and 3 respectively in Table 2.

However, for this study, said experimental results were calculated with monodisperse distribution assumption with values of MVD taken from Table 2. This was done in order to keep the results strictly within the framework of ISO 12494, as mentioned previously, and to see how well the results would compare with experimental values, if this simplification of monodispersed droplet distribution is employed. Again, the present authors did contact Dr. Makkonen for the droplet distributions in (Makkonen and Stallabrass, 1987) experiments, however, due to significant passage of time since those experiments were conducted this data is, unfortunately, is no longer available (Makkonen, personal communication).

As it can be seen from results, for Makkonen and Stallabrass experiments there is in general a very good agreement among all tested models and experimental values, for 1.024 and 3.183 cm cylinder at 20 m/s wind speed conditions, which correspond to cases 1–10 in Tables 2, and 5, with exception of test 3, where all models and reference results are somewhat higher than actual experimental overall collision efficiency, which may be explained by some slight discrepancy in operating conditions for this particular test. Using the formulae from previous sections, the value of droplet's inertia K for those particular test cases is in the range of $0.66 < K < 3$ which is "medium" to "high" values of droplet's inertia parameter.

Two additional peculiarities can be inferred from tests 1–10 in Tables 2 and 5. First, is that in test 1 the Langmuir and Blodgett predicts significantly higher overall collision efficiency than the rest of the models in present study. From Table 5 it can be seen that for this particular case $E > 0.5$, therefore a change in parameterization scheme should be used, as follows from Table 1 in order to calculate the overall collision efficiency at such high values of it. Further inspection of Table 5 reveals that overall collision efficiency $E > 0.5$ occurs in tests 1, 3 and 22–24. Comparing the values of overall collision efficiency between Langmuir and Blodgett model with the rest of analytical parameterizations for those cases shows that Langmuir and Blodgett model predicts significantly higher overall collision efficiency values than the remaining models and experimental values, with exception of test 3, however, for this particular case all models exceed the experimental values, which, as was mentioned previously, may be due to slight discrepancy in operating condition in this test.

Therefore, it can be said that Langmuir and Blodgett model will tend to overestimate the values of overall collision efficiency for cases where $E > 0.5$ is expected, however, the possible effect of empirical fit from Table 1is not ruled out, and this fit may cause this sort of "aggressive" scaling. However, as shown in (Langmuir and Blodgett, 1946), for $E > 0.5$, following parameterization is used:

$$E = \frac{K}{K + H_e} \tag{29}$$

where

$$H_e = 1 + 0.57808(C_D Re/24) - 0.73\times10^{-4} Re^{1.38} \tag{30}$$

The term H_e is dependent on droplet's drag coefficient ($C_D Re/24$), and thus it is necessary to calculate the ultra-Stokesian drag coefficient λ/λ_s. While (Langmuir and Blodgett, 1946) provide λ/λ_s values in their work for a range of different Reynolds numbers, the precise estimation of the effect of term H_e on overall collision efficiency values would require numerical evaluation of λ/λ_s integral equation, and for this the droplet trajectories have to be evaluated. However, this sort of calculations is deemed too extensive and left outside the scope of present work. As a result only a preliminary conclusion of Langmuir and Blodgett model predicting measurably higher collision efficiencies for $E > 0.5$ can be made.

Second, observe that the MVD approximation yields higher overall collision efficiency results when compared to the reference values of Makkonen and Stallabrass, under E_{theory} column in tests 1–9 and 21–27. This behavior is expected as argued in (Lamgmuir and Blodgett, 1946), that for high values of droplet's inertia K the monodisperse distribution would provide higher values of overall collision efficiency than the droplet distribution spectrum, and, vice versa, the inverse situation, i.e., droplet distribution spectrum would provide higher overall collision efficiency values at low values of K. In their work Langmuir and Blodgett derived this conclusion using a number of empirical "volume-median" distributions with matching MVD in a series of numerical examples. These distributions, denoted Langmuir distributions (also referred in literature as gamma distributions) are given in Figure 4.

Figure 4 – Langmuir distributions. Each bar corresponds to an individual bin.

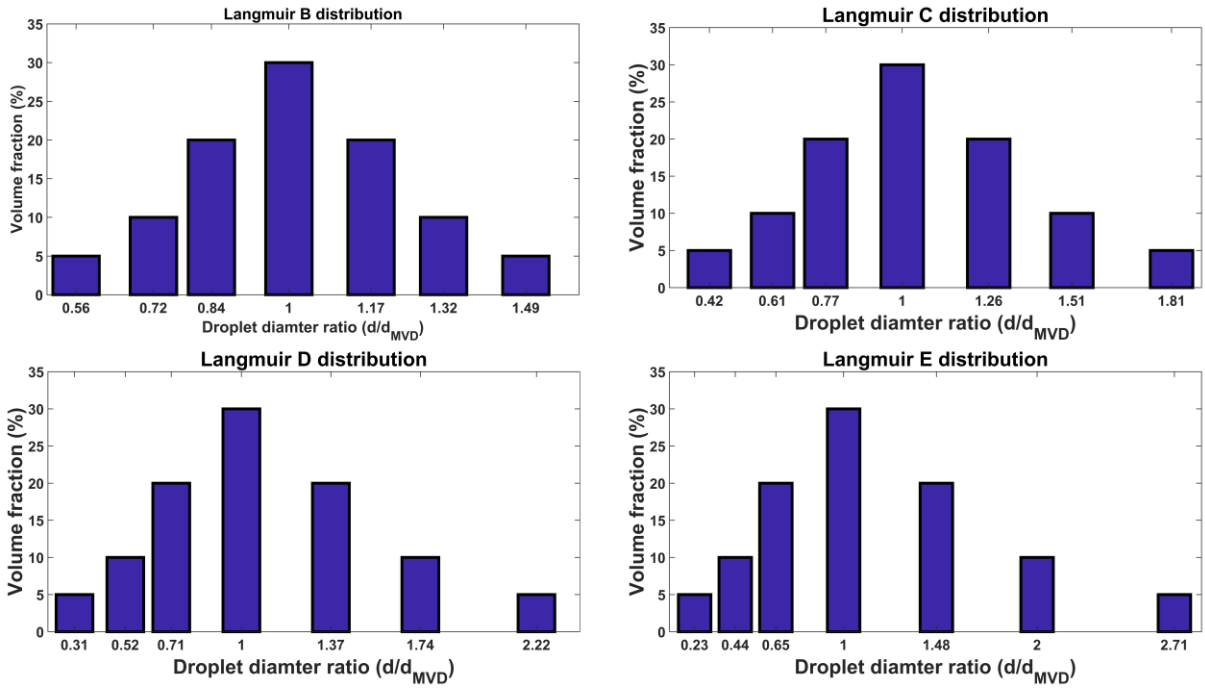

Based on the results from Tables 5 this conclusion is mostly valid, more so for the values of $K \geq 1$, where the calculated values with MVD approximation, using Finstad et al. model are higher than the reference values, provided by Makkonen and Stallabrass calculated with the full distribution spectra. In addition, for lower values of droplet's inertia, corresponding, for example, to experimental cases with 4.44 and 7.609 cm cylinders, which are tests 11–21 in Tables 2 and 5 , the droplet distribution spectra values, provided by Makkonen and Stallabrass are higher, and in general, much closer to experimental values than the results of monodispersed approximation calculations, with exception of test 21, where MVD approximation for all models significantly overestimates the overall collision efficiency value. Observe that in Table 2, test 16 has the same operating conditions as the test 21, with only difference being droplet distribution category. When comparing overall collision efficiency values from Table 5 for these two tests it can be seen that they are roughly identical, with difference coming from mean cylinder diameter, caused by difference in ice accretion values.

However, when comparing overall collision efficiency values from Table 5 it can be seen that for test 16 analytical models tend to underestimate collision efficiency significantly, while for test 21 the opposite is true. While, Cansdale and McNaughtan parameterization for test 21 yields very good results, when compared with experiment, when comparing it with remaining tests, it is revealed that this parameterization tends in general to produce one of the lowest, if not the lowest values for overall collision efficiency. Thus, tests 16 and 21 are good example of a significant effect the droplet distribution spectrum can have on ice accretion, and how this effect may be lost when calculating results with monodisperse distribution. Moreover, observe that for cases 11–21 out of compared analytical models Makkonen two-point parameterization in general produces the closest fit with the data.

It is interesting to note that this particular two-point parameterization was developed in order to collapse multiple collision efficiency curves, corresponding to different droplet sizes within the distribution into a single curve, and as such, it has the property to "emulate" the droplet distribution spectra to an extent.

In addition, note that Makkonen two-point parameterization has a satisfactory agreement with Stallabrass model over the range of values in Table 5. It is interesting in the context that while both models were developed with the goal of collapsing overall collision efficiency parameterization to the single curve, they achieve it by employing different underlying assumption - Makkonen model tries to collapse the range of different droplet size collision efficiencies into the single curve, while Stallabrass model tries to collapse multiple K and ϕ curves of (Langmuir and Blodgett, 1946).

Expanding onto the models, it can be seen from Table 5 that Cansdale and McNaugthan generally only has a satisfactory agreement with tests, featuring 1.024 cm cylinder, by extension - tests with highest values of droplet inertia parameter K. This may be result of said model being developed for helicopter blade icing, where the droplet's inertia is expected to have a large value, and it may be reflected by the choice of numerical fit in said model. When comparing Langmuir and Blodgett and Lozowski et al. formulations it can be seen that they have a satisfactory agreement, for cases when $E < 0.5$, where Langmuir and Blodgett model tends to overestimate the overall collision efficiency values, due to possible reasons, mentioned previously.

In general, Langmuir and Blodgett model produces values, which agree with experimental ones slightly better, with exception of low K value cases, which typically correspond to largest cylinder. In those cases, Lozowski et al. model is closer to the experimental values. It may suggest that the correction values for low E in Langmuir and Blodgett are slightly on conservative side. However, both models produce markedly lower results than Finstad et al. model for said range of overall collision efficiencies.

The Makkonen and Stallabrass results for 36 m/s wind speed test cases won't be described here as the values in there follow roughly the same pattern as in case of 20 m/s wind speed tests, therefore, the discussion for them in this section should be relevant for 36 m/s wind speed tests. Instead, FRonTLINES test cases will be described, based on results from Tables 6 and 7.

From Table 6 it can be seen that Makkonen two-point formulation is in general the better approximation from the analytical models, when calculated with MVD approximation, with exception of cases, where relative error of majority, if not all, analytical models is equal to –100%, i.e., the models fail to produce any sort of result. In those cases Finstad et al., model is better, simply due to restriction of $E = 0.01$ if $K < 0.17$ being used. Furthermore, observe that spectrum-weighted overall collision efficiencies in Table 6 can be significantly higher than experimental overall collision efficiency.

This can be explained by the facts, that the final cylinder diameter in those experiments is not known, and thus only initial diameter has been used, in addition to using the same restriction of $E = 0.01$ for $K < 0.17$ in calculation of collision efficiencies of separate bins of the distribution from Table 3, which may result in bins with smaller droplet diameters being limited by the indicated constraints. As a result, these two factors may explain, at least to some extent, why spectrum-weighted overall collision efficiencies are higher than the experimental ones.

Moreover, the experimental collision efficiency in FRonTLINES experimental tests is below 0.10 for all cases, with exception of test 6, and, with exception of tests 1 and 6 the experimental collision efficiencies are below 0.07, which is the lower limit tested in (Makkonen and Stallabrass, 1987) and

how it is noted in the respective work, the icing theory is verified for the rang $0.07 < E < 0.63$, below which there is no present icing parameterization with sufficient experimental validation.

When comparing analytical and numerical results from Table 7 it is immediately noticeable that CFD simulations give lower value of collision efficiencies in all cases, for all situations – MVD, VWD and spectrum-averaged values. Moreover, when comparing the monodisperse CFD results from Table 7 with analytical parameterizations results from Table 6 it can be seen that CFD values are always consistently lower than all analytical results, with exception of cases where analytical results show $E = 0$, as overall collision efficiency is always greater than zero in CFD results. The zero value for case 5 in Table is due to rounding to three decimal places.

It is likely that the "over-estimation" of E values in analytical results primarily from potential flow approximation, used in all analytical icing parameterizations. In viscous flow, boundary layer growth, which can be treated as a displacement thickness, deflects airflow streamlines and, therefore, pushes the droplet trajectories from cylinder, which can be treated as effective increase in cylinder diameter. Flow separation from cylinder is another feature of viscous flow which cannot be treated adequately by potential flow theory. Flow separation deflects airflow away from body in essence altering the cylinder shape downstream from separation location. This may affect droplet trajectories possibly reducing E further.

The assumption of undisturbed airflow is valid when concentration of airborne droplets is small, or droplets are very small when compared to the cylinder diameter. However, around the leading edge of cylinder airflow streamlines are contracted, droplet trajectories are highly curved and thus droplet concertation can become high enough to affect the airflow by displacing it away, again reducing the overall collision efficiency.

The preceding discussion is based on discussion in (Yoon and Ettema, 1993), who have observed in their experiments that overall collision efficiency, measured using Laser Doppler Velocimetry (LDV) is approximately half of that, predicted by overall collision efficiency formulations of Langmuir and Blodgett, Finstad et al. and Ackley and Templeton. When comparing the CFD results against analytical results obtained using Finstad et al. model in Table 7 the similar trend can be seen for monodisperse values, though spectrum-averaged and VWD values are closer to each other.

When comparing the results from Table 7 against experimental results it can be seen that spectrum-averaged and VWD values are noticeably closer to the experimental values than the MVD ones, both for analytical and CFD results. Note that analytical spectrum-averaged results are higher than experimental results in all cases. In addition to previous discussion it may also be explained by restriction of $E_i = 0.01$ if $K_i \leq 0.17$ imposed for all bins. For some of the cases, like cases 1 and 2 VWD approximation thus gives better results, however, as it can be seen from case 6, for higher values of K, VWD approximation will produce higher values of E as it is, in essence, a monodisperse distribution with larger droplet diameter and thus is fully susceptible to the effects of monodisperse distributions, as was discussed previously and shown in (Langmuir and Blodgett, 1946).

In general terms, when directly comparing analytical and numerical results for MVD, VWD approximations and spectrum-averaged values with experimental values, the spectrum-averaged results

show the best agreement, for all cases, with exception of 170 mm cylinder and 4 m/s wind speed, which has $K = 0.054$, which can be treated as very low value of droplet's inertia. For this particular case the analytical spectrum-averaged values are the closest fit. The results using monodisperse distribution produces the worst agreement, both for analytical and CFD results, while VWD results are in-between the two. Those results show that modern specialized CFD tools are capable of simulating in-cloud icing even at more extreme conditions, granted the full droplet distribution spectrum is used.

As noted in ISO 12494 (ISO, 2001) the overall collision efficiency parameterization tends to underestimate the overall collision efficiency values for $E < 0.10$. Several factors have been attributed to this phenomenon, for example surface roughness elements, acting as individual collectors, sublimation and deposition, effects of electrical charge on power lines, turbulence and boundary layer effects etc. (ISO, 2001), (Makkonen and Stallabrass, 1987), (Finstad et al., 1988a). This may result that in order to calculate precise values of overall collision efficiency for those ranges of E significantly higher amount of effects and physical phenomena has to be taken into account, however, to the best of authors knowledge, no study has tried to ascertain those frequently cited factors to any significant quantifiable aspects.

Recently, Makkonen et al. performed a series of numerical simulations (Makkonen et al., 2018) using Euler-Langrangian approach with full droplet distribution spectrum and history term from eq. (22) included. Moreover, Spalart-Allmaras turbulence model was used as turbulence closure instead of opting for potential flow approximation. The results of that study suggest that approach based on numerical simulations of full distribution spectrum with history term included is well suitable for modeling of ice accretion at low values of K.

Therefore, a question arises how to model the ice accretion in cases where the droplets' inertia parameter is low. Such conditions may arise, for example, in modeling of large structures, such as masts and towers, at low values of wind speeds. Undoubtedly, obtaining the overall collision efficiency as a result from trajectory equations, calculated using full droplet distribution spectra, using the procedure, described in this study is the most accurate option available. However, its main disadvantages, if specialized software is not used, are computational complexity, laboriousness due to large number of equations involved and difficulty of transferring results readily to the next "case" to be evaluated, as the results of the modeling will be tied to the operating conditions, used in calculations, without accumulating large database and performing necessary analyses first.

If this is not possible, other possible approach is evaluation of overall collision efficiency using full droplet distribution spectrum with spectrum-averaging carried afterwards. The main disadvantage here, is that the exact droplet distribution in real case scenario is not readily available and measuring it might be difficult, if not high impossible without specialist equipment. One possibility here is the use of Langmuir distributions in order to obtain some *ad hoc* distribution, however, as it was discussed previously, even at the same MVD and operating conditions, different droplet distributions might produce markedly different values for overall collision efficiencies, as such extra care is needed when operating with assumed distributions.

As a sort of reference distribution, the Langmuir D distribution might be preferred due its extensive and successful usage in in-flight and aircraft icing studies (Wright, 2008), (Bidwell, 2012), (Papadakis et al., 2007). If usage of assumed droplet distributions leads to undesirable uncertainty towards, as droplet distributions in nature may not be normal, as Langmuir distributions, the values of overall collision efficiency, arising from distribution change, one of the other analytical parameterization schemes in this study can be used, which provides higher overall values of collision efficiency, such as Makkonen two-point approximation.

5 Conclusion

Within the scope of this work several major ice accretion parameterizations have been investigated, staring from original Langmuir and Blodgett work on the water droplet trajectories, up to and including the Finstad et al., mathematical model of overall collision efficiency parameterization, which is part of current governing ISO standard, thus covering a timeframe of several decades of investigation in icing modeling. The paper provides a general and mathematical overview of those parametrizations, presents necessary formulae for calculations of overall collision efficiency, starting with trajectory evaluation, and discusses underlying assumptions and approximations made by respective authors in those models, as well as includes discussion and comparison with some of the newer concepts in ice modeling, such as Volume Weighted Diameter and makes use of CFD simulations to estimate feasibility of using said CFD tools to simulate ice accretion at low values of K.

As an application example, two experimental datasets have been used for overall collision efficiency calculations and comparison of said parameterizations. Those experiments span large amount of operating conditions, thus giving the droplet's inertia parameter range $0.1 < K < 4.6$, and overall collision efficiency $0.01 < E < 0.63$which should cover majority of possible icing conditions. The results show several important points, namely, that for higher ranges of droplets inertia, approximately $K > 0.8$, the monodisperse droplet distribution yields good agreement with the experimental values, however, for values of K below that, as droplets' inertia decrease further and characteristic length of the object increases, the monodisperse droplet distribution approximation tends to underestimate the overall collision efficiency when compared to the experimental and spectrum calculated values. In those cases, the empirical fit of Makkonen (Makkonen, 1984) for the calculation of overall collision efficiency produces better results, than Finstad et al. model (Finstad et al., 1988a) with MVD approximation, as said parameterization by Makkonen was developed with the purpose of collapsing the different droplet spectrum collision efficiencies into single curve.

However, for very low values of K and E, roughly corresponding to $K \leq 0.3$ and $E \leq 0.07$, respectively, the MVD approximation, using any present model in this study tends to underestimate the overall collision efficiency significantly. For those cases the recalculation of droplet trajectories using full spectrum is recommended. However, due to extensive work needed to carry this analysis, a simplified approach using, full droplet distribution, if available, with the Finstad et al. model, with constraint of $E = 0.01$ for $K < 0.17$ is suggested as an alternative, and in general this yields good agreement with experimental results, though, as it has been shown this approach may have overestimate the overall collision efficiency. As was discussed, the reason for this overestimation is primarily due to potential flow approximation, flow disturbances (Yoon and Ettema, 1993) and constraint of $E = 0.01$ for $K \leq 0.17$.

The numerical results obtained with modern CFD software show good potential of modeling in-cloud icing at low values of *K*, with possible exception of extremely low values of *K*, granted full droplet distribution spectrum is used in the simulations. The results with MVD approximation for those cases show even lower values than analytical parameterizations, which already tend to underestimate the overall collision efficiency values. Moreover, the CFD results tend to produce lower values than analytical parameterizations for all tested droplet size parameters, namely MVD, VWD and spectrum-averaged values, however, again, this comes to usage of potential flow theory in analytical parameterizations over viscous flow in CFD results, and the results are in line with experimental observations of (Yoon and Ettema, 1993). Alternatively, the history term can be included in CFD simulations, as it has been shown to produce excellent agreement with experimental results (Makkonen et al., 2018).

If actual droplet distribution spectrum is not available, it is recommended to carry out the analysis using Langmuir distributions, such as widely used Langmuir D distribution and to check the results against different Langmuir distributions and Makkonen two-point approximation in order to obtain rough estimate of overall collision efficiency. While Volume Weighted Diameter (VWD) concept also aims to solve the issue of underestimating the overall collision efficiency at low values of *K*, in order to use it the full droplet distribution spectrum should be known, at which case the spectrum-averaging using the full droplet distribution spectrum may produce better results.

Acknowledgement

The work reported in this paper is funded by the Research Council of Norway, FRonTLINES - project no. 245370 and IceBOX – project no. 282403. Authors would like to acknowledge Mr. TimoKarlsson and Mr. MikoTiihonen from VTT for providing icing wind tunnel experimental data used in this research work as part of FRonTLINES project

References

1. Anderson, D.N., 2004. Manual of Scaling Methods. NASA/CR—2004-212875
2. Bain, M., Gayet, J.F., 1982. Aircraft measurements of icing in supercooled and water droplet/ice crystal clouds. Journal of Applied Meteorology, 21, 631-641.doi:10.1175/1520-0450(1982)021<0631:AMOIIS>2.0.CO;2
3. Beard, K.V., Pruppacher, H.R., 1969. A Determination of the Terminal Velocity and Drag of Small Water Drops by Means of a Wind Tunnel. Journal of Atmospheric Sciences 26, 1066-1072. doi:10.1175/1520-0469(1969)026<1066:ADOTTV>2.0.CO;2
4. C. S. Bidwell, 2012, Particle Trajectory and Icing Analysis of the E3 Turbofan Engine Using LEWICE3D Version 3, NASA/TM–2012-217696, NASA
5. Cansdale, J., McNaughtan, M., 1977. Calculation of Surface Temperature and Ice Accretion Rate in a Mixed Water Droplet/ice Crystal Cloud.
6. Finstad, Karen, J., 1986. Numerical and experimental studies of rime ice accretion on cylinders and airfoils. Ph.D. thesis. University of Alberta, Canada.doi:10.7939/R3N58CS1V.
7. Finstad, K.J., Lozowski, E.P., Gates, E.M., 1988a. A computational investigation of water droplet trajectories. Journal of Atmospheric and Oceanic Technology, 5, 160-170.doi:10.1175/1520-0426(1988)005<0160:ACIOWD>2.0.CO;2

8. Finstad, K.J., Lozowski, E.P., Makkonen, L., 1988b. On the median volume diameter approximation for droplet collision efficiency. Journal of the Atmospheric Sciences 45, pp. 4008–4012.doi: 10.1175/1520-0469(1988)045<4008:OTMVDA>2.0.CO;2
9. FENSAP-ICE User Manual
10. ISO 12494:2001(E), 2001. Atmospheric icing of structures. Standard. International Organization for Standardization. Geneva, CH.
11. Landau, L., and E. M. Lifshitz, "Fluid Mechanics," Pergamon Press, pp. 96-98, 1959.
12. Langmuir, I., Blodgett, K., 1946. A Mathematical Investigation of Water Droplet Trajectories. Army Air Forces technical report 5418. Army Air Forces Headquarters, Air Technical Service Command.
13. Lozowski, E.P., Makkonen, L., 2005. Fifty years of progress in modelling the accumulation of atmospheric ice on power network equipment, in: Proceedings of the 11th International Workshop on Atmospheric Icing of Structures.
14. Lozowski, E.P., Stallabrass, J.R., Hearty, P.F., "The icing of an unheated, non-rotating cylinder in liquid water droplet-ice crystal clouds," National Research Council of Canada, Ottawa, CANADA, Mechanical Engineering Report LTR-LT-96, Feb. 1979.
15. Lozowski, E.P., Stallabrass, J.R., Hearty, P.F., 1983a. The icing of an un-heated, nonrotating cylinder. part I: A simulation model. Journal of Applied Meteorology 22, 2053-2062.doi:10.1175/1520-0450(1983)022<2053:265 TIOAUN>2.0.CO;2
16. Lozowski, E.P., Stallabrass, J.R., Hearty, P.F., 1983b. The icing of an unheated, nonrotating cylinder. part II: Icing wind tunnel experiments. Journal of Applied Meteorology 22, 2063-2074.doi:10.1175/1520-0450(1983)022<2063:TIOAUN>2.0.CO;2
17. Macklin, W.C., 1962. The density structure of ice formed by accretion. Quarterly Journal of Royal Meteorological Society, vol. 88 pp. 30–50.
18. Makkonen, L., 1984. Modeling of Ice Accretion on Wires. Journal of Applied Meteorology 23, 929-939. doi:10.1175/1520-0450(1984)023<0929:MOIAOW>2.0.CO;2
19. Makkonen, L., 1985. Heat transfer and icing of a rough cylinder. Cold Regions Science and Technology 10. 105-116.doi:10.1016/0165-232X(85)90022-9
20. Makkonen, L., Stallabrass, J.R., 1987. Experiments on the cloud droplet collision efficiency of cylinders. Journal of Applied Meteorology 26, 1406-1411.doi:10.1175/1520-0450(1987)026<1406:EOTCDC>2.0.CO;2
21. Makkonen, L., 2000. Models for the growth of rime, glaze, icicles and wet snow on structures. Phil. Trans. R. Soc., Lond. A 2000 358 2913-2939; DOI: 10.1098/rsta2000.0690. Published 15 Nov. 2000
22. Makkonen, L., Zhang, J., Karlsson, T., Tiihonen, M., Modelling the growth of large rime ice accretions, CRST, 151 (2018), 133-137.
23. Messinger, B.L., 1953. Equilibrium temperature of an unheated icing surface as a function of airspeed. Jour. Aeronautical Sci., 20, 29 – 41
24. Oleskiw, M.M., 1982. a Computer Simulation of Time-Dependent Rime Icing on Airfoils. Ph.D. thesis. University of Alberta, Canada.doi:10.7939/R3QR4NW8V.
25. Papadakis M., Wong, S.-C., and Rachman, 2007, A, Large and Small Droplet Impingement Data on Airfoils and Two Simulated Ice Shapes, NASA/TM—2007-213959,
26. Pearcey, T and Hill, G.W., 1956. The accelerated motion of droplets and bubbles. Aust. Jour. Phys., 9, 19–30.
27. Ruff, G.A., "Analysis and Verification of the Icing Scaling Equations," AEDC-TR-85-30, vol. 1 (rev), March 1986.
28. Stallabrass, J.R., 1980. Trawler Icing: A Compilation of Work Done at N.R.C. (Givrage Des Chalutiers: Compilation Des Recherches Effectuees Au C.N.R.). Defense Technical Information Center.

29. VTT Technical Brochure, 2016. URL: http://www.vttresearch.com/Documents/Low%20Carbon%20Energy/Wind%20energy/Icing_Wind_Tunnel_02022016.pdf
30. W. Wright, 2008, User's Manual for LEWICE Version 3.2, NASA/CR–2008-214255, NASA
31. Yoon, B., Ettema, R., Droplet trajectories and icing collision efficiencies for cylinders determined using LDV. CRST 21, 4, July 1993, pp. 381-397
32. Zhang, J., Qing, H., Makkonen, L., A novel water droplet size parameter for calculation of icing on power lines. Coltec (2017) https://doi.org/10.1016/j.coldregions.2018.01.021, pre-print

Paper 2. Droplet Distribution Spectrum Effects on Dry Ice Growth on Cylinders

Pavlo Sokolov and Muhammad Shakeel Virk

Cold Regions Science and Technology, 2019, Volume 160. pp. 80 – 85.

DOI: 10.1016/j.coldregions.2019.01.002

Author's Contribution

Pavlo Sokolov has contributed substantially in the proposal of research idea, literature review, modelling, computing, analytical and numerical analysis, and writing of the paper.

Droplet Distribution Spectrum Effects on Dry Ice Growth on Cylinders

*Pavlo Sokolov & Muhammad S. Virk

Institute of Industrial Technology,

UiT – The Arctic University of Norway

*Email: pavlo.sokolov@uit.no

ABSTRACT

A detailed parametric analytical study along with a series of viscid multiphase numerical simulations of ice accretion were performed in comparison with experimental data of ice accretion on a 30 mm diameter cylinder. The study was performed for droplet distribution spectra, *Langmuir (A-J)*, in addition to an experimental droplet distribution obtained in an icing tunnel. Analysis shows that droplet distribution spectrum has a pronounced effect on cloud impingement parameters, such as droplet overall collision efficiency (E), droplet local collision efficiency (β_0), droplet maximum impingement angle (θ), droplet impact velocity (V_0), accreted ice mass and density. The values of these parameters can significantly change at the same operating conditions and median volume diameter (MVD) with a change of droplet distribution spectrum. These differences are more pronounced at low values of droplet inertia parameter, (*K)*. Further experimental, analytical and numerical investigations into those aspects at lower values of droplet inertia parameter are deemed necessary in order to expand the understanding of different cloud impingement parameters on the ice accretion process and performance of current icing theory in cases with low values of K. For the low values of *K*, which correspond to the values of $E \leq 0.10$, the use of the full droplet spectrum is recommended in calculations instead of monodispersed. In addition, based on the results of this and previous works the Langmuir D distribution is recommended as standard or "first guess" distribution.

Keywords: ice accretion; cylinder; collision efficiency; droplet distribution spectrum; MVD; CFD.

1 Introduction

The interest in modeling ice accretion on cylindrical objects primarily comes from preventing structural damage or collapse of objects such as overhead transmission lines or communication masts due to the accreted ice mass leading to dynamic instabilities. Ice mass accretion in these cases primarily comes from atmospheric icing such as in-cloud or precipitation icing. In studying these one prime interest lies in the parameterization of characteristics of in-cloud droplet impingement on cylinders. The study of in-cloud icing is not a new scientific field with some major milestones in terms of mathematical models being works by (Langmuir and Blodgett, 1944), (Cansdale and McNaugthon, 1977), (Lozowski et al., 1979), (Stallabrass, 1980), (Makkonen, 1984) and (Finstad et al., 1988a). The latter being independently verified by (Stallabrass and Makkonen, 1987) serves as a current benchmark model for atmospheric icing and it is part of governing standard ISO:12494 "*Atmospheric Icing of Structures*" (ISO, 2001). The

core of the Finstad et al. model uses a so-called "Median Volume Diameter approximation" (MVD) in order to parameterize the in-cloud droplet spectrum using a singular value and an assumption that the cloud droplet distribution can be adequately represented using a uniform droplet distribution, where all the droplets have the same diameter, corresponding to cloud MVD. The verification of the concept was carried out by Finstad in the doctoral thesis (Finstad, 1986), later expanded in paper of (Finstad et al., 1988b) and based on the results of (Makkonen and Stallabrass, 1987) it can be stated that the Finstad et al. model is applicable for the ranges of droplets overall collision efficiencies of $0.07 < E < 0.63$.

Jones (Jones et al., 2014) showed that MVD approximation may not always be valid and in natural conditions such as on Mt. Washington in USA, the use of a droplet distribution spectrum can yield significantly better results over a monodisperse distribution when comparing ice accretion data on a multicylinder device. ISO 12494 standard states that the Finstad et. al model has a tendency to under estimate the overall collision efficiency for cases, when $E < 0.10$. Recently, (Makkonen et al., 2018) shown that modern Computational Fluid Dynamics (CFD) tools can achieve good results in modeling of ice accretion on cylinders for cases when $E < 0.10$, granted full droplet distribution spectrum is used. When it comes to estimating the cloud impingement parameters of ice accretion, $X(K, \phi)$, those parameters depend on the droplet inertia parameter (K) and Langmuir parameter ϕ, which are defined as (ISO, 2001):

$$K = \frac{\rho_p d_p^2 u}{18 \mu_f c} \tag{1}$$

$$\phi = \frac{Re^2}{K} \tag{2}$$

where ρ_p is droplet (water) density, u is the freestream wind speed, μ_f is air density, c is the characteristic length of the object, being radius in case of a cylinder and d_p is the droplet MVD. When it comes to calculations of droplet impingement parameters using full droplet distribution spectrum, one can see that:

$$K_{spec} = \sum w_i K_i \tag{3}$$

$$X(K, \phi)_{spec} = \sum w_i X(K_i, \phi)_i \tag{4}$$

where w_i is fractional weight of bin i, subscript i refers to a given parameter calculated for bin i, while subscript *spec* shows spectrum averaged values. The spectrum values are linearly dependent on the per-bin values, as spectrum values, $X(K, \phi)_{spec}$ are obtained by summation of per-bin values $X(K_i, \phi)_i$ using LWC fraction w_i as a weighting constant. Conversely, per bin values are dependent as square of bin's MVD, and independent of ϕ as it can be seen from the structure of it in eq. (2). Such dependence may result in a significant change of cloud impingement parameter values, when droplet distribution spectrum is changed, even in the case where different droplet distributions have matching MVD value of the entire spectrum. This study aims to address; the impact of different droplet distribution spectra with matching MVDs on the ice accretion process, the changes of the key model parameters, introduced

by the change of droplet distribution spectra and some of the aspects of utilizing some simplistic constraints and performance of modern CFD software for multiphase numerical simulations of low wind speed in-cloud icing events.

Recently, (Makkonen et al., 2018) performed a series of CFD simulations using the full droplet distribution spectrum. However, unlike their work, which used Lagrangian specification of flow field, current work utilizes the Eulerian specification of flow field, which will be detailed in subsequent sections. The main reason for choosing the Eulerian formulation is that the majority of previous studies, mentioned earlier in this section, have used the Lagrangian flow formulation. It is deemed worthwhile to investigate how the Eulerian flow formulation used in CFD will perform in the modeling of the ice accretion process. Finally, one of the prime practical applications of the approaches used in this study is the possible improvement in ice load maps generation, using mesoscale modeling in WRF/NWP (Weather Research and Forecasting/Numerical Weather Prediction), particularly if the assumed droplet distribution spectra, given in subsequent section, can be implemented in the WRF/NWP model. Again, the practical application here is generating the ice load maps for the wind power and power transmission industries.

2 Design of the Experiment

In this study, the icing tunnel experiments were performed with the focus on low values of *K*. A 30 mm rotating cylinder at wind speed of 4 m/s was chosen for in-depth parametric and numerical investigation. The rotation of cylinder has been chosen in order to keep the results easily transferable to the ISO 12494 (ISO, 2001) procedure of estimated ice loads, in addition, to keeping in line with assumption (Makkonen, 1984) of slowly rotating iced power lines, which are assumed to be the prime object in ice load maps generation. The operating conditions for this test case are given in Table 1. The conditions chosen should be typical of a dry growth condition, thus the sticking and freezing efficiencies are assumed to be equal to unity.

Table 1 – Icing tunnel experiment conditions.

Parameter	***Value***
Cylinder diameter (mm)	30
Cylinder length (mm)	157
Air velocity (m/s)	4
Air temperature (°C)	–5
Altitude (m.a.s.l)	10
Icing duration (min)	30
LWC (g/m^3)	0.4
Rotational speed (RPM)	5

The parametric study is done via the analytical calculations, using the Finstad et al. model (Finstad et al., 1988a) for the calculation of overall collision efficiency (E), stagnation line droplet local collision efficiency (β_0), maximum impingement angle (θ) and stagnation line droplet impact velocity (V_0) and density. The impact of the overall collision efficiency on the ice accretion process is straightforward enough, as the accreted ice mass is directly dependent on it, via the "Makkonen model" formulation

(Makkonen, 2001). While the ISO 12494 standard, based on the "Makkonen model" does not explicitly deal with other cloud impingement parameters, their effect on the icing process and the physical properties of the accreted ice has been investigated in some previous icing studies and icing parameterizations.

For instance, the stagnation line impact velocity, V_0 directly influences the accreted ice density via the "Macklin parameter" (Macklin, 1962). Several empirical icing density parameterizations has been developed, based on the Macklin parameter, for example, the formulation in (Makkonen, 1984) for estimation of density of accreted ice of rotating cylinder at each given time step *i*, primarily used for the power line icing. While the stagnation line collection efficiency β_0 is primarily of importance in the icing parameterizations which focus only on the flow past the stagnation line, such as (Cansdale and McNaughtan, 1977) parameterization, this parameter is still of importance in more "advanced" parameterizations, such as (Finstad et al., 1988a), primarily, when used in conjunction with the maximum impingement angle α_{max}, mostly for the estimation of an accreted ice shape, as an empirical function $\beta(\alpha)$ for the non-rotating cylinder, with the formulations of $\beta(\alpha)$ given in (Lozowski et al., 1983) and (Finstad, 1986), as well as estimating the maximum accreted ice thickness on the stagnation line, as β_0 is the maximum local stagnation efficiency, and thus it corresponds to maximum thickness for the non-rotating cylinder. In the rotating cylinder case, the impact of these two parameters is somewhat "smoothed" due to symmetry and continued rotation, but these parameters become of importance when analyzing the accretion on slowly rotating cylinders, in cases where the fine temporal resolution is needed (along with necessary modifications to the procedure in (Makkonen, 1984)), i.e. $dt < t_0$, where t_0 is the time needed to complete one revolution.

The formulation of (Makkonen, 1984) is used for the analytical calculation of accreted ice density, cylinder surface temperatures and iced cylinder diameter change at each time step. The numerical modeling is done via a series of viscid CFD simulations using Reynolds-Averaged Navier-Stokes (RANS) equations. These simulations are performed on a rotating cylinder. In both cases, the droplet distribution in the icing tunnel, as provided by VTT Technical Research Centre of Finland is used. This droplet distribution is given in Figure 1. The calculated MVD of this distribution is 18.73 microns.

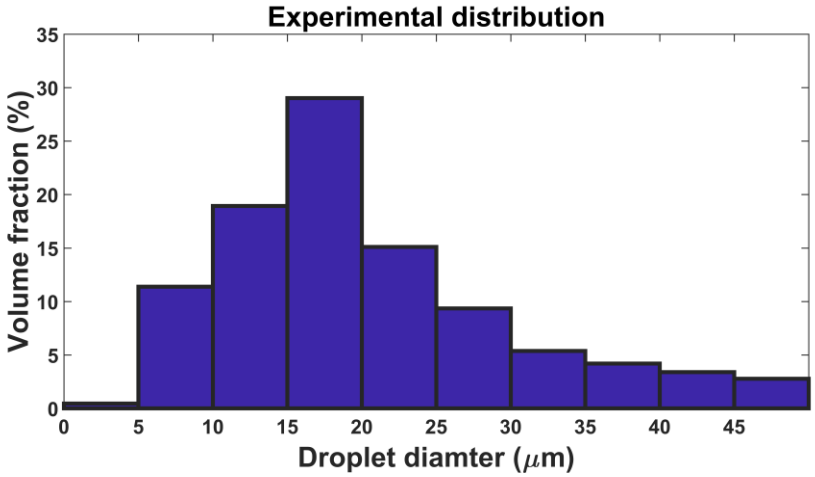

Figure 1 – Experimental droplet distribution spectrum.

Moreover, in order to study the effect of droplet distribution on the ice accretion process different parameterizations of the droplet spectrum, namely the gamma distributions (also referred as Langmuir distributions) are used (Howe, 1990). The gamma distributions used in this study are given in Table 2 in terms of diameter ratios. All gamma distributions have MVD of 18.73 with 'distribution A' being monodispersed. These droplet distributions progressively get "wider" as the ratio of diameters increases, meaning that for distributions with higher value of diameter ratios, the diameters of bins will become progressively smaller or larger, when compared with "preceding" distribution. For the droplet spectrum, each bin collision efficiency is calculated independently and then weighted using the LWC fraction, in order to obtain the overall collision efficiency of the entire spectrum.

Table 2 – Langmuir distributions.

LWC fraction	***A***	***B***	***C***	***D***	***E***	***F***	***G***	***H***	***J***
0.05	1.00	0.56	0.42	0.31	0.23	0.18	0.13	0.10	0.06
0.1	1.00	0.72	0.61	0.52	0.44	0.37	0.32	0.27	0.19
0.2	1.00	0.84	0.77	0.71	0.65	0.59	0.54	0.50	0.42
0.3	1.00	1.00	1.00	1.00	1.00	1.00	1.00	1.00	1.00
0.2	1.00	1.17	1.26	1.37	1.48	1.60	1.73	1.88	2.20
0.1	1.00	1.32	1.51	1.74	2.00	2.30	2.64	3.03	4.00
0.05	1.00	1.49	1.81	2.22	2.71	3.31	4.04	4.93	7.34

The Langmuir distributions B–E were initially presented in (Langmuir and Blodgett, 1944) as a mathematical approximations of the droplet distribution spectra in fog and rising clouds on Mt. Washington observatory. Later, (Howe, 1990) presented "wider" droplet distributions F–J, based on previous observations on Mt. Washington observatory, in order to adequately capture bimodal and trimodal droplet distributions, which are expected to happen in nature.

2.1 Analytical Model

The cloud impingement parameters are calculated in accordance to (Finstad et al., 1988a) as:

$$\mathrm{X}(K,\phi) = \left[C_{X,1}K^{C_{X,2}}\exp\left(C_{X,3}K^{C_{X,4}}\right) + C_{X,5}\right] - \left[C_{X,6}(\phi - 100)^{C_{X,7}}\right] \times \left[C_{X,8}K^{C_{X,9}}\exp\left(C_{X,10}K^{C_{X,11}}\right) + C_{X,12}\right] \quad (5)$$

where X is either the overall collision efficiency E, the stagnation line collision efficiency β_0, the maximum impingement angle α_{max}, or the non-dimensional impact velocity V_0. The constants $C_{X,n}$ are listed in Table 3.

Table 3 – Coefficient values of cloud impingement parameters (Finstad et al., 1988a).

Coefficient	**X = β_0**	**X = α_{max}**	**X = E**	**X = V_0**
$C_{X,1}$	1.218	2.433	1.066	1.030
$C_{X,2}$	-6.70×10^{-3}	-4.70×10^{-3}	-6.16×10^{-3}	1.68×10^{-3}
$C_{X,3}$	–0.551	–0.375	–1.103	–0.796
$C_{X,4}$	–0.643	–0.576	–0.688	–0.780
$C_{X,5}$	–0.170	–0.781	–0.028	–0.040

$C_{X,6}$	3.05×10^{-3}	8.50×10^{-3}	6.37×10^{-3}	9.44×10^{-3}
$C_{X,7}$	0.430	0.383	0.381	0.344
$C_{X,8}$	2.220	1.757	3.641	2.657
$C_{X,9}$	–0.450	–0.298	–0.498	–0.519
$C_{X,10}$	–0.767	–0.420	–1.497	–1.060
$C_{X,11}$	–0.806	–0.960	–0.694	–0.842
$C_{X,12}$	–0.068	–0.179	–0.045	–0.029

The ice deposit diameter D_i of cylinder is calculated as (Makkonen, 1984):

$$D_i = \left[\frac{4(M_i - M_{i-1})}{\pi\rho_i} + D_{i-1}^2\right]^{1/2} \tag{6}$$

Where M is the mass accretion value per unit length, ρ is the ice density and subscript i indicates the time step. In all analytical calculations the time step used is, t =12 seconds. This is to ensure that the cylinder rotates at least 360° degrees along its longitudinal axis on each time step to ensure even ice deposit on the surface, in accordance with (Makkonen, 1984). The accreted ice density at any given time step is calculated as (Makkonen, 1984).:

$$\rho_i = 378 + 425\log_{10}(R_m) - 82.3\left(\log_{10}(R_m)\right)^2 \tag{7}$$

where, R_m is the Macklin density parameter, given as:

$$R_m = -\frac{V_0 d}{2t_s} \tag{8}$$

Where d is the MVD in microns, V_0 is the impact velocity of the droplet in m/s and t_s is the surface temperature of the ice deposit in Celsius. In the case of dry growth the surface temperature of the ice deposit can be obtained numerically as:

$$\frac{2}{\pi}Evw\left(L_f + c_w t_a - c_i t_s\right) = h\left[(t_s - t_s) + \frac{kL_s}{c_p p_a}(e_s - e_a) - \frac{rv^2}{2c_p}\right] + \sigma\alpha(t_s - t_s) \tag{9}$$

where L_f and L_s are latent heats of fusion and sublimation respectively, c_w, c_i, and c_p are specific heats of water, ice and air respectively, p_a, e_s and e_a are air pressure, saturation water vapour pressures at surface and air temperatures respectively, h is the overall heat transfer coefficient, k = 0.62, r is the recovery factor, with value of 0.79 being used for cylinder, t_s and t_a are surface and air temperatures in Celsius, σ is the Stefan-Boltzmann constant and $\alpha = 8.1 \times 10^7$ K^3. More details on the terms of heat transfer and derivation of heat transfer equations are given in (Makkonen, 1984).

2.2 Experimental Setup

The experiments were conducted in the VTT icing wind tunnel. This is an “open-loop” tunnel placed entirely inside a large cold room. The cross-section of the tunnel mouth is 0.7m by 0.7m. Ice was accumulated on 0.157m long smooth aluminium cylinder, 30mm in diameter, placed vertically and

rotated by a motor at a constant 5 RPM. The schematic of the icing wind tunnel is given in Figure 2. To rule out the effect of blockage, the cylinder was located in front of the exit of the tunnel. The temperature and wind speed in the test section were measured using calibrated sensors. The liquid water content (LWC) was calibrated for each wind speed and temperature pair by measuring the ice growth on a 30mm cylinder and using the formulas defined in ISO 12494 (ISO, 2001). Under the test conditions, LWC was 0.4 g/m^3. The air temperature was –5 °C and wind speed 4 m/s. The droplet size distribution in the icing tunnel has been calibrated by using The Cloud, Aerosol and Precipitation Spectrometer probe (CAPS), which can measure small particles between 0.61 and 50 µm by utilizing the light scattering principle (CAPS, Droplet Measurement Technologies, Boulder, CO, USA).

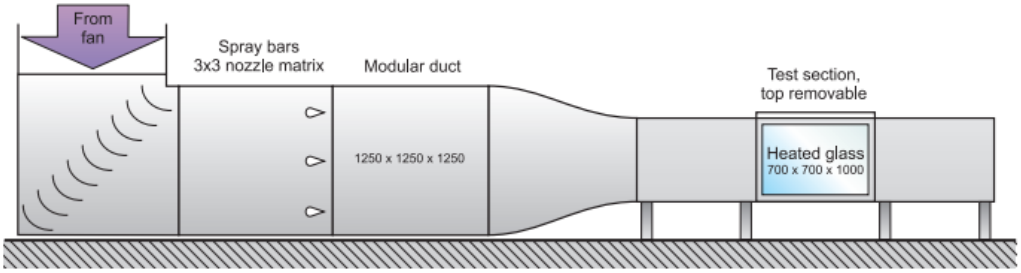

Figure 2 – Icing wind tunnel schematic (VTT, 2016).

The cylinder in the experiments was weighted using electronic scales with precision of ±0.001 gram. The diameter of the cylinder after the ice accretion was measured using cooled calipers. Those measurements were conducted every 30 minutes. An example of ice shape obtained from the icing tunnel experiments is shown in Figure 3.

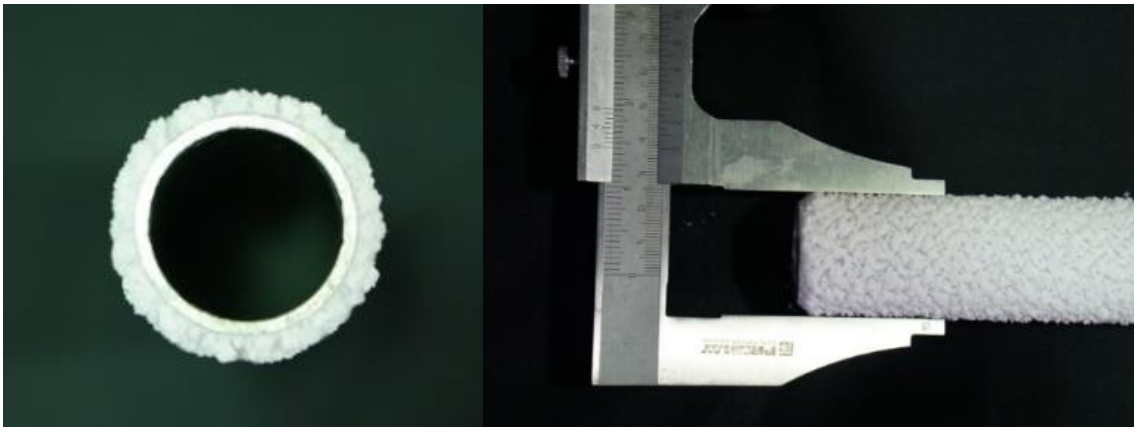

Figure 3 –Ice shape from icing tunnel experimentations for 30 mm cylinder.

2.3 Numerical Setup

The multiphase CFD based numerical simulations were carried out using ANSYS FENSAP-ICE, which uses an Eulerian water droplet impingement solver. The general Eulerian two-phase model for viscous flow consists of the Navier-Stokes equations augmented by the droplets continuity and momentum equations (FENSAP User Manual):

$$\frac{\partial \alpha}{\partial t} + \vec{\nabla} \cdot \left(\alpha \overrightarrow{V_d}\right) = 0 \tag{10}$$

$$\frac{\partial \left(\alpha \overrightarrow{V_d}\right)}{\partial t} + \vec{\nabla}\left[\alpha \overrightarrow{V_d} \otimes \overrightarrow{V_d}\right] = \frac{C_D Re_d}{24K} \alpha \left(\overrightarrow{V_a} - \overrightarrow{V_d}\right) + \alpha \left(1 - \frac{\rho_a}{\rho_d}\right) \frac{1}{Fr^2} \tag{11}$$

where the variables α and $V_{d,a}$ are mean field values of, respectively, the water volume fraction and droplet velocity. The first term on the right-hand-side of the momentum equation represents the drag acting on droplets of mean diameter *d*. It is proportional to the relative droplet velocity, its drag coefficient C_D and the droplet Reynolds number:

$$Re_d = \frac{\rho_a d V_{a,\infty} \left\| \overrightarrow{V_a} - \overrightarrow{V_d} \right\|}{\mu_a} \tag{12}$$

$$K = \frac{\rho_d d^2 V_{a,\infty}}{18 L_\infty \mu_a} \tag{13}$$

Where L_∞ is the characteristic length of the object. In case of the cylinder, the characteristic length is cylinder radius. The second term represents buoyancy and gravity forces, and is proportional to the local Froude number:

$$\mathrm{Fr} = \frac{\left\| V_{a,\infty} \right\|}{\sqrt{L_\infty g_\infty}} \tag{14}$$

These governing equations describe the same physical droplet phenomenon as the Lagrangian particle tracking approach. Only the mathematical form in which these equations are derived changes, using Partial Differential Equations instead of Ordinary Differential Equations. The droplet drag coefficient is based on an empirical correlation for flow around spherical droplets, or:

$C_D = (24/Re_d)\,(1 + 0.15 Re_d^{0.687})$ for $Re_d \leq 1300$

$C_D = 0.4$ for $Re_d > 1300$

The droplet local collision efficiency is calculated as follows:

$$\beta = -\frac{\alpha \overrightarrow{V_d} \cdot \vec{n}}{(\mathrm{LWC}) V_\infty} \tag{15}$$

where α is the local volume fraction (kg/m^3) and $\vec{n}$ is the surface normal vector. The total collision efficiency is an integration of local collision efficiencies over the surface area and is given as:

$$\beta_{\mathrm{tot}} = \frac{\int \beta \, dA}{L_\infty^2} \tag{16}$$

The ice density calculation procedures in FENSAP follows that given in the analytical model.

Detailed mesh sensitivity analysis were carried out to accurately determine the boundary layer characteristics (shear stress and heat fluxes), a *y*+ values of less than 1 is used near the cylinder wall surface. Number of mesh elements and *y*+ value was selected based upon the heat flux calculations, where a numerical check was imposed that the heat flux computed with the classical formulae dt/d*n* should be comparable with the heat flux computed with the Gresho's method.

3 Results and Discussion

3.1 Analytical Modeling

In this subsection the focus is to demonstrate the effect of the droplet distribution spectrum on cloud impingement parameters using the analytical procedure. The comparison is done using a series of graphs, which show the average value for each parameter, using algebraic value of all time steps. The purpose of this is to take into account the effect of the continued ice accretion process on respective values. Figure 4 shows the values for inertia parameter (K), normalized impact velocities at stagnation line in m/s (V_0), stagnation line local collision efficiencies (β_0), maximum impingement angles (θ) and overall collision efficiencies (E), respectively for all distributions. The "*spectrum averaged*" graphs present the spectrum averaged values of the respective parameter and how much each distribution contributes towards the average value with the exception of maximum impingement angles. The color code of Figures 4 and 5 should be read as follows: each unique color represents a single bin from any given distribution used from Figure 1 or Table 1. The right-hand side of Figures 4 and 5, which shows the "spectrum-averaged" values in a "stacked" way "stacks" the individual values of each bin, weighted by its respective LWC in order to obtain the "spectrum-averaged" values, where again, each unique color represents the contribution of individual bin towards the final value of a given cloud impingement parameter.

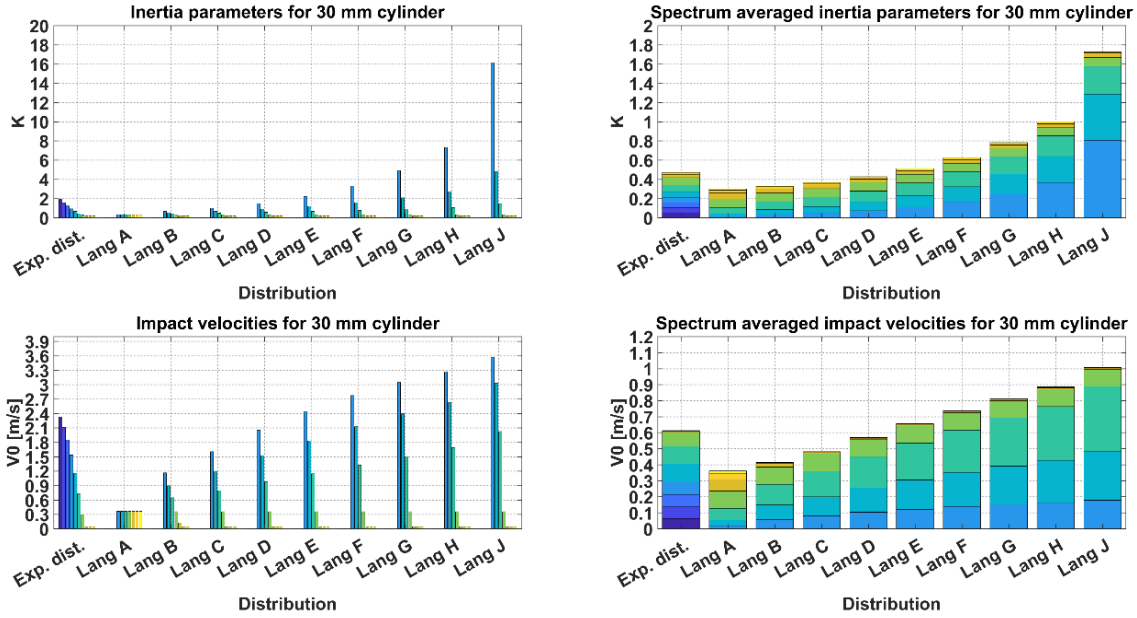

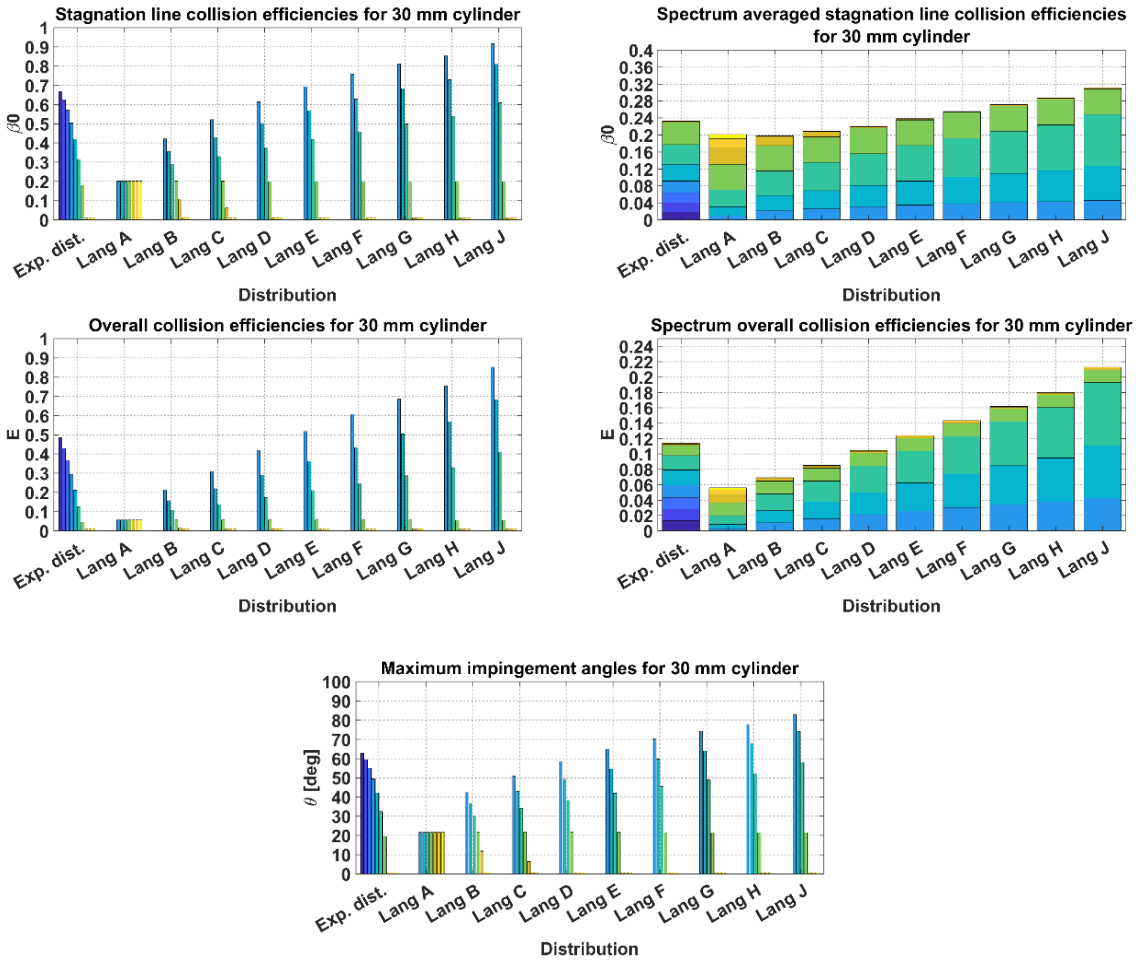

Figure 4 – The values of cloud impingement parameters in the analytical model on per-bin basis (left) and spectrum-averaged values (right).

While it may be hard to estimate the change of any of the respective parameters during the process from the figures, the typical observed differences between start and end values for all parameters are within 2–3% for the ice accretion process under operating conditions from Table 1. However, for bins with smaller diameters, the limit of $K = 0.17$ is quickly reached and for distribution D and above the three smallest bins are consistently below the constraint value, meaning that limits of $E = \beta_0 = \nu_0 = \theta = 0.01$ are enforced and there is virtually no distinction between. However, the change in parameters of interest between larger droplet diameters in said distributions, when compared to the MVD value of 18.73 microns is of considerably larger magnitude, which smooths the impact of the constrained values to a large extent. In order to investigate the differences in values of cloud impingement parameters in a more concise manner, Table 4 lists the results of analytical calculations for all cloud impingement parameters with distributions from Figure 1 and Table 2 for MVD of 18.73 micron. In Tables 4 and 5 the "*Exp. dist. (E.d.)*" row refers to the results obtained using the experimental distribution from Figure 1, while the "*Experiment*" row refers to the experimentally measured values.

Table 4 – Spectrum weighted parameters values in analytical model.

Distribution	*Parameter*							
	K	***V₀* (m/s)**	**β₀**	**θ (deg)**	***E***	***M* (g)**	***D* (mm)**	**ρ**
A	0.302	0.362	0.201	21.615	0.056	0.768	30.3	305.893
B	0.327	0.416	0.198	42.305	0.069	0.948	30.4	332.773
C	0.365	0.481	0.209	50.776	0.085	1.165	30.4	360.764
D	0.428	0.572	0.220	58.435	0.105	1.433	30.5	392.476
E	0.512	0.657	0.238	67.745	0.124	1.698	30.5	417.314
F	0.627	0.737	0.256	70.007	0.143	1.964	30.6	437.845
G	0.784	0.813	0.272	74.309	0.162	2.221	30.7	454.717
H	1.002	0.885	0.287	77.795	0.180	2.474	30.7	469.165
J	1.725	1.008	0.312	82.816	0.213	2.926	30.8	490.821
Exp. dist. (E.d.)	0.471	0.612	0.232	62.899	0.114	1.560	30.5	405.348
Experiment	0.458	–	–	–	**0.086**	**1.163**	–	–

As it is seen from Table 4, all cloud impingement parameters increase in their respective values with the increase of value in the droplet inertia parameter *K*, associated with change of the droplet distribution spectrum. The primary reason for said increase in the values of *K* is the significantly larger contribution to the spectrum-averaged values of droplet inertia parameter of individual bins with large droplet sizes, as it is seen from Figure 4. The resultant increase in values of the cloud impingement parameters is non-linear, primarily due to the structure of eq. (5) itself, and secondly, due to non-linear increase in the values of *K* associated with the change of the droplet distribution spectrum.

3.2 Numerical Analysis

The numerical simulations results for all distributions and bins are given in Figure 5, following the same methodology as was used in presenting the analytical results in Figure 5.

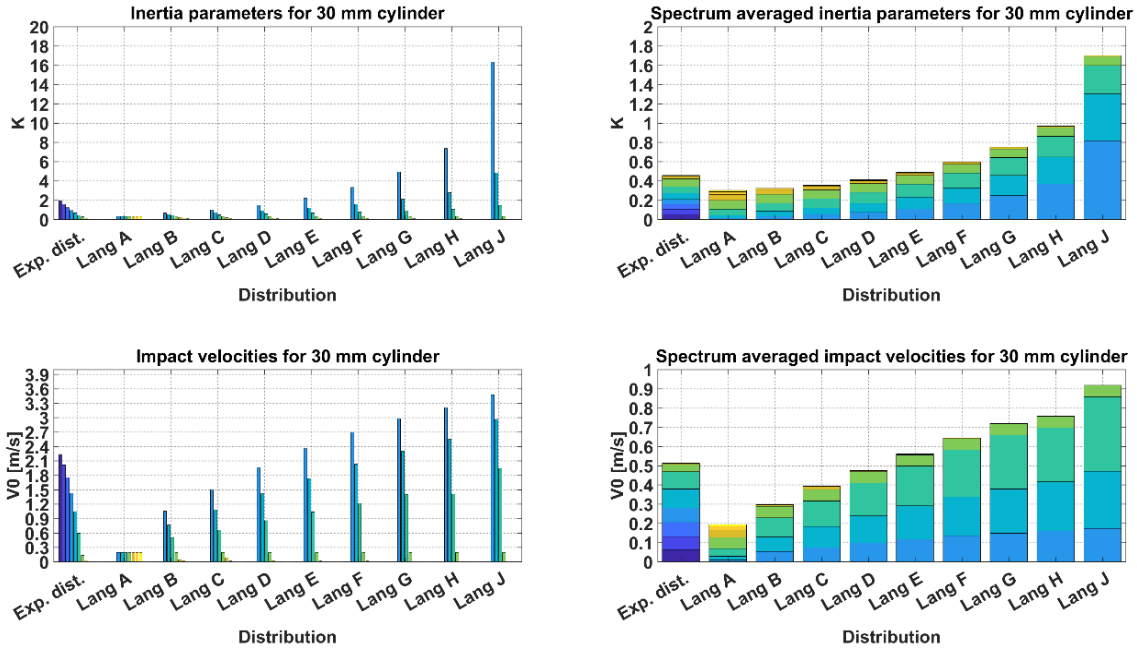

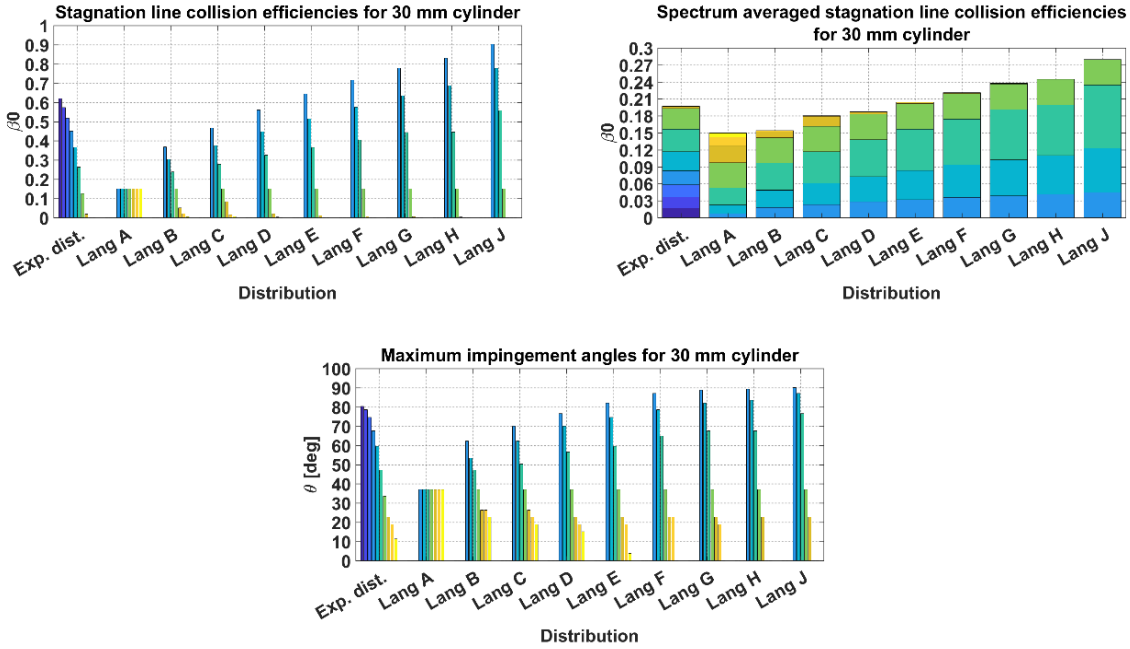

Figure 5 – The values of cloud impingement parameters in the numerical model on per-bin basis (left) and spectrum-averaged values (right).

Numerical analysis show that in Figure 5, the maximum impingement angle remains unchanged for some droplets with different diameters, typically pertaining to smaller bins. The reason for this is that simulation data is output in terms of discrete "nodes" with coordinates and values of the respective parameter of that node, meaning that the precision is inherently limited to the amount of cylinder nodes in the simulation, as if any given property reaches value of zero in-between the nodes it will be rounded-up to the coordinates of the closest node. Furthermore, observe that in some of the cases, the reported value of the stagnation line collision efficiency is zero, while the impingement angle is not. The reason for this is the rounding to the three significant digits. Furthermore, since the values of inertia parameter in numerical simulations are not restricted in the same manner as in the analytical model, the values of impingement parameters can be below 0.01. Observe, that in numerical simulations the stagnation line collision efficiency and maximum impingement angles are equal to zero only for very small droplets, typically of the diameter of 5 microns or less, which gives a rough value of inertia parameter of 0.03. This differs from the assumptions of (Langmuir and Blodgett, 1944) and (Finstad, 1986) that those respective values can be equal to zero in cases of $K < 0.125$ and $K < 0.14$ respectively. Moreover, the impact velocities in the numerical simulations are never equal to zero. The total ice masses and the overall collision efficiency values after 30 minutes of ice accretion along cylinder with spectrum weighted data from Figure 5 are given in Table 5.

Table 5 – Spectrum weighted parameters values from numerical simulations.

Distribution	***Parameter***					
	K	***V*₀ (m/s)**	**β₀**	**θ (deg)**	***E***	***M* (g)**
A	0.304	0.198	0.150	37.066	0.037	0.506
B	0.320	0.299	0.154	62.272	0.053	0.713
C	0.356	0.382	0.169	70.002	0.067	0.915

D	0.412	0.474	0.187	76.639	0.086	1.163
E	0.489	0.560	0.204	82.013	0.104	1.415
F	0.599	0.643	0.221	87.097	0.123	1.674
G	0.753	0.720	0.238	88.705	0.142	1.928
H	0.971	0.758	0.245	89.272	0.153	2.073
J	1.700	0.921	0.280	90.000	0.195	2.641
Exp. dist. (E.d.)	0.458	0.534	0.198	81.09	0.095	1.286
Experiment	0.458	–	–	–	**0.086**	**1.163**

Summarizing the results in Tables 4 and 5, the rotating cylinder in CFD simulations for all tested distributions exhibits smaller values in impact velocities, stagnation line and overall collision efficiencies, and by extension, the total accreted ice masses, while the values of maximum impingement angle are bigger than in the analytical model, even considering the potential impact of cylinder surface discretization and resultant nodes placement impact on maximum impingement angle in numerical simulations. Moreover, the use of modern CFD tools allows for in-depth investigation of a several concepts, not covered within the scope of the ISO 12494 model, such as viscous and boundary layer effects, liquid water content and droplet concentrations, vorticity and vorticity shedding, etc. As an example, Figure 6 shows droplet velocity magnitudes, impingement angles and local collision efficiencies for a few selected distributions.

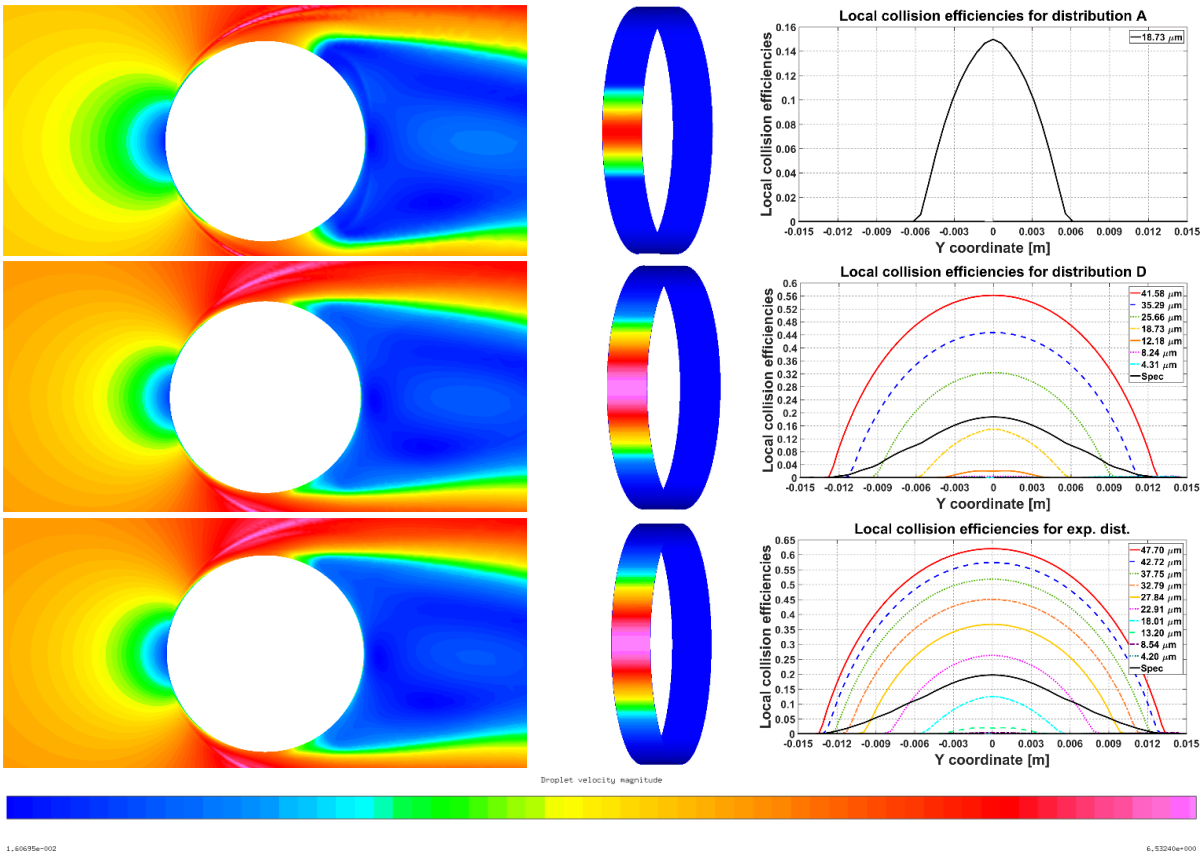

Figure 6 – Droplet velocity magnitude (left), impingement angles (middle) and local collision efficiencies (right) for monodisperse (top), Langmuir D (middle) and experimental (bottom) distributions.

Figure 6 shows that the droplet behaviour changes extensively, depending on the droplet distribution spectrum used. Observe the significant difference in the maximum impingement angles, local collision efficiencies and much more “intricate” structure of the local collision efficiencies values, which directly correspond to the spectrum-weighted collision efficiencies, denoted as solid black line in Figure 6. Moreover, the maximum impingement angles seem to coincide well with the velocity minima from the velocity magnitude plots. In addition, the flow separation is much more clearly observed in said plots for experimental and Langmuir D distributions. As an overall, the numerical simulations are well suited for detailed studies of the droplet distribution spectrum effects and the ice accretion modeling in general, as multiple different cloud impingement parameters can be investigated and compared in detailed manner, which is not possible using analytical approach.

3.3 Comparison of Analytical, Numerical and Experimental Analysis

Summarizing the results from Tables 4 and 5, the analytical model tends to predict higher values of the stagnation line droplet collision efficiencies and impact velocities and as a result, the accreted ice masses. Contrary, the numerical results have higher values of the maximum impingement angles. Moreover, the relative increase in the values of the stagnation line collision efficiency and impact velocity, the overall collision efficiency and the total accreted ice mass, arising with the change of droplet distribution spectrum is also higher in the numerical results, while the relative increase in the values of the maximum impingement angle is higher in the analytical results. The higher values of the overall collision efficiency in the analytical results are expected to some extent due to the potential flow theory limitations, as discussed in (Yoon and Ettema, 1993).

In comparison, the experimental accreted ice mass is 1.163 grams, which results in an overall collision efficiency of 0.086. When comparing with analytical and numerical results from Tables 4 and 5 respectively, the closet fit distributions are distribution C for analytical results and distribution D for numerical results, respectively, with values of total ice mass and overall collision efficiency of 1.165 grams, 0.085 and 1.163 grams and 0.086, respectively. This match experimental results within the margin of error considering the rounding-up in calculations. Albeit unexpectedly the experimental distribution tends to produce higher values of overall collision efficiency and total ice mass in both analytical and numerical results, being 1.560 grams and 0.114 respectively for analytical results and 1.286 grams and 0.095 for numerical results respectively. Some of this difference can be explained by restricting the inertia parameter in the analytical model and some possible uncertainty when it comes to the measured droplet spectrum in the tunnel. Moreover, the overestimation of overall collision efficiency can also be explained by the potential flow theory limitations, as was discussed in (Yoon and Ettema, 1993).

From Tables 4 and 5, it can be seen that results from monodisperse distribution are bad when compared to the experimental values. Monodispersed distribution failed to reproduce experimental values both in analytical and numerical calculations, and gave the lowest values for all the parameters across all distributions. However, based on the experimental verification of the Finstad et. al model done by (Makkonen and Stallabrass, 1987) along with discussion on some spectra properties done by (Langmuir

and Blodgett, 1944), with recent investigation of droplet spectra effects by (Jones et. al., 2014) may suggest that this conclusion applies to cases with low values of inertia parameter only.

Furthermore, the governing theory from the ISO 12494 standard does not focus directly on the aspects of different cloud impingement parameters on ice accretion process other than the overall collision efficiency. While, as was discussed previously, the ISO 12494 theory and conducted experimental verification, such as in (Makkonen and Stallabrass, 1987) make the theory well developed and understood for the majority of typical icing situations and related engineering applications, especially those at higher wind speeds for long-term or extreme icing events the impact of those parameters, associated with the droplet distribution spectrum may be important in order to properly estimate the extreme or long term loads such icing conditions can exert on cylindrical structures, such as power lines or masts. Moreover, other factors, not accounted for in this study, such as surface roughness, sublimation and deposition, viscous and boundary layer effects may become prominent in cases where the inertia parameter is sufficiently low. However, the usage of the CFD tools as with this work, in addition to some recent results (Makkonen et al., 2018) show the CFD simulations are well suited for modeling of the ice accretion at the low values of *K*. As an example, a graphical comparison of the overall collision efficiency values in the analytical and numerical results is given in Figure 7. The practical meaning of Figure 7 is to display the difference in relative ice accretion values between the analytical and the numerical model in a concise manner.

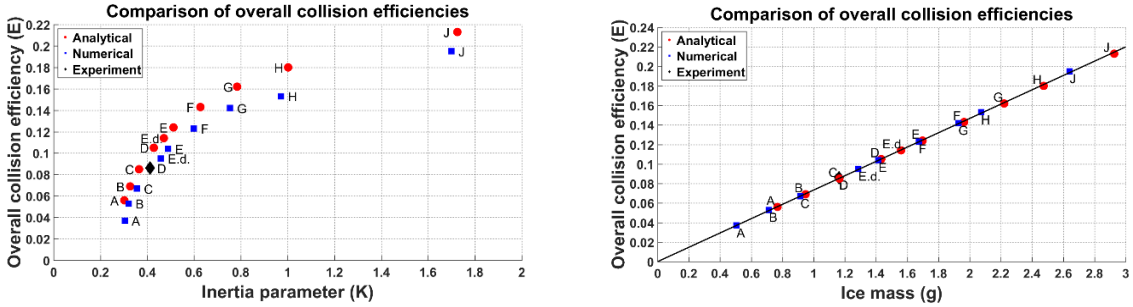

Figure 7 – Comparison of analytical and numerical overall collision efficiency values. The distributions used are marked by the text. The numerical results are displayed below the reference line.

As it can be seen from the Figure 7, the monodisperse distribution (labelled "*A*") in both analytical and numerical cases tends to significantly underestimate the overall collision efficiency when compared to the actual experimental value (represented by the diamond). On the other hand, Langmuir D distribution yields good agreement with the experiment for the analytical case, and matches it exactly in the CFD simulations, while in the analytical results distribution C is very close to the experimental value of overall collision efficiency. The experimental distributions for both cases tends to overestimate the value of overall collision efficiency, however, for the CFD results the absolute error is approximately 0.01. Moreover, as it can be seen from Figure 7, the CFD and analytical results normally follow each other well, with the analytical results t having slightly higher values of the overall collision efficiency. This shows that modern CFD tools are well capable of simulating the ice accretion at low values of *K*, with $K \approx 0.4$ ($K \approx 0.3$ if calculated with MVD approximation) for the conditions in this study.

While it is difficult to properly judge the effects of surface roughness, due to associated issues with proper experimental measurements and modeling, both analytical and numerical, the viscous and boundary layer effects may be more explicable and easily observed in future experiments, provided strict control over experimental conditions is established and proper measuring devices are used. Overall, further experimental, analytical and numerical investigations into those aspects are deemed necessary in order to expand the understanding of connected terms on ice accretion process. In addition, the usage of the Langmuir D distribution as sort of a “first guess" distribution is recommended, as it is typically and successfully employed for aircraft icing studies (Bidwell, 2012), (Papadakis et. al, 2007), (Wright, 2008).

4 Conclusion

Within the scope of this paper a detailed analytical study along with a series of numerical simulations were performed for experimental data of ice accretion on a 30 mm cylinder. Results show that the droplet distribution spectrum change has a significant effect on the overall and local collision efficiencies, maximum impingement angles, droplet impact velocities, ice densities and ice mass accretion. The associated changes in the results are significant enough to cause the theory to either under estimate, be within the margin of error or significantly over estimate experimental results, depending on the droplet distribution chosen. Moreover, the numerical and analytical results tend to have some differences in the results, with tendency towards better agreement in the results of wider distributions with higher value of inertia parameter. This shows that care is needed when dealing with droplet distributions even with matching MVDs as those distributions do not have the same value of inertia parameter. The reported results are deemed valid for low values of droplet inertia parameter *K*.

Some of those differences can be explained using viscous, boundary layer and surface roughness effects, however, due to limitations of existing theory, particularly when it comes to inviscid flow assumption of the ISO model, further investigation in those aspects necessitates more experimental evidence in carefully controlled conditions, as it has been shown how a change in droplet distribution spectrum affects ice accretion on the cylinders, at lower values of droplet inertia. Overall, the further experimental, analytical and numerical investigations into those aspects at lower values of the droplet inertia parameter are deemed necessary in order to expand the understanding of connected terms on ice accretion process and performance of current icing theory in cases with low values of droplet inertia parameter. Out of those, the CFD simulations show good results for the low values of *K*, and as it has been shown in this work, allow for studying the variety of different parameters and their effect on the ice accretion process. For the low values of *K*, which correspond to the values of *E* being 0.10 or less the usage of the full droplet spectrum is recommended in calculations. In addition, based on the results of this and previous works the Langmuir D distribution is recommended as a first guess distribution.

Summarizing, the numerical model results produce the best agreement with the experimental results for narrower distributions B–E, while wider distributions tend to overestimate the accreted ice values. The analytical results tend to match experimental results well for distributions B–D, however, in general they tend to overestimate the accreted ice more than the numerical results, in particular for wider distributions F–J, however, this property can be exploited in the extreme value analysis of the icing events and ice maps generation.

Acknowledgment

The work reported in this paper is funded by the Research Council of Norway, FRonTLINES- project no. 245370 & IceBOX- project no 282403. Authors would like to acknowledge Mr. Timo Karlsson and Mr. Miko Tiihonen from VTT for providing icing wind tunnel experimental data used in this research work.

References

1. Bidwell, C.S., 2012, Particle Trajectory and Icing Analysis of the E3 Turbofan Engine Using LEWICE3D Version 3, NASA/TM–2012-217696, NASA
2. Cansdale, J., McNaughton, M., 1977. Calculation of Surface Temperature and Ice Accretion Rate in a Mixed Water Droplet/ice Crystal Cloud.
3. Finstad, K. J. 1986. Numerical and experimental studies of rime ice accretion on cylinders and airfoils. Ph.D. thesis. University of Alberta, Canada.doi:10.7939/R3N58CS1V.
4. Finstad, K.J., Lozowski, E.P., Gates, E.M., 1988a. A computational investigation of water droplet trajectories. Journal of Atmospheric and Oceanic Technology, 5, 160-170.doi:10.1175/1520-0426(1988)005<0160:ACIOWD>2.0.CO;2
5. Finstad, K.J., Lozowski, E.P., Makkonen, L., 1988b. On the median volume diameter approximation for droplet collision efficiency. Journal of the Atmospheric Sciences 45, pp. 4008–4012.doi: 10.1175/1520-0469(1988)045<4008:OTMVDA>2.0.CO;2
6. Howe, J.B. 1990. The rotating multicylinder method for the measurement of cloud liquid water content and droplet size. CRREL Report.
7. ISO 12494:2001(E), 2001. Atmospheric icing of structures. Standard. International Organization for Standardization. Geneva, CH
8. Jones, K.F., Thompson, G., Claffey, K.J., Kelsey, E.P, 2014, Gamma Distribution Parameters for Cloud Drop Distributions from Multicylinder Measurements. Journal of Applied Meteorology and Climatology, vol. 53, pp. 1606 – 1617. doi: 10.1175/JAMC-D-13-0306.1
9. Landau, L., and E. M. Lifshitz, "Fluid Mechanics," Pergamon Press, pp. 96-98, 1959.
10. Langmuir, I., Blodgett, K., 1946. A Mathematical Investigation of Water Droplet Trajectories. Army Air Forces technical report 5418. Army Air Forces Headquarters, Air Technical Service Command.
11. Lozowski, E.P., Stallabrass, J.R., Hearty, P.F., "The icing of an unheated, non-rotating cylinder in liquid water droplet-ice crystal clouds," National Research Council of Canada, Ottawa, CANADA, Mechanical Engineering Report LTR-LT-96, Feb. 1979.
12. Lozowski, E.P., Makkonen, L., 2005. Fifty years of progress in modelling the accumulation of atmospheric ice on power network equipment, in: Proceedings of the 11th International Workshop on Atmospheric Icing of Structures.
13. Macklin, W.C., 1962. The density structure of ice formed by accretion. Quarterly Journal of Royal Meteorological Society, vol. 88 pp. 30–50.
14. Makkonen, L., 1984. Modeling of Ice Accretion on Wires. Journal of Applied Meteorology 23, 929-939. doi:10.1175/1520-0450(1984)023<0929:MOIAOW>2.0.CO;2
15. Makkonen, L., Stallabrass, J.R., 1987. Experiments on the cloud droplet collision efficiency of cylinders. Journal of Applied Meteorology 26, 1406-1411.doi:10.1175/1520-0450(1987)026<1406:EOTCDC>2.0.CO;2
16. Makkonen, L., 2000. Models for the growth of rime, glaze, icicles and wet snow on structures. Phil. Trans. R. Soc., Lond. A 2000 358 2913-2939; DOI: 10.1098/rsta2000.0690. Published 15 Nov. 2000

17. Makkonen, L., Zhang, J., Karlsson, T., Tiihonen, M., Modelling the growth of large rime ice accretions, CRST, 151 (2018), 133-137.
18. Papadakis M., Wong, S.-C., and Rachman, A, Large and Small Droplet Impingement Data on Airfoils and Two Simulated Ice Shapes, NASA/TM—2007-213959, October 2007
19. Ratvasky, T.P., Barnhart, B.P., Lee, S. Current Methods for Modeling and Simulating Icing Effects on Aircraft Performance, Stability and Control, NASA/TM—2008-215453, AIAA–2008–6204
20. Stallabrass, J.R., 1980. Trawler Icing: A Compilation of Work Done at N.R.C. (Givrage Des Chalutiers: Compilation Des Recherches Effectuees Au C.N.R.). Defense Technical Information Center.
21. Tsao, J.-C., Anderson, D.N, Additional Study of Water Droplet Median Volume Diameter (MVD) Effects on Ice Shapes, Conference: 42n AIAA Aerospace Sciences Meeting and Exhibit, At Reno, NV, Volume: AIAA 2004-0413, January 2004
22. http://www.vttresearch.com/Documents/Low%20Carbon%20Energy/Wind%20energy/Icing_Wind_Tunnel_02022016.pdf
23. Wagner, T. Modelling of Wind Borne Ice Accretion on Power Transmission Lines, Doctoral Thesis, University of Braunschweig, August 2010
24. Wiberg, B.D., Fujiwara, G.E.C., Woodard, B.S., and Bragg, M.B., "Large-Scale, Swept-Wing Icing Simulations in the NASA Glenn Icing Research Tunnel Using LEWICE3D," AIAA Paper 2014-2617, June 2014.
25. Wright, W., 2008, User's Manual for LEWICE Version 3.2, NASA/CR–2008-214255, NASA

Paper 3. An Investigation into Empirical Ice Density Formulations for Dry Ice Growth on Cylinders

Pavlo Sokolov and Muhammad Shakeel Virk

Cold Regions Science and Technology, 2019, Volume 169. pp. 119 – 127.

DOI: 10.1016/j.coldregions.2019.102906

Author's Contribution

Pavlo Sokolov has contributed substantially in the proposal of research idea, literature review, modelling, computing, analytical, experimental and numerical analysis, and writing of the paper.

An Investigation into Empirical Ice Density Formulations for Dry Ice Growth on Cylinders

Pavlo Sokolov[1,†], Muhammad S.Virk[1]

[1] *Institute of Industrial Technology, University of Tromsø – The Arctic University of Norway, Post Box 385, 8505, Narvik*

†*Corresponding Author Email: pavlo.sokolov@uit.no*

Abstract

This paper describes an investigation into the empirical accreted icing density formulations, namely the numerical fits by (Makkonen and Stallabrass, 1984) and (Jones, 1990). Typically, the icing severity is estimated by the masses of the accreted ice, however, for this study the focus is primarily on the accreted ice densities and thicknesses for the main purpose of estimating the ice loads, in particular for the cases when the ice mass measurements are not readily available and other indirect measurements such as observed ice thicknesses can to be used as an estimate. The results were obtained for both the analytical and numerical modeling in comparison with the icing tunnel experiments. Seven different diameters of cylinders ranging from 20 to 298 mm are used. Analysis show that Makkonen and Stallabras (M&S) fit tends to have good agreement with the smaller cylinders, while it tends to underestimate the icing thicknesses for the larger cylinder diameters. On the other hand, the Jones ice density formulation shows consistently better results for almost all tested cases and especially for the larger cylinder diameters. The results with the MVD approximation show good agreement mainly for smaller diameter cylinders whereas the agreement for the larger cylinders is not good primarily due to low values of droplet inertia parameter *K*, which puts the results using the MVD approximation outside of the verified range of the current icing theory. Thus, calculations with the full droplet distribution spectrum are recommended.

Keywords: Ice accretion; Ice density; Ice thickness; Cylinder; Droplet distribution spectrum; MVD.

1 Introduction

The interest in modeling ice accretion on cylindrical objects primarily comes from preventing structural damage or collapse of objects such as overhead transmission lines or communication masts due to the accreted ice mass leading to dynamical instabilities. The theoretical modelling of icing is covered by ISO 12494, where the icing theory framework is valid for the droplet overall collision efficiency range of $0.07 < E < 0.63$ (Makkonen *et al*., 2018), though, the ISO 12494 model framework scope is rather limited when it comes to the long term modeling of the in-cloud icing events on the power lines and structures. Such long-term icing events can lead to significant ice loads over longer timeframes, where the ice can accrete in multiple "stages" under different operating conditions. These events can be more critical in remote areas, where frequent monitoring of structures and accreted ice is unlikely.

The primary attribute of continued ice accretion, which is the change of the object's characteristic length, in case of circular structures this length being the diameter, have been theoretically modeled by

(Makkonen, 1984). However, the accreted ice mass and its density govern the change in the object's diameter. While the accreted ice mass and its modeling is the primary focus of the ISO 12494 theoretical framework, the accreted ice density had received less attention in it. This may be critical if direct measurements of the accreted ice deposit on the structure cannot be performed and only indirect measurements such as visual estimation of deposit thickness can be performed.

Currently, there are several empirical accreted ice density formulations, such as (Macklin, 1962), (Pfaum and Pruppacher, 1979), (Bain and Gayet, 1983), (Makkonen and Stallabrass, 1984), (Jones 1990) etc. As noted in (Jones, 1990) all empirical ice density formulations, which are based on the usage of the Macklin parameter, were obtained based on the cold room icing wind tunnel experimental results (Macklin, 1962), (Makkonen and Stallabrass, 1984), instrumented wind tunnel in natural conditions (Bain and Gayet, 1983), or in cloud chamber (Pfaum and Pruppacher, 1979). On the contrary, the empirical ice density in (Jones, 1990) was developed based on the multicylinder measurements in natural conditions on Mt. Washington.

These empirical ice density formulations are also incorporated in the modern CFD solvers, which have now become increasingly popular for the modeling of atmospheric icing on structures. Therefore, the focus of this study is to ascertain how these empirical icing density formulations, both in the analytical and numerical analyses are suitable for modeling of ice density and thickness, in order to investigate their suitability for modeling of long-term icing events, especially when the direct ice masses measurements are not available.

2 Models setup

2.1 Analytical Model

The cloud impingement parameters are calculated in accordance to (Finstad *et al*., 1988):

$$\begin{aligned} \mathrm{X}(K,\phi) = &\left[C_{X,1}K^{C_{X,2}}\exp\left(C_{X,3}K^{C_{X,4}}\right) + C_{X,5}\right] - \left[C_{X,6}(\phi - 100)^{C_{X,7}}\right] \\ &\times\left[C_{X,8}K^{C_{X,9}}\exp\left(C_{X,10}K^{C_{X,11}}\right) + C_{X,12}\right] \end{aligned} \quad (1)$$

where X is either the overall collision efficiency E, the stagnation line collision efficiency β_0, the maximum impingement angle α_{max}, or the non-dimensional impact velocity V_0. The values of constants $C_{X,n}$ can be found in (Finstad *et al*., 1988).

The spectrum-averaged cloud impingement parameters are calculated as:

$$X(K, \phi)_{spec} = \sum w_i X(K_i, \phi) \quad (2)$$

where K is the droplet inertia parameter, and ϕ is the Langmuir parameter, defined as (Langmuir and Blodgett, 1946):

$$K_i = \frac{\rho_a d_i^2 v}{9\mu_a D} \tag{3}$$

$$\phi = \frac{18\rho_a^2 D v}{\rho_d \mu_a} = \frac{Re^2}{K} \tag{4}$$

where ρ_a and ρ_d are air and droplet's densities, respectively, μ_a is the density if air, D is the cylinder diameter, v is the operating wind speed and Re is the droplet's Reynolds number. Moreover, w is the volume fraction, d_i is the droplet MVD with the subscript "i" referring to the ith bin of the droplet distribution spectrum and subscript "$spec$" referring to the spectrum-averaged values. In the analytical model the constraint $X_i(K_i, \phi) = 0.01$ for $K_i \leq 0.17$ is used as per (Finstad *et al*., 1988).

The ice deposit diameter D_i of cylinder is calculated as (Makkonen, 1984):

$$D_i = \left[\frac{4(M_i - M_{i-1})}{\pi\rho_i} + D_{i-1}^2\right]^{1/2} \tag{5}$$

where M is the mass accretion value per unit length, ρ is the ice density and subscript i indicates the time step. In all analytical calculations the time step used is t =15 seconds. This is to ensure that the cylinder rotates at least 360° degrees along its longitudinal axis on each time step to ensure even ice deposit on the cylinder surface, in accordance with (Makkonen, 1984). The accreted ice density at any given time step is calculated as (Makkonen and Stallabrass, 1984):

$$\rho_i = 378 + 425\log_{10}(R) - 82.3\left(\log_{10}(R)\right)^2 \tag{6}$$

where, R is the Macklin ice density parameter, given as:

$$R = -\frac{V_0 d}{2T_s} \tag{7}$$

where d is the MVD in microns, V_0 is the impact velocity of the droplet in m/s and T_s is the surface temperature of the ice deposit in Celsius. In the case of dry growth the surface temperature of the ice deposit can be obtained numerically as (Makkonen, 1984):

$$\frac{2}{\pi} Evw\left(L_f + c_w t_a - c_i t_s\right) = h\left[(t_s - t_s) + \frac{kL_s}{c_p p_a}(e_s - e_a) - \frac{rv^2}{2c_p}\right] + \sigma\alpha(t_s - t_s) \tag{8}$$

where L_f and L_s are latent heats of fusion and sublimation respectively, c_w, c_i and c_p are specific heats of water, ice and air respectively, p_a, e_s and e_a are air pressure, saturation water vapor pressures at surface and air temperatures respectively, h is the overall heat transfer coefficient, k = 0.62, r is the recovery factor with value of 0.79 being used for cylinder, t_s and t_a are surface and air temperatures in Celsius, σ is the Stefan-Boltzmann constant and $\alpha = 8.1 \times 10^7$ K^3. More details on the terms of heat transfer and derivation of heat transfer equations are given in (Makkonen, 1984).

The “intermediate version” of icing density formulation of (Jones, 1990) is given as:

$\rho = 0.210R^{0.53}$ $\quad R \leq 10$

$\rho = R/(1.15R + 2.94)$ $\quad 10 < R < 60$

$\rho = 0.84$ $\quad R \geq 60$

This parametric fit using the Macklin parameter was obtained using the best-fit curves for three out of six cylinders from the multicylinder device and the observational data from the Mt. Washington. The reason this particular fit is called “intermediate version” is, as noted in (Jones, 1990) it explains less than 50% variation of the observed rime ice densities on the Mt. Washington. Therefore, (Jones, 1990) developed different empirical icing density formulation, using a range of mathematical and statistical arguments, as well as, employing the Buckingham π theorem, statistical and multi-regression analysis. This “final version” of the Jones icing density formulation explains 80% of rime ice density variation on the Mt. Washington and is as (Jones, 1990):

$$\rho = 0.249 - 0.0840 \ln \pi_C - 0.00624\left(\ln \pi_\phi\right)^2 + 0.135 \ln \pi_K + 0.0185 \ln \pi_K \ln \pi_\phi - 0.0339(\ln \pi_K)^2 \quad (9)$$

where π_K is the droplet inertia coefficient, π_ϕ is the Langmuir parameter and the term π_C is the ratio of the convective heat flux and the heat flux due to droplet freezing and is defined as:

$$\pi_C = \frac{k_a\,(-2T)/D}{wvL_f} \quad (10)$$

As noted in (Jones, 1990) when compared to the original empirical icing density formulation in (Macklin, 1962), the Jones ice density formulation should yield higher density values at lower values of the Macklin parameter R and lower ice density values at high values of R. The (Makkonen and Stallabrass, 1984) and (Jones, 1990) empirical icing density formulations will be used in this study to test the performance of these ice density formulations obtained from rather different operating conditions. The choice of these two particular icing density formulations is governed by the fact that they are implemented in their original form in the numerical model, which is detailed in the following subsection.

2.2 Numerical Model

The multiphase Computational Fluid Dynamics (CFD) based numerical simulations are carried out using ANSYS FENSAP-ICE, which uses Eulerian water droplet impingement solver. The general Eulerian two-phase model for viscous flow consists of the Navier-Stokes equations augmented by the droplets continuity and momentum equations (FENSAP-ICE User Manual):

$$\frac{\partial \alpha}{\partial t} + \vec{\nabla} \cdot \left(\alpha \overrightarrow{V_d}\right) = 0 \quad (11)$$

$$\frac{\partial(\alpha\overrightarrow{V_d})}{\partial t} + \vec{\nabla}[\alpha\overrightarrow{V_d}\otimes\overrightarrow{V_d}] = \frac{C_D Re_d}{24K}\alpha(\overrightarrow{V_a}-\overrightarrow{V_d}) + \alpha\left(1-\frac{\rho_a}{\rho_d}\right)\frac{1}{Fr^2} \tag{12}$$

where the variables α and $V_{d,a}$ are mean field values of, respectively, the water volume fraction and droplet velocity. The first term on the right-hand-side of the momentum equation represents the drag acting on droplets of mean diameter *d*. It is proportional to the relative droplet velocity, its drag coefficient C_D and the droplets Reynolds number:

$$Re_d = \frac{\rho_a d V_{a,\infty}\|\overrightarrow{V_a}-\overrightarrow{V_d}\|}{\mu_a} \tag{13}$$

and an inertia parameter:

$$K = \frac{\rho_d d^2 V_{a,\infty}}{18 L_\infty \mu_a} \tag{14}$$

where L_∞ is the characteristic length of the object. In case of the cylinder, the characteristic length is cylinder radius as opposed to diameter in analytical model. However, the use of a constant 18 in denominator ensures that inertia parameters are equal in analytical and numerical models. The second term represents buoyancy and gravity forces and is proportional to the local Froude number:

$$\mathrm{Fr} = \frac{\|V_{a,\infty}\|}{\sqrt{L_\infty g_\infty}} \tag{15}$$

These governing equations describe the same physical droplets phenomenon as Lagrangian particle tracking approach. Only the mathematical form in which these equations are derived changes using Partial Differential Equations instead of Ordinary Differential Equations. The droplet drag coefficient is based on an empirical correlation for flow around spherical droplets, or:

$C_D = (24/Re_d)\,(1 + 0.15Re_d^{0.687})$ for $Re_d \leq 1300$

$C_D = 0.4$ for $Re_d > 1300$

The local and overall collision efficiencies are calculated following a completely different approach, when compared to Finstad et al. The local and overall collision efficiencies are calculated as follows:

$$\beta = -\frac{\alpha\overrightarrow{V_d}\cdot\vec{n}}{wV_\infty} \tag{16}$$

where α is the local volume fraction (kg/m^3) and $\vec{n}$ is the surface normal vector. The overall collision efficiency is an integration of local collision efficiencies over surface area and is given as:

$$\beta_{tot} = \frac{\int \beta \, dA}{L_\infty^2} \tag{17}$$

The turbulence model used in this study is Menster's SST k-ω model (FENSAP-ICE User Manual), (Wilcox, 1988). For surface roughness NASA sand-grain roughness model is used which is computed with an empirical NASA correlation for icing (FENSAP-ICE User Manual), (Shin and Bond, 1992).

Finally, the icing density formulations used in the numerical model are (Makkonen and Stallabrass, 1984) (referred in FENSAP-ICE as "*Macklin*") and both intermediate (referred in FENSAP-ICE as "*Jones (glaze)*") and the actual final rime ice density formulation (Jones, 1990), (referred in FENSAP-ICE as "*Jones (rime)*"), with their mathematical formulations being identical to formulations given in previous section. In order to avoid the potential confusion with the naming of different icing density parameterizations, the "M&S" will be used to refer to Makkonen and Stallabrass fit and "Jones (glaze)" and "Jones (rime)" will be used to refer to the intermediate and final versions, respectively, of the Jones icing density formulations. This naming convention will be used from this point throughout the rest of manuscript.

2.3 Experimental Setup

The icing wind tunnel experiments were conducted at Cranfield University icing wind tunnel facility. This is a "closed-loop" tunnel with 761 x 761 mm test section and is capable of operating wind speeds of Mach 0.1 to Mach 0.5, with wide range of possible droplet sizes and Liquid Water Content (LWC) due to flexible spray bars configuration. The operating parameters used for this study are summarized in Table 1.

Table 1 – Operating conditions.

Parameter	***Value***
Cylinder diameter (mm)	20, 50.05, 80.25, 99, 149.5, 249, 298
Air velocity (m/s)	30
Air temp. (°C)	–25
Altitude (m.a.g.l)	0
MVD (µm)	16.36
Liquid Water Content (g/m^3)	0.6
Icing duration (min)	20 (for 20 – 80 mm), 30 (for 99 – 298 mm diameter cylinders)
Cylinder length (mm)	50.04, 50, 67.85, 69.5, 83.5, 111.74, 50, 50

The choice of the operating air temperature is based on the need to maintain the "dry growth" regime during experimentation so that the sticking and accretion efficiencies, $\alpha_2 = \alpha_3 = 1$, respectively. The choice of LWC and MVD is based on the need to obtain a measurable ice thickness, while simultaneously keeping the droplet inertia parameter K low. The choice of wind speed corresponds to the minimum rated wind speed for the Cranfield University icing wind tunnel. During the experiments, the rotating multicylinder device, mounted in the center of the test section, was used. The rotational velocity during the experiments was set to 4 RPM. Two cylinder configurations were tested – the configuration consisting of smaller cylinders 20 – 80.25 mm in diameter, and a configuration, consisting of larger cylinders, 99 – 298 mm in diameter. The reason for testing two different configurations is that the used multicylinder device can only allow mounting of four cylinders at a time.

The choice of only rotating cylinder is based on several considerations, primarily:

1. To keep the results strictly within ISO 12494 modeling framework.
2. According to the experiments of (Makkonen and Stallabrass, 1984) on wires, the rate of rotation was in between 65 and 223 deg/hr, with large jumps in rotation occurring. This implies that for longer time period of at least several hours of ice accretion the resultant ice shape will be circular.
3. Moreover, (Makkonen, 1984) referencing Howe and Dranevic states that the ratio of the minor to the major axis on actual power line conductors is 0.88 for glaze and 0.82 for rime, on the average.
4. Following personal discussions with Bjørn Eigil Nygård (Kjeller Vindteknikk AS, Norway) and, Egill Thorsteins (EFLA Iceland), it was noted that all significant ice accretions on test spans are circular in nature.

To minimize the effect of blockage, the multicylinder device was mounted as close as possible to the center of the tunnel's test-section. The duration of the tests was chosen to give a measurable thickness of the ice deposit. Since the large cylinder configuration has significantly lower values of droplet inertia parameter and by extension – the overall collision efficiency, the test duration was increased to 30 min for large configuration in order to offset this. During the experiments the cylinders were video recorded from multiple angles, in order to observe the ice growth in the details. Examples of final ice shapes from the experiments is given in Fig. 1.

Fig. 1 – Final ice shapes of the small (left) and large (right) cylinder configurations.

Figure 2 shows intermediate ice shapes for the larger cylinder configuration during the experimentation with 10 min increments and the final ice shapes for the individual cylinders.

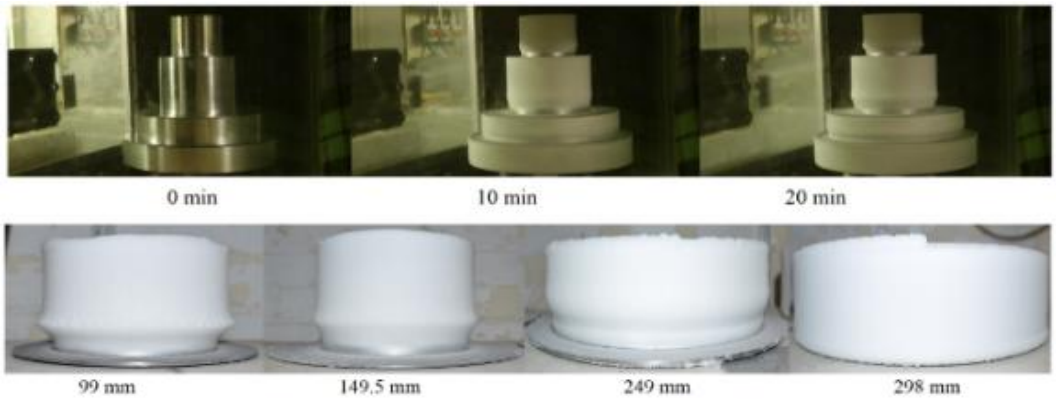

Fig. 2 – Intermediate and final ice shapes for the large cylinder configuration. The respective diameters of each cylinders are indicated.

The droplet distribution spectrum from the icing wind tunnel is given in Fig. 3. The MVD of this distribution is 16.36 μm. The droplet distribution spectrum was measured using laser diffraction methods, while (Makkonen and Stallabrass, 1984) measured their experimental droplet distribution spectra using Forward Scattering Spectrometer Probe (FSSP) in addition to the common oiled and soothed slides methods, and (Jones, 1990) estimates LWC, MVD and droplet distribution spectra based on the numerical fitting of accreted ice on the multicylinder device at Mt. Washington observatory. In order to check the stability of the operating conditions during icing wind tunnel experiments the water and air pressure in the spray bar configuration was monitored constantly. The subsequent analysis of the water and air pressure fluctuations showed that these fluctuations are within 1% of the specified operating values.

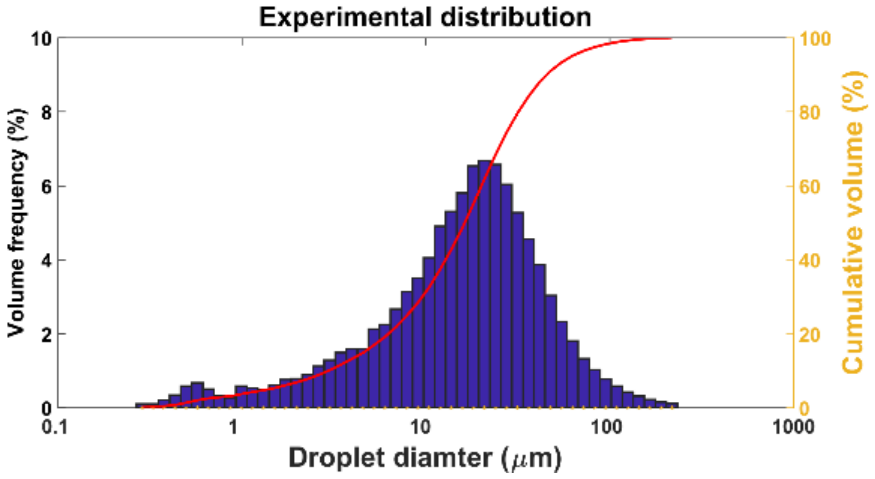

Fig. 3 – Droplet distribution spectrum for the Cranfield University (CU) experimental cases.

3 Results and Discussion

3.1 Analytical Analysis

Table 2 shows the values of the droplet inertia parameter, end iced cylinder diameter, denoted D_{end} and the accreted ice density, respectively. The analytical results in Table 2 are given as spectrum-averaged mean values taken as average from all time steps and are calculated with the full droplet distribution spectrum from Fig. 3. The experimentally measured values of the end iced cylinder diameters are given as a reference in the "*Exp.*" column.

Table 2 – Values of droplet inertia parameter, end cylinder diameter and accreted ice density in analytical calculations with full droplet distribution spectrum.

D	***K***			***D_{end} (mm)***				***ρ (kg/m^3)***		
(mm)	M&S	Jones (glaze)	Jones (rime)	M&S	Jones (glaze)	Jones (rime)	***Exp.***	M&S	Jones (glaze)	Jones (rime)
20	9.623	9.188	10.069	29.70	32.39	27.34	***32.30***	636.9	495.8	856.0
50.05	4.317	4.316	4.499	57.37	60.37	55.72	***60.45***	590.6	416.2	770.8
80.25	2.871	2.821	2.890	86.25	89.28	85.10	***87.57***	554.5	366.2	690.3
99	2.328	2.280	2.342	107.08	111.55	105.74	***113.72***	534.3	341.3	645.2

149.5	1.586	1.566	1.590	156.02	160.27	160.30	***155.36***	488.5	293.7	545.9
249	0.989	0.982	0.988	253.87	257.60	257.58	***254.06***	415.1	234.4	399.6
298	0.840	0.836	0.839	302.38	305.83	302.91	***307.06***	384.3	214.2	342.9

In general, the analytical values of end iced diameter calculated with the Jones (glaze) ice density formulation yields the closest agreement with the experimental values in most test cases. Comparatively, the M&S and the Jones (rime) icing density formulations tends to underestimate the ice thicknesses for majority of cylinders with exceptions being 149.5 and 249 mm cylinders, for which the M&S numerical fit gives the closest agreement with the experimental values. In addition, the Jones (glaze) icing density formulation has the lowest overall values of accreted ice densities, as evidenced from Table 2, with Jones (rime) Jones icing density formulation having highest values of accreted ice densities up to 249 mm cylinder, where the M&S formulation shows the best agreement with experimental values.

When it comes to the spectrum-averaged results, the biggest difference will be in the values of the droplet inertia parameter *K*, when compared to the results with the MVD approximation. This increase in the value of *K* will lead to the increase of the droplet impact velocities, as follows from the structure of Eq. (1), which will, correspondingly, increase the values of the Macklin parameter *R*. As noted in (Jones, 1990), the numerical fit of (Makkonen and Stallabrass, 1987) produces higher values of ice density than the original formulation by (Macklin, 1962). On the other hand, the Jones (glaze) formulation predicts higher densities for low values of *R* and lower densities for high values of *R* than were obtained by (Macklin, 1962).

This property of the spectrum-averaging can also explain why the Jones (rime) formulation tends to predict highest densities for almost all cases, with exception of two largest cylinder of 249 and 298 mm diameters. Instead of relying on the Macklin parameter, this formulation relies directly on the values of *K* and ϕ. While ϕ is independent of droplet diameter, the values of *K* will increase dramatically when one foregoes MVD approximation for calculations with full droplet distribution spectrum, especially, with the distribution as "wide" as experimental distribution in Fig. 3.

On the subject of the MVD approximation, Table 3 shows the analytical results of the droplet inertia parameter, end cylinder diameters and ice densities, respectively, in analytical calculations using MVD approximation as per ISO 12494 modeling framework. The primary interest in producing these values using the MVD approximation is to examine how the spectrum-averaged values compare to those, obtained by strict adherence with ISO 12494 modeling guidelines.

Table 3 – Values of droplet inertia parameter, end cylinder diameter and accreted ice density in analytical calculations with the MVD approximation.

D	***K***			***D_{end} (mm)***				***ρ (kg/m^3)***		
(mm)	M&S	Jones (glaze)	Jones (rime)	M&S	Jones (glaze)	Jones (rime)	***Exp.***	M&S	Jones (glaze)	Jones (rime)
20	2.239	2.174	2.257	29.72	32.10	30.07	***32.30***	649.0	521.1	641.1
50.05	1.042	1.028	1.038	56.09	58.83	57.82	***60.45***	575.2	394.5	451.6
80.25	0.672	0.669	0.670	84.34	86.91	86.85	***87.57***	502.3	308.3	313.9
99	0.545	0.542	0.540	103.92	107.41	108.39	***113.72***	455.8	265.9	241.0

149.5	0.366	0.367	0.362	152.6	155.07	159.36	***155.36***	329.2	184.9	100.0
249	0.221	0.224	0.225	251.06	251.06	251.06	***254.06***	100.0	100.0	100.0
298	0.185	0.187	0.188	300.06	300.06	300.06	***307.06***	100.0	100.0	100.0

From Table 3 it can be seen that while the ice density and iced cylinder diameters are comparable to those in Table 2 for the smaller cylinder configuration of 20 – 80 mm cylinders as well as the 99 mm cylinder. For the 149.5 mm cylinder, the values of end cylinder diameter, while being lower than the spectrum-averaged values for all formulations, still agrees well with the experimental values.

However, the agreement in end cylinder diameter values becomes poor for the two largest cylinders, for which the calculated ice density is below the minimum constraint of 100 kg/m^3. This constraint is used in the analytical model as an assumed estimation on the lower bound of the accreted ice density. Moreover, when comparing the values of the droplet inertia parameter in Tables 2 and 3, the significantly lower values of *K* in Table 3 will result in lower values of the cloud impingement parameters, in particular, when it comes to the droplet impact velocities and Macklin parameter values, thus significantly decreasing the accreted ice density values.

This, coupled with the MVD approximation yielding smaller values of end cylinder diameters for majority of cases in Table 6, will primarily result in an underestimation of the accreted ice masses calculated with MVD approximation, when compared to the spectrum-averaged results. This can potentially limit the applicability of using the MVD approximation in modeling of the long-term icing events, in particular when the droplet inertia parameter is low. Finally, for the MVD approximation both versions of the Jones formulation tend to be in good agreement for majority of cases, with obvious exception of two largest cylinders, where both of them are below constraint of 100 kg/m^3, unlike with the spectrum-averaged values, where Jones (rime) Jones shows consistently higher densities.

This does suggest that the procedure of spectrum-averaging might not be directly admissible for this formulation, due to significantly higher values of *K* the spectrum-averaging method produces. Contrary, the M&S and Jones (glaze) Jones formulations do not experience such sharp drop in values, as the effect on spectrum-averaging on the droplet impact velocities is not as pronounced as in the case with droplet inertia parameter, with the increase in droplet impact velocities being enough to offset the ice densities going below constraint in the spectrum-averaged values.

3.2 Numerical Analysis

Table 4 shows the results from the CFD simulations using the full droplet distribution spectrum from Fig. 3.

Table 4 – Values of droplet inertia parameter, end cylinder diameter and accreted ice density in numerical calculations with full droplet distribution spectrum.

D	***K***			***D_{end} (mm)***				***ρ (kg/m^3)***		
(mm)	M&S	Jones (glaze)	Jones (rime)	M&S	Jones (glaze)	Jones (rime)	***Exp.***	M&S	Jones (glaze)	Jones (rime)
20	4.747	6.683	9.427	79.68	50.80	30.19	***32.30***	40.7	111.1	473.8
50.05	4.308	4.040	4.349	59.78	67.06	58.74	***60.45***	376.4	202.3	425.1

80.25	2.799	2.694	2.819	88.80	95.35	87.57	***87.57***	333.8	181.9	392.9
99	2.320	2.216	2.276	104.92	114.50	108.85	***113.72***	425.9	233.0	376.7
149.5	1.560	1.525	1.540	153.77	160.77	157.69	***155.36***	444.6	246.9	343.8
249	0.945	0.936	0.940	251.75	256.37	254.55	***254.06***	444.7	246.9	295.0
298	0.792	0.786	0.787	299.70	304.36	302.87	***307.06***	440.5	243.7	276.9

In general, the CFD simulations show good agreement with the analytical modeling results for the iced cylinder diameters for 80 – 149.5 mm cylinders. For the 50 mm cylinder, the agreement depends on the formulation used, i.e., M&S and Jones (rime) formulations show better agreement than the Jones (glaze) formulation. For the 20 mm cylinder only Jones (rime) formulation shows good agreement with the rest of formulations producing significantly higher end iced diameters. Moreover, observe that the ice density values in the CFD simulations are consistently lower than in analytical model, with exception of 249 and 298 mm cylinders. The primary reason for it is the difference in the flow treatment between the analytical and the numerical model, as the analytical model uses the potential flow approximation, as opposed to viscid turbulent flow in the CFD simulations.

In particular, the difference in the accreted ice density between two models simplifies to the difference in the stagnation line impact velocities, which are used in the calculation of the Macklin parameter as given in Eq. (7). Since for majority of cylinders, the analytical and the numerical results tend to have relatively comparable end iced cylinder diameters, this suggests that the CFD simulations produce consistently lower ice accretion masses as well, which may be detrimental, if the long-term extreme value ice modeling is needed. Table 5 shows the CFD simulations results using the MVD approximation. Again, the reason for this is to keep the results consistent with the ISO 12494 framework and to allow direct comparison with the results in Table 3.

Table 5 – Values of droplet inertia parameter, end cylinder diameter and accreted ice density in numerical calculations with the MVD approximation.

D	***K***			***D_{end} (mm)***				***ρ (kg/m^3)***		
(mm)	M&S	Jones (glaze)	Jones (rime)	M&S	Jones (glaze)	Jones (rime)	***Exp.***	M&S	Jones (glaze)	Jones (rime)
20	2.133	1.859	2.226	32.44	40.17	30.25	***32.30***	374.1	201.1	473.8
50.05	1.054	1.014	1.047	56.11	60.28	56.74	***60.45***	471.9	270.1	425.1
80.25	0.677	0.662	0.678	84.93	88.76	84.70	***87.57***	373.4	200.7	392.9
99	0.555	0.548	0.552	102.58	105.06	103.60	***113.72***	486.4	283.9	376.7
149.5	0.372	0.371	0.371	150.99	152.02	151.65	***155.36***	494.6	292.2	342.8
249	0.225	0.224	0.224	249.33	249.56	249.53	***254.06***	481.4	278.9	295.0
298	0.188	0.188	0.188	298.26	298.56	298.45	***307.06***	473.5	271.5	276.9

The results from Table 5, when compared with the experimental values and the results from Table 3, do produce good agreement for the smaller cylinder configuration, in particular, for the 50 and 80 mm cylinders with Jones (glaze) formulation, and for 20 mm cylinder, using the M&S and the Jones (rime) formulations. However, for the 149.5, 249 and 298 mm cylinders the MVD approximation barely shows any ice accretion, as end iced cylinder diameters are practically unchanged from un-iced diameters.

Furthermore, CFD results with the MVD approximation have somewhat higher values of the accreted ice density than the simulations using the full droplet distribution spectrum, with the exception of Jones (rime) formulation where full droplet distribution spectrum and the MVD approximation values for the ice density are comparable. This difference can be explained by either the difference in surface temperature, differences in the flow regime, primarily due to boundary layer differences, averaging procedures for the full droplet distribution spectrum in the CFD software, or combination of these factors.

Advantageously, the CFD simulations allow for detailed investigation of these details. From the CFD results, the boundary layer is much more pronounced in the simulations using the full droplet distribution spectrum. In addition, the droplet velocity gradients are much more "sharp" for the simulations with full droplet distribution spectrum, while the droplet velocities are higher in the case of simulations with monodisperse distribution. This may explain the higher ice density values in the results using the MVD approximation, and why the results for smaller cylinders in Tables 4 and 5 generally agree for cases with higher *K* values; as this thicker boundary layer is actively "deflecting" the droplets away from the cylinder. In addition, this can probably explain the considerably higher thicknesses in the analytical results for the 249 and 298 mm cylinders, as the boundary layer is not present in the potential flow approximation, which is used in the analytical results. As an example, Fig. 4 shows the droplet velocity streamlines for a few selected cases in the CFD simulations.

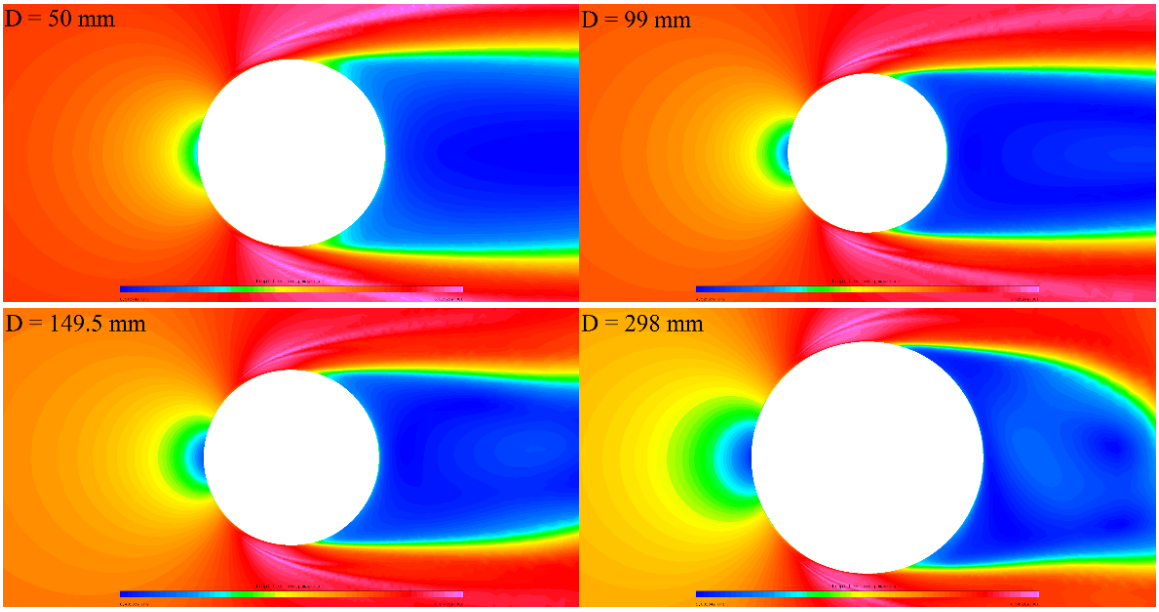

Fig. 4 – Droplet velocity contours in the CFD simulations.

In Fig. 4, the boundary layer is much more pronounced for the 298 mm and 149 mm cylinders, while for 50 mm cylinder it is barely visible. This thick boundary layer results in more pronounced flow separation for the larger cylinders. Again, this is possible explanation why the CFD simulations with the full droplet distribution spectrum tend to underestimate the accreted ice density values, when compared to the analytical and the MVD approximation results, as the impact velocities would be lower in this situation, as the thick boundary layer will "push out" the droplets from the stagnation region.

Based on the comparison of the results between the MVD approximation and full droplet distribution spectrum, it can be seen that the MVD approximation works well for higher values of droplet inertia parameter. This agrees with statements by (Makkonen *et al*., 2018) and (ISO, 2001) that the current icing parameterization is applicable for the range of the overall collision efficiency of $0.07 < E < 0.63$ and that for $E < 0.1$ the icing parameterization using MVD approximation will underestimate the ice accretion, respectively.

Thus, in modeling of long-term icing events with expected low values of the droplet inertia parameter and the overall collision efficiency, the use of full droplet distribution spectrum is advantageous, as it can reliably reproduce accumulated thicknesses in most extreme cases, as evidenced from the results of this study. Still, for the more extreme cases, e.g. 249 and 298 mm cylinders, which have very low values of the droplet inertia parameter, even full droplet distribution spectrum may underestimate the icing intensity. In those cases, the recalculation of droplet trajectories using full drag terms is advised (Finstad *et al*., 1988).

4 Validation

For the validation purposes the experimental cases from the FRonTLINES (Frost and Rime on The Overhead Transmission Line) have been selected. These test cases are characterized by the low values of the droplet inertia parameter, *K*, for most of them, except the test cases at 7 m/s wind speeds for which, the *K* value lies in "verified range". The detailed information regarding the operating conditions in these experiments as well as the experimental droplet distribution spectrum are given in (Makkonen *et al*., 2018). Unlike the previous experimental cases, discussed previously in this work, in the FRonTLINES cases the end iced masses are known, while the end cylinder diameters are unknown. Thus, this combination allows for validation of the analytical calculation procedure for the overall collision efficiency and total accreted ice mass. The results of analytical calculations for the FRonTLINES test cases are given in Tables 6 and 7 for the experimental droplet distribution spectrum and the MVD approximation, respectively.

Table 6 – Analytical results for FRonTLINES experimental cases with the experimental droplet distribution spectrum. The number in brackets shows the wind speed in m/s.

D	***D_{end} (mm)***	***K***	***ρ (kg/m^3)***	***M (g)***	***M_{exp} (g)***	***E***	***E_{exp}***
				M&S			
30 (4)	30.52	0.471	404.3	1.560	1.163	0.115	0.086
50	50.39	0.306	276.8	1.321	0.722	0.058	0.032
80	80.40	0.229	140.0	1.112	0.743	0.031	0.021
100 (4)	100.41	0.209	100.0	1.020	0.770	0.023	0.017
170	170.23	0.181	100.0	0.973	0.812	0.013	0.011
30 (7)	31.07	0.796	574.0	4.600	4.211	0.194	0.177
100 (7)	100.43	0.280	336.2	3.549	4.754	0.045	0.060
				Jones (glaze)			
30(4)	30.92	0.469	226.2	1.556	1.163	0.115	0.086
50	50.67	0.305	158.9	1.320	0.722	0.058	0.032
80	80.50	0.229	112.7	1.112	0.743	0.031	0.021
100(4)	100.41	0.209	100.0	1.020	0.770	0.023	0.017

170	170.23	0.181	100.0	0.973	0.812	0.013	0.011
30(7)	31.56	0.790	391.5	4.600	4.211	0.194	0.177
100(7)	100.77	0.280	186.5	3.546	4.754	0.045	0.060
				Jones (rime)			
30(4)	30.62	0.471	338.8	1.559	1.163	0.115	0.086
50	50.50	0.305	213.6	1.321	0.722	0.058	0.032
80	80.49	0.229	116.0	1.112	0.743	0.031	0.021
100 (4)	100.41	0.209	100.0	1.020	0.770	0.023	0.017
170	170.23	0.181	100.0	0.973	0.812	0.013	0.011
30 (7)	31.27	0.793	483.3	4.600	4.211	0.194	0.177
100 (7)	100.84	0.280	170.8	3.546	4.754	0.045	0.060

Table 7 – Analytical results for FRonTLINES experimental cases with the MVD approximation. The number in brackets shows the wind speed in m/s.

D	***D_{end} (mm)***	***K***	***ρ (kg/m^3)***	***M (g)***	***M_{exp} (g)***	***E***	***E_{exp}***
				M&S			
30 (4)	30.34	0.302	305.1	0.767	1.163	0.057	0.086
50	50.18	0.182	100.0	0.226	0.722	0.010	0.032
80	80.18	0.170	100.0	0.362	0.743	0.010	0.021
100 (4)	100.18	0.170	100.0	0.453	0.770	0.010	0.017
170	170.18	0.170	100.0	0.769	0.812	0.010	0.011
30 (7)	30.86	0.524	550.1	3.555	4.211	0.150	0.177
100 (7)	100.32	0.170	100.0	0.793	4.754	0.010	0.060
				Jones (glaze)			
30 (4)	30.60	0.300	171.0	0.762	1.163	0.056	0.086
50	50.18	0.182	100.0	0.226	0.722	0.010	0.032
80	80.18	0.170	100.0	0.362	0.743	0.010	0.021
100 (4)	100.18	0.170	100.0	0.453	0.770	0.010	0.017
170	170.18	0.170	100.0	0.769	0.812	0.010	0.011
30 (7)	31.31	0.520	359.6	3.542	4.211	0.149	0.177
100 (7)	100.32	0.170	100.0	0.793	4.754	0.010	0.060
				Jones (rime)			
30 (4)	30.49	0.301	209.9	0.764	1.163	0.056	0.086
50	50.18	0.182	100.0	0.226	0.722	0.010	0.032
80	80.18	0.170	100.0	0.362	0.743	0.010	0.021
100 (4)	100.18	0.170	100.0	0.453	0.770	0.010	0.017
170	170.18	0.170	100.0	0.769	0.812	0.010	0.011
30 (7)	31.27	0.520	372.8	3.544	4.211	0.149	0.177
100 (7)	100.32	0.170	100.0	0.793	4.754	0.010	0.060

In Tables 6 and 7, the end cylinder diameter in all cases changes insignificantly with maximum diameter increase being barely over 1 mm. This primarily can be explained by the low values of K and the choice of operating conditions, namely, the LWC being equal to 0.4 g/m^3 with the test duration of 30 min. for all cases. Moreover, the results in Table 7 show that the value of K is low enough that for majority of cases the constraint of $E = 0.01$ if $K \leq 0.17$ (Finstad *et al*., 1988) is enforced. Thus, the analytical results with the MVD approximation tend to underestimate the ice masses and the overall collision efficiencies

in most of these cases. On the other hand, the results with experimental droplet distribution spectrum show slightly elevated values of these parameters in the analytical calculations. This may be explained by the nature of spectrum-averaging procedure, as while the smallest bins in the distribution will be bounded by the constraint of $E = 0.01$ if $K \leq 0.17$, for larger bins, for which $K > 0.17$, the collision efficiency value will be calculated "as normal". As a result, the overall collision efficiency values may be slightly overestimated, when compared to the experimental results, as evidenced in Table 6.

When it comes to the values of the accreted ice densities in Tables 6 and 7, for the majority of cases the calculated accreted ice densities are below the constraint of 100 kg/m^3, in particular, for the results with the MVD approximation, where all cases, with the exception of 30 mm cylinder are below this constraint. The situation is a bit different for the spectrum-averaged results, where only two largest cylinders are below the constraint. For the cases where the calculated ice density is not below 100 kg/m^3, a large spread of values can be observed in Tables 6 and 7, with majority of those lying in the range of 250–400 kg/m^3. This coupled with very low calculated end cylinder diameters suggests that in reality the uniform layer of ice will not form and instead large, individual beads of rime ice will be present, as its expected that the individual bead height will be bigger than 0.5–1 mm, which is typical difference in the end and start diameter values in Tables 6 and 7.

Thus, for additional validation, different experimental test cases were selected, with higher values of the droplet inertia parameter, namely, two cases from the experiments of (Makkonen and Stallabrass, 1984) – test cases 6 and 16. This particular choice was governed by several reasons, in particular the closeness of diameter values to the ISO 12494 "reference collector" (case 6) and the current "limit value" of verified cylinder diameter validity range (case 16). Moreover, the LWC and MVD values for these two cases are the highest when compared to other experimental cases with same cylinder diameters, thus giving the highest possible accreted ice mass and thickness, compared to other experimental cases. The detailed operating conditions for these test cases is available in (Makkonen and Stallabrass, 1987) Table 1.

As noted in Table 1 in (Makkonen and Stallabrass, 1987) for the analytical calculations one of the three experimental droplet distribution spectra has been used, denoted as "*Droplet size distribution category*", however, due to significant passage of time the exact information on these droplet distributions is no longer available (Makkonen, personal communication). Thus, for the purpose of the modeling in this paper, these two test cases have been analyzed using the monodisperse distribution, as per ISO 12494 guidelines and the Langmuir D distribution, as it is a common distribution in in-flight icing studies. The results from analytical modeling are given in Table 8.

Table 8 – Analytical results for two test cases of (Makkonen and Stallbrass, 1987).

Test	***Distribution***	***K***	***D_{end} (mm)***	***D_{end} Exp (mm)***	***ρ (kg/m^3)***	***ρ_{exp} (kg/m^3)***	***M (g)***	***M_{exp} (g)***	***E***	***E_{theory}***	***E_{exp}***
						M&S					
6	MVD	1.115	36.15	36.50	762.8	746.1	17.533	18.70	0.299	0.30	0.32
6	Lang D	1.515	36.23	36.50	760.0	746.1	17.806	18.70	0.303	0.30	0.32
16	MVD	0.491	78.38	79.50	660.4	710.3	18.296	29.6	0.110	0.14	0.18

16	Lang D	0.673	78.96	79.50	681.3	710.3	23.732	29.6	0.142	0.14	0.18
					Jones (glaze)						
6	MVD	1.113	36.27	36.50	741.5	746.1	17.536	18.70	0.298	0.30	0.32
6	Lang D	1.513	36.35	36.50	738.5	746.1	17.814	18.70	0.302	0.30	0.32
16	MVD	0.489	78.86	79.50	545.6	710.3	18.258	29.6	0.109	0.14	0.18
16	Lang D	0.672	79.37	79.50	595.9	710.3	23.722	29.6	0.141	0.14	0.18
					Jones (rime)						
6	MVD	1.095	37.47	36.50	581.8	746.1	17.563	18.70	0.294	0.30	0.32
6	Lang D	1.500	36.94	36.50	654.7	746.1	17.851	18.70	0.301	0.30	0.32
16	MVD	0.484	80.49	79.50	339.8	710.3	18.130	29.6	0.107	0.14	0.18
16	Lang D	0.667	80.53	79.50	437.8	710.3	23.694	29.6	0.140	0.14	0.18

In Table 8 the variable "E_{theory}" shows the values of the overall collision efficiency as calculated by (Makkonen and Stallabrass, 1987) for comparison purposes to the values of the overall collision efficiency E as calculated in this work. Moreover, the variable "ρ_{exp}" shows the experimental value of the accreted ice density, calculated based on the reported ice masses and ultimate cylinder diameters in (Makkonen and Stallabrass, 1987).

From Table 8 it can be seen that in analytical calculations, expectedly, the M&S formulation shows the best agreement with experimental results, as this numerical fit was developed based on these experimental results. The Jones (glaze) formulation also shows good agreement for the 31.83 mm cylinder, however, it underestimates the value of accreted ice density for the 76.09 mm cylinder. In terms of accreted ice thicknesses in the analytical results, both Macklin and Jones (glaze) yield good agreement with the experimental values while Jones (rime) parameterization tends to slightly overestimate the ice thicknesses.

By summarizing the analytical, numerical and experimental results following conclusions can be made:

- The M&S formulation yields good agreement, in both the analytical and the numerical results for smaller cylinder configuration, 20 – 80 mm in diameter in the Cranfield University experimental cases and the 31.83 and 76.09 mm cylinders from the (Makkonen and Stallbrass, 1984) experimental cases.
- Both versions of the Jones formulation yield better agreement than the M&S formulation for majority of cylinder diameters in the Cranfield University experimental cases.
- The results using the full droplet distribution spectrum yield good agreement with the experimental results, particularly for larger cylinders.
- The results using the MVD approximation only yield acceptable agreement for the smaller cylinder configuration and 31.83 mm cylinder from the (Makkonen and Stallbrass, 1984) experimental cases.
- Between the two Jones formulations, the intermediate (glaze) formulation shows better agreement with experimental values in analytical results with full droplet distribution spectrum and in numerical with the MVD approximation, except 20 mm cylinder, while final (rime) Jones formulation shows opposite results.
- The Jones (glaze) formulation in the Cranfield University cases performed admirably, considering the surface temperature in those conditions is expected to be below –20 °C. This value is a rough "cutoff" as neither (Macklin, 1962) in his experiments nor (Jones, 1990), who employed similar analysis technique to obtain her intermediate version of the icing density parameterization, haven't

tested and/or discarded cases with lower temperature during developing of their respective formulations.

- For the (Makkonen and Stallabrass, 1984) experimental cases, the M&S and the Jones (glaze) parametrizations showed good agreement; however, Jones (rime) formulation was underestimating the ice density. The possible reasons for the underestimation of the experimental ice density by Jones parameterization in the (Makkonen and Stallabrass, 1984) experiments is given in (Jones, 1990).

5 Conclusion

In this paper the investigation into several empirical accreted ice density formulations have been conducted, with the main goal of assessing how well said empirical formulations can capture the accreted ice thicknesses. The practical purpose of it is to use the accreted ice thickness as a sort of icing severity estimate in modeling of the long-term icing events, if the accreted ice mass is an unknown value. The icing modeling in this study was done by using both the analytical modeling and the CFD simulations, in order to compare two most likely approaches of the modeling of the long term icing events. The obtained icing thicknesses were than compared to experimentally measured values.

The obtained results show that both the analytical and the numerical models can adequately estimate end iced cylinder diameters for majority of the tested cylinder diameters in this study. In particular, while the M&S formulation tends to have good agreement with the smaller cylinder configuration, it tends to underestimate the icing thicknesses for the larger cylinder configuration. On the other hand, the Jones formulations show consistently better results for almost all tested cases, and especially, for the larger cylinder configuration. However, all formulations tend to underestimate the icing thicknesses for the largest cylinders, 249 and 298 mm in diameter.

These results were obtained using the full droplet distribution spectrum from the Cranfield University icing wind tunnel. In order to keep the results consistent with the framework of ISO 12494 icing theory, the matching set of values, using the monodisperse droplet distribution with the equal MVD was obtained. The results with the MVD approximation show good agreement mainly for smaller cylinder configuration, 20 – 80 mm in diameter, and the agreement for the larger cylinder diameter is non-satisfactory, primarily due to low values of droplet inertia parameter K for these cases, which puts the results using the MVD outside of the verified range of the current icing theory. Thus, calculations with the full droplet distribution spectrum are recommended. Summarizing the findings of the validation section, both tested formulations based on Macklin parameter, i.e., the numerical fit by Makkonen and Stallabrass and the intermediate version of Jones formulation have showed better agreement than the final version of Jones formulation, however, as noted in the original work (Jones, 1990) there are several reasons for this discrepancy.

Acknowledgements

The work reported in this paper is funded by the Research Council of Norway, IceBOX – project no. 282403 and WindCoE (*Nordic Wind Energy Centre*) project within the Interreg IVA Botnia-Atlantica, as part of European Territorial Cooperation (ETC). Authors would like to acknowledge Dr. David

Hammond, Dr. Hugo Pervier and Mr. Peter West from Cranfield University, UK for assisting during icing tunnel experimentation.

References

1. Bain, M. and Gayet, J. F., (1983). Contribution to the modeling of the ice accretion process. Pp. 13–20 in *Proceedings of the First International Workshop on Atmospheric Icing of Structures*, U. S. Army CRREL Special Report 83–17.
2. Finstad, K.J., Lozowski, E.P., Gates, E.M., (1988). A computational investigation of water droplet trajectories. *Journal of Atmospheric and Oceanic Technology*, vol. 5, pp. 160-170.
3. *FENSAP-ICE User Manual*
4. ISO 12494:2001(E), (2001). *Atmospheric icing of structures*. Standard. International Organization for Standardization. Geneva, CH.
5. Jones, K.F. (1990). The density of natural ice accretions related to nondimensional icing parameters, *Quarterly Journal of Royal Meteorological Society*, vol. 116, pp. 477–496.
6. Langmuir, I., Blodgett, K., (1946). *A Mathematical Investigation of Water Droplet Trajectories.* Army Air Forces technical report 5418. Army Air Forces Headquarters, Air Technical Service Command.
7. Macklin, W.C., (1962). The density structure of ice formed by accretion. *Quarterly Journal of Royal Meteorological Society*, vol. 88 pp. 30–50.
8. Makkonen, L., (1984). Modeling of Ice Accretion on Wires. *Journal of Applied Meteorology*, vol. 23, pp. 929–939.
9. Makkonen, L., Stallabrass J.R., (1984). Ice accretion on cylinders and wires. *National Research Council of Canada*. Division of Mechanical Engineering Technical Report TR-LT-05.
10. Makkonen, L., Stallabrass, J.R., (1987). Experiments on the cloud droplet collision efficiency of cylinders. *Journal of Applied Meteorology*, vol. 26, pp. 1406–1411.
11. Makkonen, L., Zhang, J., Karlsson, T., Tiihonen, M., (2018). Modelling the growth of large rime ice accretions, *Cold Regions Science and technology*, vol. 151, pp. 133–137.
12. Pfaum, J.C. and Pruppacher, H.R., (1979). A wind tunnel investigation of the growth of graupel initiated from frozen drops. *Journal of Atmospheric Sciences*, vol. 36, pp. 680–689.
13. Shin, J. and Bond, T, (1992). Experimental and Computational Ice Shapes and Resulting Drag Increase for a NACA 0012 Airfoil, *NASA Technical Manual 105743*.
14. Wilcox, D.C., (1988). "Re-assessment of the scale-determining equation for advanced turbulence models", *AIAA Journal*, vol. 26, no. 11, pp. 1299–1310.

Paper 4. Accreted Ice Mass Ratio *(k–factor)* for Rotating Wind Turbine Blade Profile and Circular Cylinder

Pavlo Sokolov, Jia Yi Jin and Muhammad Shakeel Virk

Wind Energy, 2019, Volume 22. pp. 447 – 457.

DOI: 10.1002/we.2298

Author's Contribution

Pavlo Sokolov has contributed substantially in the proposal of research idea, literature review, modelling, computing, analytical and numerical analysis, and writing of the paper.

Accreted Ice Mass Ratio *(k–factor)* for Rotating Wind Turbine Blade Profile and Circular Cylinder

Pavlo Sokolov*, Jia Yi Jin, Muhammad S.Virk

Institute of Industrial Technology

UiT- The Arctic University of Norway

Post Box 385, 8505, Narvik

*Email: pavlo.sokolov@uit.no

Abstract— This paper describes a study to investigate the relation between ice accretion on a rotating wind turbine blade profile (airfoil) and a reference collector (circular cylinder). This relation, known as "*k*–factor" describes the ratio of accreted ice mass on a reference collector and wind turbine blade profile. Analyzes are carried out by performing a series of multiphase numerical simulations and ISO12494 based analytical calculations. The results show that *k*–factor is not equal to constant 20, contrary to currently postulated assumption[1] and can vary to a significant degree depending on a number of different operating and geometric parameters. These factors include the effects of blade geometry on ice accretion, droplet collision efficiency, droplet distribution spectrum and median volume diameter under different ambient conditions pertaining to wind speed and tip speed ratios experienced by both the reference collector and wind turbine blade. The results presented in this paper provide a simplistic explanation about *k*–factor variance, however further validation is necessary, in particular when it comes to the ice accretions on different wind turbine blade profiles under different operating and geometric conditions.

Keywords—ice accretion; wind turbine; circular cylinder; droplet collision efficiency; MVD; tip speed ratio.

1 Introduction

The interest in energy generated by the wind turbines has been steadily increasing over the last few decades and has resulted in increase of installed wind turbines in ice prone cold climate regions having good wind resources. Icing on wind turbines is an undesirable phenomenon as it causes adverse effects such as: loss in power production[2,3]; increased vibrations in structure due to unbalanced loadings, which in turn will lead to increase in fatigue damage of the components; overloading due to delayed stall and ice shedding from the wind turbine[4] .When it comes to these negative effects, the main question posed here is better way of estimation of the icing load on wind turbine blade in order to estimate the magnitude and severity of these undesirable events. However, direct measurements of ice load on wind turbines are difficult, if not impossible, and therefore some simplifications and empirical relations can be employed. In 2013, VTT technical research center of Finland proposed to use a so-called "*k*–factor"[1], a constant conversion ratio of an order of $k = 20$ at 85% of blade length deemed to be a representative value for wind turbine ice accretion.

The practical meaning of *k*–factor is a ratio of ice mass accreted on a reference collector, i.e. a slowly rotating cylinder 30 mm in diameter by 500 mm in length, mounted on a met mast to the ice mass accreted on a rotating wind turbine blade profile section in question. The *k*–factor 20 means that rotating wind turbine blade profile, in general, will accrete 20 times more ice in the same time under same operating conditions than a reference collector. However, the VTT model does not explicitly states for what icing conditions it is applicable, as it is expected that reference collector and wind turbine might have differences in ice accretion processes, primarily due to the fact that under ISO 12494 model, it is assumed that velocity vector is normal to the object, i.e., the reference collector, while for wind turbine the velocity vector would not be normal to the blade as the true air speed of the turbine blade is a function of normal velocity caused by the wind and tangential velocity as function of blade rotation. However, the precise extent of those possible differences on ice accretion process is not known as to the best of authors' knowledge and there are no experimental investigations being done for objects rotating in such a way. Nonetheless, the physical reasoning behind *k*–factor can be explained by several factors.

First, is height factor due to log wind speed profile. The height factor accounts for wind speed profile variation due to planetary boundary layer, surface roughness and viscous friction effects between air and surface in planetary boundary layer. This is a relatively well-known phenomenon and is accounted for in governing ISO standard, ISO 12494: "*Atmospheric icing of structures*"[5]. The height factor *x* is defined as:

$$x = e^{0.01H} \tag{1}$$

where *H* is the height above ground level (m). *Second*, is the tip speed ratio (TSR), λ, which is defined as the ratio of the speed of the rotor tip to the free stream wind speed:

$$\lambda = \frac{V}{v} = \frac{\omega r}{v} \tag{2}$$

where *v* is free stream wind speed (m/s), *V* is the rotor tip speed (m/s), *r* is the rotor radius (m) and ω is the blade rotational velocity (rad/s). The rotor TSR depends on the blade profile used, the number of blades and the type of wind turbine. In general, three blade wind turbines operate at a TSR value between 6 and 8, with 7 being the most typically used value. *Lastly*, airfoil geometry and droplet distribution size have the possibility to affect the *k*–factor values, however, as of current, the possible effects of those has not been ascertained in great details and thus is one of the major scopes of the work presented in this paper. In addition, another major scope of current work is to provide better estimate of ice load maps for the wind parks. This case-by-case estimate is believed to be more accurate in nature than the broad generalist approach, as was the case in Turkia et al[1].

2 Models setup

2.1 Analytical Model

The operating parameters used for this study are summarized in Table I.

The airfoils used in this study are: NACA 0012, 4412, 6412, 23012 and N-22, all having the same leading edge radius of 15 mm and maximum thickness of 12 cm. The choice of airfoils has been governed by the need to select a "type" of airfoils having same leading edge radius, thickness and chord length, differing only in the geometric shape and symmetry in order to see if those geometric features have an impact on *k*–factor or not. The choice of altitude of 10 m.a.g.l. is assumed to correspond to the standard mounting height of the reference collector on met mast, as per ISO 12494 guidelines. Other mounting heights of the reference collector and/or hub height are acceptable, granted the collector measurements are compliant with the ISO 12494[5] and the height difference between the reference collector and the turbine hub height is properly taken into account in calculations of the height factor. In this study, the pressure difference associated with the height difference between reference collector and turbine hub height is ignored. This is based on reporting in Finstad et al.[6], that the pressure difference between sea level and Mt. Washington (1916.6 m.a.s.l.) caused about 0.5% difference in overall collision efficiency values, and the height difference between assumed cylinder mounting height (10 m.a.s.l.) and typical wind turbine hub height (80 m.a.g.l.) is considerably less than the elevation of Mt. Washington. The choice of cylinder diameter matches the diameter of typical reference collector[5], while the choice of temperature, LWC, and MVD corresponds to typical conditions of dry growth under moderate icing intensity. The choice of wind speeds is based on reference in Bredesen and Refusm[7] that for global average in-cloud icing conditions ice accretes at a rate of roughly 1 kg/m/hr on a typical wind turbine blade airfoil section at 85 % of the blade span for wind speeds of 7 m/s corresponding to a airfoil section velocity of 60 m/s.

The rate of icing on a structure can be calculated according to ISO 12494, based on expression by Makkonen[8] is given in eq. (3):

$$\frac{\mathrm{d}m}{\mathrm{d}t} = \alpha_1 \alpha_2 \alpha_3 v A w \tag{3}$$

where dm is the change in ice mass (g), dt is the change in time (s), α_1, α_2 and α_3 are dimensionless collision, sticking and accretion efficiency of a droplet, respectively, v is the wind speed (m/s), A is the cross-sectional area of an object (m^2) and w is the liquid water content (hereafter, LWC, g/m^3). For this study an assumption of "dry ice growth" regime on a reference collector is made, meaning that $\alpha_2 = \alpha_3 = 1$, i.e. all impinging droplets freeze on impact. The collision efficiency, α_1, can be obtained[5] as:

$$\alpha_1 = A - 0.028 - C(B - 0.0454) \tag{4}$$

where

$$A = 1.066K^{-0.00616} \exp(-1.103K^{-0.688}) \tag{5}$$

$$B = 3.641K^{-0.498} \exp(-1.497K^{-0.694}) \tag{6}$$

$$C = 0.00637(\phi - 100)^{-0.688} \tag{7}$$

Where K is the dimensionless droplet's inertia parameter and ϕ is the dimensionless Langmuir parameter, respectively, defined as follows:

$$K = \frac{v\rho_w d^2}{18\mu L} \tag{8}$$

$$\phi = \frac{Re^2}{K} \tag{9}$$

in which v is the wind speed (m/s), ρ_a and ρ_w are densities of air and water respectively (kg/m^3), μ is the absolute viscosity of air (μPa·s), d is the droplet diameter (m), Re is droplet's Reynolds number and L is the characteristic length of an object, i.e., cylinder or airfoil (m). When it comes to the estimation of the characteristic length of an object, the typical notion for the cylinder is to use radius, R while for the airfoils the typical notion is to use the leading-edge radius, c as a characteristic length[10,11]. In other words – the characteristic length of the reference cylinder and blade airfoil will be the same, provided the cylinder inscribes the leading edge radius of the airfoil, i.e., c = R.

The droplet diameter, d is typically a median volume diameter (hereafter, MVD) of a droplet spectrum of a cloud. This is a standard approximation used in the icing studies, first introduced by Langmuir and Blodgett[9] and later verified by Finstad et al[12]. The MVD approximation usage originates from the fact that apart from using a rotating multicylinder device, there is currently no equipment available to measure MVD or distribution spectra to any degree of precision on-site. However, as it has been shown recently[13], the multicylinder device may not accurately represent the actual in-cloud distribution using the MVD approximation. Moreover, as noted by Langmuir and Blodgett[6], the different distributions with same MVD will have different collision efficiency, depending on value of inertia parameter, K. As shown in Finstad et al.[12], the discrepancy in the overall collision efficiency values between the monodisperse distribution and the actual distribution spectrum under operating conditions used in that study are typically small enough to be ignored. However, considering vastly different values of the droplet inertia parameter, K, for cylinder and airfoil due to significant differences in the true air speed (TAS) faced by both the cylinder and the airfoil, it is deemed a reasonable assumption that the differences in the accreted ice mass caused by different distributions at two significantly different values of K will be significant. Therefore, in addition to the monodisperse distribution (also referred to as Langmuir A) four progressively wider distributions denoted Langmuir B – E (also referred in literature as gamma distributions) are used in this study. The distributions used in this study and their ratio of diameters, $(d/d_0)^n$ are given in Table II.

Taking values from Table II the overall collision efficiency of the spectrum (spectrum weighted overall collision efficiency) is calculated as:

$$\alpha_1 = \sum w_i \alpha_{1i} \tag{10}$$

where α_{1i} is the overall collision efficiency of ith bin and w_i is the LWC fraction of the ith bin. The overall collision efficiency of the ith bin is calculated as in eqs. (4) – (9). Finally, the restriction α_{1i} = 0.01 for cases when $K_i \leq 0.17$ is employed, based on Finstad et al[6].

2.2 Numerical Model

The multiphase Computational Fluid Dynamics (CFD) based numerical simulations are carried out using ANSYS FENSAP-ICE, which uses Eulerian water droplet impingement solver. The existing analytical models of the droplet behavior such and Langmuir and Blodgett, Finstad et al. etc. solve the droplet trajectories using the Lagrangian particle tracking approach. The Eulerian method treats the particle phase as a continuum and develops its conservation equations on a control volume basis and in a similar form as that for the fluid phase. The Lagrangian method considers particles as a discrete phase and tracks the pathway of each individual particle. By studying the statistics of particle trajectories, the Lagrangian method is also able to calculate the particle concentration and other phase data. On the other hand, by studying particle velocity vectors and its magnitudes in Eulerian method, it is possible to reconstruct the pathways and trajectories of particles in a phase. The general Eulerian two-phase model for viscous flow consists of the Navier-Stokes equations augmented by the droplets continuity and momentum equations[14]:

$$\frac{\partial \alpha}{\partial t} + \vec{\nabla} \cdot \left(\alpha \overrightarrow{V_d}\right) = 0 \tag{11}$$

$$\frac{\partial \left(\alpha \overrightarrow{V_d}\right)}{\partial t} + \vec{\nabla}\left[\alpha \overrightarrow{V_d} \otimes \overrightarrow{V_d}\right] = \frac{C_D Re_d}{24K} \alpha \left(\overrightarrow{V_a} - \overrightarrow{V_d}\right) + \alpha \left(1 - \frac{\rho_a}{\rho_d}\right) \frac{1}{Fr^2} \tag{12}$$

where the variables α and $V_{d,a}$ are mean field values of, respectively, the water volume fraction and droplet velocity. The first term on the right-hand-side of the momentum equation represents the drag acting on droplets of mean diameter *d*. It is proportional to the relative droplet velocity, its drag coefficient C_D and the droplets Reynolds number:

$$Re_d = \frac{\rho_a d V_{a,\infty} \left\| \overrightarrow{V_a} - \overrightarrow{V_d} \right\|}{\mu_a} \tag{13}$$

and an inertia parameter:

$$K = \frac{\rho_d d^2 V_{a,\infty}}{18 L_\infty \mu_a} \tag{14}$$

Where L_∞ is the characteristic length of the object. In case of the cylinder, the characteristic length is cylinder radius as opposed to diameter in analytical model. However, the use of a constant 18 in denominator ensures that inertia parameters are equal in analytical and numerical models. The second term represents buoyancy and gravity forces and is proportional to the local Froude number:

$$\mathrm{Fr} = \frac{\left\| V_{a,\infty} \right\|}{\sqrt{L_\infty g_\infty}} \tag{15}$$

These governing equations describe the same physical droplets phenomenon as Lagrangian particle tracking approach. Only the mathematical form in which these equations are derived changes, using

Partial Differential Equations instead of Ordinary Differential Equations. The droplet drag coefficient is based on an empirical correlation for flow around spherical droplets, or:

$C_D = (24/Re_d)\,(1 + 0.15Re_d^{0.687})$ for $Re_d \leq 1300$

$C_D = 0.4$ for $Re_d > 1300$

The local and overall collision efficiencies are calculated following a completely different approach, when compared to Finstad et al. The local and overall collision efficiencies are calculated as follows:

$$\beta = -\frac{\alpha \overrightarrow{V_d} \cdot \vec{n}}{wV_\infty} \tag{16}$$

where α is the local volume fraction (kg/m^3) and $\vec{n}$ is the surface normal vector. The overall collision efficiency is an integration of local collision efficiencies over surface area and is given as:

$$\beta_{tot} = \frac{\int \beta \, dA}{L_\infty^2} \tag{17}$$

The turbulence model used in this study if Menster's SST *k-ω* model[14,15]. The surface roughness model used in CFD simulations is NASA sand-grain roughness which is computed with an empirical NASA correlation for icing[14,16].

3 Results and discussion

This section describes the results obtained from the CFD based numerical simulations and the analytical model (ISO 12494) in this study. CFD simulations are mainly used for obtaining the values of *k*–factor, as was the case in original work of Turkia et al.[1] and analyzing the potential effects of the airfoil geometry on the *k*–factor itself. The main reason of using the CFD simulations in this study is the detailed treatment of airflow and the droplet impingement characteristics as compared to the potential flow approximation used in the analytical calculations. The use of analytical tools is governed by the necessity of making the results ISO 12494 compliant, as well as describing the *k*–factor values and any associated changes of it using the currently established framework. Moreover, the use of the ISO 12494 model allows for coupling of the analytical results with the mesoscale modeling, the sheer size of which makes them computationally infeasible for extensive CFD usage. This coupling allows for wind park icing load maps estimations in mesoscale simulations, while making sure that any obtained results are governed by the currently accepted icing modeling framework.

3.1 k–factor Values

Table III shows the ice mass accretion and *k*–factor values from the CFD based numerical simulations for reference cylinder and the airfoils used in this study. The values of ice accretions are in g/m, and the values of *k*–factor are given with respect to each droplet distribution spectrum. The ice accretion masses on airfoils are given for 60 m/s wind speed, while ice accretion for reference cylinder are given for 7 m/s wind speed.

As it can be seen from Table III, the values of *k*–factor tend to vary among different distributions and airfoils, with the maximum obtained value being 35.78 and minimum being 17.24, and in general, having the tendency to decrease as distribution becomes progressively "wider". In addition, there is a small difference in the *k*–factor values for all the airfoils in this study. From the results in Table III, it can be said that the *k*–factor also depends on the airfoil type/geometry and the droplet distribution spectrum used.

3.2 Effect of Airfoil Geometry

The effect of airfoil geometry on the ice accretion and the *k*–factor values are investigated by comparing the overall collision efficiency values for the cylinder and the airfoils at 7 and 60 m/s wind speed conditions using the CFD based numerical simulations which were carried out for this study. In order to permit the direct comparison, Table IV shows the ice masses in the numerical simulations for 7 m/s wind conditions, while the ice masses from 60 m/s conditions are given in Table III. Table V shows the overall collision efficiency values in the numerical simulations, in addition to "*Reference*" row showing the overall collision efficiency values for the analytical calculations. The overall collision efficiency values are obtained for the operating conditions in Table I with the droplet distributions given in Table II.

Table V shows an interesting situation. If the geometry would not be important, all values for the respective distribution would be equal, as airfoils with same characteristic length should accrete the same amount of mass as the cylinder with the same characteristic length under same operating conditions, which is the case in the analytical calculations and assumptions. Instead at 7 m/s wind speed the airfoils tend to accrete significantly less ice mass than the reference collector, while at 60 m/s wind speed conditions, the situation reverses and all airfoils accrete more mass than the reference collector. Furthermore, Table V shows that for wider distributions the reference collector (cylinder) tends to accrete less ice mass as the distributions widen, for 60 m/s wind speed conditions, in full accordance with Langmuir and Blodgett[9]. However, this is not the case for any of the tested airfoils, which tend to accrete more mass with the wider distributions, for both 7 and 60 m/s wind speed conditions. Moreover, if ice accretion on all airfoils should be the same, by extension, the ice shapes should also be the same. Contrary, if there are tangible differences present, such as change in local collision efficiency or maximum impingement angle values, one can see those by investigating ice shapes. Figure 1 presents comparison of ice shapes of NACA 0012, 23012, 4412 and 6412 airfoils at 60 m/s wind speed conditions for all droplet distribution spectra in this study.

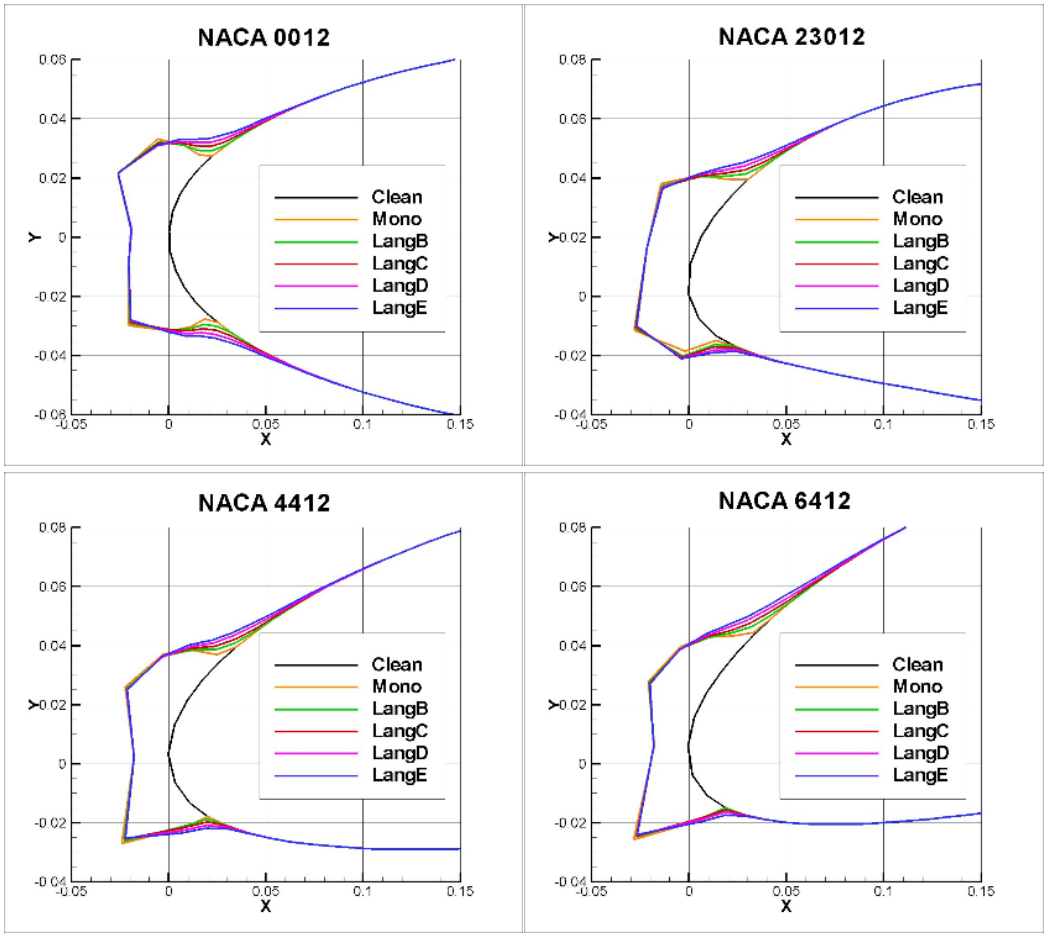

Figure 1 – Ice shapes of NACA 0012, 4412, 6412 and 23012.

Figure 1 shows that the ice shape becomes asymmetric, when comparing NACA airfoils and this asymmetry roughly follows the shape of leading edge of the airfoil. In addition, observe the changes to the maximum impingement angles occurring with the droplet distribution spectrum change, while stagnation line thicknesses are relatively the same across all the droplet distribution spectra. Furthermore, if variance in ice mass is caused by the effects of distribution spectra only, the relative values of the overall collision efficiencies would change by the same factor with the change of the droplet distribution spectrum when using, for example, the monodisperse distribution as a reference, assuming that dry growth assumption of $\alpha_2 = \alpha_3 = 1$ is valid. As it can be seen from Table V the overall collision efficiency values change by different ratios for all objects with the change of droplet distribution spectrum, which clearly indicates the effect of the geometry on the ice accretion. Two possible reasons are identified:

a) The inertia parameter for airfoils is not the same, most likely due to characteristic dimension being different.
b) Different airfoils experience different airflow and thus associated effects, for example, boundary layer effects become important.

The first reason, while highly logical, seems unlikely as it goes against core concepts of well-established in-flight icing theory. The second possible reason seems more likely, as compared to the cylinder, the

airfoil is aerodynamically streamlined object, specifically designed for maximizing lift and minimizing drag, thus creating the possibility of different flow conditions, experienced by different airfoils. However, without experimental study of airfoil ice accretion in similar conditions the verification of this claim is complicated. Finally, note the difference in the overall collision efficiency values between thee analytical results in the "*Reference*" row of Table V and the numerical results elsewhere. The difference in the overall collision efficiency values can be explained by fundamentally different treatment of the fluid flow in the analytical and numerical models. The analytical model treats the fluid flow as inviscid potential flow, while the numerical model treats it as viscid turbulent flow. Thus, the difference in the overall collision efficiency values can be attributed to the potential flow theory approximation limitations.

3.3 Effect of Droplet Distribution Spectrum and MVD

As seen from Table III the *k*–factor values depend on the droplet distribution spectrum used both in numerical and analytical results. The effect of the droplet distribution change on the *k*–factor values is investigated within the framework of the analytical model of ISO 12494 standard. Following the analytical procedure from section IIa, it is possible to calculate the ratio of the accreted ice between the wind turbine blade and the reference collector as:

$$\frac{\left(\mathrm{d}m/\mathrm{d}t\right)_b}{\left(\mathrm{d}m/\mathrm{d}t\right)_c} = \frac{(\alpha_1\alpha_2\alpha_3 vAw)_b}{(\alpha_1\alpha_2\alpha_3 vAw)_c} \tag{18}$$

where subscript *b* stands for the blade, and subscript *c* stands for the collector, assuming that dry growth conditions are maintained for both the collector and airfoil, thus $\alpha_2 = \alpha_3 = 1$, and eliminating the common variables, the ratio of accreted ice mass in g/m/hr can be obtained as:

$$\frac{\mathrm{d}m_b}{\mathrm{d}m_c} = \frac{\alpha_{1\mathrm{b}} v_b}{\alpha_{1\mathrm{c}} v_c} = \frac{\alpha_{1b}}{\alpha_{1c}}\frac{v_b}{v_c} = v_r\alpha_{1r} \tag{19}$$

where v_r and α_{1r} are ratios of wind speeds and overall collision efficiency. In addition, it can be noted that ratio of wind speeds is equal to the ratio of droplet inertia parameters, under previously mentioned assumptions, between the reference collector and the wind turbine blade, as the droplet inertia parameter *K* is linearly dependent on the wind speed *v*. Thus assuming constant $v_r = 60/7 = 8.571$ under operating conditions from Table I and computing the values of α_{1r} using the analytical model of ISO 12494, one can introduce the "pseudo" *k*–factor, γ calculated as:

$$\gamma = v_r\alpha_{1r} \tag{20}$$

Again, assuming $v_r = 8.571$ from the operating conditions in Table I and computing α_1 values for the droplet distribution spectra from Table II, the resultant values of "pseudo" *k*–factor, γ for the droplet distributions in this study are given in Table VI.

The agreement between *k*–factor values in Tables VI and III is somewhat reasonable, with the differences in values not exceeding 20%, with agreement having a tendency to improve as the

distribution progressively "widens". Again, some of this discrepancy can be explained by the difference in fluid flow modeling between the CFD simulations and the analytical model. Moreover, Table VII shows the calculated γ values for conditions in Turkia et al.[1] for comparison purposes. While Turkia et al. have used the monodisperse distribution (distribution A in this study), the results have been tabulated for all distributions in this study. Here the agreement with value k = 20 is sufficiently good and small discrepancies in numbers can be explained by possible differences in handling small connected values, for example pressure or viscosity. However, in their study, Turkia et al. assumed MVD of 25 microns. As MVD being one of the most important parameters in the ice accretion modeling, it is necessary to investigate how the change in the MVD value will affect the *k*–factor values. Table VIII shows the value of the "pseudo" *k*–factor, γ for the range of different MVDs under operating conditions from Table I. From Table VIII it can be seen that "pseudo" *k*–factor γ tends to vary significantly, depending on the MVD with maximum value being approximately 60 and smallest being approximately 12, both for Langmuir A distribution, at 15 and 50 microns, respectively. Moreover, observe that for lower values of MVD, the wider distributions tend to have smaller values of γ, however, for bigger MVD sizes, for example, 40 – 50 microns, the situation is opposite and narrower distributions tend to have smaller values of γ. The only row of values, where γ is close to 20 for all the distributions is for 25 microns MVD, the same value used by Turkia et al. in their study. Turkia et al. used NREL 5 MW reference turbine. An important question here, how the *k*–factor will change for different turbines, as TSR value can change based on hub height and RPM, and TSR and γ are connected values as one can see from preceding discussion.

3.4 Effect of Blade Tip Speed Ratio

For investigation of Tip Speed Ratio (TSR) on values of *k*–factor, two wind turbines have been selected – Siemens SWT-2.3-93[17] and Vestas V112-3.45[18]. The operating parameters for those turbines are listed in Table IX.

It should be noted that these wind turbines have options when it comes to hub height, for example, Vestas V112-3.45 has optional hub heights of 80, 94, 119 and 140 meters. The hub height of 80m has been selected for both turbines for consistency purposes. The calculations are performed using the analytical model of ISO 12494, as this allows to estimate the wide range of possible TSRs and their impact on *k*–factor values in quick and concise manner. The operating conditions for this examples are from Table I. It is worth mentioning that the wind speed of 7 m/s is assumed to be the value at the reference collector, being mounted on met mast 10 meters in height. Moreover, for simplicity following assumptions are being made in the calculations:

- It is assumed that wind direction is always normal to rotor plane.
- It is assumed that the reference collector and the blade at 85% of length have the same value of characteristic length, i.e., cylinder diameter or twice the leading edge radius respectively.
- It is assumed that RPM of wind turbine is independent of freestream wind speed.

The last assumption is made purely for illustrative purposes, while second assumption is made for simplification purposes. If it is known that reference object and the blade at 85% of the length have different characteristic lengths than the γ ratio has to be modified as:

$$\gamma = v_r \alpha_{1r} A_r \tag{21}$$

where A_r is the ratio of areas, provided dry growth regime is maintained for both the reference collector and wind turbine blade. It should be noted that in this case the ratio of overall collision efficiency will be more complicated due to its non-linear dependence on inertia parameter, which in turn depends on characteristic length. Noting that first assumption results in that the normal velocity component, which is a product of freestream wind speed and height effect and tangential component, which is a product of blade length and turbine RPM. Thus, the true air speed of the blade at 85% section can be obtained as $V = \sqrt{(xv)^2 + (r\omega)^2}$, where x is height factor, v is freestream velocity, r is the radial distance at 85% section and ω is rotational velocity of the blade in rad/s. The value of V is then used to compute the overall collision efficiency and the inertia parameter of the blade. The k–factor is computed by dividing previously mentioned values by overall collision efficiency and the inertia parameter of the reference collector. Figure 2 shows the graphical comparison of calculated k–factors for the conditions, specified in Table IX. The dotted horizontal line in Figure 2 corresponds to value of k–factor $k = 20$. Moreover, Figure 2 shows the results for all distributions (A – E) in this study to additionally show the effect of droplet distribution spectrum.

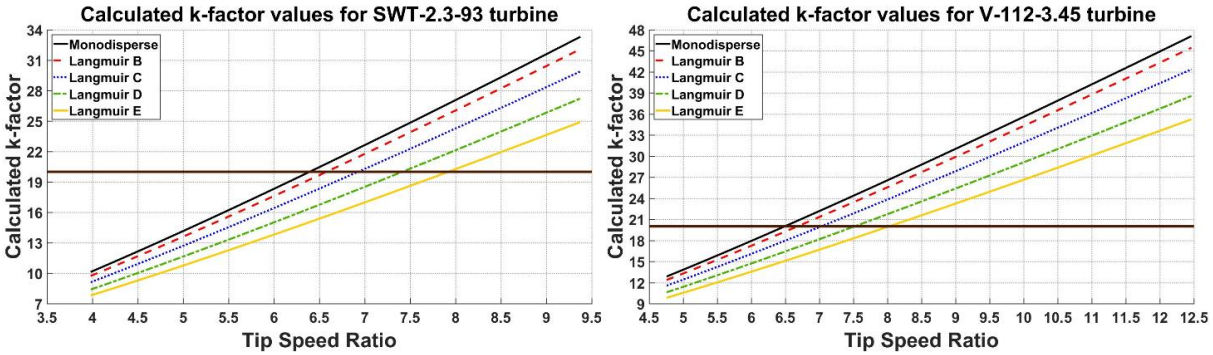

Figure 2 – k–factor values for Siemens SWT-2.3-93 wind turbine (left) and Vestas V112-3.45 wind turbine (right).

Summarizing the value of k–factor depends on a few critical parameters, namely:

- The droplet distribution used.
- The value of median volume diameter.
- Wind speed ratio and TSR.
- Airfoil geometry.

Since the droplet distribution spectra is somewhat difficult to estimate in practice, the usage of Langmuir distributions is recommended in addition to the monodisperse distribution, and in particular, the Langmuir D distribution, as it is a "standard" distribution for in-flight icing studies[19–21]. In addition, as it is seen from Table VIII the Langmuir D distribution has the value of the “pseudo” k–factor $\gamma = 20.17$, which is close to $k = 20$, as was initially proposed by Turkia et al.

4 Conclusion

In this paper the investigation into *k*–factor, describing the ratio of ice accretion on reference collector and wind turbine blade has been carried out by performing a series of numerical simulations using modern CFD software and analytical calculations within the framework of the existing ice accretion theory (ISO 12494). The results show that *k*–factor is not equal to constant 20, contrary to currently postulated assumption and can vary to a significant degree, depending on a number of different parameters not accounted in present model for it. These factors include the effect of object's geometry on ice accretion, droplet overall collision efficiencies, droplet distribution spectrum and median volume diameter under significantly different ambient conditions, pertaining to wind speed and tip speed ratios experienced by both the reference collector and wind turbine blade. While the results presented in this paper can be considered somewhat simplistic, the explanation of *k*–factor variance is established based on effects of MVD, droplet distribution, tip speed ratios and geometry effects. However, further numerical experimentations and experimental validation are necessary, in particular, when it comes to the ice accretions on different airfoils under different operating conditions. Despite this, the obtained results still show the shortcomings of current implementation for empirical *k*–factor ratio and as a result modifications and improvements for this ratio are needed. Considering the complexity of the process in question, there is a significant chance that ice accretion on a wind turbine, when compared to ice accretion of reference collector cannot be explained using simple, constant, dimensionless ratio.

References

1. V. Turkia, S. Huttunen, T. Wallenius. Method for estimating wind turbine production losses due to icing, VTT, 2013, Finland
2. B. Tammelin, M. Cavaliere, H. Holttinen, C. Morgan, H. Seifert, K. Säntti,2000Wind energy production in cold climates (WECO), Finnish Meteorological Institute, EUR 19.398
3. W.J. Jasinski, S.C. Noe, M.S. Selig, Bragg, M.B. Wind Turbine Performance Under Icing Conditions, Transactions of the ASME, Journal of solar energy engineering. New York, NY, USA. February, Vol. 120, pp 60-65.
4. H. Seifert, A. Westerhellweg, J. Kröning, 2003 Risk Analysis Of Ice Throw From Wind Turbines.
5. ISO 12494:2001(E), 2001. Atmospheric icing of structures. Standard. International Organization for Standardization. Geneva, CH.
6. K. J. Finstad, E.P. Lozowski, E. M. Gates, 1988. A computational investigation of water droplet trajectories. Journal of Atmospheric and Oceanic Technology, 5, pp. 160-170.doi:10.1175/1520-0426(1988)005<0160:ACIOWD>2.0.CO;2
7. R. E. Bredesen, H. Refsum, 2015, IceRisk - Methods for evaluating risk causedby ice throw and ice fall from wind turbines and other tall structures, 16thInternational Workshop on Atmospheric Icing, Uppsala, Sweden
8. L. Makkonen, 2000 (Models for the growth of rime, glaze, icicles and wet snow on structures, Phil. Trans. R. Soc. Lond. A 2000 358 2913-2939; DOI: 10.1098/rsta.2000.0690. Published 15 November 2000)
9. I. Langmuir, K. Blodgett, 1946. A Mathematical Investigation of Water Droplet Trajectories. Army Air Forces technical report 5418. Army Air Forces Headquarters, Air Technical Service Command.
10. J.-C. Tsao, S. Lee, 2012, Evaluation of Icing Scaling on Swept NACA 0012 Airfoil Models, NASA/CR–2012-217419, NASA
11. J.-C. Tsao, D.N. Anderson, 2005, Additional Study of Water Droplet Median Volume Diameter (MVD) Effects on Ice Shapes, NASA/CR–2005-213853

12. K. J. Finstad, E. P. Lozowski, L. Makkonen, 1988b. On the median volume diameter approximation for droplet collision efficiency. Journal of the Atmospheric Sciences 45, pp. 4008–4012.doi: 10.1175/1520-0469(1988)045<4008:OTMVDA>2.0.CO;2
13. K. F. Jones, G, Thompson, K.J. Claffey, E.P. Kelsey Gamma Distribution Parameters for Cloud Drop Distributions from Multicylinder Measurements. Journal of Applied Meteorology and Climatology, vol. 53, pp. 1606 – 1617, 2014. doi: 10.1175/JAMC-D-13-0306.1
14. FENSAP-ICE Technical Manual
15. D.C., Wilcox, 1988, "Re-assessment of the scale-determining equation for advanced turbulence models", AIAA Journal, vol. 26, no. 11, pp. 1299-1310.
16. J. Shin and T. Bond, 1992, Experimental and Computational Ice Shapes and Resulting Drag Increase for a NACA 0012 Airfoil, NASA Technical Manual 105743, 1992
17. Siemens SWT 2.3-93 Technical Specifications
18. Vestas V112-3.45 Technical Specifications
19. W. Wright, 2008, User's Manual for LEWICE Version 3.2, NASA/CR–2008-214255, NASA
20. C. S. Bidwell, 2012, Particle Trajectory and Icing Analysis of the E3 Turbofan Engine Using LEWICE3D Version 3, NASA/TM–2012-217696, NASA
21. M. Papadakis, S.-C. Wongm A. Rachman, K. E. Hung, G. T. Vu, C. S. Bidwell, 2007, Large and Small Droplet Impingement Data on Airfoils and Two Simulated Ice Shapes, NASA/TM–2007-213959

Table I – Operating condtions

Parameter	***Value***
Cylinder radius [leading edge radius of airfoil] (mm)	15
Air velocity (m/s)	7 (cylinder), 60 (airfoil)
Air temperature (°C)	–5
Altitude (m.a.g.l)	10 (cylinder), 80 (hub)
MVD (µm)	20
Liquid Water Content (g/m^3)	0.4
Icing duration (min)	60
Chord length (m)	1
Droplet distribution	Langmuir A – E

Table II – Langmuir distributions

LWC fraction	**d/d_o** ***Langmuir B***	**$(d/d_o)^{1.5}$** ***Langmuir C***	**$(d/d_o)^{2.0}$** ***Langmuir D***	**$(d/d_o)^{2.5}$** ***Langmuir E***
0.05	0.56	0.42	0.31	0.23
0.1	0.72	0.61	0.52	0.44
0.2	0.84	0.77	0.71	0.65
0.3	1.00	1.00	1.00	1.00
0.2	1.17	1.26	1.37	1.48
0.1	1.32	1.51	1.74	2.00
0.05	1.49	1.81	2.22	2.71

Table III – Ice Mass at 60 m/s and k–factor values from CFD simulations

Distribution ***Object***	***A (g/m)***	***B (g/m)***	***C (g/m)***	***D (g/m)***	***E (g/m)***
Cylinder (7 m/s)	44.140	45.692	53.279	59.367	73.432
NACA 0012	1506.483	1520.233	1560.729	1636.556	1735.632
NACA 4412	1525.261	1518.949	1549.694	1625.232	1715.327
NACA 6412	1579.491	1565.593	1613.423	1695.436	1787.881
NACA 23012	1471.361	1500.879	1530.999	1597.035	1660.198
N-22	1519.840	1519.856	1566.159	1639.767	1719.454
			k–*factor values*		
NACA 0012	34.13	33.27	29.29	27.57	23.64
NACA 4412	34.55	33.24	29.09	27.38	23.36
NACA 6412	35.78	34.26	30.28	28.56	24.35
NACA 23012	33.33	32.85	28.74	26.90	22.61
N-22	34.43	33.26	29.40	27.62	23.42

Table IV – Ice accretions for airfoils at 7 m/s wind speed from CFD simulations

Distribution ***Airfoil***	***A (g/m)***	***B (g/m)***	***C (g/m)***	***D (g/m)***	***E (g/m)***
Cylinder	44.140	45.692	53.279	59.367	73.432

NACA 0012	12.991	18.041	23.813	31.536	40.790
NACA 4412	14.512	20.147	25.248	31.786	41.011
NACA 6412	19.713	22.879	27.137	33.722	43.131
NACA 23012	16.724	21.209	26.565	33.852	41.452
N-22	17.126	21.020	26.164	33.921	42.599

Table V – Overall collision efficiency values

Distribution ***Airfoil***	***Langmuir A***	***Langmuir B***	***Langmuir C***	***Langmuir D***	***Langmuir E***
			Wind speed = 60 m/s		
Reference (Analytical)	0.613	0.600	0.589	0.580	0.570
			CFD- 60 m/s		
Cylinder	0.519	0.508	0.501	0.494	0.488
NACA 0012	0.581	0.587	0.602	0.631	0.670
NACA 4412	0.588	0.586	0.598	0.627	0.662
NACA 6412	0.609	0.604	0.622	0.654	0.690
NACA 23012	0.568	0.579	0.591	0.616	0.641
N-22	0.586	0.586	0.604	0.633	0.663
			Wind speed = 7 m/s		
Reference (Analytical)	0.179	0.182	0.191	0.206	0.220
			CFD- 7 m/s		
Cylinder	0.146	0.151	0.176	0.196	0.243
NACA 0012	0.043	0.060	0.079	0.104	0.135
NACA 4412	0.048	0.067	0.083	0.105	0.136
NACA 6412	0.065	0.076	0.090	0.112	0.143
NACA 23012	0.055	0.070	0.088	0.112	0.137
N-22	0.057	0.070	0.087	0.112	0.141

Table VI – Analytical comparison of spectrum-weighted inertia parameter (K), overall collision efficiency (α_{1r}) and "pseudo" k–factor γ for Langmuir Distributions at 7 and 60 m/s wind speed for reference collector

Distribution	***MVD (μm)***	**K *(7 m/s)***	***α_1 (7 m/s)***	**K *(60 m/s)***	***α_1 (60 m/s)***	***α_1 ratio (α_{60}/ α_7)***	***γ***
Langmuir A	20.0	0.606	0.179	5.191	0.613	3.425	29.35
Langmuir B	20.0	0.647	0.182	5.542	0.600	3.328	28.26
Langmuir C	20.0	0.714	0.191	6.093	0.589	3.084	26.33
Langmuir D	20.0	0.828	0.206	7.045	0.580	2.816	24.00
Langmuir E	20.0	0.988	0.220	8.366	0.570	2.591	21.94

Table VII – Values of "pseudo" k–factor γ for conditions in (Turkia et al.,2012)

Distribution	***A***	***B***	***C***	***D***	***E***
γ	21.44	21.39	20.96	20.17	19.37

Table VIII – Dependance of "pseudo" k–factor on MVD in analytical calculations

Distribution	***A***	***B***	***C***	***D***	***E***
MVD (µm)					
15	59.98	50.08	41.55	33.96	28.63
20	29.35	28.26	26.33	24.00	21.94
25	20.86	20.74	20.19	19.22	18.31
30	17.03	17.14	17.00	16.55	16.09
35	14.89	15.06	15.07	14.90	14.63
40	13.55	13.73	13.80	13.77	13.63
45	12.63	12.81	12.91	12.94	12.90
50	11.97	12.14	12.25	12.32	12.35

Table IX – Operating parameters of Siemens SWT-2.3-93[17] and Vestas V112-3.45[18] wind trubines

Parameter	***SWT-2.3-93***	***V112-3.45***
Blade length (m)	45	54.65
RPM	6 – 16	6.2 – 17.7
Hub height (m)	80	80

Paper 5. Modeling of Dry Ice Accretion on Cylinders – A Case Study of Present Analytical State

Pavlo Sokolov and Muhammad Shakeel Virk

Proceedings – 18th Int. Workshop on Atmospheric Icing of Structures, 2019, IWAIS 2019 - Reykjavík, June 23 – 28.

URL: https://iwais2019.is/images/Papers/055_iwais-sokolov-virk.pdf

---

Author's Contribution

Pavlo Sokolov has contributed substantially in the proposal of research idea, literature review, modelling, computing, analytical, experimental and numerical analysis, and writing of the paper.

Modeling of Dry Ice Accretion on Cylinders – A Case Study of Present Analytical State

Pavlo Sokolov[1], Muhammad S.Virk[1]

[1] *Arctic Technology & Icing Research Group, Institute of Industrial Technology, UiT – The Arctic University of Norway*

pavlo.sokolov@uit.no, muhammad.s.virk@uit.no

***Abstract*–** The present aggregated knowledge on the atmospheric icing of structures is covered under the framework of the ISO 12494 [1] standard "*Atmospheric Icing on Structures"*. When it comes to the ice growth and in particular – the droplet impingement on structural objects, the ISO model is well validated for the rotating cylinders of up to 76 mm in diameter based on experiments of Makkonen and Stallabrass [2] and/or operating conditions which result in the value of the droplet inertia parameter $K > 0.25$ [3]. Recently, Makkonen et al., 2018 [4] have recalculated the droplet trajectories using CFD approach for the values of $0.01 \leq K < 0.25$. Their results show good agreement between the theory and experimental values; however, this does not answer the question of analytical modeling of icing for larger cylinders fully. This work compares two approaches of the analytical modeling with possible application towards the modeling of icing on large conductors – the "spectrum-averaged" calculations using the full droplet distribution spectrum when compared to the Volume Weighted Diameter (VWD) approximation recently proposed by Zhang et al. [5]. The obtained results show that for the value of $K > 0.5$ both approaches tend to be in good agreement with each other and the experimental results, however, for the very high values of $K > 1.5$, the behavior of VWD approximation does not change as with the spectrum-averaged values. For the range of $0.3 < K < 0.5$, the agreement between spectrum-averaged results and the VWD approximation is somewhat worse and depends, in large, on the source distribution(s) used, with wider distributions producing worse agreement. Finally, for the values of $0.25 < K$, the VWD approximation produces significantly lower values of the overall collision efficiencies, albeit, still higher than the MVD approximation, which can potentially be detrimental in designing for and estimating icing loads in such conditions.

Keywords– *ice accretion; cylinder; collision efficiency; droplet distribution spectrum; MVD; VWD.*

1 Introduction

The study of in-cloud icing is not a new scientific field with significant amount of theoretical knowledge regarding modeling of the atmospheric ice accretion accumulated over several dozen years. At present, this aggregated knowledge is incorporated in the governing standard of atmospheric icing modeling the ISO 12494 "*Atmospheric Icing of Structures*" [1]. The theoretical modeling core of it is the Finstad et al. [3] collision efficiency parameterization, which relies on the concept of the so-called "Median Volume Diameter approximation" (MVD) in order to parameterize the in-cloud droplet spectrum using a singular value with the assumption that the cloud droplet distribution can be adequately represented using a uniform droplet distribution, where all the droplets have the same diameter, corresponding to

cloud MVD. The initial verification of the concept was carried out by Finstad in the doctoral thesis [6], later expanded in [3], and based on the results of experimental verification of Finstad et al. model by Makkonen and Stallabrass [2] it can be stated that the Finstad et al. model is applicable for the ranges of droplets overall collision efficiencies of $0.07 < E < 0.63$.

However, there are a few potential limitations when it comes to the MVD approximation. First, as noted in [3] the results with MVD approximation tend to underestimate the overall collision efficiencies in cases where the droplet inertia parameter $K < 0.25$. Second, the ISO 12494 also states that the Finstad et al. parameterization tends to underestimate the overall collision efficiencies if $E < 0.10$. Finally, Jones et al. [7] have showed that MVD approximation may not always be valid and in natural conditions, such as on Mt. Washington Observatory, the use of a droplet distribution spectrum can yield significantly better results over a monodisperse distribution when comparing ice accretion data on a multicylinder device.

Recently, it was shown [4] that modern Computational Fluid Dynamics (CFD) tools can achieve good results in modeling of ice accretion on cylinders for cases when $E < 0.10$, granted full droplet distribution spectrum with the "history term" is used. This term (also known as the Basset force) describes the vorticity diffusion from accelerating droplets' surface and the induced mass increase of the droplet due to accelerating air in immediate surroundings are important factors of non-steady state drag term, and term is defined as [6]:

$$F = -\frac{18\rho_f}{\left(2\rho_p + \rho_f\right) d}\left(\frac{\mu}{\pi\rho_f}\right)^{\frac{1}{2}} \int_{-\infty}^{t} \frac{\mathrm{d}u(\tau)}{\mathrm{d}\tau} \frac{\mathrm{d}\tau}{\sqrt{t-\tau}} \tag{1}$$

where d is the particle diameter, ρ_p and ρ_f are particle and fluid densities, respectively, and $u(\tau)$ is droplet's absolute velocity. As it can be seen from the structure of this term, its singular under integration, and thus is not being possible to solve for "directly", necessitating the usage of certain approximations, such as so-called "window methods" in order to obtain the non-singular closure to it. The question of good approximation of the Basset force is an open problem in fluid dynamics for several decades, which became more popular with increase in widespread usage in CFD tools and availability of computational resources.

The issue of the Basset force is of a certain complexity when it comes to the numerical modeling, however, the complexity is magnified in scope when it comes to the analytical modeling. Thus, the question is, what to do if analytical modeling of icing is required for cases where the overall collision efficiency is expected to be low?

Recently, Zhang et al. [5] have proposed the usage of so-called "Volume Weighted Diameter" approximation, as more "stable" parameter than MVD, in addition alleviating some of the issue of the underestimating the overall collision efficiencies for low K values. Moreover, Finstad et al. recommends to use a full droplet distribution spectrum for $K < 0.25$. Comparing these two approaches thus will be the main focus of this paper.

2 Design of the Experiment

For the benchmark for comparison, several experimental cases of Makkonen and Stallabrass [2] have been selected. The experiments of Makkonen and Stallabrass were conducted at Low Temperature Laboratory, National Research Council of Canada. The experiments employed a single atomizing spray nozzle at the centerline of 30.5 cm × 30.5 cm test section. Due to expected tunnel blockage effects for some test cases, plenum chambers with perforated walls were installed in place of test section floor and ceiling in order to achieve porosity of test section of 10%. Icing tests were made on horizontally mounted rotating cylinders of 1.024, 3.183, 4.440 and 7.609 cm in diameter. The speed of rotation was 2 RPM.

A water micromanometer was used to measure the dynamic pressure in the tunnel test section. The total temperature of the tunnel air was controlled and measured by a thermostat. The static temperature in the test section (as listed in Table 2 in [2]) was lower than the total temperature, due to the adiabatic expansion of the air accelerating within the contraction. LWC was measured using the single rotating cylinder method while droplet size measurements were done with the Forward Scattering Spectrometer Probe (FSSP). Measurements of the droplet size distributions (listed in the Table 2 in [2]) as "droplet size distribution category") were made at four wind velocities and nozzle settings. More information about experimental setup is available in the original source [2] while the test matrix for this study is given in Table I.

Unfortunately, due to the passage of time the information on droplet distributions in those experiments is no longer available, based on personal communication by Makkonen, so it is not possible to recalculate the results with full distribution spectrum for those experiments, in order to directly compare the results, however, several "synthesized" distributions will be used instead for this work.

Out of all 33 experimental cases, only the cases with highest values of MVD and LWC were selected, as to give the biggest expected ice accretion thickness. To compensate, additional cylinder diameters of 80 – 298 mm have been added for use in further modeling, as to simulate the effect of ice accretion on larger structures and/or for the low values of *K*. As it is shown in [2] they have utilized a variety of different icing durations in their experiments. However, for this work a "common denominator" of 30 min. icing duration has been used in order to somewhat streamline the comparison. It is expected that this alteration would not skew the values of the overall collision efficiencies by much.

Table I – Operating conditions.

Parameter	***Value***
Cylinder diameter (mm)	10.24, 20, 30, 50, 76.09, 80, 100, 149.5, 170, 249, 298
Cylinder length (m)	0.1
Air velocity (m/s)	20
Air temperature (°C)	–4.5
Icing duration (min)	30
LWC (g/m^3)	0.36
MWD (μm)	17.1
Rotational speed (RPM)	2

In order to study the effect of droplet distribution on the ice accretion process different parameterizations of the droplet spectrum, namely the gamma distributions (also referred as Langmuir distributions) are used [8]. The gamma distributions used in this study are given in Table II in terms of diameter ratios. All gamma distributions have MVD of 17.1 with 'distribution A' being monodispersed. These droplet distributions progressively get "wider" as the ratio of diameters increases, meaning that for distributions with higher value of diameter ratios, the diameters of bins will become progressively smaller or larger, when compared with "preceding" distribution. For the droplet spectrum, each bin collision efficiency is calculated independently and then weighted using the LWC fraction, in order to obtain the overall collision efficiency of the entire spectrum.

Table II – Langmuir distributions.

LWC fraction	***A***	***B***	***C***	***D***	***E***	***F***	***G***	***H***	***J***
0.05	1.00	0.56	0.42	0.31	0.23	0.18	0.13	0.10	0.06
0.1	1.00	0.72	0.61	0.52	0.44	0.37	0.32	0.27	0.19
0.2	1.00	0.84	0.77	0.71	0.65	0.59	0.54	0.50	0.42
0.3	1.00	1.00	1.00	1.00	1.00	1.00	1.00	1.00	1.00
0.2	1.00	1.17	1.26	1.37	1.48	1.60	1.73	1.88	2.20
0.1	1.00	1.32	1.51	1.74	2.00	2.30	2.64	3.03	4.00
0.05	1.00	1.49	1.81	2.22	2.71	3.31	4.04	4.93	7.34

The Langmuir distributions B–E were initially presented in [9] as a mathematical approximations of the droplet distribution spectra in fog and rising clouds on Mt. Washington observatory. Later, Howe [8] has presented "wider" droplet distributions F–J, based on previous observations on Mt. Washington observatory, in order to adequately capture bimodal and trimodal droplet distributions, which are expected to happen in nature.

2.1 Analytical Model

The cloud impingement parameters are calculated in accordance with [3] as:

$$\begin{aligned} \mathrm{X}(K,\phi) = &\left[C_{X,1}K^{C_{X,2}}\exp\left(C_{X,3}K^{C_{X,4}}\right) + C_{X,5}\right] - \\ -&\left[C_{X,6}(\phi - 100)^{C_{X,7}}\right] \times \left[C_{X,8}K^{C_{X,9}}\exp\left(C_{X,10}K^{C_{X,11}}\right) + C_{X,12}\right] \end{aligned} \tag{2}$$

where X is the cloud impingement parameter of interest, in this particular case the overall collision efficiency E. The constants $C_{X,n}$ are given in [3].

For the analytical calculations, suing the full droplet distribution spectrum, the "spectrum-averaging" procedure is employed, which is given as:

$$X(K, \phi)_{spec} = \sum w_i X(K_i, \phi)_i \tag{3}$$

where w_i is fractional weight of bin i, subscript i refers to a given parameter calculated for bin i, while subscript *spec* shows spectrum averaged values. The spectrum values are linearly dependent on the per-bin values, as spectrum values, $X(K, \phi)_{spec}$ are obtained by summation of per-bin values $X(K_i, \phi)_i$ using

LWC fraction w_i as a weighting constant. In addition, the constraint of $X(K_i, \phi)_i = 0.01$ for $K_i \leq 0.17$ is used as per [3]. Conversely, the VWD is calculated as [5]:

$$\text{VWD} = \sum w_i d_i \tag{4}$$

where d_i is the MVD value of bin i of the droplet distribution spectrum. The VWD approach despite looking similarly to the spectrum-averaging procedure in eq. (3) works a bit differently. The VWD approach first calculates the actual VWD value itself from the distribution, for example, the distributions in Table II, and then estimates the overall collision efficiency from eq. (3) in one iteration, unlike the spectrum-averaging procedure which estimates the overall collision efficiency of each bin of the distribution separately and then sums up the results. However, as evidenced by the structure of the VWD term, the VWD value of the distribution will differ from that of MVD, with Table III giving the VWD values of distributions from Table II, all of which have the MVD value of 17.1 μm.

Table III – VWD values for distributions from Table II.

Distribution	***A***	***B***	***C***	***D***	***E***	***F***	***G***	***H***	***J***
VWD (μm)	17.10	17.25	17.61	18.27	19.10	20.17	21.52	23.21	27.58

The ice deposit diameter D_i of cylinder is calculated as [10]:

$$D_i = \left[\frac{4(M_i - M_{i-1})}{\pi \rho_i} + D_{i-1}^2\right]^{1/2} \tag{5}$$

where M is the mass accretion value per unit length, ρ is the ice density and subscript i indicates the time step. In all analytical calculations the time step used is, t = 30 seconds. This is to ensure that the cylinder rotates at least 360° degrees along its longitudinal axis on each time step to ensure even ice deposit on the surface, in accordance with [10]. The accreted ice density at any given time step is calculated as [10]:

$$\rho_i = 378 + 425 \log_{10}(R_m) - 82.3\left(\log_{10}(R_m)\right)^2 \tag{6}$$

where, R_m is the Macklin density parameter, given as:

$$R_m = \frac{V_0 d}{2 t_s} \tag{7}$$

where d is the MVD in microns, V_0 is the impact velocity of the droplet in m/s and t_s is the surface temperature of the ice deposit in Celsius. In the case of dry growth, the surface temperature of the ice deposit can be obtained as [10]:

$$\frac{2}{\pi} Evw\left(L_f + c_w t_a - c_i t_s\right) =$$
$$= h\left[(t_s - t_a) + \frac{kL_s}{c_p p_a}(e_s - e_a) - \frac{rv^2}{2c_p}\right] + \sigma\alpha(t_s - t_a) \tag{8}$$

where L_f and L_s are latent heats of fusion and sublimation respectively, c_w, c_i, and c_p are specific heats of water, ice and air respectively, p_a, e_s and e_a are air pressure, saturation water vapour pressures at surface and air temperatures respectively, h is the overall heat transfer coefficient, k = 0.62, r is the recovery factor, with value of 0.79 being used for cylinder, t_s and t_a are surface and air temperatures in Celsius, σ is the Stefan-Boltzmann constant and $\alpha = 8.1 \times 10^7$ K^3. More details on the terms of heat transfer and derivation of heat transfer equations are given in [10].

2.2 Numerical Setup

The multiphase CFD based numerical simulations were carried out using ANSYS FENSAP-ICE, which uses an Eulerian water droplet impingement solver. The general Eulerian two-phase model for viscous flow consists of the Navier-Stokes equations augmented by the droplets continuity and momentum equations [11]:

$$\frac{\partial \alpha}{\partial t} + \vec{\nabla} \cdot \left(\alpha \overrightarrow{V_d}\right) = 0 \tag{9}$$

$$\frac{\partial\left(\alpha \overrightarrow{V_d}\right)}{\partial t} + \vec{\nabla}\left[\alpha \overrightarrow{V_d} \otimes \overrightarrow{V_d}\right] =$$
$$= \frac{C_D Re_d}{24K} \alpha\left(\overrightarrow{V_a} - \overrightarrow{V_d}\right) + \alpha\left(1 - \frac{\rho_a}{\rho_d}\right)\frac{1}{Fr^2} \tag{10}$$

where the variables α and $V_{d,a}$ are mean field values of, respectively, the water volume fraction and droplet velocity. The first term on the right-hand-side of the momentum equation represents the drag acting on droplets of mean diameter d. It is proportional to the relative droplet velocity, its drag coefficient C_D and the droplet Reynolds number [11]:

$$Re_d = \frac{\rho_a d V_{a,\infty} \left\| \overrightarrow{V_a} - \overrightarrow{V_d} \right\|}{\mu_a} \tag{11}$$

$$K = \frac{\rho_d d^2 V_{a,\infty}}{18 L_\infty \mu_a} \tag{12}$$

where L_∞ is the characteristic length of the object. In case of the cylinder, the characteristic length is cylinder radius. The second term represents buoyancy and gravity forces, and is proportional to the local Froude number [11]:

$$\mathrm{Fr} = \frac{\left\| V_{a,\infty} \right\|}{\sqrt{L_\infty g_\infty}} \tag{13}$$

These governing equations describe the same physical droplet phenomenon as the Lagrangian particle tracking approach. Only the mathematical form in which these equations are derived changes, using Partial Differential Equations instead of Ordinary Differential Equations. The droplet drag coefficient is based on an empirical correlation for flow around spherical droplets, or [11]:

$C_D = (24/Re_d)\,(1 + 0.15Re_d^{0.687})$ for $Re_d \leq 1300$

$C_D = 0.4$ for $Re_d > 1300$

The droplet local collision efficiency is calculated as follows [11]:

$$\beta = -\frac{\alpha \overrightarrow{V_d} \cdot \vec{n}}{(LWC)V_\infty} \tag{14}$$

where α is the local volume fraction (kg/m^3) and $\vec{n}$ is the surface normal vector. The total collision efficiency is an integration of local collision efficiencies over the surface area and is given as [11]:

$$\beta_{tot} = \frac{\int \beta \, dA}{L_\infty^2} \tag{15}$$

The ice density calculation procedures in FENSAP follows that given in the analytical model.

Detailed mesh sensitivity analysis was carried out to accurately determine the boundary layer characteristics (shear stress and heat fluxes), a *y*+ values of less than 1 is used near the cylinder wall surface. Number of mesh elements and *y*+ value was selected based upon the heat flux calculations, where a numerical check was imposed that the heat flux computed with the classical formulae d*t*/d*n* should be comparable with the heat flux computed with the Gresho's method.

3 Results and Discussion

Tables IV and V list the overall collision efficiency values for the Langmuir distributions and the VWD, respectively. The "*Ref*" column shows the values of the experimental overall collision efficiencies from [2], where applicable.

Table IV – Analytical values of overall collision efficiencies using Langmuir distributions.

D (mm)	***Mono***	***Lang B***	***Lang C***	***Lang D***	***Lang E***	***Lang F***	***Lang G***	***Lang H***	***Lang J***	***Ref***
10.24	0.554	0.541	0.532	0.525	0.518	0.512	0.508	0.505	0.502	0.56
20	0.414	0.405	0.401	0.401	0.402	0.402	0.406	0.411	0.417	–
31.83	0.303	0.298	0.300	0.306	0.312	0.320	0.329	0.338	0.353	0.32
50	0.196	0.197	0.204	0.216	0.229	0.241	0.254	0.268	0.294	–
76.09	0.111	0.117	0.128	0.143	0.158	0.176	0.192	0.209	0.238	0.18
80	0.102	0.109	0.120	0.135	0.151	0.168	0.185	0.202	0.231	–
100	0.067	0.076	0.087	0.104	0.121	0.138	0.155	0.172	0.203	–
149.5	0.022	0.035	0.046	0.060	0.074	0.090	0.107	0.123	0.155	–

170	0.012	0.026	0.036	0.048	0.062	0.077	0.093	0.109	0.141	–
249	0.010	0.013	0.019	0.027	0.038	0.050	0.064	0.078	0.109	–
298	0.010	0.011	0.014	0.020	0.029	0.040	0.052	0.065	0.094	–

Table V – Analytical values of overall collision efficiencies using VWD approximation.

D (mm)	***Mono***	***VWD B***	***VWD C***	***VWD D***	***VWD E***	***WVD F***	***WVD G***	***VWD H***	***WVD J***	***Ref***
10.24	0.554	0.557	0.566	0.581	0.598	0.619	0.644	0.671	0.727	0.56
20	0.414	0.418	0.428	0.445	0.465	0.490	0.518	0.551	0.621	–
31.83	0.303	0.307	0.316	0.334	0.354	0.380	0.411	0.446	0.523	0.32
50	0.196	0.199	0.208	0.224	0.243	0.268	0.297	0.333	0.413	–
76.09	0.111	0.114	0.120	0.133	0.150	0.170	0.196	0.228	0.305	0.18
80	0.102	0.105	0.111	0.124	0.139	0.160	0.185	0.216	0.292	–
100	0.067	0.069	0.075	0.085	0.098	0.116	0.138	0.166	0.236	–
149.5	0.022	0.023	0.027	0.033	0.042	0.054	0.069	0.090	0.145	–
170	0.012	0.013	0.016	0.021	0.029	0.039	0.052	0.070	0.120	–
249	0.010	0.010	0.010	0.010	0.010	0.010	0.015	0.027	0.060	–
298	0.010	0.010	0.010	0.010	0.010	0.010	0.010	0.013	0.039	–

From the Tables IV and V it can be seen that for higher values of the droplet inertia parameter, $K > 0.5$ the VWD approximation tends to yield higher values of the overall collision efficiencies for all tested distributions. Furthermore, observe that for very high value of $K > 1.5$, corresponding to cases of 10.24 and 20 mm cylinders, the Langmuir distributions are giving the smaller values of E than the monodisperse distributions. This behavior as was originally noted in [9] who first implemented the distributions B–E. However, since the VWD approximation is a monodisperse distribution, the similar behavior does not apply to it, so the values of the overall collision efficiency will continue to increase with the increase of K, in addition, the bigger VWDs have higher value of K by default as they are larger diameter droplets.

For the ranges of $0.4 < K < 0.75$, corresponding to the 50–100 mm cylinders both VWD and spectrum-averaged values are in relatively good agreement, with exception of results for wide distributions G–J, for which VWD tends to scale up in values much more "aggressively". In general, the VWD approximation is more sensitive to the change in droplet distribution spectrum than the spectrum-averaging procedure for the higher values of K. However, for the cases of 149.5–298 mm cylinders, which corresponds to the value of $K < 0.25$ the situation reverses and the spectrum-averaged results show higher values of overall collision efficiencies and bigger changes arising with the change of distribution.

This can be explained by the fact that in such conditions, the bigger sized droplets within a distribution are a dominating factor when it comes to the values of the overall collision efficiency, due to highly non-linear dependence of it on droplet size, while the smaller droplets contribute less, but still add to the overall collision efficiency due to constraint of $X(K_i, \phi)_i = 0.01$ for $K_i \leq 0.17$ being enforced. While there is not enough experimental data for validation of both said concepts at very low values of K, in general, the usage of spectrum-averaging is a more "safe" choice when it comes to design guidelines, as this method will provide considerably higher ice masses in the theoretical modeling.

Tables VI and VII present the numerical results in the CFD simulations and the comparison between numerical and analytical results, respectively. However, due to rather significant time expenditures on the CFD simulations, only cases D and E in addition to monodisperse distributions simulations have been performed. The choice of distributions D and E is deemed to be "representative" as they are mostly being "in the middle" as it can be seen from Tables II and III.

Table VI – Numerical values of overall collision efficiencies in CFD simulations.

D (mm)	***Mono***	***VWD D***	***VWD E***	***Lang D***	***Lang E***
10.24	0.562	0.592	0.610	0.533	0.526
20	0.386	0.419	0.439	0.380	0.383
31.83	0.249	0.278	0.296	0.261	0.270
50	0.171	0.199	0.217	0.194	0.208
76.09	0.081	0.101	0.114	0.116	0.116
80	0.082	0.096	0.109	0.117	0.125
100	0.051	0.067	0.079	0.088	0.104
149.5	0.015	0.022	0.028	0.045	0.058
170	0.009	0.015	0.019	0.038	0.051
249	0.003	0.004	0.005	0.017	0.025
298	0.002	0.002	0.003	0.010	0.017

Table VII – Comparison of overall collision efficiencies across the models.

D (mm)	***Mono Num***	***Mono Ana***	***VWD D Num***	***VWD D Ana***	***VWD E Num***	***VWD E Ana***	***Lang D Num***	***Lang D Ana***	***Lang E Num***	***Lang E Ana***
10.24	0.562	0.554	0.592	0.581	0.61	0.598	0.533	0.525	0.526	0.518
20	0.386	0.414	0.419	0.445	0.439	0.465	0.380	0.401	0.383	0.402
31.83	0.249	0.303	0.278	0.334	0.296	0.354	0.261	0.306	0.270	0.312
50	0.171	0.196	0.199	0.224	0.217	0.243	0.194	0.216	0.208	0.229
76.09	0.081	0.111	0.101	0.133	0.114	0.150	0.116	0.143	0.116	0.158
80	0.082	0.102	0.096	0.124	0.109	0.139	0.117	0.135	0.125	0.151
100	0.051	0.067	0.067	0.085	0.079	0.098	0.088	0.104	0.104	0.121
149.5	0.015	0.022	0.022	0.033	0.028	0.042	0.045	0.060	0.058	0.074
170	0.009	0.012	0.022	0.021	0.028	0.029	0.038	0.048	0.058	0.062
249	0.003	0.010	0.004	0.010	0.005	0.010	0.017	0.027	0.025	0.038
298	0.002	0.010	0.002	0.010	0.003	0.010	0.011	0.020	0.017	0.029

As it can be seen from Tables VI and VII the behavior of both spectrum-averaging and VWD approximations in the CFD simulations is relatively the same as in case with analytical modeling, thus the preceding discussion and its conclusions do apply for numerical modeling also, however, some of the obtained values in CFD when compared to analytical results are somewhat different and thus need explanation.

First, observe that for majority of cases tested the CFD values show lower overall collision efficiencies. This can be explained by the viscous treatment of the flow, as the boundary layer effects are much more prominent and do influence smaller droplet's "pushing" them "away" from the cylinder into the flow's

streamline. This effect becomes more significant with the increase of cylinder's diameter as it can be inferred from the results for the monodispersed case. Second, observe significantly lower values for the larger cylinder diameters, in particular 249 and 298 mm one in the CFD simulations. The reason for this is that the constraint of $X(K_i, \phi)_i = 0.01$ for $K_i \leq 0.17$ is not employed in the numerical simulations, thus the overall collision efficiency can be an arbitrary small positive value much less than 0.01. Therefore, based on these results, the CFD modeling can be used for both the spectrum-averaging and the VWD approximation approaches, and as with the VWD approach itself, the best results are reached for the cases with $K > 0.5$. Finally, the results from Table VII are given in graphical form in Fig. 1 for the ease of quick comparison.

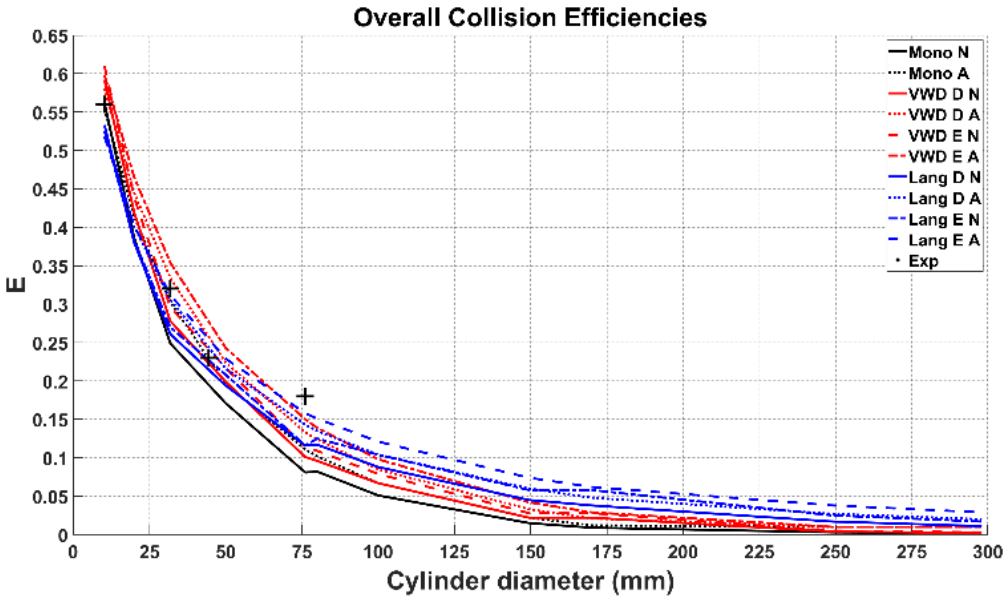

Fig. 1 – Overall collision efficiencies for the cases from Table VII. The black crosses represent experimental values from the (Makkonen and Stallabrass, 1987) experiments. Letters "A" and "N" indicate the analytical and the numerical results, respectively.

4 Conclusion

In this work the detailed comparison between the "spectrum-averaging" procedure and the Volume Weighted Diameter (VWD) has been performed for the wide range of cylinder diameters in order to test the applicability and performance of both concepts over a wide range of values of the droplet inertia parameter K. The results show that for the value of $K > 0.5$ both approaches tend to be in good agreement with each other and the experimental results, however, for the very high values of $K > 1.5$, the behavior of VWD approximation does not change as with the spectrum-averaged values. In general, for $K > 0.5$ the VWD approximation is very sensitive towards the source distribution(s). For the range of $0.3 < K < 0.5$, the agreement between spectrum-averaged results and the VWD approximation is somewhat worse and depends, in large, on the source distribution(s) used, with wider distributions producing worse agreement. Finally, for the values of $0.25 < K$, the VWD approximation produces significantly lower values of the overall collision efficiencies, albeit, still higher than the MVD approximation, which can

potentially be detrimental in designing for and estimating icing loads in such conditions, such as, long-term accretion of power lines, power line and communication towers etc.

Fundamentally, while VWD approximation does alleviate some issues of the MVD approximation, for low values of K, such as $0.25 < K$, it does not achieve much added performance when it comes to estimating the overall collision efficiencies, while, simultaneously, for very high values of K it can overestimate the overall collision efficiency. Ultimately, its lesser complexity when compared to the spectrum-averaging does not warrant the use in these sort of conditions, while for higher values of K, i.e., $0.3 < K < 0.7$ its usage may be warranted over the MVD approximation to produce higher estimates of the overall collision efficiency.

Acknowledgement

The work reported in this paper is funded by the Research Council of Norway, IceBOX- project no 282403.

References

1. ISO 12494:2001(E), 2001. *Atmospheric icing of structures*. Standard. International Organization for Standardization. Geneva, CH
2. Makkonen, L., Stallabrass, J.R., 1987. *Experiments on the cloud droplet collision efficiency of cylinders*. Journal of Applied Meteorology 26, 1406-1411.doi:10.1175/1520-0450(1987)026<1406:EOTCDC>2.0.CO;2
3. Finstad, K.J., Lozowski, E.P., Gates, E.M., 1988. *A computational investigation of water droplet trajectories*. Journal of Atmospheric and Oceanic Technology, 5, 160-170.doi:10.1175/1520-0426(1988)005<0160:ACIOWD>2.0.CO;2
4. Makkonen, L., Zhang, J., Karlsson, T., Tiihonen, M., *Modelling the growth of large rime ice accretions*, CRST, 151 (2018), 133-137.
5. Zhang, J., Qing, H., Makkonen, L., *A novel water droplet size parameter for calculation of icing on power lines*. Coltec (2017) https://doi.org/10.1016/j.coldregions.2018.01.021, pre-print
6. Finstad, K. J. 1986. *Numerical and experimental studies of rime ice accretion on cylinders and airfoils*. Ph.D. thesis. University of Alberta, Canada.doi:10.7939/R3N58CS1V.
7. Jones, K.F., Thompson, G., Claffey, K.J., Kelsey, E.P, 2014, *Gamma Distribution Parameters for Cloud Drop Distributions from Multicylinder Measurements*. Journal of Applied Meteorology and Climatology, vol. 53, pp. 1606 – 1617. doi: 10.1175/JAMC-D-13-0306.1
8. Howe, J.B. 1990. *The rotating multicylinder method for the measurement of cloud liquid water content and droplet size*. CRREL Report.
9. Langmuir, I., Blodgett, K., 1946. *A Mathematical Investigation of Water Droplet Trajectories*. Army Air Forces technical report 5418. Army Air Forces Headquarters, Air Technical Service Command.
10. Makkonen, L., 1984. *Modeling of Ice Accretion on Wires*. Journal of Applied Meteorology 23, 929-939. doi:10.1175/1520-0450(1984)023<0929:MOIAOW>2.0.CO;2
11. FENSAP–ICE User Manual

Paper 6. Aerodynamic Forces on Iced Cylinder for Dry Ice Accretion – A Numerical Study

Pavlo Sokolov and Muhammad Shakeel Virk

Journal of Wind Engineering & Industrial Aerodynamics, 2020, Volume 206.

DOI: 10.1016/j.jweia.2020.104365

Author's Contribution

Pavlo Sokolov has contributed substantially in the proposal of research idea, literature review, modelling, computing and numerical analysis, and writing of the paper.

Aerodynamic Forces on Iced Cylinder for Dry Ice Accretion – A Numerical Study

Sokolov Pavlo*, Muhammad Shakeel Virk

Institute of Industrial Technology

University of Tromsø – The Arctic University of Norway,

*Email: pavlo.sokolov@uit.no

Abstract

Within this paper the ISO 12494 assumption of standard of slowly rotating reference collector under ice accretion has been tested. This concept, introduced by (Makkonen, 1984), suggests that the power line cables, which are the basis of the "reference collector" in the ISO framework, are slowly rotating under ice load, due to limited torsional stiffness. For this purpose, several Computational Fluid Dynamics (CFD) simulations of the atmospheric ice accretion and transient airflow conditions over iced cylinder at different angles of attack were performed. In order to ascertain the similarity, several parameters were chosen, namely, drag, lift and moment coefficients, pressure and viscous force. The results suggest that the benchmark cases of rotating and uniced cylinder have "similar" aerodynamic loads when compared with the "averaged" results at different angles of attack (AoA), namely, the values of total pressure and viscous force. However, on individual and instantaneous basis the difference in the airflow regime between AoA cases and the benchmark cases can be noticeable. The results from the ice accretion simulation suggest that at long term the gravity force will be the dominating one, with rotating cylinder being a good approximation to the "averaged" angle of attack cases for the ice accretion.

Keywords: atmospheric icing; cylinder; CFD; numerical; angle of attack; drag; lift; transient; comparison.

1 Introduction

The study and modeling of the atmospheric icing of structures is of a prime importance in ice-prone regions, in particular in the High North. The primary importance of it lies in the estimation of ice loads on objects, in order to evaluate potential threats of damage on infrastructural objects due to the accreted ice. At present, the aggregated knowledge on atmospheric icing of structures, as well as modeling and measuring guidelines for ice loads are being governed by the ISO 12494 standard "*Atmospheric Icing on Structures*" (ISO, 2001). When it comes to modeling and classifying the ice loads under its' framework, one of the primary key points in the ISO 12494 is the notion of a "reference collector" – a slowly rotating 30 mm in diameter cylinder by 500 mm in length. The notion of using a rotating cylinder is of a particular interest, and, sometimes, its usage results in questions.

The choice of a rotating cylinder as a reference collector can be explained by several reasons. First, the usage of a rotating cylinder results in uniform shape of accreted ice, which is rather simple to model, as the cylinder's cross-section, remains circular throughout entire period of the ice accretion, and any possible effects, arising due to a potentially asymmetric shape in the icing of a non-rotating cylinder, are not applicable in the rotating case. This simplifies the analytical model procedure significantly. Second, the Finstad et al. icing parameterization (Finstad et al., 1988) which is the main part of theoretical modeling in ISO 12494, and has been independently verified by (Makkonen and Stallabrass, 1987) assumes the rotating cylinders. Lastly, the idea of using a rotating cylinder in the modeling of the ice accretion was originally proposed by (Makkonen, 1984) in connection to the power line icing. The primary assumption behind this is that the conductor cable is slowly rotating under induced loading, due to limited torsional stiffness of the conductor cable.

The phenomenon of rotation of the power line cables under icing loads has been widely observed in nature, with the ice shape being circular under long term conditions, both as referenced in (Makkonen, 1984). However, to the best of authors' knowledge, this exact treatment of this phenomenon received very limited experimental investigation, in particular, when it comes to the start of the rotation and the rate of rotation of the cable under ice loads. Only (Makkonen and Stallabrass, 1984) have performed some experimental investigation, on a model wires, approximately 1 and 4 cm in diameter, attached to the springs, to emulate the torsional stiffens of an actual wire. In the wind tunnel experiments they have measured the rotation rates of 65 and 224 °/hr for 1 and 4 cm "wire" respectively. Again, as referenced in (Makkonen, 1984), the cause of rotation of power lines is attributed to the limited torsional stiffness of power line against the force, caused by the gravity of the accreted deposit.

This has certain potential implications for the ice modeling on power lines, in conjunction with the previously postulated assumption of uniform slow rotation. If the rotation rate is slow, or happens only in large "increments" after the significant icing load is accumulated first, the accreted ice shape is not going to be uniform, unless a large time interval is used in the modeling of icing, which can negatively affect the accuracy of it. Moreover, while the gravity has been so far assumed to be the dominating factor causing power line rotation, to the best of authors knowledge there have been no rigorous attempts to quantify the aerodynamic forces, generated by the iced conductor in cross flow, and their potential impact on power line cables rotation.

Therefore, this study attempts to addresses some of the potential effects of these. The main purpose of this work is to ascertain, using a series of CFD based numerical simulations, how the aerodynamic forces and the airflow behavior around iced cylinder change for a number of different angles of attack. It is believed that such analysis can assist and supplement in the estimation of the combined effects of wind and atmospheric icing, for example, in the methodology, attempted by (Rossi et al, 2020). The comparison of obtained results is made against the rotating cylinder case, in order to check if the ISO 12494 approach of "reference collector" and rotating conductor assumption are a representative way of modeling the icing events on power lines under slow rotation assumption as postulated by (Makkonen, 1984). This is done by comparing drag, lift and moment coefficients in addition to Strouhal number and total pressure and viscous force of an iced cylinder as primary descriptors of "flow similarity".

2 Design of Experiment

2.1 Operating Conditions

As a baseline for comparison, the case no. 2 from (Fu et al., 2006) has been selected. This particular choice was governed by several reasons, namely the need to select the case with known experimental ice shape, under "dry growth" conditions, and with the cylinder diameter, which is representative of a diameter of a power line conductor. In particular, having the information on the experimental ice shape allows for an ease of validation of the numerical results, while operating with the "dry growth" conditions reduces the amount of variables that can influence the ice growth. The operating conditions for this study are given in Table 1, while the comparison between the simulated ice shape at 0° AoA and the experimental shape from (Fu et al., 2006) is shown in Figure 1. Since the droplet distribution spectrum information was not provided in (Fu et al., 2006), the simulations were performed using Langmuir D distribution, as it is a common distribution in the in-flight icing studies (Bidwell, 2012), (Papadakis et. al, 2007), (Wright, 2008).

Table 1 – Operating conditions.

Parameter	***Value***
Air speed (m/s)	5
Temperature (°C)	–15
MVD (µm)	35
Cylinder diameter (mm)	35
LWC (g/m^3)	1.2
Icing duration (min)	30
Angle of attack	0°, 30°, 60°, 90°

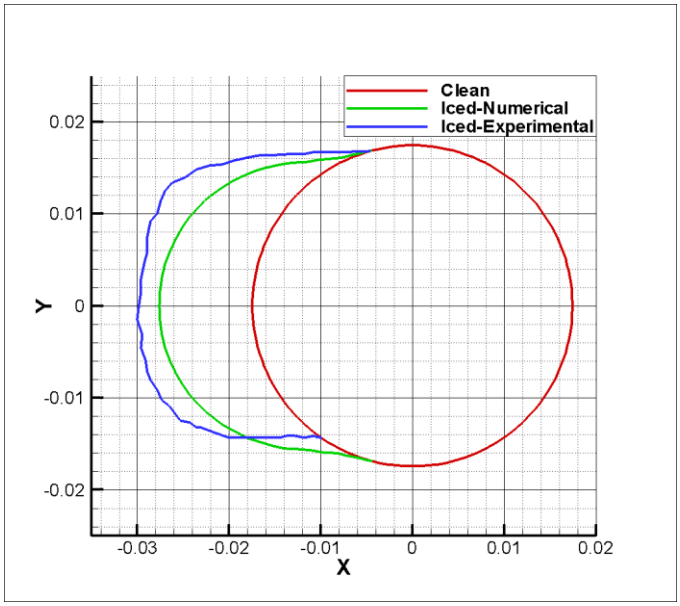

Figure 1 – Comparison of experimental and simulated ice shape.

The main reason for choosing this particular combination of AoA's is to provide a decent coverage in the 0–90° quarter. Opting out of simulations with AoA more than 90° is based on the assumption that the results will be "symmetric" with respect to the 0–90° quarter. The numerical simulations of the ice accretion were performed at all AoAs specified in Table 1, while the transient airflow simulations were performed at 0° AoA for all cases. The reasoning for this is two-fold – first, is to investigate the effect of AoA on the ice accretion process and to keep the amount of variables in the airflow simulations to the minimum. In addition, the assumption of cable rotation happening only after the ice load has been accumulated on it has been made, which ties into the previously mentioned reasoning. For consistency purposes both the ice accretion and the transient airflow simulations were run with the same values for the characteristic length and area. These values are D = 35 mm, corresponding to the diameter of the uniced cylinder and $A = DL$, where A is the area, and L is the length of the object in z-direction, being equal to 1 m in all cases.

2.2 Numerical Model

The multiphase CFD numerical simulations of ice accretion were carried out using ANSYS FENSAP-ICE, which uses Eulerian water droplet impingement solver. The existing analytical models of droplet behavior, for example, the ISO 12494/Finstad et al. solve droplet trajectories using Lagrangian particle tracking approach. The Eulerian method treats the particle phase as a continuum and develops its conservation equations on a control volume basis and in a similar form as that for the fluid phase. The Lagrangian method considers particles as a discrete phase and tracks the pathway of each individual particle. By studying the statistics of particle trajectories, the Lagrangian method is also able to calculate the particle concentration and other phase data. On the other hand, by studying particle velocity vectors and its magnitudes in Eulerian method, it is possible to reconstruct the pathways and trajectories of particles in a phase.

The general Eulerian two-phase model for viscous flow consists of the Navier-Stokes equations augmented by the droplets continuity and momentum equations:

$$\frac{\partial \alpha}{\partial t} + \vec{\nabla} \cdot \left(\alpha \overrightarrow{V_d}\right) = 0 \tag{1}$$

$$\frac{\partial \left(\alpha \overrightarrow{V_d}\right)}{\partial t} + \vec{\nabla}\left[\alpha \overrightarrow{V_d} \otimes \overrightarrow{V_d}\right] = \frac{C_D Re_d}{24K} \alpha \left(\overrightarrow{V_a} - \overrightarrow{V_d}\right) + \alpha \left(1 - \frac{\rho_a}{\rho_d}\right) \frac{1}{Fr^2} \tag{2}$$

where the variables α and $V_{d,a}$ are mean field values of, respectively, the water volume fraction and droplet velocity. The first term on the right-hand-side of the momentum equation represents the drag acting on droplets of mean diameter d. It is proportional to the relative droplet velocity, its drag coefficient C_D and the droplets Reynolds number:

$$Re_d = \frac{\rho_a d V_{a,\infty} \left\| \overrightarrow{V_a} - \overrightarrow{V_d} \right\|}{\mu_a} \tag{3}$$

and the droplet inertia parameter:

$$K = \frac{\rho_d d^2 V_{a,\infty}}{18 L_\infty \mu_a} \tag{4}$$

Where L_∞ is the characteristic length of the object. In case of the cylinder the characteristic length is cylinder radius.

The second term represents buoyancy and gravity forces, and is proportional to the local Froude number:

$$Fr = \frac{\left\| V_{a,\infty} \right\|}{\sqrt{L_\infty g_\infty}} \tag{5}$$

These governing equations describe the same physical droplets phenomenon as Lagrangian particle tracking approach. Only the mathematical form in which these equations are derived changes, using Partial Differential Equations instead of Ordinary Differential Equations. The droplet drag coefficient is based on an empirical correlation for flow around spherical droplets, or:

$C_D = (24/Re_d)\,(1 + 0.15 Re_d^{0.687})$ for $Re_d \leq 1300$

$C_D = 0.4$ for $Re_d > 1300$

The local and overall collision efficiencies are calculated as follows:

$$\beta = -\frac{\alpha \overrightarrow{V_d} \cdot \vec{n}}{w V_\infty} \tag{6}$$

where α is the local volume fraction (kg/m^3) and $\vec{n}$ is the surface normal vector. The overall collision efficiency is an integration of local collision efficiencies over surface area and is given as:

$$\beta_{tot} = \frac{\int \beta \, dA}{L_\infty^2} \tag{7}$$

Since the FENSAP-ICE is a 3D Reynolds-Averaged Navier-Stokes (RANS) solver a choice of turbulence closure for the RANS equations is needed. As it can be seen from operating conditions in Tables 1 and 2, the expected Reynolds number for the cylinder in numerical simulations is of an order of 1×10^4, thus the flow is fully turbulent. Moreover, detailed mesh sensitivity analysis was carried out to accurately determine the boundary layer characteristics (shear stress and heat fluxes), a *y*+ values of less than 1 is used near the cylinder wall surface. Number of mesh elements and *y*+ value was selected based upon the heat flux calculations, where a numerical check was imposed that the heat flux computed with the classical formulae d*T*/d*n* should be comparable with the heat flux computed with the Gresho's method.

Based on this information the turbulence model chosen for the FENSAP-ICE is the Menter's SST *k-ω* model. The detailed information on Menter's SST *k-ω* model is given in (Menter, 1994). The choice between the Spalart-Allmaras, low *Re k-ω* model and Menter's SST *k-ω* model in FENSAP–ICE was

based on the robustness of the *k-ω* SST model in the near-wall region and the discussions in the (Elkoury, 2016) about applicability of SA and *k-ω* SST models for the turbulent flow past bluff bodies. The surface roughness model used in CFD simulations is Shin et al. sand-grain roughness formulation (Shin et al., 1992). The accreted ice density model used in the numerical simulation was rime ice with Jones (rime) icing density model, given as (Jones, 1990):

$$\rho = 0.249 - 0.0840 \ln \pi_C - 0.00624(\ln \pi_\phi)^2 + 0.135 \ln \pi_K + 0.0185 \ln \pi_K \ln \pi_\phi - 0.0339(\ln \pi_K)^2 \quad (8)$$

where π_K is the droplet inertia coefficient, π_ϕ is the Langmuir parameter defined as:

$$\pi_\phi = \frac{18\rho_a^2 L_\infty V_{a,\infty}}{\rho_d \mu_a} = \frac{Re_d^2}{K} \quad (9)$$

where Re_d is the droplet's Reynolds number. Finally, the term π_C is the ratio of the convective heat flux and the heat flux due to droplet freezing and is defined as:

$$\pi_C = \frac{k_a(-2T)/L_\infty}{wV_{a,\infty}L_f} \quad (10)$$

where L_∞ is the object characteristic dimension i.e., cylinder radius. The reason for choosing rime icing model and Jones (rime) icing density formulation in the numerical simulations was the fact that this particular combination provided the best match with experimental ice shape of (Fu et al., 2006). After the icing simulation completion, the displaced grid was generated in FENSAP-ICE, using the Arbitrary Lagrangian-Eulerian (ALE) method.

However, since FENSAP-ICE is a 3D solver exclusively, and it was decided to perform transient airflow simulations using Ansys Fluent in 2D, for the purpose of computational efficiency, it was necessary to perform the "dimensional reduction" before the transient airflow simulations could be carried out. In order to do this, the .stl output files from the FENSAP-ICE were used and the mesh extension in *z*-direction was removed in order to use the displaced grid in the Fluent. For consistency, the Menter's *k*–ω SST model, along with Shin et al. surface roughness model has been used in ANSYS Fluent. The pressure based solver and the coupled scheme for the pressure-velocity coupling has been chosen in ANSYS FLuent. The spatial discretization employed is second order upwind and the transient formulation was set to the second order implicit. The time step chosen for the transient simulations is 0.7071 ms. The choice of time step is based on the assumption of Strouhal number being equal to 0.2 for cylinder for the value of cylinder Reynolds number range, as calculated from the operating conditions in Table 1. Thus by reverse calculation, the frequency of flow has been found and from there the time step has been obtained. The amount of iterations per time step has been set to 50, with 7500 total time steps, as this particular combination has been found to provide good convergence along with parameters of interest reaching the "steady-state". Thus, the total transient simulation time was approximately equal to 5.3 s.

The forces and moments in the ANSYS Fluent simulations are obtained as:

$$F_a = \vec{a} \cdot \overrightarrow{F_p} + \vec{a} \cdot \overrightarrow{F_v} \tag{11}$$

and

$$\overrightarrow{M_A} = \overrightarrow{r_{AB}} \times \overrightarrow{F_p} + \overrightarrow{r_{AB}} \times \overrightarrow{F_v} \tag{12}$$

where a is the specified force vector, F_p is the pressure force vector F_v is the viscous force vector and r_{AB} is the moment vector. The values of C_D, C_L and C_M, are obtained from the values of drag force F_D, lift force F_L, and moment M, by dividing these respective values by the term $\frac{1}{2}\rho v^2 A$, where A is the reference area and it is equal to 0.035 m^2. This area represents the projected area, as viewed normal to the flow and ρ and v are the reference values for air density and velocity, respectively. Finally, the operating conditions in the ANSYS Fluent simulations are matching those given in Table 1.

3 Results and Discussion

3.1 Ice Accretion

The primary purpose of this subsection is to establish if the rotating cylinder is a good approximation to a non-rotating one at different angles of attack, and if there are any significant differences in ice accretion process between them. The main parameters of interest in the ice accretion simulations are the ice shapes, iced areas, maximum ice thicknesses, overall collision efficiencies (α_1), mean values of iced surface bead height and the accreted ice densities. Figure 2 shows the comparison of the ice shapes simulated in FENSAP-ICE at different AoAs (0 – 90°) for the incoming multiphase flow, while Table 2 shows the values of parameters of interest, mentioned previously.

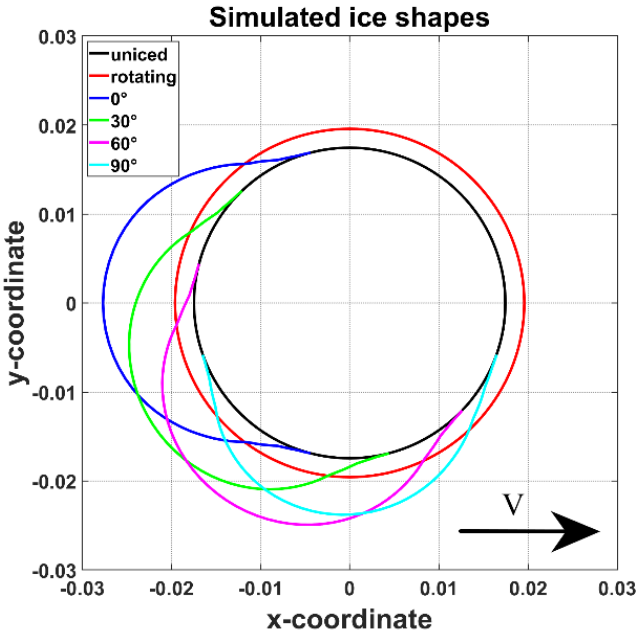

Figure 2 – Comparison of simulated ice shapes at different AoA.

Table 2 – Values of ice accretion parameters of interest.

AoA	*Iced Area (mm^2)*	*Max. Ice Thickness (mm)*	*Ice mass (g/m)*	*Overall Droplet Collision Efficiency (α_1)*	*ρ (kg/m^3)*	*Mean Bead Height (mm)*
0°	302.97	10.1	110.5	0.292	364.7	1.31
30°	257.77	8.5	109.3	0.289	424.0	1.24
60°	265.07	8.6	112.4	0.297	424.0	1.22
90°	157.67	6.3	72.35	0.191	458.9	1.35
Rotating	246.47	2.1	110.5	0.292	448.3	3.53

In the Table 2, the iced area is calculated by taking the geometry profile of the iced cylinder at any given AoA or a rotating cylinder, calculating its total area, and then importing the geometry of an uniced cylinder and subtracting its total area. The resultant value will be the area covered by ice accretion only and this area is the "iced area".

From Figure 2, it can be seen that the only apparent difference is the maximum ice thickness, with ice shape at 0° AoA being the "thickest" and 90° being the "thinnest" with the results at 30° and 60° AoA having the maximum ice thickness values in-between and closely matching each other. From Table 2 it can be also seen that the iced areas also follow the exact same pattern, and the iced area for rotating cylinder is comparable to that of 30° and 60° AoA simulations. For the ice masses, all cases, with the exception of 90° AoA show good agreement among each other. This follows from the results of the overall collision efficiencies values, which also match well, with the maximum difference in values of *E* being within 0.01, again, with exception of 90° AoA.

The abnormal results in the ice accretion simulations of the cylinder at 90° AoA can be explained by the deficiency in the setup. The numerical deficiency for this particular case is that the mesh used for the simulations is an O grid and the ice accretions simulations have been performed by rotating the inflow angle. For the 90° AoA case the inlet and outlet boundary conditions "interface" coincides with the direction of the incoming flow. For the transient airflow simulations this is not the case as the incoming flow angle is 0° for all cases. This is considered an acceptable compromise, since the FENSAP-ICE is an Eulerian solver and changing the mesh just for this one case can cause additional differences to arise, as the Eulerian methods are mesh-dependent. Finally, the maximum surface roughness from beading is the same is all cases, and its equal to 3.53 mm. This is a rather large value, considering that Shin et al. surface roughness formulation gives a surface roughness value of 33 μm.

Summarizing, when it comes to the ice accretion itself, the results of the simulations at different angles of attack and the rotating cylinder show good agreement, for the most parameters of interest. Since the dry growth regime in this study was maintained and verified from the mass balance in FENSAP-ICE, i.e., for all cases in this study, the masses of water film, water vapour etc. are all equal to 0, this means that the sticking and freezing efficiencies $\alpha_2 = \alpha_3 = 1$. Thus, from the ISO 12494 "*Atmospheric Icing on Structures*" modeling viewpoint:

$$\frac{\mathrm{d}M}{\mathrm{d}t} = \alpha_1 \alpha_2 \alpha_3 v w D L t \tag{13}$$

and since the operating conditions from Table 1 are the same, with the exception of the AoA, it follows that the ice accretions in this study are very similar. Therefore, for the accretion process itself, the rotating cylinder is a good approximation to the non-rotating cylinder at different angles of attack. However, this comparison is incomplete without investigating the flow behavior and aerodynamic forces across all cases in this study.

3.2 Airflow behavior

For the comparison of the airflow behavior of the different cylinder configurations, the plots of mean pressure distributions and velocity magnitudes and streamlines were obtained from transient airflow simulations, and they are given in Figures 3 – 5, respectively.

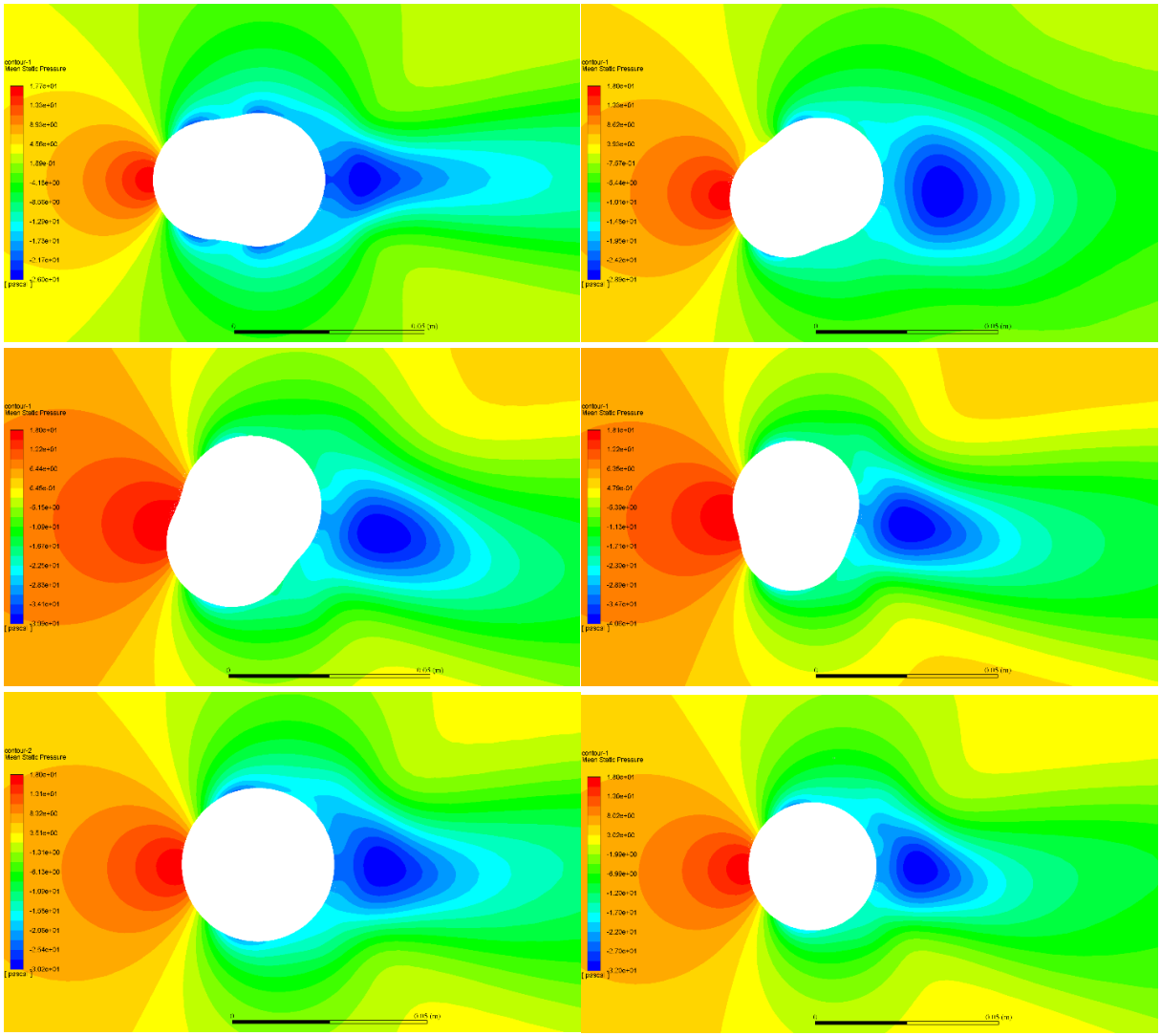

Figure 3 – Pressure distributions in numerical simulations. From top to bottom, left to right: 0°, 30°, 60°, 90° AoA, rotating and uniced cylinder. The values shown are the mean values across all time steps.

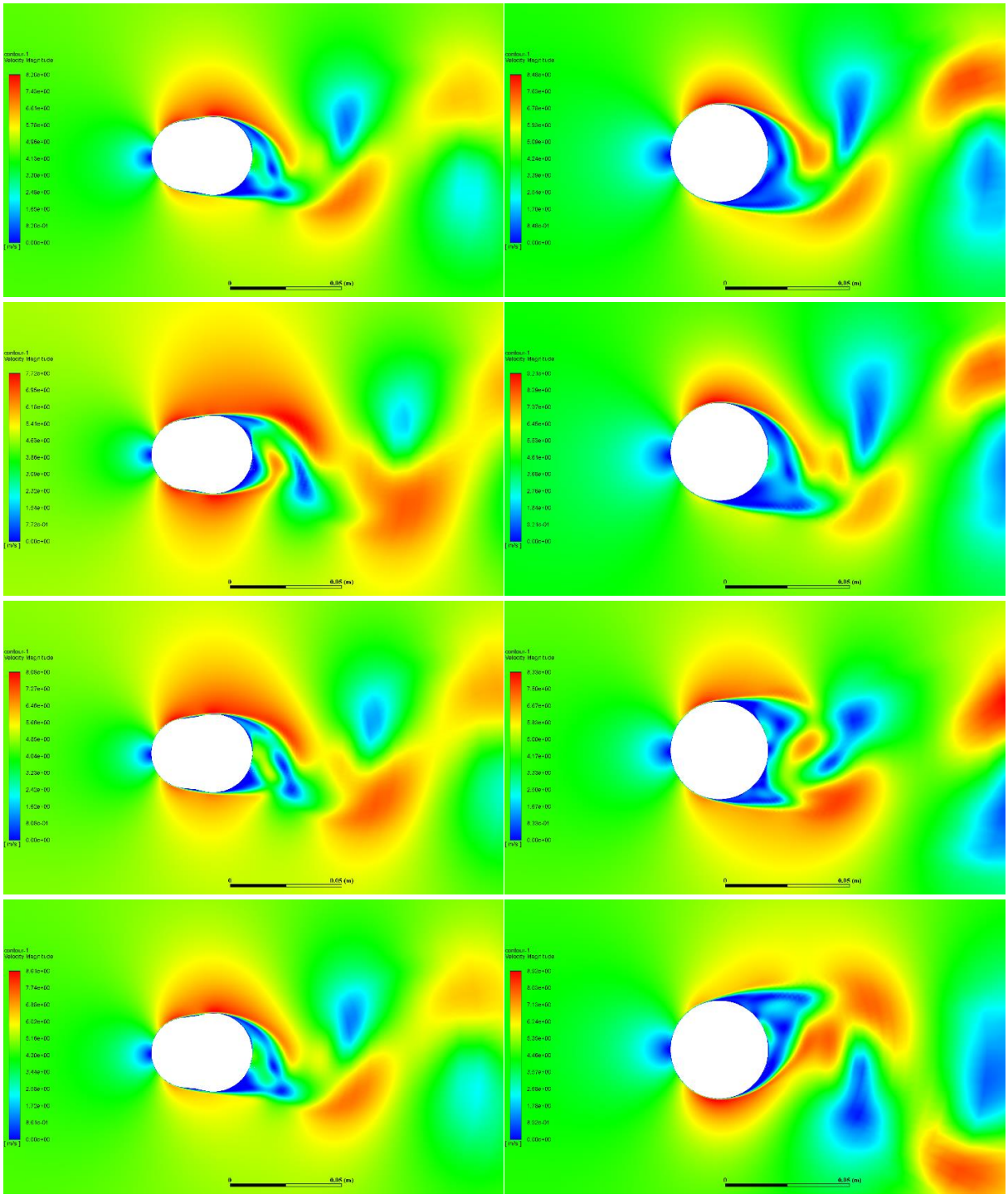

Figure 4 – Velocity magnitudes in numerical simulations for 0° AoA (left) and rotating (right) cylinder. From top to bottom the time step values are t = 1, 2, 3 and 5 seconds.

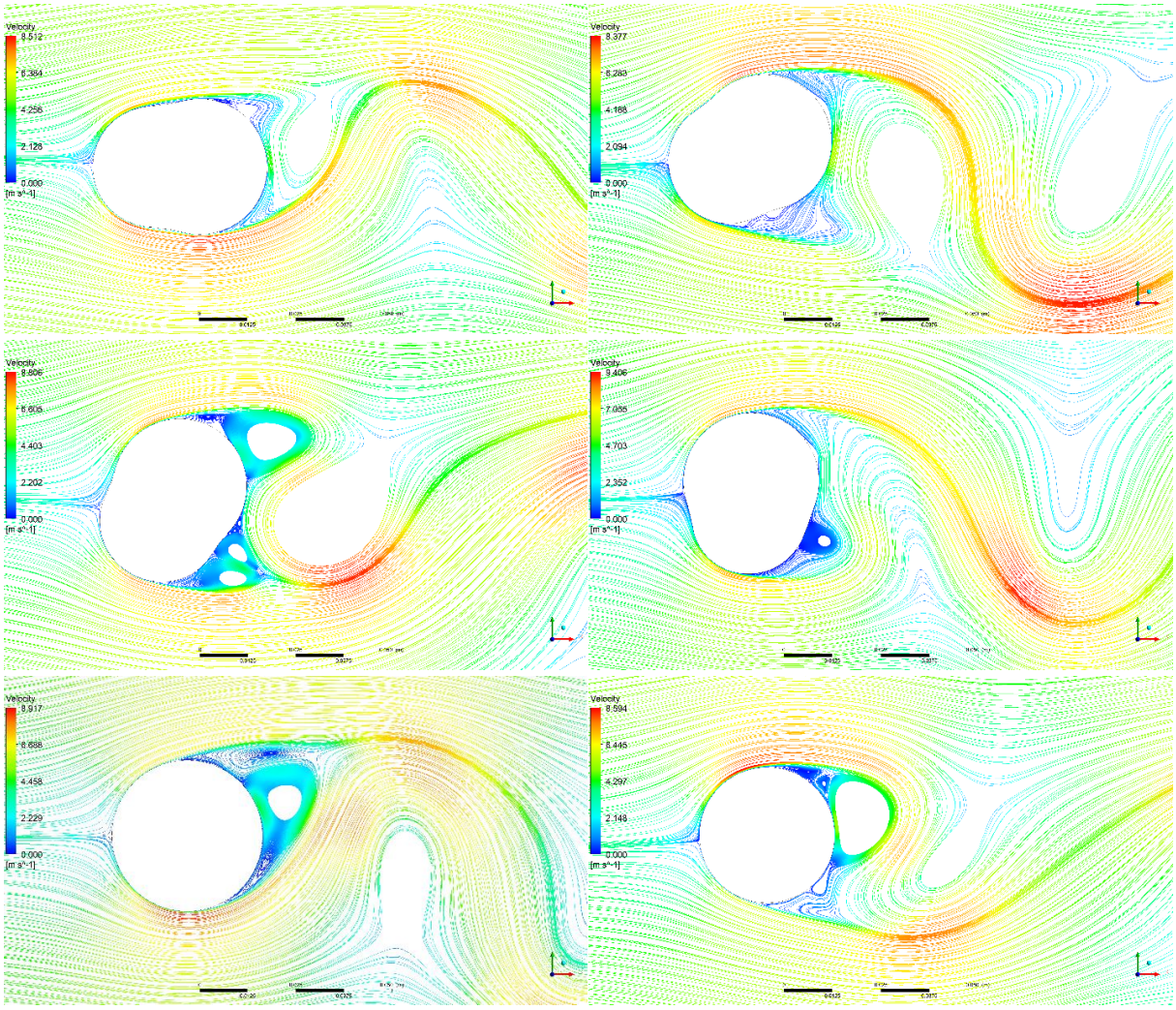

Figure 6 – Velocity streamlines in numerical simulations. From top to bottom, left to right: 0°, 30°, 60°, 90° AoA, rotating and uniced cylinder. The streamlines shown are for the last time step (t = 5.3 seconds).

The flow around cylinder at 0° AoA in Figure 3 shows much more narrow wake, with the region of maximum negative pressure and the stagnation point pressure field are also narrower. This suggests that the flow separation occurs more gradually, and the flow "reconnects" past the cylinder in a similar, gradual fashion, as evidenced by low pressure zone in the wake of cylinder being rather protracted in *x*-direction. For the 30° AoA case the majority of "top side" is a pressure zone, while the "bottom side" is a suction zone, thus indicating that the cylinder experiences a downward acting lift. This coupled with the fact that the flow separation appears to be "gradual" similar to 0° AoA case and its unlike the 60° and 90° AoA cases, for which the pressure gradients are rather "sharp", thus indicating that 0° and 30° AoA cases should have lower values of C_D compared to 60° and 90° AoA cases.

On the other hand, the cylinder at 60° and 90° AoA experiences more significant pressure gradients and rapid flow separation, thus indicating that its subjected to the higher values of aerodynamic loads in these cases. Moreover, for the 60° and 90° AoA cases the stagnation pressure zone extends almost to the edges of the cylinder. This coupled with the significant pressure gradients in these cases suggests that maximum amplitude of aerodynamic loads, drag in particular, should be significantly higher for

those cases than for the 0° and 30° AoA cases. Similar to the 30° AoA case, the cylinder at 60° AoA also shows the "top-side" of the cylinder being the pressure side, thus, again giving the indication of downwards acting lift. For the 90° case, however, the pressure distribution at the cylinder "edges" remains symmetric, similar to the 0° AoA case, thus indicating that for this case the C_L value should be very close to zero.

Comparatively, the benchmark cases of the rotating and the uniced cylinder, are in the "middle" between 0°, 30° and 60°, 90° AoA cases, as it is seen from Figures 3 and 4, when it comes to flow field parameters, in particular the pressure distributions, as the pressure gradients and the extent of the stagnation pressure zones being "in-between" the 0°, 30° and 60°, 90° AoA cases. This by extension, implies that the aerodynamic loads, and in particular the drag values, should be higher than for 0° and 30° AoAs but lower than in 60° and 90° cases. Moreover, the same also true when comparing maximum negative pressures. The maximum negative pressures are –26 and –29 Pa for 0° and 30° AoA cases, respectively, while for 60° and 90° AoA cases, the maximum negative pressure is approximately –40 Pa for both cases. For the benchmark cases, these values are approximately –30 and –32 Pa for rotating and uniced cylinder, respectively. The maximum positive pressure is approximately 18 Pa for all cases. Thus, the results for the airflow behavior from Figure 3 and 4 do suggest that there are differences in the instantaneous flow conditions in the transient CFD simulation present across all cases. This is further exacerbated by the instantaneous velocity streamlines plots, shown in Figure 5. The characteristics of velocity streamlines change significantly between the reference cases of the rotating and uniced cylinders vs. the non-rotating iced cylinders. For the ice shape at 0° AoA the vorticity shedding occurs immediately past the cylinder, and for the cases with the ice shapes at non-zero AoA additional vortices are present behind the cylinder, when compared to the ice shape at 0° AoA. Again, in those cases the vorticity shedding starts immediately past the cylinder as opposed to the rotating and uniced cylinders, for which the shedding starts a bit further downstream. The turbulent shedding modes for the uniced cylinder are in good agreement with the turbulent shedding at $Re = 8 \times 10^3$ captured by smoke-visualizations in (Norberg, 2003), albeit the turbulent shedding in their case starts slightly further downstream than for the reference cylinder in this study.

Although the instantaneous flow behavior characteristics past different cylinders in this study does vary to a significant degree, the question, however, is how much these instantaneous differences can affect the aerodynamic loads, on the time frame of the typical icing event, with timeframes from minutes to hours.

3.3 Aerodynamic loads

The transient airflow simulation results are presented in terms of combined plots of parameters of interest, namely the drag, lift and moment coefficients, combined pressure and viscous force (denoted as force) as well as the Strouhal number for all cases in this study. These plots are given in Figure 6 and show the transient curves for the last 1.3s of the flow, which corresponds to approximately last 2000 time steps. To avoid cluttering multiple different curves on a single plot, any given parameter of interest is presented by two subplots – first showing the values for the AoA cases, and second showing the values for the benchmark cases. In order to keep the comparison visually simple, the black curve,

corresponding to 0° AoA case is presented in all subplots and the axis limits are kept consistent between the respective subplots.

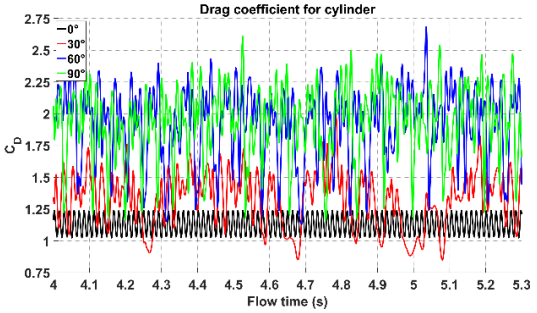

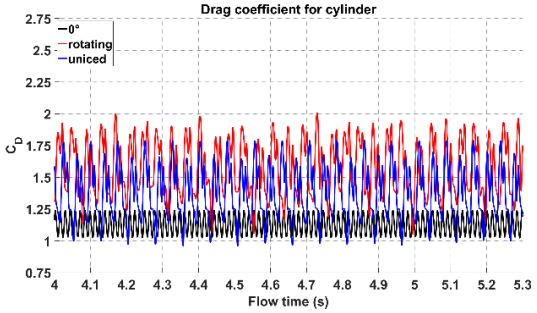

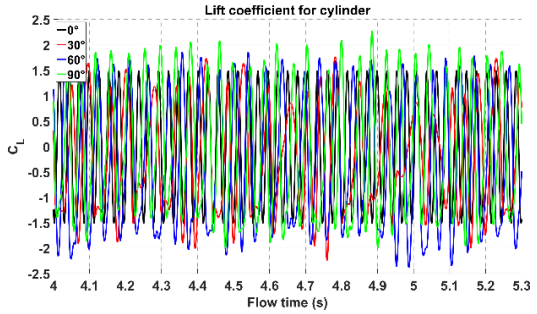

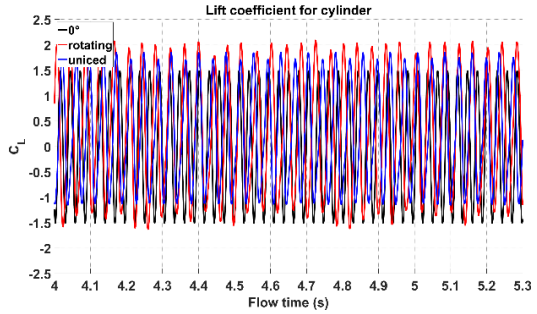

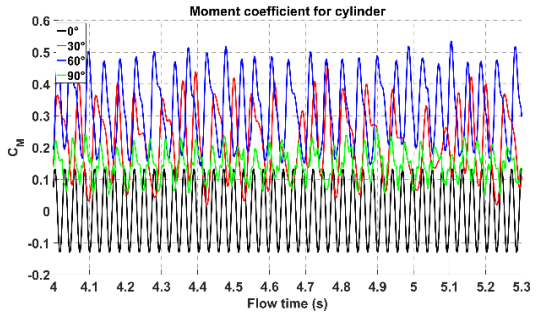

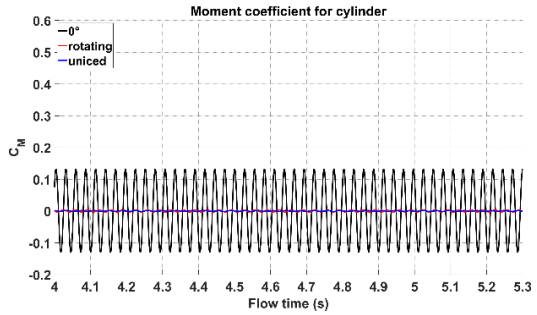

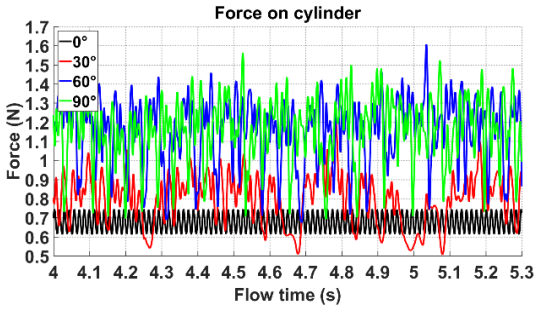

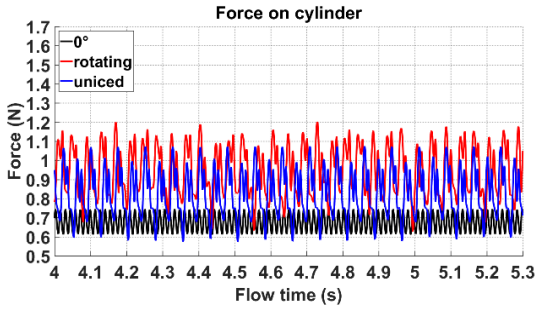

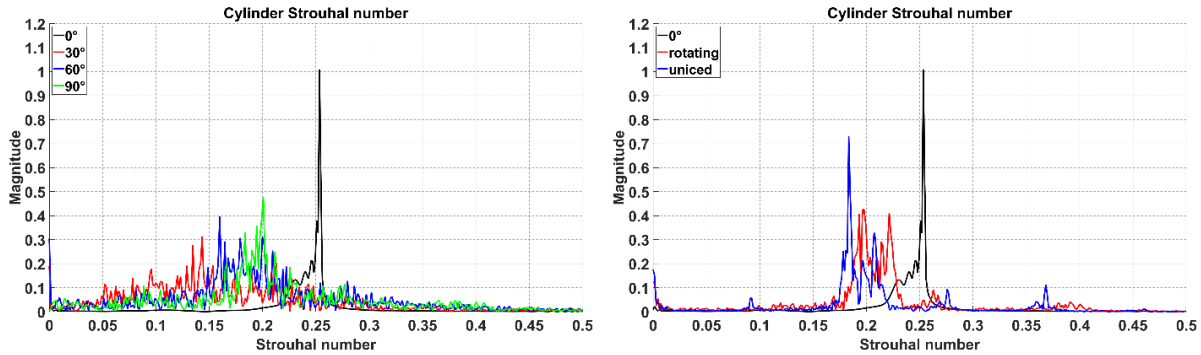

Figure 6 – Drag, lift, moment coefficients, force and Strouhal number values. The AoA values are given in legends.

Table 3 shows the mean values of C_D, C_L, C_M and total pressure and viscous force F, while the Strouhal number given in it corresponds to the value associated with the maximum magnitude. The mean values reported in Table 3 were taken from the last 2000 time steps of the airflow simulations, in order to avoid possible skewing of the resulting from taking into account the values at the beginning of the simulations, where results may not yet be converged.

Table 3 – Values of parameters of interest in the numerical simulations.

Variable	***0°***	***30°***	***60°***	***90°***	***Rotating***	***Uniced***
C_D	1.13	1.34	1.93	1.93	1.58	1.38
C_L	–0.01	–0.21	–0.37	–0.03	0.26	0.27
C_M	0.00	0.21	0.32	0.15	0.00	0.00
F	0.68	0.79	1.16	1.15	0.95	0.83
Strouhal	0.25	0.14	0.16	0.20	0.20	0.18

The results from benchmark cases for the drag coefficient and Strouhal number compare favorably with the results of Relf and Simmons, as reported by (Tanida et al, 1973) and (Gerrard, 1961), with C_D values in this work being slightly higher than these experimental values, possibly due to higher turbulence intensity in the numerical simulations in this work. Moreover, the C_D values of uniced and 90° AoA match closely those in the numerical simulations of (Keyhan, 2012) for the 5 m/s wind speed cases, and the C_D values with respect to angle behave in a similar trend, as in (Rossi et al, 2020), even if their C_D values are different, due to different Reynolds number and the ice shapes. Moreover, the behavior of C_D and C_L curves and values, follows closely the ones in the (Selvam, 1997) for the unicied cylinder at *Re* = 10^4 who used Large Eddy Simulation (LES) in their study, contrary to the Unsteady Reynolds Averaged Navier-Stokes (URANS) in this work.

The comparison of the results from Table 3 with the experimental data of (Demartino et al., 2013) shows that the obtained results follow similar trend to the case CC V2 in their work, in particular when it comes to the change in values of C_D, C_L and C_M. However, when it comes to magnitudes, especially for C_D their obtained values are somewhat lower than in this work, which can be explained by significantly higher values of *Re* in their experimental cases, arising from vastly different operating conditions, and thus it was deemed unnecessary to perform the comparison of ice accretion between this work and the experimental data of (Demartino et al., 2013). Moreover, when it comes to their results it should be noted that aerodynamic forces and trends in magnitudes in the experimental cases change significantly

from one experimental case to another, even though the operating conditions do not change significantly. This fact, coupled with the results of numerical simulations in (Keyhan, 2012) show that the ice shape does have prominent effect on the aerodynamic loads.

Returning to the results in this work, the first interesting result, as inferred from the Figure 6 and Table 3 is that the iced cylinders at 0° and 30° AoA has smaller values of the drag and total pressure and viscous force, when compared to the rotating iced and uniced cylinder benchmarks. Several possible explanations of these phenomena can be made. First, the cylinder shape, especially for the 0° AoA case is rather streamlined, which may result in flow separation to be more gradual when compared to rotating and/or uniced cylinder. Second, is the airflow behavior around the cylinder, as discussed in the previous section. Moreover, it also can be observed from Figures 1 and 2, that the leading edge of the iced cylinder is smaller than the diameter of an uniced cylinder. Finally, since all numerical simulations have used Shin et al. surface roughness model, the actual effect of iced surface roughness for the iced cases can be underestimated when compared to the uniced cylinder.

The cylinder at 30° angle of attack also experiences lower average values of the drag coefficient and force when compared to the uniced and rotating cylinder, however, the amplitude of fluctuation of C_D and F is higher than in benchmark cases. Again, same arguments can be made in this case as with 0° AoA case as to why the mean values of C_D and F are lower however, the significant amplitude of C_D and F fluctuations does suggest that this configuration can experience more significant aerodynamic loading, at maximum, than the benchmark cases. As for the 60° and 90° AoA cases, they exhibit an "expected" behavior, i.e., higher values of all the parameters of interest and higher amplitude of fluctuations. This suggests that the cylinder in these cases experiences higher aerodynamic loads than the reference cases of rotating and uniced cylinders. Furthermore, the moment coefficient is higher in the cases of 30° and 60° AoA, as compared to 90° AoA. A possible explanation here is that the 90° AoA is a mostly "symmetric" situation, with this sort of symmetry naturally reducing the C_M value, also indicated by the C_L value being zero for this case, as expected from the "symmetric" situation.

In addition, the positive moment convention in the numerical simulations is the counter-clockwise, thus the positive value of C_M for the 30°, 60° and 90° AoA cases indicate their tendency to pitch in the leading edge "down" direction, towards the increase in the value of AoA. On the other hand, the C_M value for the 0° AoA is expectedly zero, however, the amplitude of fluctuation of it is not, thus indicating that this configuration is prone to oscillation around $y = 0$ line. Finally, it is interesting to note the similarity of mean values of C_D and F for the 60° and 90° AoA cases. This can be explained, by the deficiencies of the numerical setup for the 90° case in the ice accretion simulations, as was discussed previously. As a consequence of it, the 90° shape in the simulations is not as "thick" as it should have been, thus resulting in 90° AoA case being less of an "obstacle" to the flow, in the geometric sense of it.

However, several peculiarities have been observed in the results in Figure 6 and Table 3. First, the similarity in the amplitude of C_L values in the results for all tested configurations. While the maximum C_L oscillations do increase with change of configuration, for example, changing from 0° to 90° AoA, the magnitude of the fluctuations is not nearly as close as amplitude fluctuations in C_D values. This indicates that while configurations at extreme AoAs are more aerodynamically loaded, in absolute terms, they are just marginally more loaded in C_L terms. Second, is the non-zero C_L values for the uniced

and the rotating cylinders, with the C_L being equal to 0.27 and 0.26, respectively. This may indicate possible asymmetry of the flow separation from the cylinder edges. When comparing these C_L values with an available results for the circular cylinder at the Reynolds number $Re = 10^4$ the results in this study for the circular cylinders are on the low range of the C_L values as measured in experiments by (Gopalkrishnan, 1992) with mean value of stationary circular cylinder C_L being 0.38.

Finally, the Strouhal number values, obtained from the C_L oscillations show a wide range of values, from 0.14 for the 30° AoA case to the 0.25 for the 0° AoA case. From reverse calculation, the frequency values of 36, 18, 19, 24, 25 and 26 Hz for the lift force oscillations were obtained, for the 0°–90° AoA, rotating and uniced cylinder, respectively, and twice the indicated frequencies for the drag force oscillations. The respective values, obtained from the Fast Fourier Transform (FFT) in Fluent are within ±1 Hz. Therefore, the cylinder at 0° AoA tends to have higher frequency of vortex shedding at smaller amplitudes, while 30° and 60° AoA cylinder have considerably higher amplitudes at smaller frequency. The 90° AoA and the benchmark cases fall in-between, and thus, the rotating cylinder "equivalence" assumption compares favorably.

Summarizing, since the cases with the 0° and 30° AoA are less aerodynamically loaded, while the 60° and 90° AoA cases are more aerodynamically loaded than the benchmark cases of the rotating and the uniced cylinder. It suggests that the "averaged" values across all 0–90° AoA cases should be comparable to the benchmark, and thus the "rotating" assumption should be mostly equivalent. To illustrate this, Figure 6 shows the averaged values of total pressure and viscous force vs. benchmark cases. The total pressure and viscous force has been chosen as a parameter to compare, as it is independent of reference length and area in the numerical simulation, thus being the most "direct" way of comparing the results.

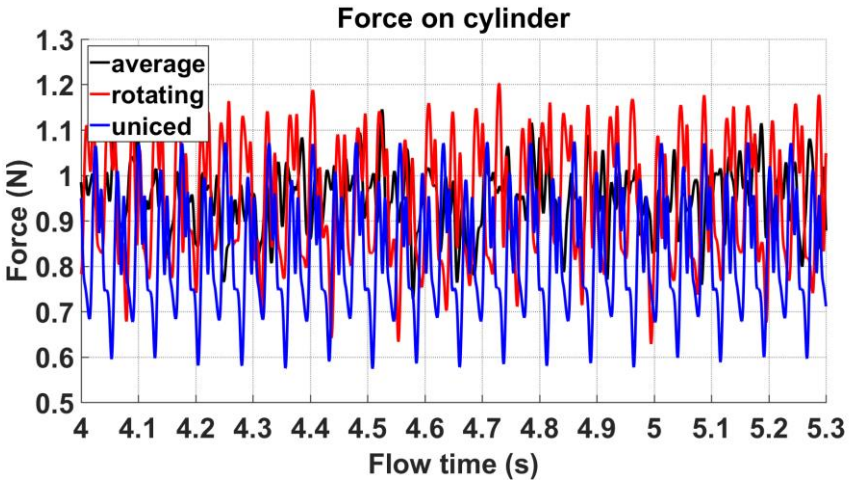

Figure 7 – Averaged drag coefficient vs. benchmark cases.

The results from Figure 7 tend to support this previous assumption, as the combined F curve lies mostly on the rotating cylinder F curve in the steady state range, with mean value of F for the "averaged" curve being 0.95 which matches the value for rotating case from Table 3 within the rounding error. Thus, from the viewpoint of total aerodynamic force, acting on the cylinder, the rotating cylinder is equivalent to the "averaged" case of 0°–90° AoA.

Speaking about gravity force and their comparison with the aerodynamic forces, the following relation can be used to estimate the drag force per unit length for circular cylinder (Tritton, 1988):

$$C_D \equiv \frac{f_D}{\frac{1}{2}\rho v^2 D} \tag{13}$$

where f_D is the drag force per unit length. Using the value of C_D for the 0° AoA case from Table 4, as the drag force is the most significant aerodynamic force, the drag force per unit length obtained for that particular case is 0.68 N/m, using the previous relation. Using the value of accreted ice mass per unit length from Table 3, and using the operating conditions from Table 1 in calculations, the gravity force per unit length for the 0° AoA case is 1.08 N/m. Thus, already after 30 min of ice accretion, the gravity force is larger than the drag force, and it should continue to rise as the ice accretion continues, while the drag force won't be increasing as much, unless a significant change in configuration occurs. While this analysis is rather simplistic in nature it does show that while the drag force is proportional to the product of characteristic length and wind speed as Dv^2, given sufficiently large time frame of continued ice accretion, the gravity force, caused by this ice accretion will eventually dominate the aerodynamic forces, acting on cylinder. However, the exact time dependent model, mechanisms and their impact on actual rotation and twisting of the power lines are deemed to be too extensive to be properly developed in this work, although, the provided quantitative baseline, done in this work, does provide some insights into this matter.

4 Conclusion

Within the scope of this work numerous CFD simulations of the atmospheric ice accretion and the transient airflow behavior over iced cylinder with different angles of attack were performed. The objective was to investigate how commonly postulated assumption of slow, continuous rotation on a reference collector and/or power line (ISO, 2001), (Makkonen, 1984) compares with non-rotating iced cylinder at different angles of attack, which is deemed to be representative of very slow and/or spontaneous rotation. For the basis of comparison several flow parameters have been chosen in order to ascertain similarity, namely, ice shapes, maximum ice thicknesses and iced areas, accreted ice mass, ice densities, overall collision efficiencies, drag, lift and moment coefficients, pressure and viscous force, velocity magnitudes and pressure distributions.

The obtained results compare favorably for the hypothesis of rotating cylinder being "equivalent" to the series of non-rotating cylinder at different AoAs. In particular, the results tend to agree very well for the comparison of ice accretion parameters, where all cases, with the exception of 90° AoA, compare well to the rotating cylinder benchmark. The discrepancy in the 90° AoA case can be explained by the deficiencies in the numerical setup.

The comparison of the aerodynamic forces suggests that the benchmark cases of rotating and uniced cylinders, do have "similar" aerodynamic loads when compared to the "averaged" AoA simulations results, namely, when it comes to the values of total pressure and viscous force, which for the "averaged" case matches the rotating one within the rounding error. However, on individual basis the difference in the airflow regime between AoA cases and the benchmark cases can be significant, particularly, if

checking the instantaneous values for the velocity magnitudes and pressure distributions in the transient airflow separation. In particular, the results from small AoA simulations (0° and 30°) show that the cylinder is less aerodynamically loaded than the benchmark cases. On the other hand, the results from simulations at large AoA (60°and 90°) produced "expected" results, as the cylinder in these configurations is significantly more aerodynamically loaded than the reference cases. However, as it was discussed previously, given sufficient enough time frame for continued ice accretion, the gravity force, exerted by the accreted ice deposit, will, eventually, be the dominating force, however, the exact situation will depend on the operating conditions and the shape of the developing ice deposit.

The comparison of the results from this work with the results of numerical simulations of (Keyhan, 2012) and experimental data of (Demartino et al., 2013) shows good agreement, where applicable, however, one apparent trend in both (Keyhan, 2012) and (Demartino et al., 2013) is that the resultant aerodynamic loads are not only a function of Reynolds number but the accreted ice shape as well.

Acknowledgment

The work reported in this paper is funded by the Research Council of Norway, FRonTLINES- project no. 245370 & IceBOX- project no 282403.

References

1. Bidwell, C.S., 2012, Particle Trajectory and Icing Analysis of the E3 Turbofan Engine Using LEWICE3D Version 3, NASA/TM–2012-217696, NASA
2. Demartino C., Koss, H.H., Ricciardelli F., 2013 Experimental study of the effect of icing on the aerodynamics of circular cylinders - Part I: Cross flow. 6th European and African Wind Engineering Conference.
3. Elkhoury, M. 2016. Assessment of turbulence models for the simulation of turbulent flows past bluff bodies. Journal of Wind Engineering and Industrial Aerodynamics, vol. 154, pp. 10–20.
4. Finstad, K.J., Lozowski, E.P., Gates, E.M., 1988. A computational investigation of water droplet trajectories. Journal of Atmospheric and Oceanic Technology, 5, 160-170.doi:10.1175/1520-0426(1988)005<0160:ACIOWD>2.0.CO;2
5. FENSAP-ICE User Manual
6. Fluent User Manual
7. Fu, P., Farzaneh, M., Bouchard, G., 2006. Two-dimensional modelling of the ice accretion process on transmission line wires and conductors. CRST, vol. 46, pp. 132–146.
8. Gerrard, J. H., 1961, An experimental investigation of the oscillating lift and drag of a circular cylinder shedding turbulent vortices. Journal of Fluid Mechanics, vol. 11, part 2, pp. 244–256
9. Gopalkrishnan, R. 1992. Vortex-Induced Forces on Oscillating Bluff Cylinders. Ph.D. Thesis, MIT/WHOI, WHOI-92-38.
10. ISO 12494:2001(E), 2001. Atmospheric icing of structures. Standard. International Organization for Standardization. Geneva, CH.
11. Jones, K.F. 1990, The density of natural ice accretions related to nondimensional icing parameters, Quarterly Journal of Royal Meteorological Society, vol. 116, pp. 477–496.
12. Keyhan, H., 2012, Fluid Structure Interaction (FSI) Based Wind Load Modeling for Dynamic Analysis of Overhead Transmission Lines. Ph.D. Thesis. Department of Civil Engineering and Applied Mechanics, McGill University.

13. Makkonen, L., 1984. Modeling of Ice Accretion on Wires. Journal of Applied Meteorology 23, 929-939. doi:10.1175/1520-0450(1984)023<0929:MOIAOW>2.0.CO;2
14. Makkonen, L., Stallabrass, J.R., 1987. Experiments on the cloud droplet collision efficiency of cylinders. Journal of Applied Meteorology 26, 1406-1411.doi:10.1175/1520-0450(1987)026<1406:EOTCDC>2.0.CO;2
15. Menter, F. R. 1994. Two-Equation Eddy-Viscosity Turbulence Models for Engineering Applications. AIAA Journal, 32 (8): 1598–1605, Bibcode:1994AIAAJ..32.1598M, doi:10.2514/3.12149
16. Norberg, C. 2002. Fluctuating lift on a circular cylinder: review and new measurements. Journal of Fluids and Structures, vol. 17, pp. 57–96.
17. Papadakis M., Wong, S.-C., and Rachman, A, Large and Small Droplet Impingement Data on Airfoils and Two Simulated Ice Shapes, NASA/TM—2007-213959, October 2007
18. Rossi, A., Jubayer, C., Koss, H., Arriaga, D., Hangan H. 2020. Combined effects of wind and atmospheric icing on overhead transmission lines. Journal of Wind Engineering and Industrial Aerodynamics, vol. 204.
19. Selvam, R.P., 1997. Finite element modelling of flow around a circular cylinder using LES. Journal of Wind Engineering and Industrial Aerodynamics, vol. 67&68, pp. 129–139.
20. Shin, J. and Bond, T, 1992, Experimental and Computational Ice Shapes and Resulting Drag Increase for a NACA 0012 Airfoil, NASA Technical Manual 105743, 1992
21. Tanida, Y., Okajima, A., Watanabe, Y., 1973, Stability of a circular cylinder oscillating in uniform flow or in a wake. Journal of Fluid Mechanics, vol. 61, part 4, pp. 769–784.
22. Tritton, D. J. Physical Fluid Dynamics, 2nd ed. Oxford, England: Oxford University Press, 1988.
23. Wright, W., 2008, User's Manual for LEWICE Version 3.2, NASA/CR–2008-214255, NASA

Paper 7. Study of Dry Ice Growth on Duplex Cylinders

Pavlo Sokolov and Muhammad Shakeel Virk

Cold Regions Science and Technology, 2021, Under Review.

Manuscript submission ref.: CRST-S-2021-00112

This copy is reprinted with permission from co-authors.

Author's Contribution

Pavlo Sokolov has contributed substantially in the proposal of research idea, literature review, modelling, computing, and numerical analysis, and writing of the paper.

Study of Dry Ice Growth on Duplex Cylinders

[*]Pavlo Sokolov & Muhammad S.Virk

Artic Technology & Icing Research Group

Institute of Industrial Technology

UiT – The Arctic University of Norway

*Email: pavlo.sokolov@uit.no

ABSTRACT

A study of dry ice growth on the bundled (duplex) cylinders has been performed using icing wind tunnel experiments and Computational Fluid Dynamics (CFD) numerical simulations. The aim of this study is to "fill the gaps" in the works of (Wagner, 2010) and (Qing et al., 2018). The numerical simulations cover a range of possible icing conditions by varying the operating wind speed, median volume diameter, and for some cases – the angle of incidence between the cylinders. The obtained results for the 0° AoA show that the accreted ice masses ratio between the leeward and windward cylinder varies from ≈100% to ≈30%. The accreted ice masses ratio decreases with the increase in the wind speed and/or median volume diameter. For the cases with non-zero AoA, the accreted ice masses become approximately equal, when the AoA is large enough to produce a vertical separation equal or greater to one cylinder diameter.

Keywords: CFD; icing wind tunnel; ice accretion; droplet collision efficiency; cylinder; bundle.

1 Introduction

The study of atmospheric icing on power lines is a well-established field, with analytical models of power line icing specifically originating as early as 1980's (Makkonen, 1984). These models, in turn, are based on the theoretical work on atmospheric icing of structures, dating back to the works of (Langmuir and Blodgett, 1946) and other research, conducted at the Mt. Washington Observatory in the same timeframe. The resultant aggregated theoretical knowledge has been incorporated in the ISO 12494 standard "*Atmospheric Icing of Structures*". ISO 12494 modeling framework received widespread attention when it comes to the analytical modeling of ice accretion on simple geometries, which can be approximated by circular cylinder, such as simplex power line conductors, tubular telecommunication masts, etc.

Consequently, the modeling of atmospheric icing on structures with other geometrical configurations has received limited attention. One practical example of such a case is modeling of atmospheric icing on bundled conductors – duplex, triplex, hexa etc. bundled configurations. Such geometric

configurations are of significant importance in the modeling of atmospheric icing on the overhead transmission lines, as the majority of high-voltage transmission networks consist of bundled conductors. However, to the best of authors' knowledge only limited amount of work has been done in modeling of atmospheric ice accretion on bundled cylinders and/or conductors, those primarily being the works of (Wagner, 2010) and (Qing et al., 2018). Thus, there is a need to better understand such types of ice accretion and droplet impingement, although, it is not certain how or if ISO 12494 can handle the modeling of the atmospheric ice accretion on bundled conductors, nor how one could easily validate the obtained results.

Therefore, the use of Computational Fluid Dynamics (CFD) solvers is employed, which have been steadily increasing in popularity for the purposes of modeling atmospheric ice accretion (Lozowski and Makkonen, 2005). The results of CFD modeling of atmospheric icing on structures have been extensively validated, primarily in the in-flight icing studies, for example, works by (Papadakis et al., 2007), (Ratvasky et al., 2008), (Wiberg et al., 2014) etc. The setup of the numerical simulations, performed in this study, is aiming to represent the icing on the bundled conductors on typical power line under a range of possible icing conditions. For simplicity, the usage of circular cylinders is employed, and they are deemed an acceptable approximation to the actual stranded conductor with ribbed bare surface, especially after initial accretion smoothens the conductor surface.

2 Previous Studies

Recently, (Qing et al., 2018) have performed a similar analysis of the rime ice accretion on bundled conductors, focusing primarily on the effect of the distance and separation angle on the rime ice accretion. However, the presentation of the results of their analysis leaves a few open questions.

Qing et al. specify that the turbulence model used in their analysis is standard k–ε model. Upon closer inspection it is apparent that the eq. (4) and the unnumbered equation after it in their paper is not a standard k–ε model but rather the Lam-Bremhorst (Lam and Bremhorst, 1981; Schmidt and Patankar, 1988) Low-Reynolds-number extension (LRN) to the k–ε model that employs a transport equation for the total dissipation rate, with the advantage that the model requires no additional source terms. However, a disadvantage of the Lam-Bremhorst model is that one of the damping functions requires the calculation of the local distance to the nearest wall. Qing et al. do not present the information about the mesh used in their paper, nor the $y+$ value of their setup is known.

Since neither the wall treatment nor the $y+$ values are known it poses some questions regarding applicability of their results for the modeling of the viscous sublayer in their CFD simulations. This matter is of importance as the droplets experience highest degrees of momentum change in the boundary layer near the wall. Another question what was the turbulence intensity used in the Qing et al. simulations as the LB LRN k–ε model has some potential issues with not predicting the turbulence transition for the turbulence intensities of an order of 1% and lower (Schmidt and Patankar, 1988). In addition, none of the k–ε models is implemented in the FENSAP–ICE. The importance of this point is discussed below.

For the discrete phase, Qing et al. present the mass and momentum conservation equations matching that of the FENSAP–ICE. Cross-referencing with the (Fluent Theory Guide) shows that the discrete phase governing equations in the Fluent are different from the equations in the FENSAP–ICE/Qing et al. The usage of FENSAP–ICE is not mentioned in the source paper (Qing et al., 2018). The authors specify that "*Numerical simulations were done by Fluent and Matlab*." This makes of the nature of implementation of the discrete phase simulation in their work an open question.

Furthermore, an unnumbered equation immediately after the eq. (6) shows a peculiar definition of the drag coefficient C_D (original notation preserved):

$$C_D = \frac{0.44}{Re_w}$$

where "C_D *is the drag coefficient;* Re_w *is the droplets Reynold number;*". The authors of this work assume that this is the expression for the droplet drag coefficient. If this assumption is true, this formulation of the droplet drag coefficient differs significantly from the spherical droplet drag coefficients in the Fluent, FENSAP–ICE and analytical icing parameterizations models. For example, FENSAP–ICE uses the following droplet drag coefficient expression (FENSAP–ICE User Manual):

$C_D = (24/Re_d)\,(1 + 0.15Re_d^{0.687})$ for $Re_d \leq 1300$

$C_D = 0.4$ for $Re_d > 1300$

where Re_d is the droplets Reynolds number. Fluent in the Discrete Phase Modeling (DPM) uses the droplet drag coefficient of (Morsi and Alexander, 1972) given as:

$C_D = 24/Re_d$ for $Re_d < 0.1$

$C_D = 22.73/Re_d + 0.0903/Re_d^2 + 3.69$ for $0.1 < Re_d < 1$

$C_D = 29.1667/Re_d - 3.7778/Re_d^2 + 1.22$ for $1 < Re_d < 10$

$C_D = 46.5/Re_d - 116.67/Re_d^2 + 0.6167$ for $10 < Re_d < 100$

$C_D = 98.33/Re_d - 2778/Re_d^2 + 0.3644$ for $100 < Re_d < 1000$

$C_D = 148.62/\mathrm{Re_d} - 4.75\times10^4/\mathrm{Re_d}^2 + 0.357$ for $1000 < Re_d < 5000$

$C_D = -490.546/Re_d - 57.87\times10^4/Re_d^2 + 0.46$ for $5000 < Re_d < 10000$

$C_D = -1662.5/Re_d - 5.4167\times10^6/Re_d^2 + 0.5191$ for $10000 < Re_d < 50000$

Finstad in her doctoral thesis (Finstad, 1986) uses the droplet drag coefficients of (Beard and Pruppacher, 1969) and (Langmuir and Blodgett, 1946). These droplet drag coefficients are given as (Finstad, 1986):

$$(C_D Re/24) = 1 + 0.102 Re^{0.955} \quad \text{for} \quad 0.2 \le Re_d \le 2.0$$

$$(C_D Re/24) = 1 + 0.115 Re^{0.802} \quad \text{for} \quad 2.0 \le Re_d \le 21.0$$

$$(C_D Re/24) = 1 + 0.189 Re^{0.632} \quad \text{for} \quad 21.0 \le Re_d \le 200.0$$

$$(C_D Re/24) = 1 + 0.197 Re^{0.63} + 2.6 \times 10^{-4} Re^{1.38} \quad \text{for} \quad 200 < Re_d$$

where the last parameterization is the droplet drag coefficient of (Langmuir and Blodgett, 1946) which they apply for the full range of droplet's Reynolds number Re_d.

Essentially, it makes the droplet trajectories, when calculated with the Qing et al. expression for the droplet drag coefficient almost a straight line, as in the absence of a significant drag, acting on the droplet, the inertia dominates the droplet motion. Fig. 1 illustrates this concept. The droplet trajectories in Fig. 1 are obtained from the code, replicated from the Finstad's Ph.D. thesis (Finstad, 1986). The code's performance was validated against the experimental data of (Makkonen and Stallabrass, 1987). The operating conditions in the trajectory calculations are identical to the ones in Table 1 in (Qing et al., 2018). The only difference is the droplet drag coefficient parameterization used – Qing et al. vs. (Beard and Pruppacher, 1969), as implemented by Finstad herself in the original code. The droplet's staring coordinates (x_0, y_0) are (–10R, 1/3R), where R is the cylinder radius.

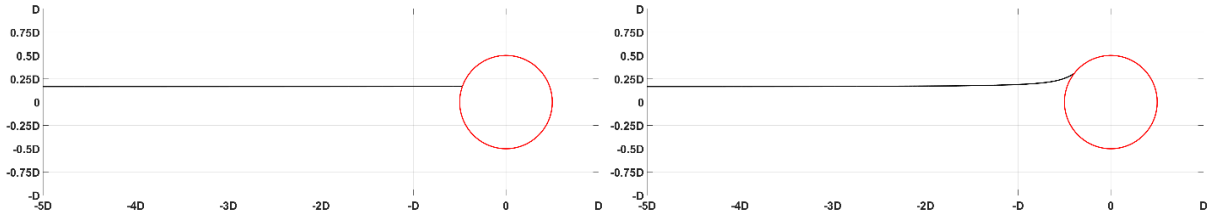

Fig. 1 – Droplet trajectories obtained using the Qing et al. droplet drag coefficient (left) and Beard and Pruppacher drag coefficient (right).

The resultant overall collision efficiencies obtained from the trajectory calculations for this case are E = 0.37 with Beard and Pruppacher droplet drag coefficient, and E = 0.97 with Qing et al. droplet drag coefficient. The ISO 12494 (ISO, 2001) overall collision efficiency formula gives for this particular case the overall collision efficiency E = 0.37. Furthermore, reverse calculating the overall collision efficiencies from Tables 2 and 3 in (Qing et al., 2018) for the windward conductor at the same operating condition yields the consistent value of the overall collision efficiency of E = 0.34. Such discrepancy between the obtained analytical results and the presented simulation results is puzzling.

Another major work focusing on the ice accretion on the bundled conductors in the Ph.D. thesis of (Wagner, 2010). In their work, for the dispersed phase, Wagner uses their own code, which is a Lagrangian particle tracking approach, based on the application of Newton's Second Law, with the total force F, acting on the particle being the sum of drag, buoyancy and gravity forces. The trajectories equations are solved using Runge-Kutta fourth and fifth order algorithm. For the droplet drag coefficient, Wagner uses the following fit to the droplet drag coefficient of Langmuir and Blodgett:

$$C_D = (24/Re_d)\left(1 - 0.391Re_d^{0.3289} + 0.5648Re_d^{0.4561}\right) \quad \text{for} \quad 0 < Re_d \leq 10$$

$$C_D = (24/Re_d)\left(1 + 0.1767Re_d^{0.6536}\right) \quad \text{for} \quad 10 < Re_d \leq 200$$

$$C_D = (24/Re_d)\left(4 + 0.01052Re_d^{1.048}\right) \quad \text{for} \quad 200 < Re_d$$

Similarly, the droplet drag coefficient by (Wagner, 2010) performs well in the trajectory calculations, using the analytical code from (Finstad, 1986). The value of the overall collision efficiency obtained with this coefficient is E = 0.36, which is very close to the value of the overall collision efficiency E = 0.37, obtained by using ISO 12494 formulae and the unmodified Finstad code. The example of droplet trajectory calculations is given in Fig. 2, with the same operating and initial conditions as in Fig. 1.

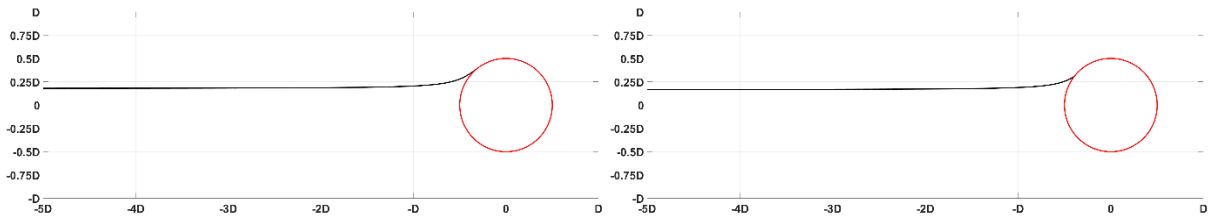

Fig. 2 – Droplet trajectories obtained using the Wagner droplet drag coefficient (left) and Beard and Pruppacher drag coefficient (right).

In graphical form, the comparison of all aforementioned droplet drag coefficient parameterizations is given in Fig. 3 for the droplets Reynolds number range 0 < Re_d < 100, which is believed to cover the majority of typical icing conditions.

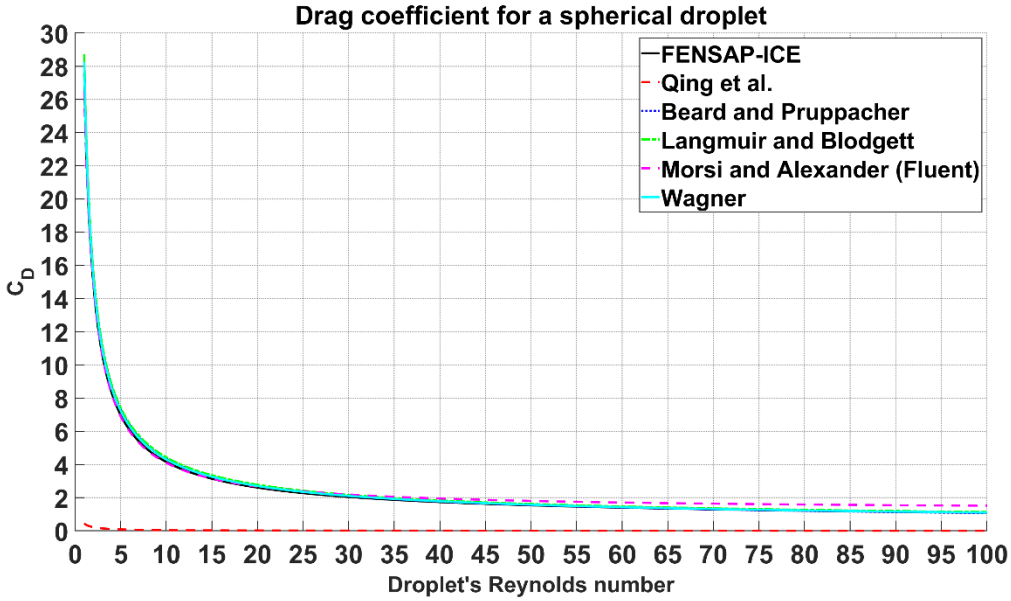

Fig. 3 – Droplet drag coefficient C_D for a spherical droplet as a function of droplet's Reynolds number Re_d.

As it can be seen from Fig. 3 nearly all droplet drag coefficient parameterizations have a good agreement among each other for the entire range of droplet's Reynolds number. All, but the one presented in (Qing

et al., 2018), which gives the results of $C_D < 1$ for $Re_d > 0.44$, along with $C_D \rightarrow 0$ as droplet's Reynolds number increases. It is unknown where (Qing et al., 2018) have obtained this expression for the spherical droplet drag coefficient. It is not present in references of (Bourgault et al., 1999; Fluent, 2006), associated with the governing equations for the droplet motion in their paper.

In addition, Qing et al. write (original notation preserved): "*Due to wind, air and super-cooled water droplets move with respect to the conductor. While air bypasses the conductor, water droplets collide onto the conductor because of their inertia, as shown in Fig. 1. The local collision efficiency is then defined as follows:*

$$\alpha_1 = \mathrm{d}y/\mathrm{d}L$$

where α_1 is the local collision efficiency, dy is the ordinate difference of two starting points, and dL is the distance along the conductor between two impact points." This statement is followed by: "*The flow of air and water droplets follows the principle of fluid mechanics and can be regarded as gas-liquid twophase flow. Here, the Euler's model was used to analyze the two-phase flow (Bourgault et al., 1999). In this model, both air and water droplets are treated as continuous phase, and the volume of one phase cannot be occupied by the other. By establishing the governing equations for each phase, the characteristic of flow field can be calculated*."

Such definition of local collision efficiency is consistent with the descriptions of (Finstad, 1986) and (Finstad et al, 1988). However, such definition of the local collision efficiency is valid for the Lagrangian approach and not Eulerian approach. Since Eulerian approach does not track individual particles such definition of local collision efficiency makes no sense. For example, the FENSAP–ICE, which is an Eulerian solver, defines the local collision efficiency as (FENSAP–ICE User Manual):

$$\beta = -\frac{\alpha \overrightarrow{V_d} \cdot \vec{n}}{w V_\infty} \tag{1}$$

where α is the local volume fraction (kg/m^3), w is the Liquid Water Content (LWC), V_∞ is a freestream wind speed and $\vec{n}$ is the surface normal vector. The overall collision efficiency is then calculated as the integration of local collision efficiencies over surface area and is given as:

$$\beta_{tot} = \frac{\int \beta \, \mathrm{d}A}{L_\infty^2} \tag{2}$$

The integral is normalized by a characteristic length L_∞.

Furthermore, since the cloud impingement parameters, i.e., the overall and local collision efficiencies, impact velocities and maximum impingement angles are all coupled with each other and depend on the droplet inertia parameter K and the Langmuir parameter ϕ as it can be seen from the equations and discussion in (Finstad, 1986) and (Finstad et al., 1988), an overestimation of one of them, e.g. the overall collision efficiency, in an analytical calculations will result in an overestimation of the rest of them. Since, Qing et al. use the local collision efficiency definition given by (Finstad, 1986) and (Finstad et al., 1988), and as it was shown previously – the trajectory calculations with their droplet drag coefficient

overestimate the overall collision efficiency significantly, it will also result in serious overestimation of the local collision efficiencies.

This presents a question – how did Qing et al. actually carry out their analysis? The combination of purely Lagrangian definition of the local collision efficiency with statements regarding an Eulerian approach for multiphase flow, along with mixing together governing equations from both Fluent and FENAP–ICE is challenging to reconcile within the scope of one model. Was Fluent predominantly used and coupled with FENSAP–ICE? Or vice-versa? To what extent the numerical simulations were performed in Matlab? And what was the setup of them? Was the Fluent DPM used? These questions make their simulation setup nigh impossible to replicate and validate the data in this work against it.

In their work (Wagner, 2010) has used a standard k–ε model with Launder–Sharma values for constants $C_{\varepsilon 1}$, $C_{\varepsilon 2}$, σ_k and σ_ε. Since their $y+$ values are in the range of $30 \leq y+ \leq 300$ the usage of the logarithmic wall function is implemented. The choice of the standard k–ε model was governed by, quoting (Wagner, 2010): "*Other turbulence models may overestimate the extension of the wake and therefore its effect on the ice accretion, like the k–ω model for instance. Hence, the chosen approach is on the safe side, which is beneficial for investigating whether there is an effect of tandem arrangement of conductors on the ice accretion or not*." They also note a few shortcomings to their fluid dynamics model, in particular, applied wall model does not account for adverse pressure gradients in the boundary layer, meaning that the pressure decreases in flow direction. In addition, the near wake, is significantly underestimated and the separation angle is overestimated, compared to the experiment (Wagner, 2010). The flow field simulations are performed in COMSOL in their study.

Finally, in their parametric study Wagner focuses on the effects of the wind speed, Median Volume Diameter (MVD), conductor temperature etc. on the wet and dry ice formation. Unfortunately, the parametric study on the characteristics of icing of bundled conductors is limited in their work. The only practical conclusion in their parametric study is shown in Fig. 4.

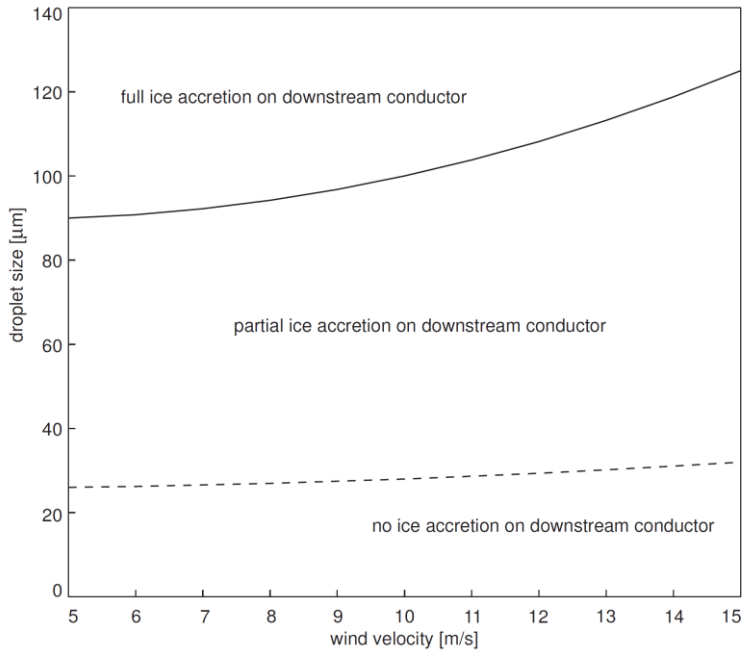

Fig. 4 – Influence of wind velocity and droplet size on ice accretion on a generic conductor bundle. The bundle consists of two conductors with a diameter of 40mm arranged inline with a spacing of 400mm (Wagner, 2010).

Unfortunately, Wagner did not attempt to quantify the "full", "partial" and "no ice accretion on downstream conductor" further in their work, unlike (Qing et al., 2018), which present the accreted ice masses. Although, as it was discussed previously, the authors of this work have certain reservations towards the results in (Qing et al., 2018). Out of presented conclusions in their work, the authors of this study have confidence in two of them. First, being the increase in the angle of incidence between the conductors in the bundle "normalizing" the ice accretion on bundled conductors. The smallest angle (Qing et al., 2018) tested was 30° at 400 mm separation, which gives the vertical separation of 200 mm, or, alternatively ten conductor diameters. Second being "*at a distance of more than 1000 mm the influence on the leeward conductor by the windward conductor becomes very small*." Such horizontal separation to conductor diameter ratio (L/D) = 50 makes any sort of wake effects perturbing the airflow around the leeward conductor highly unlikely, unlike the horizontal separation to conductor ratio of (Wagner, 2010), being equal to 10.

Thus in order to perform a meaningful study and to "fill the knowledge gaps" between the works of (Wagner, 2010) and (Qing et al., 2018) the choice of operating conditions should be "in between" these two works, in order to not replicate one or both of the studies. The aggregated operating conditions in (Wagner, 2010) and (Qing et al., 2018) are given in Table 1.

Table 1 – Summary of operating conditions in (Wagner, 2010) and (Qing et al., 2018).

	Wagner
Wind speed (m/s)	5 – 15
Droplet size (µm)	0 – 140
Conductor diameter (mm)	40
Conductor length (m)	Unspecified
Horizontal separation (mm)	400
Vertical separation (°)	0, 0.96, 1.91, 2.86
Liquid Water Content (g/m^3)	Unspecified, assumed to be 1.2, based on information in the same section.
Operating temperature (°C)	Unspecified, assumed to be –5, based on the same reasoning as above.
Icing duration (min)	Unspecified
	Qing et al., Simulation
Wind speed (m/s)	10
Droplet size (µm)	20 (MVD)
Conductor diameter (mm)	20
Conductor length (m)	1
Horizontal separation (mm)	200, 400, 600, 800, 1000
Vertical separation (°)	0, 30, 40, 60, 90 (at a total separation of 400 mm)
Liquid Water Content (g/m^3)	0.5
Operating temperature (°C)	–10
Icing duration (min)	30
	Qing et al., Experiment
Wind speed (m/s)	10, 20
Droplet size (µm)	19 (MVD)
Conductor diameter (mm)	30

Conductor length (m)	0.5
Horizontal separation (mm)	200, 300, 400, 600, 940
Vertical separation (°)	–
Liquid Water Content (g/m^3)	0.5
Operating temperature (°C)	–5
Icing duration (min)	30

Furthermore, two additional goals are deemed to be worth investigating within the scope of this study. First, is an attempt to "expand" the work by (Wagner, 2010), by presenting the accreted ice mass ratios for the simulations within this study, in attempt to further quantify the "partial ice accretion on downstream conductor" statement. Second, is to ascertain the viability of the commercial CFD package in the modeling of the dry ice accretion on the bundled conductor, as opposed to creating the in-house code. If such ice accretions can be viably modeled by a commercial CFD software, then it would be readily possible to extend this work further, in an attempt to produce the accreted ice masses ratio between the windward and the leeward conductor as a function of the operating conditions.

3 Design of the Experiment

Table 2 shows the operating conditions in this study with Fig. 5 giving a schematic overview of the duplex bundled cylinders setup.

Table 2 – Operating conditions.

Parameter	***Value***
Cylinder diameter (mm)	30
Air velocity (m/s)	4, 7, 10, 20
Air temperature. (°C)	–5
Altitude (m.a.g.l)	10
Median Volume Diameter (µm)	15, 20, 25, 30, 40
Liquid Water Content (g/m^3)	0.4
Icing duration (min)	30
Cylinder separation (mm)	500
Droplet distribution spectrum	Monodisperse

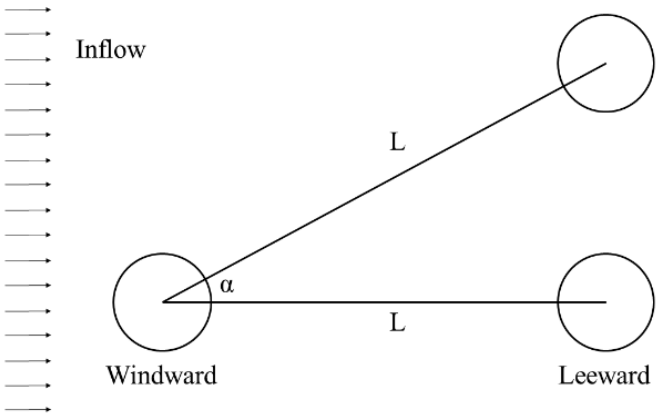

Fig. 5 – Schematic overview.

The choice of cylinder diameter and separation is deemed to be representative of an actual diameter and separation of a typical duplex conductor bundle. This is based on personal communications with Prof. Jiang Xingliang, (Chongqing University, China), and EFLA, Iceland. In both countries, the separation of ≈30 mm conductors in a bundle is equal to 450 – 470 mm. The range of air velocities in this study is deemed representative of simulating in-cloud icing in typical conditions, and the choice of Median Volume Diameters (MVDs) should also be sufficient to represent the naturally-occurring variation, without going into the Supercooled Large Droplet (SLD) size ranges, thus introducing potential issues with splashing and bouncing of the droplets.

Furthermore, the case of a cylinder bundle being exposed to icing at operating wind speed of 10 m/s and MVD of 20 μm was selected for further investigation of the effect of an angle/vertical separation on the icing on bundled conductors. The vertical separations chosen are one cylinder radius (15 mm; ≈1.7° angle), one cylinder diameter (30 mm; ≈3.4°), two cylinder diameters (60 mm, ≈6.8°) and 129.4 mm, corresponding to the angle of 15° exactly. This range of vertical separations fits in between the simulation cases, performed at different angle by (Wagner, 2010) and (Qing et al., 2018). The reason for performing numerical simulations at different angles is to simulate the gradual sag of the conductor bundle (1.7° – 6.8° angles) and extreme sag due to significant ice accretion (15° angle). Larger angles are not considered in this study as its assumed that the leeward conductor would not be "shielded" by a windward one past this point and thus the flow conditions and the ice accretion on both of them would be almost identical, as covered by (Qing et al., 2018).

Finally, in order to streamline the subsequent analysis some assumptions and simplifications have been made in this study. First, the assumption of "dry ice growth", i.e., all droplets stick and freeze on impact, and that the temperature of –5° C is sufficient for this. Second, is the choice of using the monodisperse distribution for modeling purpose. The reason for this is two-fold – to keep the obtained results "in compliance" with the ISO 12494 framework; and to avoid any potential discrepancies the usage of droplet distribution spectrum can introduce on the leeward cylinder, i.e., as the different bins in the distribution will have different overall collision efficiencies, MVD and Liquid Water Content (LWC) values along with the possibility that actual droplet distribution spectrum can be different from the windward cylinder, thus increasing the number of potential variables in the analysis.

3.1 Numerical Setup

The multiphase CFD based numerical simulations were carried out using ANSYS FENSAP-ICE, which uses Eulerian water droplet impingement solver. The existing analytical models of droplet behavior such as (Langmuir and Blodgett, 1946), (Finstad et al., 1988) etc. solve droplet trajectories using Lagrangian particle tracking approach. The Eulerian method treats the particle phase as a continuum and develops its conservation equations on a control volume basis and in a similar form as that for the fluid phase. The Lagrangian method considers particles as a discrete phase and tracks the pathway of each individual particle. By studying the statistics of particle trajectories, the Lagrangian method is also able to calculate the particle concentration and other phase data. On the other hand, by studying particle velocity vectors and its magnitudes in Eulerian method, it is possible to reconstruct the pathways and trajectories of particles in a phase.

Detailed mesh sensitivity analysis were carried out to accurately determine the boundary layer characteristics (shear stress and heat fluxes), a $y+$ values of less than 1 is used near the cylinder wall surface. Number of mesh elements and $y+$ value was selected based upon the heat flux calculations, where a numerical check was imposed that the heat flux computed with the classical formulae dT/dn should be comparable with the heat flux computed with the Gresho's method.

The calculation of $y+$ value is performed in the following way (White, 2002):

$$Re = \frac{\rho_f U_\infty L_\infty}{\mu_f} \tag{3}$$

$$C_f = \frac{0.026}{Re^{1/7}} \tag{4}$$

$$\tau_{wall} = \frac{C_f \rho_f U_\infty^2}{2} \tag{5}$$

$$U_{fric} = \sqrt{\frac{\tau_{wall}}{\rho_f}} \tag{6}$$

$$\Delta s = \frac{y^+ \mu_f}{U_{fric} \rho_f} \tag{7}$$

where ρ_f and μ_f are the density and dynamic viscosity of the continuous phase (air), U_∞ is the freestream velocity, L_∞ is the characteristic length, i.e., cylinder diameter, C_f is the skin friction coefficient, τ_{wall} is the shear stress at the wall, U_{fric} is the friction velocity and Δs is the wall spacing (first cell height). These computations are based on the flat-plate boundary layer theory from (White, 2002). Based on the highest operating wind speed in the Table 2 being equal to 40 m/s, this gives the $\Delta s = 12.2 \times 10^{-6}$ m for $y+ = 1$. Thus, the first cell height used in the meshes in this study, and being equal to $\Delta s = 1 \times 10^{-6}$ m yields a $y+$ value of $y+ = 0.08$ for the highest freestream wind speed value of 20 m/s.

The computational mesh used for all CFD simulations at 0° incidence is a hybrid mesh, consisting of structured quad elements near the cylinders and the unstructured tri elements elsewhere. The first cell height at both cylinders is 1×10^{-6} m with exponential growth factor of 1.1 and a total of 100 inflation layers. In addition, the length of the cylinder "wall" itself is divided into a 100 nodes. This results in 30000 structured quad elements per cylinder (since FENSAP–ICE is exclusively a 3D solver, a three cell extrusion in z-direction is used), for a total of 60000 structured quad elements. The rest of the mesh is filled with unstructured tri mesh, for a total cell count of 105960 cells in the computational domain. The computational mesh is also shown in Fig. 6.

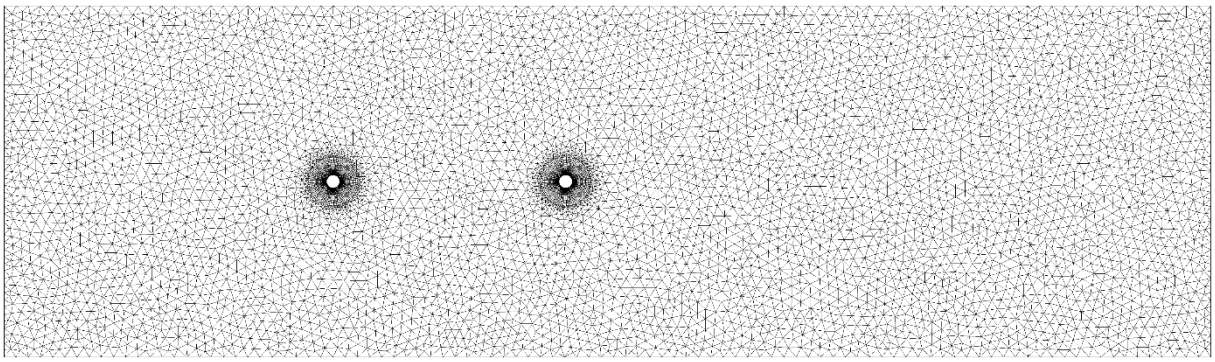

Fig. 6 – Computational mesh.

The turbulence model chosen for this study is a *k*–ω Shear Stress Transport (SST) model (Menter, 1992). This choice is governed by a few factors. First, in authors opinion, this model is the best option for this particular type of modeling, when considering other available turbulence models in FENSAP–ICE, those being laminar, Spalart-Allmaras, and LRN *k*–ω model (FENSAP–ICE User Manual). Second, is to test the hypothesis of (Wagner, 2010) of the potential overestimate of wake extension of *k*–ω models and their impact on the resultant ice accretion. Third, is to test the performance of the *k*–ω SST model itself for this type of atmospheric ice modeling, as the *k*–ω SST is a widely used turbulence model, which combines the robustness of *k*–ω model in near-wall and boundary layer region with the reliability of *k*–ε model in the farfield region. Last, is to ascertain, if the dry ice accretion of the bundled conductors can be carried within the constraints of one commercial CFD package, without coupling the solution procedure to other CFD packages, e.g. Fluent or the in-house code.

4 Results and Discussion

From the physics perspective, the modeling of the atmospheric ice accretion on bundled cylinders presents more challenge when compared to the single cylinder. The ice accretion of single cylinders can be adequately modeled analytically by the inviscid, potential flow approximation (Langmuir and Blodgett, 1946), (Finstad, 1986), with later model being experimentally verified by (Makkonen and Stallabrass, 1987) for the range of overall collision efficiencies of $0.07 < E < 0.63$. In the modeling of ice accretion on single conductors there is no value in modeling droplet trajectories past the cylinder as the most important characteristic of it – collision with cylinder or miss will already be determined.

For bundled configuration this is insufficient, as the information about the droplet not colliding with the windward cylinder is insufficient to determine whether or not the droplet in question will collide with the leeward cylinder. Thus, recovering the state of the multiphase flow past the windward conductor is of primary importance for modeling of the ice accretion of the bundled cylinders. Both the airflow solution, primarily the airflow velocity components, and the droplet behavior, such as, establishing the droplets velocity components, inertia and drag have to be obtained. The problem is exacerbated by the fact that, in practice, the majority of icing events are expected to happen at cylinder Reynolds number in the range of $10^4 – 10^5$, resulting in a turbulent flow. Thus, such features of the turbulent, viscous flow as turbulent wake, vorticity, vorticity shedding, oscillations, boundary layer response etc. might be of importance, as they can affect the airflow and droplet behavior. An example of multiphase flow solution

from the CFD simulations in this study is presented in Figs. 7 and 8 showing the droplet velocity magnitudes and LWC distributions respectively, for some selected cases from Table 2.

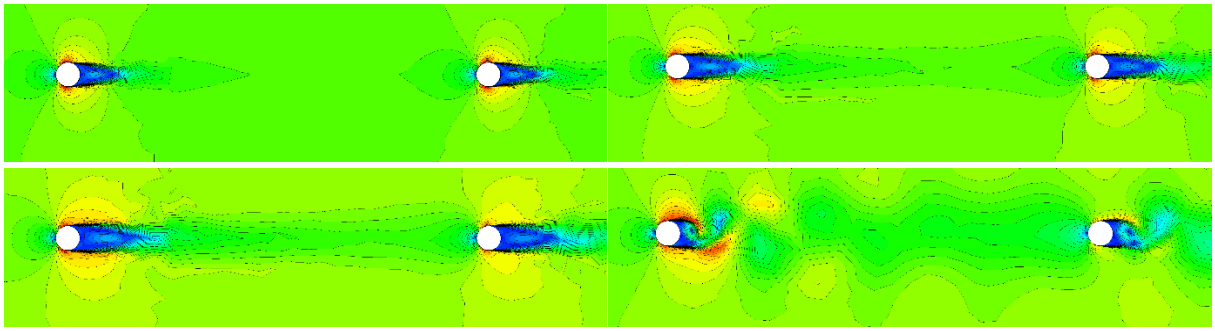

Fig. 7 – Air velocity magnitudes in CFD simulations. The operating conditions are V = 4 m/s (top left); V = 7 m/s, (top right); V = 10 m/s (bottom left); and V = 20 m/s (bottom right).

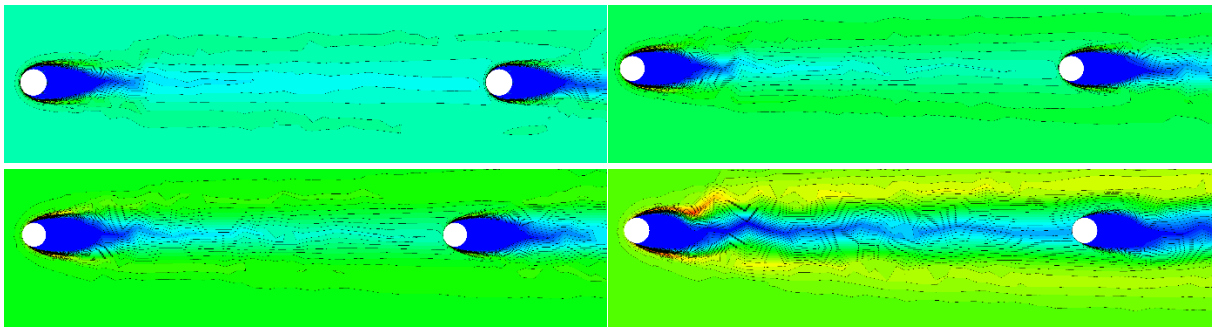

Fig. 8 – Liquid water content distributions in CFD simulations. The operating conditions are V = 4 m/s (top left); V = 7 m/s (top right); V = 10 m/s; and V = 20 m/s (bottom right). The MVD = 25 μm for all cases.

Tables 3 and 4 show the overall collision efficiencies (E) and their ratios between the windward and the leeward cylinders respectively for all test cases from Table 2.

Table 3 – Overall collision efficiencies on the windward (W) and leeward (L) cylinders.

MVD	***15***		***20***		***25***		***30***		***40***	
V	**W**	**L**	**W**	**L**	**W**	**L**	**W**	**L**	**W**	**L**
4	0.005	0.007	0.057	0.054	0.140	0.122	0.224	0.186	0.371	0.277
7	0.052	0.045	0.154	0.122	0.256	0.193	0.347	0.242	0.490	0.298
10	0.103	0.077	0.223	0.150	0.330	0.204	0.421	0.238	0.557	0.278
20	0.233	0.095	0.372	0.139	0.479	0.163	0.563	0.181	0.679	0.209

Table 4 – Overall collision efficiencies ratios of leeward to windward cylinders.

MVD	***15***	***20***	***25***	***30***	***40***
V					
4	121%	94%	87%	83%	75%
7	87%	79%	75%	70%	61%
10	75%	67%	62%	57%	50%
20	41%	37%	34%	32%	31%

Since for the "dry growth" regime the sticking and freezing efficiencies, $\alpha_2 = \alpha_3 = 1$ respectively, the accreted ice mass ratios between the windward and the leeward cylinders will be identical to overall collision efficiencies ratios from Table 4. Visually, the ratio from Table 4 is given in Fig. 9. For the dry ice growth, the overall collision efficiencies ratio will also be equal to the accreted ice masses ratio.

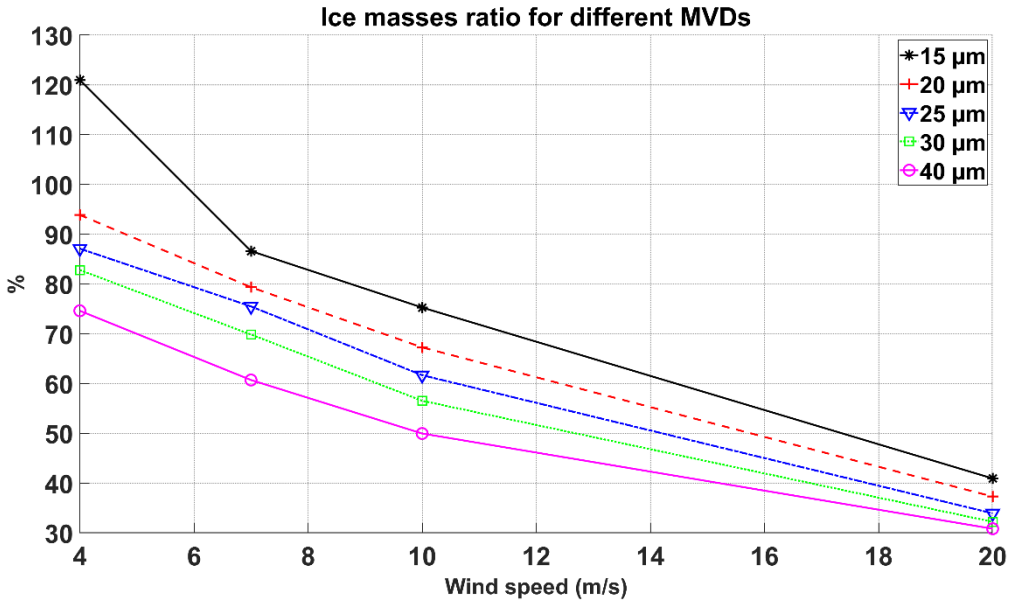

Fig. 9 – Overall collision efficiencies for bundled cylinders in this study.

From Table 3 and Fig. 9 the conclusion that can be made is that with the increase in the MVD and/or wind speed values, the ratio overall collision efficiencies between the leeward and the windward cylinder decreases from "full accretion" to a "partial accretion" of an around 31%. The decrease in the overall collision efficiencies is more "steeper" for smaller MVDs. This decrease can be directly correlated to the increase in the droplet's inertia parameter K, and to lesser extent – the Langmuir parameter ϕ. These parameters are obtained as:

$$K = \frac{\rho_p d_p^2 V}{9\mu_f D} \tag{8}$$

$$\phi = \frac{Re^2}{K} = \frac{9\rho_f^2 DV}{\mu_f \rho_p} \tag{9}$$

where d_p is droplet diameter, D is the cylinder diameter, V is the wind speed, ρ and μ are density and dynamic viscosity, respectively with subscripts f and p referring to fluid and particle, respectively. From the operating conditions in Table 1 the values of cylinder diameter, separation, particle and fluid densities and viscosities are constant, thus it follows that any variance in ice mass ratios in Table 3 must be explainable as a function of K, which depends on the value of product Vd_p^2 and ϕ which depends on the wind speed alone (granted, both of the aforementioned products also depend on the cylinder diameter D, however, in this study this value is constant).

The physical explanation behind the decrease of the accreted ice mass ratios, associated with the increase in values of K and ϕ is two-fold. First, with the increase of droplet's inertia, associated with the increase of MVD and/or wind speed, the inertia will be dominating the droplet movement and thus the characteristic time for the droplet to adapt to the new conditions will increase. For example, the increase in the wind speed will result in shorter "time window" for the droplet, passing over the windward cylinder, to adjust to new trajectory, such that allows for the collision with the leeward cylinder, at a given separation. In addition, higher wind speeds result in the wake effects being prominent, potentially affecting the ice accretion of the leeward conductor as it can be inferred from Fig. 7.

For completeness purposes, the values of droplet inertia parameter K and Langmuir parameter ϕ for the test cases in this study are given in Table 5.

Table 5 – Values of droplet inertia parameter K and Langmuir parameter ϕ for the bundled cylinders.

MVD	***15***		***20***		***25***		***30***		***40***	
V	***K***	**ϕ**	***K***	**ϕ**	***K***	**ϕ**	***K***	**ϕ**	***K***	**ϕ**
4	0.19	110	0.35	110	0.54	110	0.78	110	1.38	110
7	0.34	192	0.61	192	0.95	192	1.36	192	2.42	192
10	0.49	274	0.87	274	1.35	274	1.95	274	3.46	274
20	0.97	548	1.73	548	2.70	548	3.89	548	6.92	548

For the values of $K < 0.25$ (Finstad et al., 1988) advise to "*recalculate the droplet trajectories using the appropriate drag coefficients for each droplet size in the spectra*." The FENSAP–ICE uses the following expression for the droplet's continuity and momentum equations:

$$\frac{\partial \alpha}{\partial t} + \vec{\nabla} \cdot \left(\alpha \overrightarrow{V_d}\right) = 0 \tag{10}$$

$$\underbrace{\frac{\partial\left(\alpha \overrightarrow{V_d}\right)}{\partial t} + \vec{\nabla}\left[\alpha \overrightarrow{V_d} \otimes \overrightarrow{V_d}\right]}_{\text{I}} = \underbrace{\frac{C_D Re_d}{24K} \alpha\left(\overrightarrow{V_a} - \overrightarrow{V_d}\right)}_{\text{II}} + \underbrace{\alpha\left(1 - \frac{\rho_a}{\rho_d}\right)\frac{1}{Fr^2}}_{\text{III}} \tag{11}$$

where the variables α and $V_{d,a}$ are mean field values of, respectively, the water volume fraction and droplet velocity.

The terms of this equation are, respectively, the:

- I – material derivative of acceleration.
- II – (steady-state) drag action the droplets of mean diameter d.
- III – buoyancy and the gravity forces.

As such, FENSAP–ICE lacks the term pertaining to the calculation of the "history term", which for the cases of $K < 0.25$ can make significant difference, when it comes to the overall collision efficiencies, as discussed in the (Finstad et al., 1988). As such, the "physical meaning" of the simulation results at V = 4 m/s and MVD = 15 μm, which results in the accreted ice masses ratio of 121% can be questioned.

Furthermore, Fig. 10 shows the overall collision efficiencies ratio from Table 4 compared to the value of the droplet inertia parameter *K*.

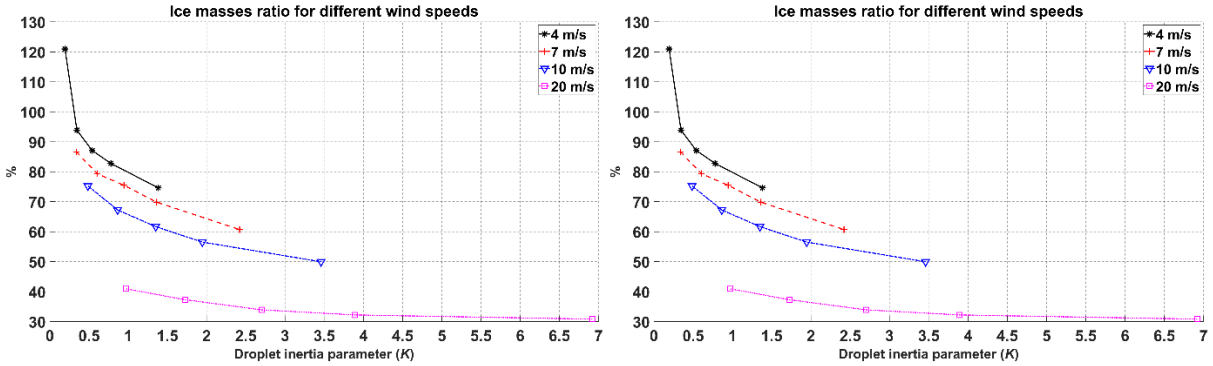

Fig. 10 – Accreted ice masses ratio vs. droplet inertia parameter K for different wind speeds (left) and MVDs (right). Each marker in the plot corresponds to one pair of wind speed and MVD from Table 4.

Fig. 10 shows that the accreted ice masses ratio decreases in the similar fashion for all combinations of wind speeds and/or MVDs with the increase in the value of *K*. Moreover, the curves, featuring inherent larger changes in values of *K*, for example, at 4 m/s wind speed or at MVD of 15 μm tend to decrease the accreted ice masses ratio faster. This is in agreement with the results of (Wagner, 2010), shown in the Fig. 4, especially for the curve dividing "full" and "partial" accretion, as in that plot the higher values of *K* are towards upper right of the plot. Unfortunately, it is not possible to quantify the results further, as (Wagner, 2010) haven't presented the overall collision efficiencies or the accreted ice masses ratios in their work.

In addition, an interesting point in the results from Table 4 and Fig. 10 is a rapid drop in the accreted ice masses ratio at the 20 m/s wind speed, for all tested MVDs, when compared to the results at 4 – 10 m/s wind speed. From Figs. 7 and 8 it can be seen that the wake behavior changes significantly at 20 m/s, with the significant vortex shedding present in the wake. When comparing the airflow behavior in the wake for the results in (Wagner, 2010) and the references contained within, for the flow at $Re = 4.5\times10^4$ (for the 20 m/s operating conditions in this study, the cylinder Reynolds number is $Re = 4.6\times10^4$), the wake length is significantly larger and the relative velocities in the wake are lower in this work. These effects of the wake on the leeward cylinder, coupled with the possible entrainment of droplets in the vortices, can explain the sudden drop of the accreted ice masses ratio at 20 m/s operating wind speed.

When it comes to the change in the overall collision efficiencies between the windward and the leeward cylinders, the increase of the overall collision efficiency values on the leeward conductor will not scale linearly with the corresponding increase of the overall collision on the windward conductor. As per (Finstad et al., 1988) the general expression for the calculation of the overall collision efficiency α_1, stagnation line impact velocity V_0 and collision efficiency β_0 and the maximum impingement angle θ is:

$$\begin{aligned} X(K,\phi) = &\left[C_{X,1}K^{C_{X,2}}\exp\left(C_{X,3}K^{C_{X,4}}\right) + C_{X,5}\right] - \left[C_{X,6}(\phi - 100)^{C_{X,7}}\right] \\ &\times \left[C_{X,8}K^{C_{X,9}}\exp\left(C_{X,10}K^{C_{X,11}}\right) + C_{X,12}\right] \end{aligned} \quad (12)$$

with the value of constants $C_1 - C_{12}$ available in the original source (Finstad et al., 1988). This equation has a non-linear dependence on the values of the of cloud impingement parameters, primarily the overall collision efficiency, on K and ϕ values.

FENSAP–ICE estimates the accreted ice mass in a similar way to ISO 12494 as:

$$M = \alpha_1 \alpha_2 \alpha_3 w V A t \tag{13}$$

where w is the liquid water content, α_1, α_2 and α_3 are the non-dimensional collision, sticking and freezing efficiencies respectively, t is the icing duration and A is the surface area of the object. The only difference between the FENSAP–ICE and the ISO 12494 estimation of the accreted ice mass is in the value of the area A. The FENSAP–ICE uses the surface area of an object while ISO 12494 uses the $A = DL$ expression for a circular cylinder where D is the diameter and L is the cylinder length. For the case of a circular cylinder, it is simple to account for the difference in the area used and thus the accreted ice masses for bundled cylinders in this study are given in Table 6.

Table 6 – Accreted ice masses on the windward (W) and leeward (L) cylinders. Values are in g/m.

MVD	***15***		***20***		***25***		***30***		***40***	
V	**W**	**L**	**W**	**L**	**W**	**L**	**W**	**L**	**W**	**L**
4	0.5	0.6	5.0	4.7	12.1	10.5	19.4	16.0	32.0	23.9
7	7.9	6.8	23.3	18.5	38.7	29.2	52.4	36.6	74.2	45.0
10	22.2	16.7	48.1	32.4	71.3	44.0	90.8	51.4	120.3	60.1
20	100.6	41.2	160.5	59.9	207.0	70.2	243.0	78.3	293.4	90.4

Fig. 11 shows the accreted ice masses for all operating conditions in this study plotted against the droplet inertia parameter K. In addition, a curve has been added, corresponding to the analytical calculations for the accreted ice mass on the windward conductor, carried out using ISO 12494 formulae/trajectories calculation method. The value of the droplet inertia parameter K was estimated from the eq. (8).

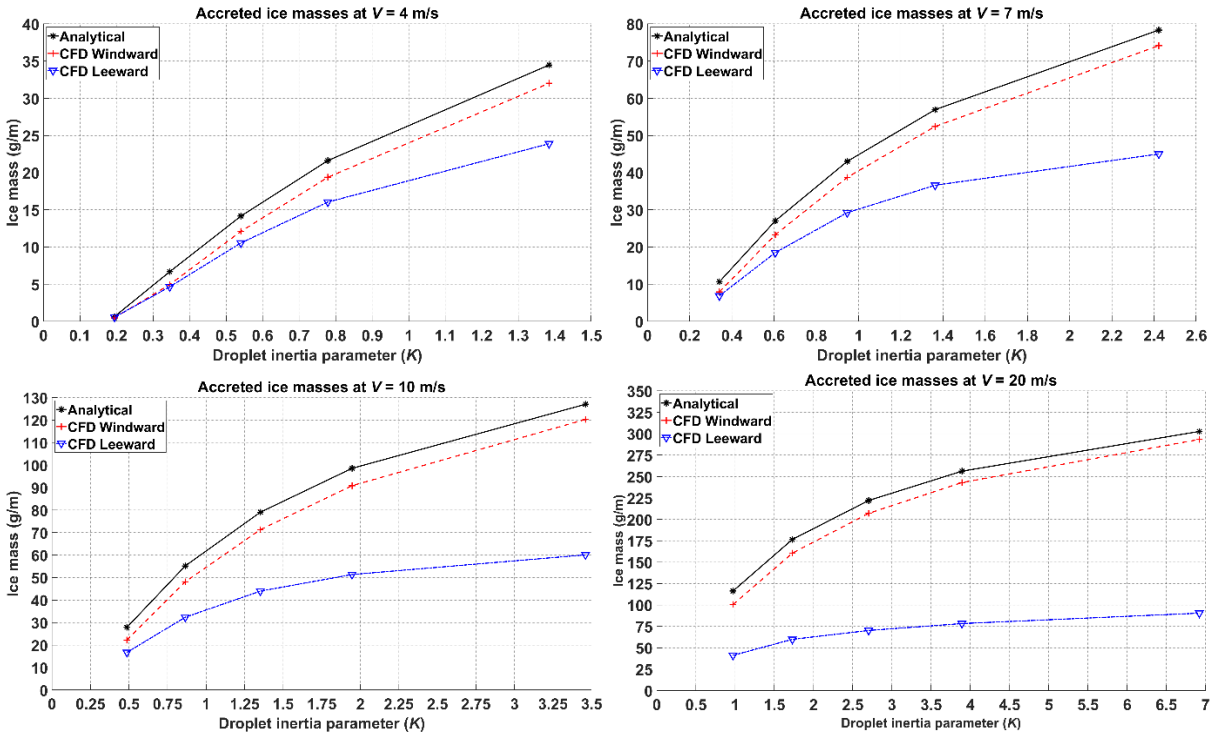

Fig. 11 – Accreted ice masses vs. droplet inertia parameter K for different wind speeds. Each marker in the plot corresponds to one MVD from Table 4.

From Fig. 11 it can be seen that the analytical and the CFD results for the windward conductor agree well. On the contrary, the leeward conductor behaves rather differently from the windward conductor in CFD and analytical model, with an interesting tendency of "flat lining" in terms of accreted ice masses for the values of $K > 4$.

Having established the results for the ice accretion on the bundled cylinders at different operating conditions for the 0° incidence angle, the results of the effect of the angle on the ice accretion on the bundled cylinders will be presented. For brevity, only one test case was selected from Table 2 for the purpose of studying the effect of the angle on the atmospheric ice accretion on the bundled cylinders. The selected test case has the MVD of 20 μm and the wind speed of 10 m/s. As with all cases the distance between cylinders is held constant at 500 mm and the desired angle is achieved by manipulating the horizontal and the vertical separation distances. The results from the ice accretion simulations on the angled bundle are given in terms of the overall collision efficiencies, their ratios and the accreted ice masses, and they are given in Table 7. As with all test cases in this study, the "dry growth" icing conditions are maintained, therefore, the accreted ice mass ratios are identical to the overall collision efficiencies ratios.

Table 7 – Overall collision efficiencies, ratios and accreted ice masses on the angled cylinders.

Vertical separation (mm)	***Angle***	***Overall Collision Efficiency***		***Accreted Ice Mass (g/m)***		***Overall Collision Efficiency Ratio***
		W	**L**	**W**	**L**	
15	1.7°	0.22	0.14	47.3	31.3	66%

30	3.4°	0.22	0.24	47.8	52.5	110%
60	6.8°	0.22	0.24	47.7	50.9	107%
129.4	15°	0.21	0.22	45.6	46.7	103%

Fig. 12 shows the distribution local collision efficiencies for the angled bundle configuration. For the dry growth conditions, the distribution local collision efficiencies are also representative of the accreted ice shapes.

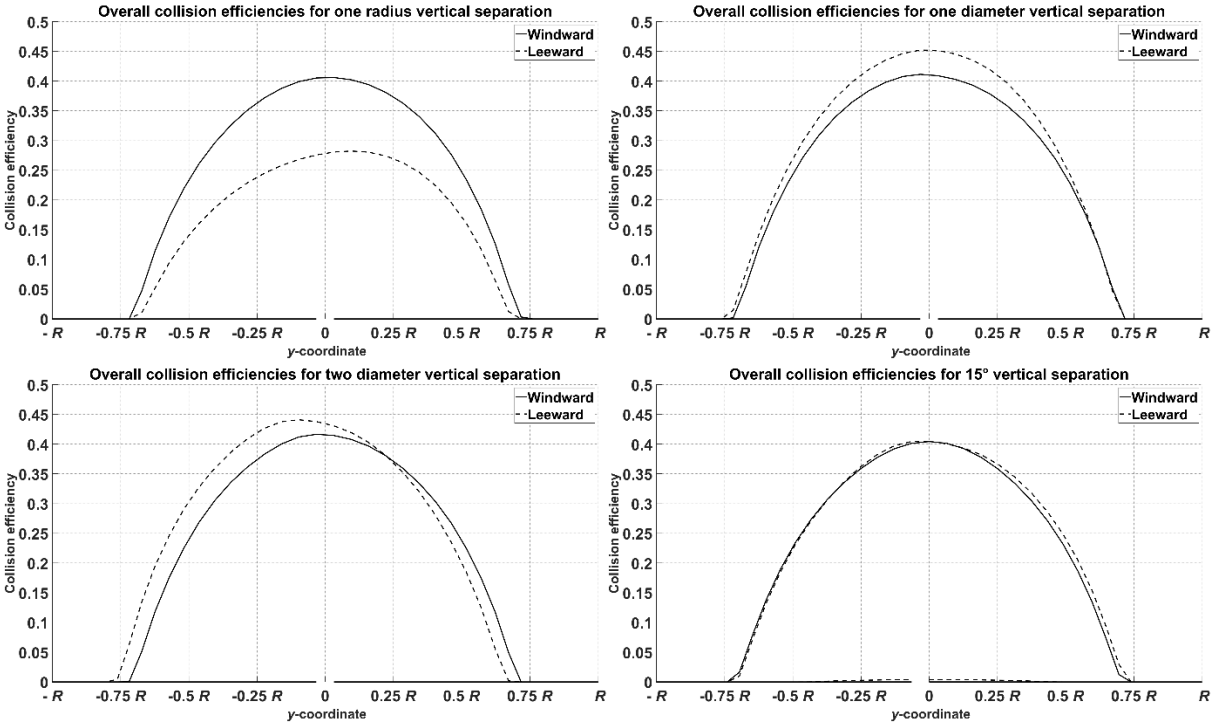

Fig 12 – Local collision efficiencies of the angled cylinders configuration. The vertical separations are 15 mm (one cylinder radius; top left); 30 mm (one cylinder diameter; top right); 60 mm (two cylinder diameters; bottom left); and 129.4 mm, corresponding to the angle of 15° (bottom right).

Fig. 13 shows the accreted ice masses and their ratios for the angled bundle configuration.

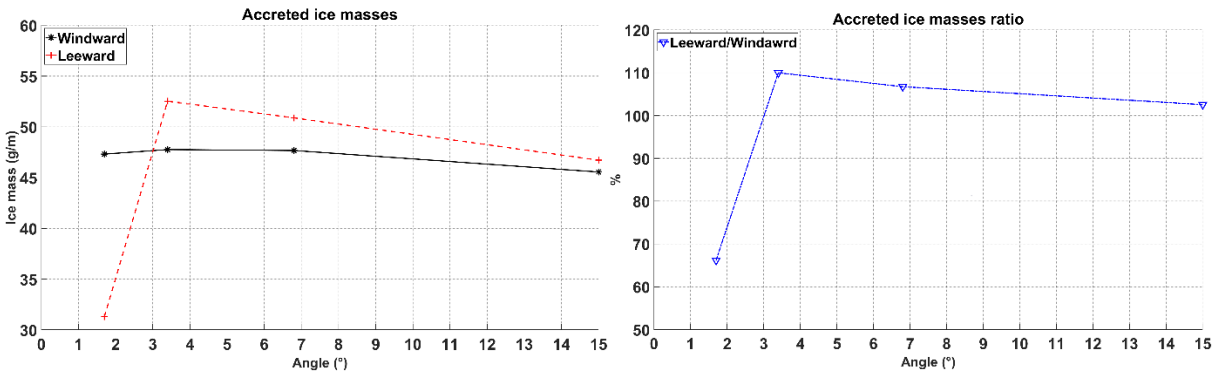

Fig 13 – Accreted ice masses (left) and their ratios (right) for the angled cylinders configuration.

From the results in Table 6 and Figs. 12 and 13, it can be seen that at vertical separation of 15 mm, equal to the one cylinder radius, the "shielding" effects from the windward cylinder are very pronounced,

limiting the amount of accumulated ice mass on the leeward cylinder at 67%, compared to the windward cylinder. This value is almost identical to the corresponding case from Table 4 simulated at 0° incidence. At the vertical separations of 30 and 60 mm, equal to the one and two cylinder diameters respectively, the ice accretion on the leeward cylinder "normalizes", becoming equal and even slightly higher than on the windward cylinder. This is more pronounced for the leeward conductor at one cylinder diameter vertical separation, which accretes approximately 10% more ice mass. This increased accretion can be explained by part of the multiphase flow, carrying significant LWC concentration at high speed being redirected from the top edge of windward cylinder onto the leeward one. The effect dissipates with the increase of vertical separation, as evidenced from the results at 15° angle, corresponding to the vertical separation of 129.4 mm which is slightly more than four cylinder diameters. In this case both cylinders accrete almost identical ice masses, within 3% of each other.

These results tend to agree well with the ones from (Wagner, 2010), who notes that for the angle of twist of 1.91°, corresponding to the vertical separation of 13.33 mm, the leeward conductor accreted 86% ice mass, compared to the windward conductor. For the angle of 2.86° (vertical separation of 19.96 mm) the accreted ice mass ratio is almost 100%. However, some discrepancies between results of (Wagner, 2010) and this work are present. For the angle of 0.96° (6.7 mm), their leeward conductor accretes only 11% mass, and for the conductor at 0° Wagner writes that "*the downstream cable without any ice deposit*". Contrary, in this work the cable at 0° incidence accretes 67% ice mass. When comparing the operating conditions of (Wagner, 2010) with this work, the values of the droplet inertia parameter K and the Langmuir parameter ϕ are different, being $K = 0.87$ and $\phi = 273.8$ for this work and $K = 1.27$ and $\phi = 365.1$ in (Wagner, 2010), along with the ratio of the cylinder separation L to the diameter D. In this work $(L/D) = 16.67$ and for Wagner it is $(L/D) = 10$. The windward cylinders Reynolds number are 2.3×10^4 and 3.1×10^4, respectively.

The practical meaning of this phenomenon in the ice accretions on actual power lines with bundled conductors is, when the windward conductors accretes enough ice mass in order to sag sufficiently enough to no longer "shield" the leeward conductor, the ice accretions on the both conductors in the bundle will be almost equal and thus they can be modeled using simplex configuration in CFD along with the formulae of ISO 12494, if desired. This does not take into account the possibility and potential implications of vibrations or rotations of the conductors, due to fluid-structure interaction. It is assumed that these interactions can cause the windward conductor to no longer "shield" the leeward conductor at even earlier point in time during an icing event. However, these potential effects are not within the focus of current study and will not be ascertained here.

5 Icing Tunnel Experiments

For the validation of the numerical model and obtained results in this study the ice accretion values from the duplex cylinders in the icing wind tunnel are used. The operating conditions in the icing wind tunnel are similar of these in Table 1 with exceptions of wind speed being 4 m/s and instead of monodispersed distribution with MVD of 20 μm, the actual experimental droplet distribution spectrum is used in numerical simulations. This experimental distribution is given in Fig. 14 and Table 8.

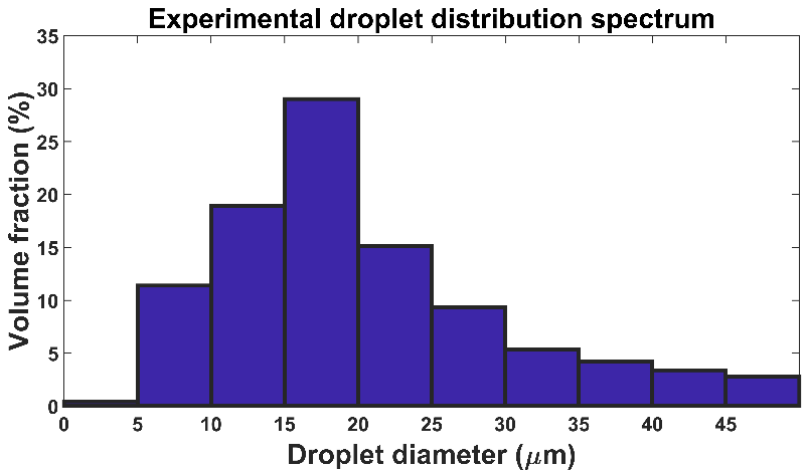

Fig. 14 – Experimental distribution.

Table 8 – Experimental distribution.

Bin (µm)	***Bounds (µm)***	***LWC fraction***
5	0.61-5	0.0045
10	5 - 10	0.1138
15	10 - 15	0.1893
20	15 - 20	0.2902
25	20 - 25	0.1510
30	25 - 30	0.0935
35	30 - 35	0.0537
40	35 - 40	0.0419
45	40 - 45	0.0339
50	45 - 50	0.0277

The experiments were conducted in the VTT Technical Research Centre of Finland icing wind tunnel. This is an "open-loop" tunnel placed entirely inside a large cold room. The cross-section of the tunnel mouth is 0.7 m by 0.7 m. Ice was grown on 0.5 m long smooth aluminum cylinders, 30 mm in diameter, placed vertically close to the center of the tunnel. The schematic of the icing wind tunnel is given in Fig. 15. To rule out the effect of blockage, the cylinders were located in front of the exit of the tunnel. The temperature and wind speed in the test section were measured using calibrated sensors. The liquid water content (LWC) was calibrated for each wind speed and temperature pair by measuring the ice growth on a 30 mm cylinder and using the formulas defined in ISO 12494 (ISO, 2001). Under the test conditions, LWC was 0.4 g/m^3. The air temperature was –5 °C and wind speed 4 m/s. The droplet size distribution in the icing tunnel has been calibrated by using The Cloud, Aerosol and Precipitation Spectrometer probe (CAPS), which can measure small particles between 0.61 and 50 µm by utilizing the light scattering principle. The calculated MVD of this distribution is 18.73 µm.

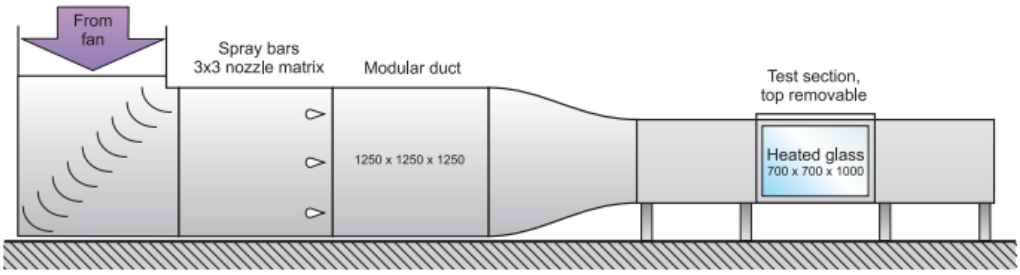

Fig. 15 – Icing wind tunnel schematic (VTT, 2016).

An example of ice shape obtained from the icing tunnel experiments is shown in Fig. 16.

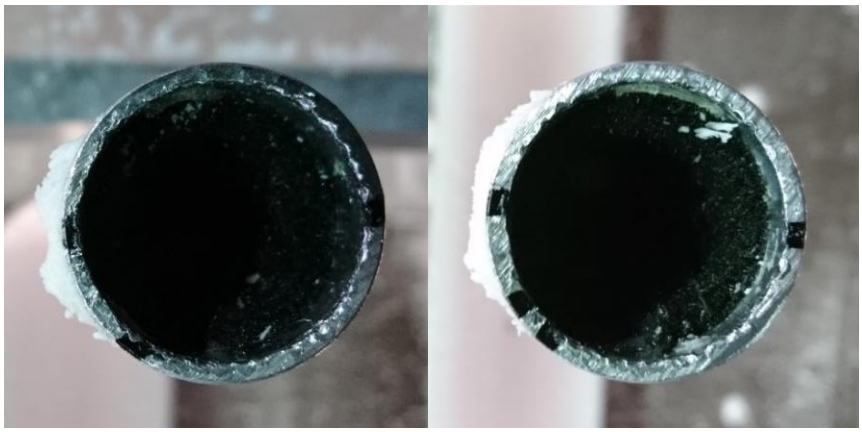

Fig. 16 – Sample ice accretion shapes in the icing wind tunnel for the windward (left) and leeward (right) cylinders.

Table 9 lists the comparison of numerical simulation results compared to the experimental values.

Table 9 – Overall collision efficiencies, accreted ice masses and ratios in experimental vs. numerical results.

Test case	***Wind speed (m/s)***	***Overall Collision Efficiency***		***Accreted Ice Mass (g)***		***Ice Masses Ratio***
		W	**L**	**W**	**L**	
Experiment	4	0.12	0.09	5.1	3.9	77%
CFD Spectrum		0.10	0.08	4.2	3.3	79%
CFD Monodispersed		0.04	0.04	1.6	1.6	100%
Experiment	7	0.23	0.17	17.5	12.6	72%
CFD Spectrum		0.17	0.12	13.0	9.3	72%
CFD Monodispersed		0.13	0.10	9.6	7.8	81%
Experiment	10	0.22	0.17	23.7	18.6	78%
CFD Spectrum		0.23	0.14	24.5	14.9	61%
CFD Monodispersed		0.19	0.13	20.8	14.3	69%
Experiment	20	0.38	0.23	82.9	50.4	61%
CFD Spectrum		0.35	0.11	75.7	22.8	30%
CFD Monodispersed		0.34	0.13	73.3	28.8	39%

Visually, the results from Table 9 are also given in Figs. 17 and 18 in a graphical form.

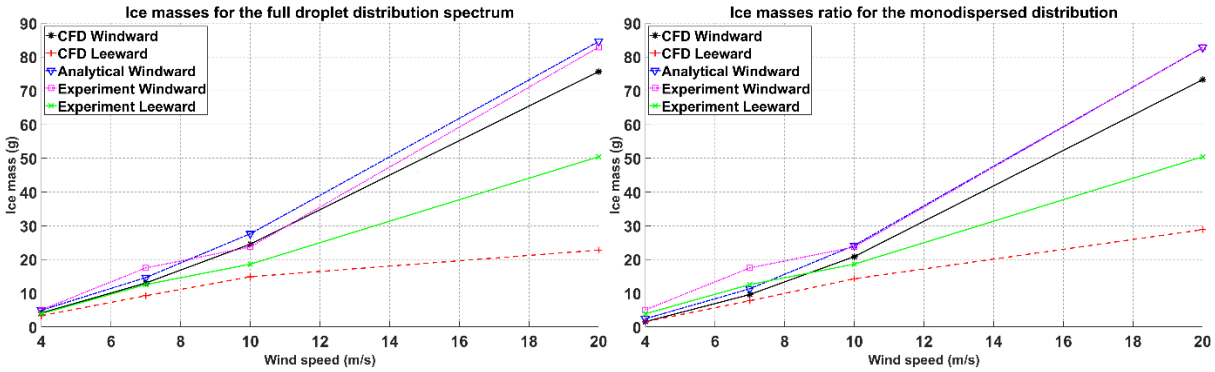

Fig. 17 – Accreted ice masses for the full droplet distribution spectrum (left) and monodispersed distribution (right).

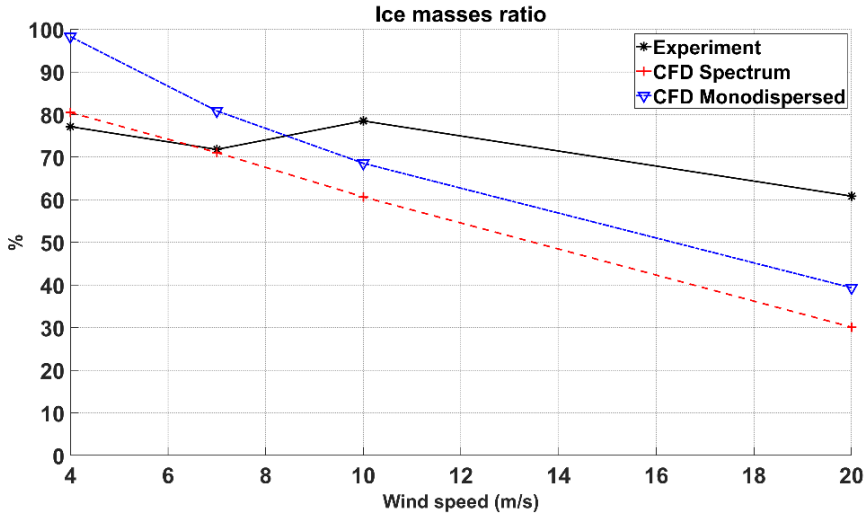

Fig. 18 – Accreted ice masses ratio.

From the values in Table 9 and Figs. 17 and 18 it can be seen that the CFD simulations results tend to underestimate the values of accreted ice masses and overall collision efficiencies, in particular on the leeward cylinder at 20 m/s wind speed. The accreted ice masses ratio in the CFD simulations has good agreement with the experimental values, for the 4 and 7 m/s wind speed conditions, acceptable agreement for the 10 m/s wind speed conditions (keeping in mind the apparent increase in the accreted ice masses ratio at this wind speed, as seen from Fig. 18) and rather poor agreement at 20 m/s wind speeds.

The possible reason for underperformance of the CFD model at 10 and 20 m/s wind speeds, when compared to the experimental values is twofold. First, (Qing et al., 2018) do not have the experimental data point, corresponding to the 500 mm cylinder separation. The "experimental value" presented in this study is taken as average value between (Qing et al, 2018) results at 400 and 600 mm cylinder separation. Second, is the "attachment" of the "end plate" of the bundled cylinders during their wind tunnel experiments, and its potential effects on the airflow conditions during the experiments.

In addition, the ratio of the overall collision efficiencies lines up with the previously established trend from Table 4, where the decrease in the operating wind speed and/or the value of MVD leads to the increase in the overall collision efficiencies ratios between the leeward and the windward cylinders. Overall, the agreement between the CFD simulation results and the experimental values is acceptable. Furthermore, the results with MVD approximation in Fig. 18 consistently given the higher accreted ice mass ratio, than the results with the full droplet distribution spectrum. Similarly, the primary reason behind this is the high sensitivity of the spectrum averaged results to the largest droplet sizes in the distribution and the tendency of decreasing of the accreted ice masses ratio with the increase in the values of the droplet inertia parameter *K*, with the larger droplets obviously possessing higher values of *K*. Fig. 19 illustrates this concept in more details, showing per bin overall collision efficiencies ratio of the experimental distribution under experimental operating conditions.

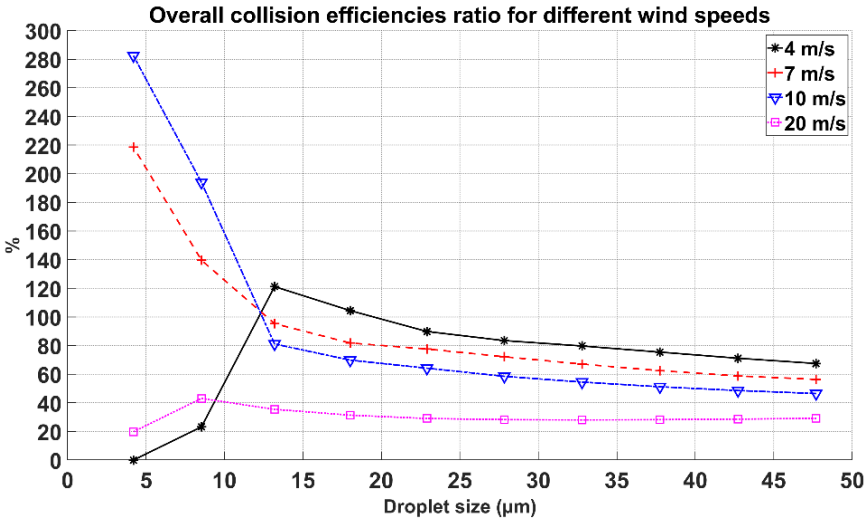

Fig. 19 – Per bin overall collision efficiencies ratio.

Disregarding some cases of the overall collision efficiencies ratio being significantly in excess of 100% (same arguments as with the test case at V = 4 m/s with MVD = 15 μm and the resultant value of K can be made) and possible lack of physical meaning of it (for those smaller droplet sizes the overall collision efficiencies are of an order of less than 0.01), the overall trend is clear. The overall collision efficiencies ratio of the larger droplet sizes, for example 40–50 μm is significantly lower than the ratio for the smaller bins, e.g. 20 – 25 μm. Since the monodispersed distribution contains only one droplet size in it, the results for it are not being affected in the similar fashion.

6 Conclusion

Within this work a series of CFD simulations have been performed on the bundled cylinders under the dry ice growth regime. The primary interest of modeling of such geometric configurations comes from the need of modeling the ice accretion on bundled conductors on the power lines. First, is to "fill the gaps" in the works of (Wagner, 2010) and (Qing et al., 2018), mostly, in an attempt to "expand" the work by (Wagner, 2010), by presenting the accreted ice mass ratios for the simulations within this study, in attempt to further quantify the "partial ice accretion on downstream conductor" statement. Second, is

to ascertain the viability of the commercial CFD package in the modeling of the dry ice accretion on the bundled conductor, as opposed to creating the in-house code. If such ice accretions can be viably modeled by a commercial CFD software, then it would be readily possible to extend this work further, in an attempt to produce the accreted ice masses ratio between the windward and the leeward conductor as a function of the operating conditions.

For this purpose, a circular cylinder is considered an acceptable approximation. The performed simulations cover a wide range of possible icing conditions by varying the operating wind speed, from 4 to 20 m/s and MVDs from 15 to 40 μm respectively. The obtained results for the 0° angle of incidence show that the overall collision efficiencies and accreted ice mass ratios between the leeward and the windward cylinders varies from ≈100% to ≈30%. This ratio decreases with the increase in the values of the operating wind speed and/or median volume diameter. This can be explained by the increase in the droplet inertia, corresponding to the increase of droplet's inertia parameter *K*, as a function of droplet's size and wind speed. Specifically, with the increase in the operating wind speed, the droplets have less "window time" to adapt to the flow conditions past the windward conductor and move into a trajectory which allows a collision with the leeward cylinder.

For the comparison with the experimental data, the CFD simulations have a good agreement in terms of the accreted ice masses ratio for the 4 and 7 m/s wind speed conditions, acceptable agreement at 10 m/s wind speed and rather poor agreement at 20 m/s. The latter is believed to be primarily the factor of the changes in the wake behavior at this wind speed, with the significant vortex shedding present. As a result, a significant portion of the droplets is entrained in the said vortices. Overall, the CFD simulations tend to underestimate the accreted ice masses in the experiment, to an extent, particularly, for the monodispersed distribution, and the monodispersed distribution consistently shows the higher ratio of the accreted ice masses. This "feature" is believed to be again the primary impact of the droplet inertia parameter *K* on the accreted ice masses ratio. In the full droplet distribution spectrum, the "spectrum-average" results depend significantly on the larger droplets in the spectrum, which, by the nature of them being of the larger diameter, have higher value of *K*, when compared to the rest of the droplet sizes and/or the monodispersed distribution. The monodispersed distribution, featuring only one droplet size, is lacking this "feature".

For a case of bundled cylinders at 10 m/s wind speed and 20 μm MVD, the angle of incidence was varied from 0° to 15°, and angles corresponding to the vertical separations being equal to one cylinder radius and one and two cylinder diameters, respectively. This was primarily done in order to ascertain the effects of an angle and potential sag due to accreted ice on the power line. For the cases with non-zero angle of incidence, the simulated overall collision efficiencies and accreted ice masses are approximately equal, with the leeward cylinder accreting slightly more ice, as soon as the angle of incidence is large enough to introduce a vertical separation equal or greater of one cylinder diameter. This can be explained by leeward cylinder being no longer "shielded" by the windward one and thus the effects of perturbed airflow past the windward cylinder are no longer significantly affect the leeward cylinder. In such cases it is deemed possible to model the resulting ice accretion on the bundled cylinders using simplex configuration and ISO 12494 analytical modeling framework.

Acknowledgment

The work reported in this paper is funded by the Research Council of Norway, FRonTLINES – project no. 245370 & IceBOX – project no. 282403. Authors would like to acknowledge Mr. Timo Karlsson and Mr. Miko Tiihonen from VTT for providing icing wind tunnel experimental data used in this research work.

Declaration of Conflicting Interests

The Authors declare that there is no conflict of interest.

References

1. Beard, K.V., Pruppacher, H.R., 1969. A Determination of the Terminal Velocity and Drag of Small Water Drops by Means of a Wind Tunnel. Journal of Atmospheric Sciences 26, 1066-1072. doi:10.1175/1520-0469(1969)026<1066:ADOTTV>2.0.CO;2
2. Bourgault, Y., Habashi, W.G., Dompierre, J., Baruzzi, G.S. 1999. A Finite Element Method Study of Eulerian Droplets Impingement Models. International Journal for Numerical Methods in Fluids, vol. 29, pp. 429 – 449.
3. FENSAP–ICE User Manual
4. Fluent User Manual
5. Finstad, K.J., 1986. Numerical and experimental studies of rime ice accretion on cylinders and airfoils. Ph.D. thesis. University of Alberta, Canada.doi:10.7939/R3N58CS1V.
6. Finstad, K.J., Lozowski, E.P., Gates, E.M., 1988. A computational investigation of water droplet trajectories. Journal of Atmospheric and Oceanic Technology, 5, 160-170.doi:10.1175/1520-0426(1988)005<0160:ACIOWD>2.0.CO;2
7. ISO 12494:2001(E), 2001. Atmospheric icing of structures. Standard. International Organization for Standardization. Geneva, CH
8. Langmuir, I., Blodgett, K., 1946. A Mathematical Investigation of Water Droplet Trajectories. Army Air Forces technical report 5418. Army Air Forces Headquarters, Air Technical Service Command.
9. Lam, C.K.G., Bremhorst, K. 1981. A Modified Form of the k – ε Model for Predicting Wall Turbulence. Journal of Fluid Engineering. Transactions of ASME, vol. 103, pp. 456 – 460.
10. Lozowski, E.P., Makkonen, L., 2005. Fifty years of progress in modelling the accumulation of atmospheric ice on power network equipment, in: Proceedings of the 11th International Workshop on Atmospheric Icing of Structures.
11. Makkonen, L., 1984. Modeling of Ice Accretion on Wires. Journal of Applied Meteorology 23, 929-939. doi:10.1175/1520-0450(1984)023<0929:MOIAOW>2.0.CO;2
12. Menter, F.R. 1992. Improved Two-Equation k – ω Turbulence Models for Aerodynamic Flows. National Aeronautics and Space Administration Ames Research Center. NASA Technical Memorandum 103975.
13. Morsi, S.A., Alexander, A.J., 1972. An investigation of particle trajectories in twophase flow systems. Journal of Fluid Mechanics, vol. 55, pp. 193 – 208, DOI: 10.1017/S0022112072001806.
14. Papadakis M., Wong, S.-C., and Rachman, A, Large and Small Droplet Impingement Data on Airfoils and Two Simulated Ice Shapes, NASA/TM—2007-213959, October 2007
15. Qing, H., Jian, Z., Mengyan, D., Dongmei., D. Makkonen, L., Tiihonen, M., 2018. Rime icing on bundled conductors. Cold Regions Science and Technology, vol. 158, pp. 230–236.
16. Ratvasky, T.P., Barnhart, B.P., Lee, S. Current Methods for Modeling and Simulating Icing Effects on Aircraft Performance, Stability and Control, NASA/TM—2008-215453, AIAA–2008–6204

17. Schmidt, R.C., Patankar, S.V. 1988. Two-Equation Low-Reynolds-Number Turbulence Modeling of Transitional Boundary Layer Flows Characteristic of Gas Turbine Blades. National Aeronautics and Space Administration Lewis Research Center, NASA Contractor Report 4145.
18. Wagner, T. Modelling of Wind Borne Ice Accretion on Power Transmission Lines, Doctoral Thesis, University of Braunschweig, August 2010
19. White, F.M. 2002. Fluid Mechanics 5th edition. McGraw-Hill Series in Mechanical Engineering, ISBN: 978-0072402179, 866 pp.
20. Wiberg, B.D., Fujiwara, G.E.C., Woodard, B.S., and Bragg, M.B., "Large-Scale, Swept-Wing Icing Simulations in the NASA Glenn Icing Research Tunnel Using LEWICE3D," AIAA Paper 2014-2617, June 2014.
21. http://www.vttresearch.com/Documents/Low%20Carbon%20Energy/Wind%20energy/Icing_Wind_Tunnel_02022016.pdf

Works cited

1. Anderson, D.N., 2004. Manual of Scaling Methods. NASA/CR—2004-212875
2. Bain, M., Gayet, J.F., 1983. Contribution to the modeling of the ice accretion process. Pp. 13–20 in Proceedings of the First International Workshop on Atmospheric Icing of Structures, U. S. Army CRREL Special Report 83–17.
3. Bain, M., Gayet, J.F., 1982. Aircraft measurements of icing in supercooled and water droplet/ice crystal clouds. Journal of Applied Meteorology, vol. 21, pp. 631-641. doi:10.1175/1520-0450(1982)021<0631:AMOIIS>2.0.CO;2
4. Beard, K.V., Pruppacher, H.R., 1969. A Determination of the Terminal Velocity and Drag of Small Water Drops by Means of a Wind Tunnel. Journal of Atmospheric Sciences 26, 1066-1072. doi:10.1175/1520-0469(1969)026<1066:ADOTTV>2.0.CO;2
5. Bidwell, C.S., 2012. Particle Trajectory and Icing Analysis of the E3 Turbofan Engine Using LEWICE3D Version 3, NASA/TM–2012-217696, NASA
6. Bourgault, Y., Habashi, W.G., Dompierre, J., Baruzzi, G.S., 1999. A Finite Element Method Study of Eulerian Droplets Impingement Models. International Journal for Numerical Methods in Fluids, vol. 29, pp. 429 – 449.
7. Bredesen, R. E., Refsum, H., 2015. IceRisk - Methods for evaluating risk causedby ice throw and ice fall from wind turbines and other tall structures, 16thInternational Workshop on Atmospheric Icing, Uppsala, Sweden.
8. Cansdale, J., McNaughtan, M., 1977. Calculation of Surface Temperature and Ice Accretion Rate in a Mixed Water Droplet/ice Crystal Cloud.
9. Cranfield University Icing Tunnel, 2018. URL: https://www.cranfield.ac.uk/facilities/icing-tunnel
10. Demartino C., Koss, H.H., Ricciardelli F., 2013 Experimental study of the effect of icing on the aerodynamics of circular cylinders - Part I: Cross flow. 6th European and African Wind Engineering Conference.
11. Elkhoury, M. 2016. Assessment of turbulence models for the simulation of turbulent flows past bluff bodies. Journal of Wind Engineering and Industrial Aerodynamics, vol. 154, pp. 10–20.
12. FENSAP–ICE User Manual
13. Fikke, S. M., Kristjánsson, J. E., Nygaard, B. E. K., 2008. Modern meteorology and atmospheric icing. In Atmospheric Icing of Power Networks, pp. 1-29, Springer Netherlands.
14. Finstad, K. J. 1986. Numerical and experimental studies of rime ice accretion on cylinders and airfoils. Ph.D. thesis. University of Alberta, Canada. doi:10.7939/R3N58CS1V.
15. Finstad, K.J., Lozowski, E.P., Gates, E.M., 1988a. A computational investigation of water droplet trajectories. Journal of Atmospheric and Oceanic Technology, vol. 5, pp. 160-170. doi:10.1175/1520-0426(1988)005<0160:ACIOWD>2.0.CO;2
16. Finstad, K.J., Lozowski, E.P., Makkonen, L., 1988b. On the median volume diameter approximation for droplet collision efficiency. Journal of the Atmospheric Sciences 45, pp. 4008–4012.doi: 10.1175/1520-0469(1988)045<4008:OTMVDA>2.0.CO;2
17. Fluent Theory Guide
18. Fluent User Manual
19. Fu, P., Farzaneh, M., Bouchard, G., 2006. Two-dimensional modelling of the ice accretion process on transmission line wires and conductors. CRST, vol. 46, pp. 132–146.
20. Gerrard, J. H., 1961, An experimental investigation of the oscillating lift and drag of a circular cylinder shedding turbulent vortices. Journal of Fluid Mechanics, vol. 11, part 2, pp. 244–256
21. Gopalkrishnan, R. 1992. Vortex-Induced Forces on Oscillating Bluff Cylinders. Ph.D. Thesis, MIT/WHOI, WHOI-92-38.

22. Gresho, P. M., Lee, R. L., Sani, R. L., Maslanik, M. K., Eaton, B. E. 1987. The Consistent Galerkin FEM for Computing Derived Boundary Quantities in Thermal and/or Fluids Problems. International Journal for Numerical Methods in Fluids, vol. 7, pp. 371 – 394.
23. Howe, J.B. 1990. The rotating multicylinder method for the measurement of cloud liquid water content and droplet size. CRREL Report.
24. Ingvaldsen, K., Nygaard, B.E.K., Byrkjedal, Ø., Iversen E.C., 2019. Validation of Modelled In-cloud Ice Accretion on Overhead Power Lines at Exposed High Altitude Sites in Norway in: Proceedings – 18th International Workshop on Atmospheric Icing of Structures, IWAIS 2019 - Reykjavík, June 23 – 28.
25. ISO 12494:2001(E), 2001. Atmospheric icing of structures. Standard. International Organization for Standardization. Geneva, CH.
26. IWAIS 2015 Photos of Iced Up Objects. URL: https://iwais.org/photos-of-iced-up-objects/. 16th International Workshop on Atmospheric Icing on Structures. Uppsala, Sweden, 2015.
27. Jasinski, W.J., Noe, S.C., Selig, M.S., Bragg, M.B. Wind Turbine Performance Under Icing Conditions, Transactions of the ASME, Journal of solar energy engineering. New York, NY, USA. February, Vol. 120, pp 60-65.
28. Jones, K.F. 1990, The density of natural ice accretions related to nondimensional icing parameters, Quarterly Journal of Royal Meteorological Society, vol. 116, pp. 477–496.
29. Jones, K.F., Thompson, G., Claffey, K.J., Kelsey, E.P, 2014, Gamma Distribution Parameters for Cloud Drop Distributions from Multicylinder Measurements. Journal of Applied Meteorology and Climatology, vol. 53, pp. 1606 – 1617. doi: 10.1175/JAMC-D-13-0306.1
30. Keyhan, H., 2012, Fluid Structure Interaction (FSI) Based Wind Load Modeling for Dynamic Analysis of Overhead Transmission Lines. Ph.D. Thesis. Department of Civil Engineering and Applied Mechanics, McGill University.
31. Lam, C.K.G., Bremhorst, K. 1981. A Modified Form of the k – ε Model for Predicting Wall Turbulence. Journal of Fluid Engineering. Transactions of ASME, vol. 103, pp. 456 – 460.
32. Landau, L., Lifshitz, E. M. 1959. Fluid Mechanics, Pergamon Press, pp. 96-98.
33. Langmuir, I., Blodgett, K., 1946. A Mathematical Investigation of Water Droplet Trajectories. Army Air Forces technical report 5418. Army Air Forces Headquarters, Air Technical Service Command.
34. Lozowski, E.P., Makkonen, L., 2005. Fifty years of progress in modelling the accumulation of atmospheric ice on power network equipment, in: Proceedings of the 11th International Workshop on Atmospheric Icing of Structures.
35. Lozowski, E.P., Stallabrass, J.R., Hearty, P.F. 1979. The icing of an unheated, non-rotating cylinder in liquid water droplet-ice crystal clouds. National Research Council of Canada, Ottawa, CANADA, Mechanical Engineering Report LTR-LT-96, Feb. 1979.
36. Lozowski, E.P., Stallabrass, J.R., Hearty, P.F., 1983a. The icing of an un-heated, nonrotating cylinder. part I: A simulation model. Journal of Applied Meteorology, vol. 22, pp. 2053-2062.doi:10.1175/1520-0450(1983)022<2053:265 TIOAUN>2.0.CO;2
37. Lozowski, E.P., Stallabrass, J.R., Hearty, P.F., 1983b. The icing of an unheated, nonrotating cylinder. part II: Icing wind tunnel experiments. Journal of Applied Meteorology, vol. 22, pp. 2063-2074.doi:10.1175/1520-0450(1983)022<2063:TIOAUN>2.0.CO;2
38. Macklin, W.C., 1962. The density structure of ice formed by accretion. Quarterly Journal of Royal Meteorological Society, vol. 88 pp. 30–50.
39. Makkonen, L., 1984. Modeling of Ice Accretion on Wires. Journal of Applied Meteorology vol. 23, pp. 929-939. doi:10.1175/1520-0450(1984)023<0929:MOIAOW>2.0.CO;2
40. Makkonen, L., 1985. Heat transfer and icing of a rough cylinder. Cold Regions Science and Technology vol. 10. pp. 105-116. doi:10.1016/0165-232X(85)90022-9
41. Makkonen, L., 1992. Analysis of Rotating Multicylinder Data in Measuring Cloud-Droplet Size and Liquid Water Content. Journal of Atmopheric and Oceanic Technology, vol. 9, pp. 258 – 263.

42. Makkonen, L., 2000. Models for the growth of rime, glaze, icicles and wet snow on structures. Phil. Trans. R. Soc., Lond. A 2000 358 2913-2939; DOI: 10.1098/rsta2000.0690. Published 15 Nov. 2000
43. Makkonen, L., Stallabrass J.R., 1984. Ice accretion on cylinders and wires. National Research Council of Canada. Division of Mechanical Engineering Technical Report TR-LT-05.
44. Makkonen, L., Stallabrass, J.R., 1987. Experiments on the cloud droplet collision efficiency of cylinders. Journal of Applied Meteorology, vol. 26, pp. 1406–1411. doi:10.1175/1520-0450(1987)026<1406:EOTCDC>2.0.CO;2
45. Makkonen, L., Zhang, J., Karlsson, T., Tiihonen, M. 2018. Modelling the growth of large rime ice accretions, Cold Regions Science and technology, vol. 151, pp. 133–137.
46. Maxey, M.R. and Riley, J.J., 1983. Equation of motion for a small rigid sphere in a nonuniform flwo. Phy Fluids 26:883–889.
47. Mei, R., and Adrian, R.J., 1992. Flow past a sphere with an oscillation in the free-stream velocity and unstead drag at finite Reynolds number. J Fluid Mech 237:323-341.
48. Menter, F.R. 1994. Two-Equation Eddy-Viscosity Turbulence Models for Engineering Applications. AIAA Journal, 32 (8): 1598–1605, Bibcode:1994AIAAJ..32.1598M, doi:10.2514/3.12149
49. Menter, F.R. 1992. Improved Two-Equation k – ω Turbulence Models for Aerodynamic Flows. National Aeronautics and Space Administration Ames Research Center. NASA Technical Memorandum 103975.
50. Messinger, B.L., 1953. Equilibrium temperature of an unheated icing surface as a function of airspeed. Jour. Aeronautical Sci., 20, 29 – 41
51. Michaelides, E.E., 1992. A novel way of computing the Basset term in unstead multiphase flow computations. Physics of Fluids A: Fluid Dynamics 4, 1579; doi: 10.1063/1.858430
52. Moreno-Casas, P.A., and Bombardelli, F.A., 2015. Computation of the Basset force: recent advances and environmental flow applications. Envirion Fluid Mech. DOI: 10.1007/s10652-015-9424-1.
53. Morsi, S.A., Alexander, A.J., 1972. An investigation of particle trajectories in twophase flow systems. Journal of Fluid Mechanics, vol. 55, pp. 193 – 208, DOI: 10.1017/S0022112072001806.
54. Murray, B.J., O'Sullivan, D., Atkinson, J.D., Webb M.E., 2012. Ice nucleation by particles immersed in supercooled cloud droplets. The Royal Society of Chemistry, vol. 41, pp. 6519 – 6554.
55. Norberg, C. 2002. Fluctuating lift on a circular cylinder: review and new measurements. Journal of Fluids and Structures, vol. 17, pp. 57–96.
56. Nygaard, B.E.K., Byrkjedal, Ø., Iversen, E., Fredbo, M., Ágústsson, H., Welgaard, Ø., Gutman, I., Karlsson, T., Virk, M.S., Mc Innes, H., 2017. Development of a reliable modeling system for the calculation of rime ice loads on overhead transmission lines, in: Proceedings of the 17th International Workshop on Atmospheric Icing of Structures, Chongqing, China.
57. Nygaard, B.E.K., Fikke, S. M., 2012. Isstorm, Ising på kraftforsyningsnettet. Norges vassdrags- og energidirektorat – rapport 44, 2012
58. Oleskiw, M.M., 1982. a Computer Simulation of Time-Dependent Rime Icing on Airfoils. Ph.D. thesis. University of Alberta, Canada.doi:10.7939/R3QR4NW8V.
59. Papadakis M., Wong, S.-C., and Rachman, A. 2007, A, Large and Small Droplet Impingement Data on Airfoils and Two Simulated Ice Shapes, NASA/TM—2007-213959, October 2007.
60. Papadakis, M., Wongm, S.-C., Rachman, A., Hung, K. E., Vu, G. T., Bidwell, C. S. 2007, Large and Small Droplet Impingement Data on Airfoils and Two Simulated Ice Shapes, NASA/TM–2007-213959
61. Pearcey, T., Hill, G.W., 1956. The accelerated motion of droplets and bubbles. Aust. Jour. Phys., 9, 19–30.
62. Pfaum, J.C., Pruppacher, H.R., 1979. A wind tunnel investigation of the growth of graupel initiated from frozen drops. Journal of Atmospheric Sciences, vol. 36, pp. 680–689.
63. Qing, H., Jian, Z., Mengyan, D., Dongmei., D. Makkonen, L., Tiihonen, M., 2018. Rime icing on bundled conductors. Cold Regions Science and Technology, vol. 158, pp. 230–236.

64. Ratvasky, T.P., Barnhart, B.P., Lee, S. Current Methods for Modeling and Simulating Icing Effects on Aircraft Performance, Stability and Control, NASA/TM—2008-215453, AIAA–2008–6204
65. Rossi, A., Jubayer, C., Koss, H., Arriaga, D., Hangan H. 2020. Combined effects of wind and atmospheric icing on overhead transmission lines. Journal of Wind Engineering and Industrial Aerodynamics, vol. 204.
66. Ruff, G.A., "Analysis and Verification of the Icing Scaling Equations," AEDC-TR-85-30, vol. 1 (rev), March 1986.
67. Schmidt, R.C., Patankar, S.V. 1988. Two-Equation Low-Reynolds-Number Turbulence Modeling of Transitional Boundary Layer Flows Characteristic of Gas Turbine Blades. National Aeronautics and Space Administration Lewis Research Center, NASA Contractor Report 4145.
68. Seifert, H., Westerhellweg, A., Kröning, J., 2003 Risk Analysis Of Ice Throw From Wind Turbines.
69. Selvam, R.P., 1997. Finite element modelling of flow around a circular cylinder using LES. Journal of Wind Engineering and Industrial Aerodynamics, vol. 67&68, pp. 129–139.
70. Shin J., Bond, T.1992, Experimental and Computational Ice Shapes and Resulting Drag Increase for a NACA 0012 Airfoil, NASA Technical Manual 105743, 1992
71. Siemens SWT 2.3-93 Technical Specifications
72. Stallabrass, J.R., 1980. Trawler Icing: A Compilation of Work Done at N.R.C. (Givrage Des Chalutiers: Compilation Des Recherches Effectuees Au C.N.R.). Defense Technical Information Center.
73. Tammelin, B., Cavaliere, M., Holttinen, H., Morgan, C., Seifert, H., K. Säntti, K., 2000 Wind energy production in cold climates (WECO), Finnish Meteorological Institute, EUR 19.398
74. Tanida, Y., Okajima, A., Watanabe, Y., 1973, Stability of a circular cylinder oscillating in uniform flow or in a wake. Journal of Fluid Mechanics, vol. 61, part 4, pp. 769–784.
75. Tritton, D. J. Physical Fluid Dynamics, 2nd ed. Oxford, England: Oxford University Press, 1988.
76. Tsao, J.-C., Anderson, D.N, Additional Study of Water Droplet Median Volume Diameter (MVD) Effects on Ice Shapes, Conference: 42n AIAA Aerospace Sciences Meeting and Exhibit, At Reno, NV, Volume: AIAA 2004-0413, January 2004
77. Tsao, J.-C., Anderson, D.N. 2005, Additional Study of Water Droplet Median Volume Diameter (MVD) Effects on Ice Shapes, NASA/CR–2005-213853
78. Tsao, J.-C., Lee, S. 2012, Evaluation of Icing Scaling on Swept NACA 0012 Airfoil Models, NASA/CR–2012-217419, NASA
79. Turkia, V., Huttunen, S., Wallenius, T. Method for estimating wind turbine production losses due to icing, VTT, 2013, Finland
80. van Hinsberg, M.A.T., ten Thije Boonkkamp, J.H.M., Clercx, H.J.H., 2011. An efficient, second order method for the approximation of the Basset history force. J Comput Phys 230(4):1465–1478.
81. Vestas V112-3.45 Technical Specifications
82. Vojir, D.J., and Michaelides E.E., 1993. Effect of the History Term on the Motion of Rigid Spheres in a Viscous Fluid. Int. J. Multiphase Flow. Vol. 20, No. 3, pp. 547–556.
83. VTT Technical Brochure, 2016. URL: http://www.vttresearch.com/Documents/Low%20Carbon%20Energy/Wind%20energy/Icing_Wind_Tunnel_02022016.pdf
84. Wagner, T. Modelling of Wind Borne Ice Accretion on Power Transmission Lines, Doctoral Thesis, University of Braunschweig, August 2010
85. White, F.M. 2002. Fluid Mechanics 5th edition. McGraw-Hill Series in Mechanical Engineering, ISBN: 978-0072402179, 866 pp.
86. Wiberg, B.D., Fujiwara, G.E.C., Woodard, B.S., and Bragg, M.B., "Large-Scale, Swept-Wing Icing Simulations in the NASA Glenn Icing Research Tunnel Using LEWICE3D," AIAA Paper 2014-2617, June 2014.

87. Wilcox, D.C., 1988, "Re-assessment of the scale-determining equation for advanced turbulence models", AIAA Journal, vol. 26, no. 11, pp. 1299-1310.
88. Wright, W., 2008, User's Manual for LEWICE Version 3.2, NASA/CR–2008-214255, NASA
89. Yoon, B., Ettema, R., Droplet trajectories and icing collision efficiencies for cylinders determined using LDV. CRST 21, 4, July 1993, pp. 381-397
90. Zhang, J., Qing, H., Makkonen, L. 2017 A novel water droplet size parameter for calculation of icing on power lines. Coltec (2017) https://doi.org/10.1016/j.coldregions.2018.01.021, pre-print

Appendix

Table A1 – Mean values, standard deviations, variances and centiles of the accreted ice masses in the Makkonen and Stallabrass experiments calculated with the Langmuir distributions in the analytical model Mean values are in g.

Test	$\bar{x}$	μ	σ	*A*	*B*	*C*	*D*	*E*	*F*	*G*	*H*	*J*
1	8.73	0.325	0.106	0.1	-2.5	-4.5	-6.0	-7.3	-8.6	-9.5	-10.1	-10.8
2	7.32	0.155	0.024	1.7	-1.0	-2.7	-3.5	-4.1	-4.8	-5.0	-4.6	-4.0
3	7.44	0.152	0.023	23.5	20.2	18.3	17.3	16.6	15.8	15.6	16.2	16.9
4	7.62	0.149	0.022	1.6	-1.1	-2.7	-3.4	-4.0	-4.6	-4.7	-4.1	-3.5
5	6.52	0.094	0.009	2.8	0.2	-1.1	-1.4	-1.5	-1.8	-1.3	-0.2	1.1
6	18.55	1.148	1.318	-6.1	-7.4	-7.0	-4.7	-2.6	0.1	3.0	6.0	11.4
7	14.43	1.709	2.921	-11.7	-11.7	-9.3	-5.0	-0.2	4.6	9.4	14.7	25.0
8	14.57	1.717	2.948	1.8	1.7	4.5	9.3	14.9	20.4	25.9	31.9	43.8
9	14.83	1.719	2.953	-3.9	-4.0	-1.5	3.0	8.0	13.2	18.3	23.9	34.9
10	11.87	1.875	3.515	-8.6	-7.5	-3.4	3.2	10.1	16.8	24.1	32.1	45.9
11	25.40	3.042	9.252	-5.1	-5.1	-2.4	2.2	7.5	12.7	18.0	23.7	34.9
12	19.15	3.777	14.263	-18.7	-16.4	-11.4	-3.3	4.6	12.7	21.9	30.8	46.5
13	19.33	3.786	14.333	-12.4	-10.1	-4.8	3.8	12.2	20.9	30.7	40.2	57.0
14	19.69	3.786	14.333	-20.8	-18.9	-14.2	-6.7	0.7	8.3	16.9	25.4	40.4
15	15.47	3.854	14.850	-11.4	-6.6	1.8	13.7	25.5	39.3	52.5	65.5	88.5
16	27.30	7.013	49.177	-38.0	-34.4	-28.3	-19.7	-11.0	-0.9	8.8	18.3	35.3
17	27.53	7.002	49.034	-41.4	-38.2	-32.5	-24.5	-16.4	-7.1	1.9	10.8	26.7
18	19.45	7.255	52.639	-35.9	-25.7	-12.9	5.4	23.7	42.5	61.1	79.7	113.7
19	19.64	7.256	52.653	-42.4	-33.6	-22.4	-6.4	9.8	26.3	42.6	59.0	89.0
20	20.02	7.247	52.523	-45.5	-37.8	-27.7	-13.4	1.3	16.3	31.1	46.0	73.3
21	15.19	6.806	46.318	-46.4	-30.4	-11.8	10.6	33.7	57.8	82.0	106.5	152.2
22	7.13	0.351	0.123	4.1	1.6	-0.4	-2.4	-4.4	-6.2	-7.6	-8.8	-11.0
23	6.41	0.255	0.065	7.8	5.1	3.0	1.3	-0.4	-1.8	-2.8	-3.7	-4.8
24	5.54	0.182	0.033	9.4	6.6	4.6	3.2	1.9	0.6	-0.1	-0.6	-1.0
25	16.69	0.362	0.131	-12.1	-13.9	-14.6	-14.1	-13.6	-13.1	-12.0	-10.5	-8.3
26	14.05	0.748	0.559	-1.0	-2.4	-2.2	-0.2	1.7	4.0	6.8	9.6	14.4
27	11.70	0.923	0.852	-2.8	-3.8	-2.7	0.4	3.3	7.0	10.6	14.5	21.6
28	23.54	1.400	1.961	-16.2	-17.3	-17.0	-15.0	-13.2	-10.9	-8.4	-5.7	-1.3
29	19.30	2.089	4.362	-4.2	-4.4	-2.1	2.1	6.6	11.4	16.3	21.3	31.5
30	15.80	2.278	5.188	6.9	7.7	11.9	18.4	25.8	33.0	40.3	48.6	63.7
31	26.54	4.291	18.417	-21.8	-20.7	-17.1	-11.5	-5.3	0.8	6.9	14.0	26.4
32	20.73	5.009	25.088	-13.5	-9.4	-2.1	9.0	19.9	32.3	44.8	57.1	79.2
33	16.50	4.908	24.092	-18.5	-12.1	-1.7	12.0	27.3	43.5	59.3	75.0	103.4

Table A2 – Mean values, standard deviations, variances and centiles of the overall collision efficiencies in the Makkonen and Stallabrass experiments calculated with the Langmuir distributions in the analytical model.

Test	$\bar{x}$	μ	σ	*A*	*B*	*C*	*D*	*E*	*F*	*G*	*H*	*J*
1	0.52	0.017	0.000	-0.9	-3.1	-4.7	-6.0	-7.2	-8.3	-9.1	-9.6	-10.2
2	0.46	0.009	0.000	0.5	-1.8	-3.2	-4.0	-4.5	-5.1	-5.3	-5.0	-4.5
3	0.46	0.008	0.000	4.2	1.9	0.4	-0.3	-0.9	-1.5	-1.6	-1.2	-0.8
4	0.46	0.008	0.000	3.6	1.3	-0.1	-0.8	-1.3	-1.9	-2.0	-1.6	-1.1
5	0.43	0.005	0.000	-4.2	-6.3	-7.4	-7.7	-7.8	-8.0	-7.7	-6.8	-5.8
6	0.31	0.018	0.000	-6.5	-7.8	-7.3	-5.2	-3.2	-0.7	2.0	4.8	9.8
7	0.25	0.029	0.001	-10.9	-10.9	-8.6	-4.5	0.1	4.7	9.3	14.2	23.9
8	0.26	0.028	0.001	-2.8	-2.9	-0.4	4.0	9.0	13.9	18.9	24.2	34.7
9	0.26	0.028	0.001	-6.0	-6.1	-3.8	0.3	5.0	9.6	14.3	19.3	29.3
10	0.22	0.034	0.001	-8.2	-7.2	-3.2	3.1	9.7	16.2	23.1	30.7	43.6
11	0.25	0.029	0.001	-4.7	-4.7	-2.1	2.4	7.4	12.4	17.4	22.8	33.4
12	0.20	0.037	0.001	-20.8	-18.7	-13.9	-6.3	1.1	8.6	17.2	25.4	39.8
13	0.20	0.037	0.001	-15.8	-13.7	-8.7	-0.8	7.0	14.9	23.8	32.5	47.6
14	0.20	0.037	0.001	-23.0	-21.2	-16.8	-9.9	-3.0	4.0	11.9	19.6	33.2
15	0.17	0.041	0.002	-16.5	-12.0	-4.3	6.6	17.4	29.9	41.8	53.4	73.9
16	0.16	0.041	0.002	-38.9	-35.4	-29.5	-21.1	-12.7	-3.0	6.3	15.4	31.5
17	0.16	0.041	0.002	-41.4	-38.2	-32.6	-24.7	-16.9	-7.8	1.0	9.6	24.8
18	0.12	0.044	0.002	-39.6	-30.1	-18.1	-1.2	15.9	33.2	50.3	67.3	98.4
19	0.12	0.044	0.002	-44.0	-35.5	-24.8	-9.4	6.0	21.7	37.1	52.6	80.7

20	0.12	0.043	0.002	-46.6	-39.2	-29.5	-15.7	-1.6	12.7	26.8	40.9	66.6
21	0.10	0.044	0.002	-44.9	-28.6	-9.7	13.0	36.4	60.7	85.0	109.5	155.0
22	0.59	0.025	0.001	0.9	-1.2	-2.9	-4.5	-6.3	-7.8	-9.0	-10.0	-11.9
23	0.54	0.019	0.000	2.5	0.2	-1.5	-2.9	-4.3	-5.5	-6.4	-7.1	-8.1
24	0.51	0.015	0.000	7.5	5.1	3.4	2.1	0.9	-0.1	-0.8	-1.3	-1.7
25	0.38	0.008	0.000	-14.8	-16.5	-17.1	-16.7	-16.2	-15.7	-14.7	-13.4	-11.4
26	0.32	0.016	0.000	-5.9	-7.2	-7.0	-5.2	-3.5	-1.4	1.1	3.7	8.0
27	0.29	0.022	0.000	-3.9	-4.8	-3.7	-0.8	2.0	5.4	8.9	12.5	19.2
28	0.31	0.018	0.000	-14.9	-16.0	-15.7	-13.7	-12.0	-9.8	-7.3	-4.8	-0.4
29	0.26	0.027	0.001	-8.5	-8.7	-6.7	-2.8	1.4	5.8	10.3	14.9	24.1
30	0.23	0.032	0.001	5.9	6.7	10.7	17.0	24.1	31.0	38.0	45.8	60.1
31	0.21	0.034	0.001	-22.2	-21.1	-17.5	-12.0	-6.0	-0.1	5.9	12.7	24.8
32	0.17	0.039	0.002	-17.2	-13.3	-6.4	4.1	14.4	26.0	37.8	49.3	69.9
33	0.14	0.042	0.002	-20.2	-13.9	-3.9	9.5	24.2	39.8	55.0	70.1	97.3

Table A3 – Mean values, standard deviations, variances and centiles of the droplet's inertia parameter in the Makkonen and Stallabrass experiments calculated with the Langmuir distributions in the analytical model.

Test	$\bar{x}$	μ	σ	***A***	***B***	***C***	***D***	***E***	***F***	***G***	***H***	***J***
1	8.73	0.325	0.106	0.1	-2.5	-4.5	-6.0	-7.3	-8.6	-9.5	-10.1	-10.8
2	7.32	0.155	0.024	1.7	-1.0	-2.7	-3.5	-4.1	-4.8	-5.0	-4.6	-4.0
3	7.44	0.152	0.023	23.5	20.2	18.3	17.3	16.6	15.8	15.6	16.2	16.9
4	7.62	0.149	0.022	1.6	-1.1	-2.7	-3.4	-4.0	-4.6	-4.7	-4.1	-3.5
5	6.52	0.094	0.009	2.8	0.2	-1.1	-1.4	-1.5	-1.8	-1.3	-0.2	1.1
6	18.55	1.148	1.318	-6.1	-7.4	-7.0	-4.7	-2.6	0.1	3.0	6.0	11.4
7	14.43	1.709	2.921	-11.7	-11.7	-9.3	-5.0	-0.2	4.6	9.4	14.7	25.0
8	14.57	1.717	2.948	1.8	1.7	4.5	9.3	14.9	20.4	25.9	31.9	43.8
9	14.83	1.719	2.953	-3.9	-4.0	-1.5	3.0	8.0	13.2	18.3	23.9	34.9
10	11.87	1.875	3.515	-8.6	-7.5	-3.4	3.2	10.1	16.8	24.1	32.1	45.9
11	25.40	3.042	9.252	-5.1	-5.1	-2.4	2.2	7.5	12.7	18.0	23.7	34.9
12	19.15	3.777	14.263	-18.7	-16.4	-11.4	-3.3	4.6	12.7	21.9	30.8	46.5
13	19.33	3.786	14.333	-12.4	-10.1	-4.8	3.8	12.2	20.9	30.7	40.2	57.0
14	19.69	3.786	14.333	-20.8	-18.9	-14.2	-6.7	0.7	8.3	16.9	25.4	40.4
15	15.47	3.854	14.850	-11.4	-6.6	1.8	13.7	25.5	39.3	52.5	65.5	88.5
16	27.30	7.013	49.177	-38.0	-34.4	-28.3	-19.7	-11.0	-0.9	8.8	18.3	35.3
17	27.53	7.002	49.034	-41.4	-38.2	-32.5	-24.5	-16.4	-7.1	1.9	10.8	26.7
18	19.45	7.255	52.639	-35.9	-25.7	-12.9	5.4	23.7	42.5	61.1	79.7	113.7
19	19.64	7.256	52.653	-42.4	-33.6	-22.4	-6.4	9.8	26.3	42.6	59.0	89.0
20	20.02	7.247	52.523	-45.5	-37.8	-27.7	-13.4	1.3	16.3	31.1	46.0	73.3
21	15.19	6.806	46.318	-46.4	-30.4	-11.8	10.6	33.7	57.8	82.0	106.5	152.2
22	7.13	0.351	0.123	4.1	1.6	-0.4	-2.4	-4.4	-6.2	-7.6	-8.8	-11.0
23	6.41	0.255	0.065	7.8	5.1	3.0	1.3	-0.4	-1.8	-2.8	-3.7	-4.8
24	5.54	0.182	0.033	9.4	6.6	4.6	3.2	1.9	0.6	-0.1	-0.6	-1.0
25	16.69	0.362	0.131	-12.1	-13.9	-14.6	-14.1	-13.6	-13.1	-12.0	-10.5	-8.3
26	14.05	0.748	0.559	-1.0	-2.4	-2.2	-0.2	1.7	4.0	6.8	9.6	14.4
27	11.70	0.923	0.852	-2.8	-3.8	-2.7	0.4	3.3	7.0	10.6	14.5	21.6
28	23.54	1.400	1.961	-16.2	-17.3	-17.0	-15.0	-13.2	-10.9	-8.4	-5.7	-1.3
29	19.30	2.089	4.362	-4.2	-4.4	-2.1	2.1	6.6	11.4	16.3	21.3	31.5
30	15.80	2.278	5.188	6.9	7.7	11.9	18.4	25.8	33.0	40.3	48.6	63.7
31	26.54	4.291	18.417	-21.8	-20.7	-17.1	-11.5	-5.3	0.8	6.9	14.0	26.4
32	20.73	5.009	25.088	-13.5	-9.4	-2.1	9.0	19.9	32.3	44.8	57.1	79.2
33	16.50	4.908	24.092	-18.5	-12.1	-1.7	12.0	27.3	43.5	59.3	75.0	103.4

Table A4 – Mean values, standard deviations, variances and centiles of the end iced cylinder diameters in the Makkonen and Stallabrass experiments calculated with the Langmuir distributions in the analytical model. Mean values are in cm.

Test	$\bar{x}$	μ	σ	***A***	***B***	***C***	***D***	***E***	***F***	***G***	***H***	***J***
1	1.56	0.014	0.000	2.4	1.7	1.2	0.8	0.4	0.1	-0.1	-0.3	-0.4
2	1.50	0.007	0.000	2.4	1.8	1.4	1.2	1.1	0.9	0.9	1.1	1.3
3	1.55	0.006	0.000	10.4	9.7	9.3	9.2	9.1	8.9	8.9	9.1	9.4
4	1.63	0.006	0.000	2.9	2.3	1.9	1.8	1.7	1.6	1.7	1.9	2.1
5	1.46	0.005	0.000	2.9	2.3	2.0	2.0	2.0	2.0	2.1	2.4	2.8
6	3.64	0.025	0.001	-0.9	-1.1	-1.0	-0.7	-0.5	-0.2	0.1	0.5	1.0
7	3.56	0.039	0.001	-0.7	-0.7	-0.4	0.0	0.4	0.9	1.3	1.8	2.6

8	3.62	0.042	0.002	1.9	2.0	2.2	2.7	3.2	3.6	4.1	4.6	5.6
9	3.71	0.047	0.002	-1.3	-1.3	-1.0	-0.6	0.0	0.5	1.0	1.5	2.5
10	3.51	0.044	0.002	-0.5	-0.4	-0.1	0.4	0.9	1.4	1.9	2.4	3.4
11	4.91	0.049	0.002	0.0	0.1	0.3	0.6	1.0	1.4	1.8	2.3	3.1
12	4.82	0.063	0.004	-1.5	-1.3	-1.0	-0.5	0.0	0.5	1.1	1.6	2.6
13	4.88	0.069	0.005	-0.5	-0.3	0.0	0.6	1.1	1.7	2.3	2.9	3.9
14	4.99	0.077	0.006	-3.2	-3.0	-2.6	-2.0	-1.4	-0.8	-0.2	0.4	1.5
15	4.76	0.067	0.004	-0.8	-0.5	-0.1	0.4	0.9	1.5	2.1	2.6	3.6
16	7.93	0.071	0.005	-1.4	-1.3	-1.0	-0.7	-0.3	0.0	0.4	0.7	1.3
17	7.99	0.077	0.006	-1.2	-1.0	-0.8	-0.4	0.0	0.4	0.8	1.1	1.8
18	7.86	0.077	0.006	-0.7	-0.5	-0.2	0.2	0.6	1.0	1.3	1.7	2.4
19	7.91	0.085	0.007	-1.2	-0.9	-0.6	-0.2	0.2	0.6	1.0	1.4	2.2
20	8.01	0.092	0.009	-3.1	-2.8	-2.5	-2.0	-1.6	-1.2	-0.7	-0.3	0.5
21	7.82	0.075	0.006	-5.2	-4.9	-4.6	-4.3	-3.9	-3.6	-3.2	-2.9	-2.2
22	1.46	0.017	0.000	0.4	-0.2	-0.7	-1.2	-1.6	-2.1	-2.4	-2.7	-3.2
23	1.43	0.012	0.000	3.5	2.9	2.5	2.1	1.8	1.4	1.2	1.0	0.8
24	1.38	0.009	0.000	3.8	3.2	2.9	2.6	2.3	2.1	1.9	1.9	1.8
25	3.57	0.008	0.000	-0.8	-1.0	-1.1	-1.0	-1.0	-0.9	-0.8	-0.6	-0.4
26	3.52	0.016	0.000	0.2	0.1	0.1	0.3	0.5	0.7	0.9	1.2	1.6
27	3.47	0.021	0.000	0.1	0.0	0.1	0.3	0.6	0.8	1.1	1.3	1.9
28	4.84	0.022	0.000	-0.7	-0.8	-0.8	-0.6	-0.5	-0.3	0.0	0.2	0.6
29	4.79	0.033	0.001	0.0	0.0	0.1	0.4	0.7	0.9	1.2	1.5	2.1
30	4.73	0.037	0.001	0.6	0.7	0.9	1.1	1.5	1.8	2.1	2.5	3.1
31	7.89	0.041	0.002	-0.8	-0.8	-0.7	-0.5	-0.3	-0.1	0.1	0.4	0.8
32	7.84	0.049	0.002	0.0	0.1	0.2	0.5	0.7	0.9	1.2	1.5	1.9
33	7.80	0.050	0.002	-0.4	-0.3	-0.1	0.1	0.4	0.6	0.9	1.1	1.6

Table A5 – Mean values, standard deviations, variances and centiles of the accreted ice densities in the Makkonen and Stallabrass experiments calculated with the Langmuir distributions in the analytical model. Mean values are in kg/m^3.

Test	$\bar{x}$	μ	σ	***A***	***B***	***C***	***D***	***E***	***F***	***G***	***H***	***J***
1	801.9	4.088	16.708	-7.1	-7.3	-7.5	-7.7	-7.9	-8.1	-8.2	-8.3	-8.5
2	776.3	3.626	13.149	-6.8	-7.1	-7.3	-7.5	-7.7	-7.8	-8.0	-8.0	-8.1
3	694.8	4.429	19.618	-14.3	-14.6	-14.9	-15.2	-15.4	-15.6	-15.7	-15.8	-15.9
4	601.1	5.143	26.445	-8.8	-9.4	-9.8	-10.1	-10.4	-10.7	-11.0	-11.1	-11.2
5	760.5	3.112	9.682	-8.7	-9.0	-9.3	-9.4	-9.6	-9.7	-9.8	-9.8	-9.9
6	759.9	2.234	4.990	-8.4	-8.7	-8.8	-8.7	-8.6	-8.5	-8.3	-8.2	-7.9
7	720.7	7.074	50.043	-4.7	-5.0	-4.9	-4.5	-4.1	-3.7	-3.3	-2.9	-2.1
8	627.7	8.432	71.095	-16.2	-16.5	-16.3	-15.9	-15.4	-14.9	-14.5	-14.0	-12.9
9	524.0	9.502	90.293	7.5	6.9	7.1	7.9	8.7	9.6	10.4	11.3	13.1
10	695.6	11.266	126.929	-3.8	-3.9	-3.6	-2.9	-2.2	-1.6	-1.0	-0.3	0.9
11	738.3	6.996	48.949	-6.2	-6.4	-6.2	-5.9	-5.5	-5.1	-4.8	-4.4	-3.6
12	692.0	15.451	238.743	0.5	0.5	1.1	2.2	3.1	4.0	4.9	5.9	7.3
13	593.5	18.193	330.993	-6.3	-6.3	-5.5	-4.2	-2.9	-1.8	-0.6	0.7	2.5
14	483.3	20.410	416.563	9.2	9.2	10.5	12.6	14.7	16.5	18.5	20.5	23.7
15	661.9	22.359	499.931	0.3	0.7	1.9	3.5	5.0	6.4	7.8	9.0	10.9
16	689.8	22.399	501.702	-5.8	-5.4	-4.3	-2.8	-1.5	-0.2	1.0	2.1	3.8
17	591.4	26.290	691.163	-18.2	-17.7	-16.5	-14.7	-13.1	-11.6	-10.0	-8.7	-6.7
18	625.9	41.275	1703.634	-10.9	-8.8	-6.0	-2.8	0.1	2.5	4.6	6.4	9.1
19	516.6	47.468	2253.178	-11.3	-8.5	-4.5	0.1	4.3	7.9	10.9	13.5	17.5
20	398.7	52.294	2734.713	6.4	11.2	18.5	26.7	34.5	41.1	46.8	51.7	59.3
21	582.5	57.367	3290.931	5.3	11.2	17.5	23.8	28.8	33.0	36.5	39.5	44.1
22	843.6	3.726	13.884	-3.5	-3.6	-3.8	-4.0	-4.1	-4.3	-4.4	-4.6	-4.8
23	825.7	3.785	14.325	-6.5	-6.7	-6.9	-7.1	-7.3	-7.4	-7.6	-7.7	-7.9
24	814.0	3.718	13.825	-6.8	-7.0	-7.2	-7.4	-7.5	-7.7	-7.8	-8.0	-8.1
25	814.3	1.484	2.203	-3.8	-4.0	-4.2	-4.2	-4.3	-4.4	-4.4	-4.3	-4.2
26	787.4	1.720	2.958	-3.9	-4.1	-4.2	-4.2	-4.1	-4.1	-3.9	-3.8	-3.5
27	769.1	3.451	11.911	-5.2	-5.5	-5.5	-5.4	-5.2	-5.0	-4.8	-4.6	-4.2
28	799.1	2.018	4.071	-4.8	-5.1	-5.2	-5.1	-5.0	-4.9	-4.8	-4.6	-4.4
29	767.6	5.763	33.210	-3.5	-3.7	-3.6	-3.3	-3.0	-2.7	-2.4	-2.0	-1.4
30	746.0	9.150	83.716	-8.0	-8.1	-7.9	-7.4	-6.9	-6.4	-6.0	-5.5	-4.6
31	764.7	10.351	107.138	1.7	1.7	2.0	2.6	3.2	3.8	4.3	4.9	5.9
32	736.9	18.715	350.236	-6.3	-6.0	-5.3	-4.1	-3.1	-2.2	-1.2	-0.3	1.1
33	692.9	27.051	731.767	0.7	1.5	3.0	4.9	6.6	8.4	9.9	11.2	13.2

Table A6 – Mean values, standard deviations, variances and centiles of the accreted ice masses in the FRonTLINES experiments calculated with the Langmuir and experimental distributions in the analytical model Mean values are in g.

Test	$\bar{x}$	μ	σ	*A*	*B*	*C*	*D*	*E*	*F*	*G*	*H*	*J*	*VTT*
1	1.72	0.652	0.425	-33.6	-18.2	0.4	23.5	46.3	69.2	91.3	113.1	151.9	34.5
2	1.60	0.979	0.958	-68.6	-26.8	10.2	57.6	109.0	164.2	220.7	278.6	388.2	83.4
3	1.60	1.191	1.418	-51.3	-46.4	-22.7	17.2	76.0	144.7	219.9	301.0	465.0	50.1
4	1.59	1.247	1.554	-41.2	-41.2	-29.2	5.6	51.2	119.8	200.6	290.3	478.7	32.7
5	1.66	1.246	1.553	-5.3	-5.3	-5.3	5.3	32.7	92.1	167.3	255.3	492.4	20.1
6	4.81	0.947	0.896	-15.3	-12.3	-6.3	3.0	11.8	21.5	31.4	40.8	57.2	9.5
7	4.58	3.000	8.998	-83.3	-72.5	-56.9	-36.1	-12.7	13.3	40.7	69.4	125.5	-25.1

Table A7 – Mean values, standard deviations, variances and centiles of the overall collision efficiencies in the FRonTLINES experiments calculated with the Langmuir and experimental distributions in the analytical model.

Test	$\bar{x}$	μ	σ	*A*	*B*	*C*	*D*	*E*	*F*	*G*	*H*	*J*	*VTT*
1	0.126	0.047	0.002	-34.2	-18.9	-0.6	22.1	44.6	67.0	88.7	110.0	147.9	32.9
2	0.070	0.043	0.002	-68.8	-27.2	9.6	56.7	107.7	162.5	218.4	275.8	384.1	82.4
3	0.044	0.033	0.001	-52.4	-47.6	-24.5	14.3	71.7	138.8	212.1	291.1	450.7	46.4
4	0.035	0.028	0.001	-41.2	-41.2	-29.2	5.6	51.1	119.7	200.6	290.2	478.2	32.7
5	0.022	0.016	0.000	-9.1	-9.1	-9.1	1.0	27.3	84.3	156.3	240.8	468.2	15.3
6	0.199	0.039	0.001	-16.3	-13.4	-7.5	1.5	10.1	19.4	29.0	38.2	53.9	7.8
7	0.058	0.038	0.001	-72.2	-54.2	-28.2	6.4	45.4	88.6	134.1	181.8	274.8	24.7

Table A8 – Mean values, standard deviations, variances and centiles of the droplet's inertia parameter in the FRonTLINES experiments calculated with the Langmuir and experimental distributions in the analytical model.

Test	$\bar{x}$	μ	σ	*A*	*B*	*C*	*D*	*E*	*F*	*G*	*H*	*J*	*VTT*
1	0.66	0.414	0.171	-12.6	-5.3	5.8	24.0	48.3	81.6	126.9	190.0	399.7	36.5
2	0.42	0.253	0.064	-12.4	3.6	16.8	35.6	60.1	93.5	139.1	202.6	413.3	47.1
3	0.30	0.157	0.025	30.8	36.1	47.1	65.9	90.5	124.0	169.8	233.4	445.0	76.6
4	0.27	0.124	0.015	63.5	65.0	73.3	87.2	111.7	145.4	191.1	254.9	466.7	101.1
5	0.21	0.066	0.004	178.7	178.7	179.2	186.4	204.3	231.5	269.8	330.7	543.5	196.1
6	1.11	0.706	0.498	-13.4	-7.6	2.1	18.7	41.3	72.9	117.3	179.7	386.9	31.6
7	0.38	0.222	0.049	-6.6	9.7	22.8	41.7	66.2	99.7	145.4	209.0	420.3	54.3

Table A9 – Mean values, standard deviations, variances and centiles of the end iced cylinder diameters in the FRonTLINES experiments calculated with the Langmuir and experimental distributions in the analytical model. Mean values are in mm.

Test	$\bar{x}$	μ	σ	*A*	*B*	*C*	*D*	*E*	*F*	*G*	*H*	*J*	*VTT*
1	30.5	0.138	0.019	-96.7	-0.3	-0.2	0.0	0.2	0.4	0.6	0.7	0.9	1.2
2	50.4	0.120	0.014	-96.0	-0.6	-0.2	-0.3	-0.3	-0.2	-0.1	0.0	0.1	0.3
3	80.4	0.108	0.012	-96.3	-0.2	-0.2	0.0	0.1	0.0	0.1	0.1	0.2	0.3
4	100.3	0.109	0.012	-96.0	-0.1	-0.1	0.0	0.1	0.2	0.1	0.1	0.1	0.2
5	170.3	0.108	0.012	-97.1	0.0	0.0	0.0	0.0	0.0	0.1	0.2	0.1	0.1
6	31.1	0.176	0.031	-80.5	0.1	0.2	0.3	0.6	0.8	1.1	1.3	1.5	1.9
7	100.5	0.162	0.026	-93.0	-0.1	-0.1	-0.1	0.0	0.0	0.1	0.2	0.3	0.4

Table A10 – Mean values, standard deviations, variances and centiles of the accreted ice densities. in the FRonTLINES experiments calculated with the Langmuir and experimental distributions in the analytical model. Mean values are in kg/m^3.

Test	$\bar{x}$	μ	σ	*A*	*B*	*C*	*D*	*E*	*F*	*G*	*H*	*J*	*VTT*
1	405	57	3219	-99.7	5.9	15.1	24.8	35.8	44.5	51.6	57.4	62.5	70.0
2	274	112	12525	-98.2	-11.9	-11.9	57.8	118.8	163.5	198.7	226.5	249.5	283.1
3	197	103	10666	-97.0	0.0	0.0	0.0	0.0	79.2	143.1	192.0	231.3	287.5
4	168	93	8567	-96.0	0.0	0.0	0.0	0.0	1.4	83.2	144.1	192.0	259.6
5	125	54	2934	-95.0	0.0	0.0	0.0	0.0	0.0	0.0	9.0	69.6	175.7
6	574	19	370	-98.8	9.9	10.0	11.2	13.1	14.8	16.3	18.0	19.6	21.9
7	329	130	16828	-96.2	-45.0	-24.1	28.0	69.2	99.2	122.7	141.2	156.5	178.9